

1

<sup>2</sup>A SEARCH FOR LONG-LIVED, CHARGED, SUPERSYMMETRIC PARTICLES  
<sup>3</sup>USING IONIZATION WITH THE ATLAS DETECTOR

<sup>4</sup>BRADLEY AXEN

5



6

September 2016 – Version 0.57

<sup>8</sup> Bradley Axen: *A Search for Long-Lived, Charged, Supersymmetric Particles using*  
<sup>9</sup> *Ionization with the ATLAS Detector*, Subtitle, © September 2016

<sup>10</sup> The dissertation of Bradley Axen, titled *A Search for Long-Lived, Charged, Super-*  
<sup>11</sup> *symmetric Particles using Ionization with the ATLAS Detector*, is approved:

<sup>12</sup> \_\_\_\_\_  
<sup>13</sup> Chair \_\_\_\_\_ Date

<sup>14</sup> \_\_\_\_\_  
<sup>15</sup> \_\_\_\_\_ Date

<sup>16</sup> \_\_\_\_\_  
<sup>17</sup> \_\_\_\_\_ Date

<sup>18</sup> University of California, Berkeley

19

Usually a quotation.

20

Dedicated to.

<sub>21</sub> ABSTRACT

---

<sub>22</sub> How to write a good abstract:

<sub>23</sub> <https://plg.uwaterloo.ca/~migod/research/beck00PSLA.html>

24 PUBLICATIONS

---

25 Some ideas and figures have appeared previously in the following publications:

26

27 Put your publications from the thesis here. The packages `multibib` or `bibtopic`  
28 etc. can be used to handle multiple different bibliographies in your document.

30 ACKNOWLEDGEMENTS

---

31 Put your acknowledgements here.

32

33 And potentially a second round.

34

35 CONTENTS

---

36	I	INTRODUCTION	1
37	1	INTRODUCTION	2
38	II	THEORETICAL CONTEXT	3
39	2	STANDARD MODEL	4
40	2.1	Action and the Lagrangian . . . . .	4
41	2.2	Gauge Invariance and Forces . . . . .	5
42	2.2.1	$SU(2) \times U(1)$ and the Electroweak Force . . . . .	7
43	2.2.2	$SU(3)$ and the Strong Force . . . . .	7
44	2.3	Noether's Theorem, Charges, and Matter . . . . .	7
45	2.3.1	Quarks . . . . .	8
46	2.3.2	Leptons . . . . .	9
47	2.3.3	Chirality . . . . .	9
48	2.4	Higgs Mechanism and Mass . . . . .	10
49	2.5	Phenomenology . . . . .	11
50	2.5.1	Electroweak Physics . . . . .	11
51	2.5.2	Strong Physics . . . . .	12
52	2.5.3	Proton-Proton Collisions . . . . .	12
53	2.6	Limitations . . . . .	13
54	2.6.1	Theoretical Concerns . . . . .	13
55	2.6.2	Cosmological Observations . . . . .	15
56	3	SUPERSYMMETRY	17
57	3.1	Structure . . . . .	17
58	3.1.1	Simplified Models . . . . .	18
59	3.2	Motivation . . . . .	19
60	3.3	Long-Lived Particles . . . . .	20
61	III	EXPERIMENTAL STRUCTURE AND RECONSTRUCTION	22
62	4	THE LARGE HADRON COLLIDER	23
63	4.1	Injection Chain . . . . .	24
64	4.2	Design . . . . .	25
65	4.2.1	Layout . . . . .	25
66	4.2.2	Magnets . . . . .	26
67	4.2.3	RF Cavities . . . . .	27
68	4.2.4	Beam . . . . .	29
69	4.3	Luminosity Parameters . . . . .	29
70	4.4	Delivered Luminosity . . . . .	30
71	5	THE ATLAS DETECTOR	33
72	5.1	Coordinate System . . . . .	35
73	5.2	Magnetic Field . . . . .	36
74	5.3	Inner Detector . . . . .	38

75	5.3.1	Pixel Detector . . . . .	41
76	5.3.2	Semiconductor Tracker . . . . .	43
77	5.3.3	Transition Radiation Tracker . . . . .	46
78	5.4	Calorimetry . . . . .	47
79	5.4.1	Electromagnetic Calorimeter . . . . .	48
80	5.4.2	Hadronic Calorimeters . . . . .	49
81	5.5	Muon Spectrometer . . . . .	51
82	5.5.1	Monitored Drift Tube . . . . .	53
83	5.5.2	Resistive Plate Chamber . . . . .	54
84	5.5.3	Cathode Strip Chamber . . . . .	54
85	5.5.4	Thin Gap Chamber . . . . .	55
86	5.6	Trigger . . . . .	56
87	6	EVENT RECONSTRUCTION	60
88	6.1	Charged Particles . . . . .	60
89	6.1.1	Pixel Neural Network . . . . .	62
90	6.1.2	Pixel dE/dx . . . . .	63
91	6.1.3	Vertex Reconstruction . . . . .	64
92	6.2	Electrons and Photons . . . . .	64
93	6.2.1	Photon Identification . . . . .	66
94	6.2.2	Electron Identification . . . . .	66
95	6.3	Muons . . . . .	66
96	6.3.1	Muon Identification . . . . .	67
97	6.4	Jets . . . . .	67
98	6.4.1	Topological Clustering . . . . .	67
99	6.4.2	Jet Algorithms . . . . .	69
100	6.4.3	Jet Energy Scale . . . . .	69
101	6.5	Missing Transverse Energy . . . . .	70
102	IV	CALORIMETER RESPONSE	73
103	7	RESPONSE MEASUREMENT WITH SINGLE HADRONS	74
104	7.1	Dataset and Simulation . . . . .	75
105	7.1.1	Data Samples . . . . .	75
106	7.1.2	Simulated Samples . . . . .	75
107	7.1.3	Event Selection . . . . .	75
108	7.2	Inclusive Hadron Response . . . . .	76
109	7.2.1	E/p Distribution . . . . .	76
110	7.2.2	Zero Fraction . . . . .	77
111	7.2.3	Neutral Background Subtraction . . . . .	79
112	7.2.4	Corrected Response . . . . .	80
113	7.2.5	Additional Studies . . . . .	82
114	7.3	Identified Particle Response . . . . .	85
115	7.3.1	Decay Reconstruction . . . . .	86
116	7.3.2	Identified Response . . . . .	87
117	7.3.3	Additional Species in Simulation . . . . .	89
118	7.4	Summary . . . . .	89
119	8	JET ENERGY RESPONSE AND UNCERTAINTY	91

120	8.1	Motivation . . . . .	91
121	8.2	Uncertainty Estimate . . . . .	91
122	8.3	Summary . . . . .	94
123	V	SEARCH FOR LONG-LIVED PARTICLES	97
124	9	LONG-LIVED PARTICLES IN ATLAS	98
125	9.1	Event Topology . . . . .	98
126	9.1.1	Detector Interactions . . . . .	99
127	9.1.2	Lifetime Dependence . . . . .	100
128	9.2	Simulation . . . . .	103
129	10	EVENT SELECTION	105
130	10.1	Trigger . . . . .	106
131	10.2	Kinematics and Isolation . . . . .	107
132	10.3	Particle Species Rejection . . . . .	111
133	10.4	Ionization . . . . .	114
134	10.4.1	Mass Estimation . . . . .	115
135	10.5	Efficiency . . . . .	116
136	11	BACKGROUND ESTIMATION	119
137	11.1	Background Sources . . . . .	119
138	11.2	Prediction Method . . . . .	120
139	11.3	Validation . . . . .	121
140	11.3.1	Closure in Simulation . . . . .	121
141	11.3.2	Validation Region in Data . . . . .	122
142	12	SYSTEMATIC UNCERTAINTIES AND RESULTS	124
143	12.1	Systematic Uncertainties . . . . .	124
144	12.1.1	Background Estimate . . . . .	124
145	12.1.2	Signal Yield . . . . .	125
146	12.2	Final Yields . . . . .	131
147	12.3	Cross Sectional Limits . . . . .	132
148	12.4	Mass Limits . . . . .	134
149	12.5	Context for Long-Lived Searches . . . . .	136
150	VI	CONCLUSIONS	139
151	13	SUMMARY AND OUTLOOK	140
152	13.1	Summary . . . . .	140
153	13.2	Outlook . . . . .	140
154	VII	APPENDIX	141
155	A	INELASTIC CROSS SECTION	142
156	B	EXPANDED R-HADRON YIELDS AND LIMITS	143
157		BIBLIOGRAPHY	149

158 LIST OF FIGURES

---

159	Figure 1	A Feynman diagram representing the interaction of the $A$ field with a generic fermion, $f$ . . . . .	7
160			
161	Figure 2	The particle content of the Standard Model ( <a href="#">SM</a> ) . . . . .	9
162	Figure 3	The Feynman diagrams representing the decays of the W and Z bosons to fermions. Here $f$ indicates a generic fermion, $\bar{f}$ its antiparticle, and $f'$ the partner of that fermion in the same generation. . . . .	12
163			
164			
165			
166	Figure 4	The parton distribution functions ( <a href="#">PDFs</a> ) for proton-proton collisions at $Q^2 = 10 \text{ GeV}^2$ and $Q^2 = 10^4 \text{ GeV}^2$ . Each shows the fraction of particles which carry a fraction $x$ of the total proton energy at the specified scale [1]. . . . .	13
167			
168			
169			
170			
171	Figure 5	An approximation of the running of the coupling constants in the <a href="#">SM</a> up to the Planck scale [ <a href="#">unification_plot</a> ].	14
172			
173	Figure 6	The distribution of velocities of stars as a function of the radius from the center of the galaxy. The contributions to the velocity from the various components of matter in the galaxy are shown [2]. . . . .	15
174			
175			
176			
177	Figure 7	An approximation of the running of the coupling constants in the <a href="#">SM</a> up to the Planck scale [ <a href="#">unification_plot</a> ].	20
178			
179	Figure 8	The decay of a gluino to quarks and an Lightest Supersymmetric Particle ( <a href="#">LSP</a> ), which precedes through a squark. . . . .	21
180			
181			
182	Figure 9	The four collision points and corresponding experiments of the Large Hadron Collider ( <a href="#">LHC</a> ). The image includes the location of the nearby city of Geneva as well as the border of France and Switzerland. . . . .	24
183			
184			
185			
186	Figure 10	The cumulative luminosity over time delivered to the A Toroidal LHC ApparatuS ( <a href="#">ATLAS</a> ) experiment from high energy proton-proton collisions since 2011. The energies of the collisions are listed for each of the data-taking periods. . . . .	25
187			
188			
189			
190			
191	Figure 11	The accelerator complex that builds up to the full design energies at the <a href="#">LHC</a> . The protons are passed in order to Linac 2, the <a href="#">PSB</a> , the <a href="#">PS</a> , the <a href="#">SPS</a> and then the <a href="#">LHC</a> . . . . .	26
192			
193			
194			
195	Figure 12	A schematic of the layout of the <a href="#">LHC</a> , not to scale. The arched and straight sections are illustrated at the bottom of the schematic, and all four crossing sites are indicated with their respective experiments. . . . .	27
196			
197			
198			

199	Figure 13	A cross section of the the cryodipole magnets which bend the flight path of protons around the circumference of the LHC. The diagram includes both the superconducting coils which produce the magnetic field and the structural elements which keep the magnets precisely aligned. . . . .	28
200			
201			
202			
203			
204			
205	Figure 14	The arrangement of four radiofrequency (RF) cavities within a cryomodule. . . . .	28
206			
207	Figure 15	The cumulative luminosity versus time delivered to ATLAS (green), recorded by ATLAS (yellow), and certified to be good quality data (blue) during stable beams for pp collisions at 13 TeV in 2015. . . . .	31
208			
209			
210			
211	Figure 16	The luminosity-weighted distribution of the mean number of interactions per crossing for the 2015 pp collision data at 13 TeV. . . . .	32
212			
213			
214	Figure 17	A cut-away schematic of the layout of the ATLAS detector. Each of the major subsystems is indicated. . . . .	34
215			
216	Figure 18	A cross-sectional slice of the ATLAS experiment which illustrates how the various SM particles interact with the detector systems. . . . .	34
217			
218			
219	Figure 19	The layout of the four superconducting magnets in the ATLAS detector. . . . .	37
220			
221	Figure 20	The arrangement of the subdetectors of the ATLAS inner detector. Each of the subdetectors is labeled in the cut-away view of the system. . . . .	39
222			
223			
224	Figure 21	A quarter section of the ATLAS inner detector which shows the layout of each of the subdetectors in detail. The lower panel shows an enlarged view of the pixel detector. Example trajectories for a particle with $\eta = 1.0, 1.5, 2.0, 2.5$ are shown. The Insertible B-Layer (IBL), which was added after the original detector commissioning, is not shown. . . . .	39
225			
226			
227			
228			
229			
230			
231	Figure 22	A computer generated three-dimensional view of the inner detector along the line of the beam axis. The subdetectors and their positions are labeled. . . . .	40
232			
233			
234	Figure 23	An alternative computer generated three-dimensional view of the inner detector transverse to the beam axis. The subdetectors and their positions are labeled. . . . .	40
235			
236			
237	Figure 24	The integrated radiation lengths traversed by a straight track at the exit of the ID envelope, including the services and thermal enclosures. The distribution is shown as a function of $ \eta $ and averaged over $\phi$ . The breakdown indicates the contributions of individual subdetectors, including services in their active volume. . . . .	41
238			
239			
240			
241			
242			
243	Figure 25	A cut away image of the outer three layers of the pixel detector. . . . .	44
244			

245	Figure 26	An image of the insertion of the <b>IBL</b> into the current pixel detector. . . . .	44
246			
247	Figure 27	A three-dimensional computer-generated image of the geometry of the <b>IBL</b> with a view (a) mostly transverse to the beam pipe (b) mostly parallel to the beam pipe. . . . .	45
248			
249			
250	Figure 28	An expanded view of the geometry of the silicon microstrip ( <b>SCT</b> ) double layers in the barrel region. . . . .	46
251			
252	Figure 29	. . . . .	47
253	Figure 30	The depth of (a) the electromagnetic barrel calorimeter in radiation lengths and (b) all calorimeters in interaction lengths as a function of pseudorapidity. . . . .	48
254			
255			
256	Figure 31	A schematic of the liquid argon ( <b>LAr</b> ) calorimeter in the barrel region, highlighting the accordion structure. . . . .	49
257			
258	Figure 32	A schematic of a hadronic tile module which shows the alternating layers of steel and plastic scintillator. . . . .	50
259			
260	Figure 33	The segmentation in depth and $\eta$ of the tile-calorimeter modules in the central (left) and extended (right) barrels. . . . .	51
261			
262	Figure 34	A cut-away diagram of the muon systems on <b>ATLAS</b> . . . . .	52
263	Figure 35	A quarter view of the muon spectrometer which highlights the layout of each of the detecting elements. The BOL, BML, BIL, EOL, EML, and EIL are all Monitored Drift Tube ( <b>MDT</b> ) elements, where the acronyms encode their positions. . . . .	52
264			
265			
266			
267			
268	Figure 36	A schematic of the cross-section of the muon spectrometer in the barrel region. . . . .	53
269			
270	Figure 37	A schematic of a single <b>MDT</b> chamber, which shows the multilayers of drift tubes as well as the alignment system. . . . .	54
271			
272			
273	Figure 38	A schematic of the Cathode Strip Chamber ( <b>CSC</b> ) end-cap, showing the overlapping arrangement of the eight large and eight small chambers. . . . .	55
274			
275			
276	Figure 39	A schematic of the Thin Gap Chamber ( <b>TGC</b> ) doublet and triplet layers. . . . .	56
277			
278	Figure 40	The L1 Trigger rate broken down into the types of triggers as a function of the luminosity block for the 2015 data collection period. . . . .	58
279			
280			
281	Figure 41	The HLT Trigger rate broken down into the types of triggers as a function of the luminosity block for the 2015 data collection period. . . . .	59
282			
283			
284	Figure 42	An illustration of the perigee representation of track parameters for an example track. The charge is not directly shown, but is indicated by the direction of curvature of the track [18]. . . . .	61
285			
286			
287			

288	Figure 43	The $x$ and $y$ locations of the hits generated in a simulated $t\bar{t}$ event in the inner detector. The hits which belong to tracks formed using the inside-out algorithm are highlighted in red, while the hits which belong to tracks formed using the outside-in algorithm are circled in black. . . . .	62
294	Figure 44	Examples of the clusters formed in a single layer of the pixel detector for (a) a single isolated particle, (b) two nearly-overlapping particles, and (c) a particle which emits a $\delta$ -ray [19]. . . . .	63
298	Figure 45	The total, fractional jet energy scale (JES) uncertainties estimated for 2015 data as a function of jet $p_T$ . . . . .	71
300	Figure 46	The $E/p$ distribution and ratio of simulation to data for isolated tracks with (a) $ \eta  < 0.6$ and $1.2 < p/\text{GeV} < 1.8$ and (b) $ \eta  < 0.6$ and $2.2 < p/\text{GeV} < 2.8$ . . . . .	77
303	Figure 47	The fraction of tracks as a function (a, b) of momentum, (c, d) of interaction lengths with $E \leq 0$ for tracks with positive (on the left) and negative (on the right) charge. . . . .	78
307	Figure 48	An illustration (a) of the geometry of energy deposits in the calorimeter. The red energy deposits come from the charged particle targeted for measurement, while the blue energy deposits are from nearby neutral particles and must be subtracted. The same diagram (b) for the neutral-background selection, described in Section 7.2.3. . . . .	79
314	Figure 49	$\langle E/p \rangle_{\text{BG}}$ as a function of the track momentum for tracks with (a) $ \eta  < 0.6$ , (b) $0.6 <  \eta  < 1.1$ , and as a function of the track pseudorapidity for tracks with (c) $1.2 < p/\text{GeV} < 1.8$ , (d) $1.8 < p/\text{GeV} < 2.2$ . . . . .	80
318	Figure 50	$\langle E/p \rangle_{\text{COR}}$ as a function of track momentum, for tracks with (a) $ \eta  < 0.6$ , (b) $0.6 <  \eta  < 1.1$ , (c) $1.8 <  \eta  < 1.9$ , and (d) $1.9 <  \eta  < 2.3$ . . . . .	81
321	Figure 51	$\langle E/p \rangle_{\text{COR}}$ calculated using LCW-calibrated topological clusters as a function of track momentum for tracks with (a) zero or more associated topological clusters or (b) one or more associated topological clusters. . . . .	82
325	Figure 52	Comparison of the $\langle E/p \rangle_{\text{COR}}$ for tracks with (a) less than and (b) greater than 20 hits in the TRT. . . . .	83
327	Figure 53	Comparison of the $\langle E/p \rangle_{\text{COR}}$ for (a) positive and (b) negative tracks as a function of track momentum for tracks with $ \eta  < 0.6$ . . . . .	84
330	Figure 54	Comparison of the $E/p$ distributions for (a) positive and (b) negative tracks with $0.8 < p/\text{GeV} < 1.2$ and $ \eta  < 0.6$ , in simulation with the FTFP_BERT and QGSP_BERT physics lists. . . . .	84

334	Figure 55	Comparison of the response of the hadronic calorimeter as a function of track momentum (a) at the EM-scale and (b) after the LCW calibration. . . . .	85
335			
336			
337	Figure 56	Comparison of the response of the EM calorimeter as a function of track momentum (a) at the EM-scale and (b) with the LCW calibration. . . . .	85
338			
339			
340	Figure 57	The reconstructed mass peaks of (a) $K_S^0$ , (b) $\Lambda$ , and (c) $\bar{\Lambda}$ candidates. . . . .	86
341			
342	Figure 58	The $E/p$ distribution for isolated (a) $\pi^+$ , (b) $\pi^-$ , (c) proton, and (d) anti-proton tracks. . . . .	87
343			
344	Figure 59	The fraction of tracks with $E \leq 0$ for identified (a) $\pi^+$ and $\pi^-$ , and (b) proton and anti-proton tracks . . . . .	88
345			
346	Figure 60	The difference in $\langle E/p \rangle$ between (a) $\pi^+$ and $\pi^-$ (b) $p$ and $\pi^+$ , and (c) $\bar{p}$ and $\pi^-$ . . . . .	89
347			
348	Figure 61	$\langle E/p \rangle_{\text{COR}}$ as a function of track momentum for (a) $\pi^+$ tracks and (b) $\pi^-$ tracks. . . . .	90
349			
350	Figure 62	The ratio of the calorimeter response to single particles of various species to the calorimeter response to $\pi^+$ with the physics list FTFP_BERT. . . . .	90
351			
352			
353	Figure 63	The spectra of true particles inside anti- $k_t$ , $R = 0.4$ jets with (a) $90 < p_T/\text{GeV} < 100$ , (b) $400 < p_T/\text{GeV} < 500$ , and (c) $1800 < p_T/\text{GeV} < 2300$ . . . . .	92
354			
355			
356	Figure 64	The JES response uncertainty contributions, as well as the total JES uncertainty, as a function of jet $p_T$ for (a) $ \eta  < 0.6$ and (b) $0.6 <  \eta  < 1.1$ . . . . .	95
357			
358			
359	Figure 65	The correlations between bins of average reconstructed jet momentum as a function of jet $p_T$ and $ \eta $ for jets in the central region of the detector. . . . .	96
360			
361			
362	Figure 66	A schematic diagram of an R-Hadron event with a lifetime around 0.01 ns. The diagram includes one charged R-Hadron (solid blue), one neutral R-Hadron (dashed blue), LSPs (dashed green) and charged hadrons (solid orange). The pixel detector, calorimeters, and muon system are illustrated but not to scale. . . . .	100
363			
364			
365			
366			
367			
368	Figure 67	A schematic diagram of an R-Hadron event with a lifetime around 4 ns. The diagram includes one charged R-Hadron (solid blue), one neutral R-Hadron (dashed blue), LSPs (dashed green) and a charged hadron (solid orange). The pixel detector, calorimeters, and muon system are illustrated but not to scale. . . . .	101
369			
370			
371			
372			
373			
374	Figure 68	A schematic diagram of an R-Hadron event with a lifetime around 5 ns. The diagram includes one charged R-Hadron (solid blue), one neutral R-Hadron (dashed blue), LSPs (dashed green) and charged hadrons (solid orange). The pixel detector, calorimeters, and muon system are illustrated but not to scale. . . . .	102
375			
376			
377			
378			
379			

380	Figure 69	A schematic diagram of an R-Hadron event with a life-time around 20 ns. The diagram includes one charged R-Hadron (solid blue), one neutral R-Hadron (dashed blue), LSPs (dashed green) and charged hadrons (solid orange). The pixel detector, calorimeters, and muon system are illustrated but not to scale. . . . .	102
381			
382			
383			
384			
385			
386	Figure 70	A schematic diagram of an R-Hadron event with a life-time around 20 ns. The diagram includes one charged R-Hadron (solid blue) and one neutral R-Hadron (dashed blue). The pixel detector, calorimeters, and muon system are illustrated but not to scale. . . . .	103
387			
388			
389			
390			
391	Figure 71	The distribution of (a) $E_T^{\text{miss}}$ and (b) Calorimeter $E_T^{\text{miss}}$ for simulated signal events before the trigger requirement. . . . .	106
392			
393			
394	Figure 72	The distribution of $E_T^{\text{miss}}$ for data and simulated signal events, after the trigger requirement. . . . .	108
395			
396	Figure 73	The trigger efficiency for the HLT_xe70 trigger requirement as a function of (a) $E_T^{\text{miss}}$ and (b) Calorimeter $E_T^{\text{miss}}$ for simulated signal events. . . . .	109
397			
398			
399	Figure 74	The dependence of $dE/dx$ on $N_{\text{split}}$ in data after basic track hit requirements have been applied. . . . .	110
400			
401	Figure 75	The distribution of $dE/dx$ with various selections applied in data and simulated signal events. . . . .	110
402			
403	Figure 76	The distribution of track momentum for data and simulated signal events, after previous selection requirements have been applied. . . . .	111
404			
405			
406	Figure 77	The distribution of $M_T$ for data and simulated signal events, after previous selection requirements have been applied. . . . .	112
407			
408			
409	Figure 78	The distribution of summed tracked momentum within a cone of $\Delta R < 0.25$ around the candidate track for data and simulated signal events, after previous selection requirements have been applied. . . . .	113
410			
411			
412			
413	Figure 79	The normalized, two-dimensional distribution of $E/p$ and $f_{\text{EM}}$ for simulated (a) $Z \rightarrow ee$ , (b) $Z \rightarrow \tau\tau$ , (c) 1200 GeV Stable R-Hadron events, and (d) 1200 GeV, 10 ns R-Hadron events. . . . .	114
414			
415			
416			
417	Figure 80	Two-dimensional distribution of $dE/dx$ versus charge signed momentum ( $qp$ ) for minimum-bias tracks. The fitted distributions of the most probable values for pions, kaons and protons are superimposed. . . . .	115
418			
419			
420			
421	Figure 81	The distribution of mass estimated using $dE/dx$ for simulated stable R-Hadrons with masses between 1000 and 1600 GeV. . . . .	116
422			
423			

424	Figure 82	The acceptance $\times$ efficiency as a function of R-Hadron (a) mass and (b) lifetime. (a) shows all of the combinations of mass and lifetime considered in this search, and (b) highlights the lifetime dependence for 1000 GeV and 1600 GeV R-Hadrons. . . . .	118
425			
426			
427			
428			
429	Figure 83	The distribution of (a) $dE/dx$ and (b) momentum for tracks in data and simulated signal after requiring the event level selection and the track selection on $p_T$ , hits, and $N_{\text{split}}$ . Each sub-figure shows the normalized distributions for tracks classified as hadrons, electrons, and muons in data and R-Hadrons in the simulated signal. . . . .	120
430			
431			
432			
433			
434			
435			
436	Figure 84	The distribution of $M_{dE/dx}$ (a) before and (b) after the ionization requirement for tracks in simulated W boson decays and for the randomly generated background estimate. . . . .	122
437			
438			
439			
440	Figure 85	The distribution of $M_{dE/dx}$ (a) before and (b) after the ionization requirement for tracks in the validation region and for the randomly generated background estimate. . . . .	123
441			
442			
443			
444	Figure 86	The trigger efficiency for the HLT_xe70 trigger requirement as a function of Calorimeter $E_T^{\text{miss}}$ for simulated data events with a W boson selection. Simulated signal events and simulated W boson events are also included. . . . .	127
445			
446			
447			
448			
449	Figure 87	The efficiency of the muon veto for R-hadrons of two different masses, as a function of $\frac{1}{\beta}$ for simulated R-Hadron tracks. . . . .	129
450			
451			
452	Figure 88	The average reconstructed MDT $\beta$ distribution for $Z \rightarrow \mu\mu$ events in which one of the muons is reconstructed as a slow muon, for both data and simulation. A gaussian fit is superimposed. . . . .	130
453			
454			
455			
456	Figure 89	The observed mass distribution of events in data and the generated background distribution in (a) the stable and (b) the metastable signal region. A few example simulated signal distributions are superimposed. . . . .	131
457			
458			
459			
460	Figure 90	The observed and expected cross section limits as a function of mass for the stable simulated signal. The predicted cross section values for the corresponding signals are included. . . . .	134
461			
462			
463			
464	Figure 91	The observed and expected cross section limits as a function of mass for each generated lifetime. The predicted cross section values for the corresponding signals are included. . . . .	135
465			
466			
467			

The excluded range of masses as a function of gluino lifetime. The expected lower limit (LL), with its experimental  $\pm 1\sigma$  band, is given with respect to the nominal theoretical cross-section. The observed 95% LL obtained at  $\sqrt{s} = 8$  TeV [80] is also shown for comparison.<sup>137</sup>

Figure 93 The constraints on the gluino mass as a function of lifetime for a split-supersymmetry model with the gluino R-Hadrons decaying into a gluon or light quarks and a neutralino with mass of 100 GeV. The solid lines indicate the observed limits, while the dashed lines indicate the expected limits. The area below the curves is excluded. The dots represent results for which the particle is assumed to be prompt or stable. . . . .

481 LIST OF TABLES

---

482	Table 1	The particles in the <b>SM</b> and their corresponding super-partners in the Minimal Supersymmetric Model ( <b>MSSM</b> ). . . . .	18
483			
484	Table 2	The design parameters of the <b>LHC</b> beam that determines the energy of collisions and the luminosity, for both the injection of protons and at the nominal circulation. . . . .	30
485			
486			
487			
488	Table 3	The performance goals for each of the subsystems of the <b>ATLAS</b> detector. The $ \eta $ coverage specifies the range where the subsystem needs to be able to provide measurements with the specified resolution. The resolutions include a $p_T$ or $E$ dependence that is added in quadrature with a $p_T/E$ independent piece. . . . .	35
489			
490			
491			
492			
493			
494	Table 4	A summary of the parameters of each of the three magnet systems on <b>ATLAS</b> . . . . .	37
495			
496	Table 5	A summary of the parameters of the inner detector and each of the subdetectors [10]. . . . .	42
497			
498	Table 6	A summary of the expected performance of the combined inner detector [14]. Included are the reconstruction efficiencies for multiple particle types as well as the momentum and impact parameter ( <b>IP</b> ) resolution for various momenta. . . . .	43
499			
500			
501			
502			
503	Table 7	The trigger menu for the 2015 data collection with $L = 5 \times 10^{33} \text{ cm}^{-2} \text{ s}^{-1}$ . Both the L1 and high level trigger ( <b>HLT</b> ) selection requirements and their trigger rates are shown measured at the specified luminosity are shown. The typical offline selections represent a typical set of offline requirements imposed after the trigger in an analysis. . . . .	57
504			
505			
506			
507			
508			
509			
510	Table 8	The dominant sources of corrections and systematic uncertainties in the <b>JES</b> estimation technique, including typical values for the correcting shift ( $\Delta$ ) and the associated uncertainty ( $\sigma$ ). . . . .	93
511			
512			
513			
514	Table 9	The expected number of events at each level of the selection for metastable 1600 GeV, 10 ns R-Hadrons, along with the number of events observed in data, for $3.2 \text{ fb}^{-1}$ . The simulated yields are shown with statistical uncertainties only. The total efficiency $\times$ acceptance is also shown for the signal. . . . .	117
515			
516			
517			
518			
519			

520	Table 10	A summary of the sources of systematic uncertainty for the data-driven background in the signal region. If the uncertainty depends on the mass, the maximum values are reported. . . . .	124
521			
522			
523			
524	Table 11	A summary of the sources of systematic uncertainty for the simulated signal yield. The uncertainty depends on the mass and lifetime, and the maximum negative and positive values are reported in the table. . . . .	126
525			
526			
527			
528	Table 12	Example of the contributing systematic variations to the total systematic for the $E_T^{\text{miss}}$ Scale, as measured in a 1200 GeV, Stable R-Hadron signal sample. . . . .	128
529			
530			
531	Table 13	The estimated number of background events and the number of observed events in data for the specified selection regions prior to the requirement on mass. The background estimates show statistical and systematic uncertainties. . . . .	131
532			
533			
534			
535			
536	Table 14	The left and right extremum of the mass window for each generated mass point with a 10 ns lifetime. . . . .	132
537			
538	Table 15	The left and right extremum of the mass window used for each generated stable mass point. . . . .	132
539			
540	Table 16	The expected number of signal events, the expected number of background events, and the observed number of events in data with their respective statistical errors within the respective mass window for each generated stable mass point . . . . .	133
541			
542			
543			
544			
545	Table 17	The expected number of signal events, the expected number of background events, and the observed number of events in data with their respective statistical errors within the respective mass window for each generated mass point with a lifetime of 10 ns. . . . .	133
546			
547			
548			
549			
550	Table 18	The observed and expected 95% CL lower limit on mass for gluino R-Hadrons for each considered lifetime. . . . .	136
551			
552	Table 19	The left and right extremum of the mass window for each generated mass point with a 50 ns lifetime. . . . .	143
553			
554	Table 20	The left and right extremum of the mass window for each generated mass point with a 30 ns lifetime. . . . .	143
555			
556	Table 21	The left and right extremum of the mass window for each generated mass point with a 10 ns lifetime. . . . .	144
557			
558	Table 22	The left and right extremum of the mass window used for each generated mass point with a lifetime of 3 ns. . . . .	144
559			
560	Table 23	The left and right extremum of the mass window used for each mass point with a lifetime of 1 ns. . . . .	144
561			
562	Table 24	The left and right extremum of the mass window for each generated mass point with a lifetime of 0.4 ns. . . . .	145
563			
564	Table 25	The left and right extremum of the mass window used for each generated stable mass point. . . . .	145
565			

566	Table 26	The expected number of signal events, the expected number of background events, and the observed number of events in data with their respective statistical errors within the respective mass window for each generated mass point with a lifetime of 50 ns. . . . .	145
567			
568			
569			
570			
571	Table 27	The expected number of signal events, the expected number of background events, and the observed number of events in data with their respective statistical errors within the respective mass window for each generated mass point with a lifetime of 30 ns. . . . .	146
572			
573			
574			
575			
576	Table 28	The expected number of signal events, the expected number of background events, and the observed number of events in data with their respective statistical errors within the respective mass window for each generated mass point with a lifetime of 10 ns. . . . .	146
577			
578			
579			
580			
581	Table 29	The expected number of signal events, the expected number of background events, and the observed number of events in data with their respective statistical errors within the respective mass window for each generated mass point with a lifetime of 3 ns. . . . .	147
582			
583			
584			
585			
586	Table 30	The expected number of signal events, the expected number of background events, and the observed number of events in data with their respective statistical errors within the respective mass window for each generated mass point with a lifetime of 1 ns. . . . .	147
587			
588			
589			
590			
591	Table 31	The expected number of signal events, the expected number of background events, and the observed number of events in data with their respective statistical errors within the respective mass window for each generated mass point with a lifetime of p4 ns. . . . .	148
592			
593			
594			
595			
596	Table 32	The expected number of signal events, the expected number of background events, and the observed number of events in data with their respective statistical errors within the respective mass window for each generated stable mass point . . . . .	148
597			
598			
599			
600			

601 LISTINGS

---

602 ACRONYMS

---

- 603 SM Standard Model  
604 CERN European Organization for Nuclear Research  
605 SUSY Supersymmetry  
606 LSP Lightest Supersymmetric Particle  
607 LHC Large Hadron Collider  
608 ATLAS A Toroidal LHC ApparatuS  
609 CMS Compact Muon Solenoid  
610 ALICE A Large Ion Collider Experiment  
611 LHCb Large Hadron Collider beauty experiment  
612 LEP the Large Electron Positron collider  
613 PS Proton Synchrotron  
614 PSB Proton Synchrotron Booster  
615 SPS Super Proton Synchrotron  
616 SCT silicon microstrip  
617 TRT Transition Radiation Tracker  
618 LAr liquid argon  
619 EM electromagnetic  
620 RPC Resistive Plate Chamber  
621 TGC Thin Gap Chamber  
622 MDT Monitored Drift Tube  
623 CSC Cathode Strip Chamber  
624 ToT time over threshold  
625 RoI Region of Interest  
626 LCW local cluster weighted  
627 MIP minimally ionizing particle  
628 IP impact parameter

- 629 EPJC European Physical Journal C  
630 JES jet energy scale  
631 LLP Long-Lived Particle  
632 CR Control Region  
633 NLO next-to-leading order  
634 NLL next-to-leading logarithmic  
635 PDF parton distribution function  
636 ISR initial state radiation  
637 RMS root mean square  
638 IBL Insertible B-Layer  
639 CP Combined Performance  
640 MDT Monitored Drift Tube  
641 RF radiofrequency  
642 HLT high level trigger  
643 QCD quantum chromodynamics  
644 BSM beyond the Standard Model  
645 MSSM Minimal Supersymmetric Model

646

## PART I

647

### INTRODUCTION

648

You can put some informational part preamble text here.

649

650 INTRODUCTION

---

651

## PART II

652

### THEORETICAL CONTEXT

653

You can put some informational part preamble text here.

654

655 STANDARD MODEL

---

656 The **SM** of particle physics seeks to explain the symmetries and interactions of  
 657 fundamental particles. The **SM** provides predictions in particle physics for in-  
 658 teractions up to the Planck scale ( $10^{15}$ – $10^{19}$  GeV). It has been tested by several  
 659 generations of experiments and has been remarkably successful; no significant  
 660 deviations from its predictions have been found.

661 The theory itself is a quantum field theory grown from an underlying sym-  
 662 metry,  $SU(3) \times SU(2) \times U(1)$ , that generates all of the interactions consistent  
 663 with experimental observations. These interactions are referred to as the Strong,  
 664 Weak, and Electromagnetic forces. Each postulated symmetry necessitates the  
 665 existence of an associated conserved charge, which appear as properties of the  
 666 observed particles in nature.

667 Although this model has been very predictive, the theory is incomplete; for  
 668 example, it is not able to describe gravity or astronomically observed dark mat-  
 669 ter. These limitations suggest a need for an extension or new theory to describe  
 670 physics at higher energies.

## 671 2.1 ACTION AND THE LAGRANGIAN

Originally, both action and the Lagrangian were constructed for an integral reformulation of the laws of classical mechanics, which is a purely mathematical step: any differential equation can be re-expressed in terms of an integral equation. The Lagrangian,  $\mathcal{L}$ , is classically given by the difference of kinetic energy and potential energy. The Lagrangian is defined this way so that the action,  $\mathcal{S}$ , given by

$$\mathcal{S}[\mathbf{q}(t)] = \int_{t_1}^{t_2} \mathcal{L}(\mathbf{q}, \dot{\mathbf{q}}, t) dt \quad (1)$$

672 returns the classical equations of motion when one requires it to be stationary  
 673 in the path,  $\mathbf{q}(t)$ . This formulation of classical mechanics is extremely useful in  
 674 calculations, and generalizes beautifully to cover all types of physics.

675 In particular, with the development of quantum mechanics in the twentieth  
 676 century, the concepts of action and the Lagrangian were found to generalize to  
 677 more complicated physics for which the classical laws do not hold. Quantum  
 678 mechanics and quantum field theory can be constructed from the action, using  
 679 the path integral formulation, by assuming that a particle undergoes all possible  
 680 paths  $\mathbf{q}(t)$  with an imaginary phase given by  $e^{i\mathcal{S}[\mathbf{q}(t)]/\hbar}$ . This reduces to classical  
 681 mechanics in the limit as  $\hbar$  goes to zero, as all paths for which the action is not  
 682 stationary interfere with each other so as to cancel their contributions. Because  
 683 the wavefunction of a particle can be completely determined through the action

and the action depends only on the Lagrangian, the Lagrangian itself is sufficient to describe the physics governing the particle.

So, in both classical and quantum mechanics, the Lagrangian of a system contains everything there is to know about the system, apart from initial conditions. Thus, the most natural way to express that a system has a certain symmetry is to require that the Lagrangian is invariant under a corresponding symmetry transformation. This makes the Lagrangian the central piece of the discussion of gauge invariance; the mathematical representation of gauge invariance is that a gauge transformation on the appropriate components of the Lagrangian returns an identical Lagrangian. That is,

$$\mathcal{L}(\psi, D^\mu) = \mathcal{L}(U\psi, D'^\mu) \quad (2)$$

where  $\psi$  is the wavefunction and  $D^\mu$  is the covariant derivative, both of which transform under a symmetry operation. There are a number of immediate and surprisingly powerful consequences of requiring that the Lagrangian is invariant under a symmetry operation.

## 2.2 GAUGE INVARIANCE AND FORCES

The simplest possible relativistic, quantum Lagrangian is the free Dirac Lagrangian, which describes a relativistic fermion in a vacuum.

$$\mathcal{L} = i\bar{\psi}\not{d}\psi - m\bar{\psi}\psi \quad (3)$$

A fermion denotes a particle with spin-1/2, and the kinematic term is chosen to correctly describe the free propagation of a fermionic particle with mass  $m$ . This equation is clearly invariant under a global  $U(1)$  transformation, that is changing  $\psi$  by a complex phase has no effect. The derivative operator commutes with a constant phase factor, and wherever  $\psi$  appears its complex conjugate also appears so as to cancel out the change of phase. However, the Lagrangian as written is not invariant under the local  $U(1)$  symmetry postulated for the SM, which can be written as  $U = e^{i\alpha(x)}$ . The piece of the Lagrangian involving a derivative will return an extra term that will break the invariance of the Lagrangian under this transformation:

$$\begin{aligned} \mathcal{L}' &= i(\bar{\psi}U^\dagger)\not{d}(U\psi) - m(\bar{\psi}U^\dagger)(U\psi) \\ &= i(\bar{\psi}U^\dagger)U(\not{d} - \gamma^\mu\partial_\mu\alpha(x))\psi - m(\bar{\psi}U^\dagger)(U\psi) \\ &= i\bar{\psi}\not{d}\psi - m\bar{\psi}\psi - i\gamma^\mu\partial_\mu\alpha(x)\bar{\psi}\psi \\ &= \mathcal{L} - i\gamma^\mu\partial_\mu\alpha(x)\bar{\psi}\psi \\ &\neq \mathcal{L} \end{aligned}$$

So, in order to enforce the required symmetry, the typical approach is to construct a covariant derivative, that is to add a term to the derivative operator

so that the unwanted term in  $\mathcal{L}'$  is exactly canceled. A generic form for such a derivative is given by

$$D^\mu = \partial^\mu - iqA^\mu$$

where at this point  $A^\mu$  is an arbitrary field that transforms under the  $U(1)$  operator and  $q$  is a scaling factor. Adding this component to the above Lagrangian gives

$$\mathcal{L}' = i(\bar{\psi}U^\dagger)U(\not{d} - \gamma^\mu\partial_\mu\alpha(x) - iq\gamma^\mu A'_\mu)\psi - m(\bar{\psi}U^\dagger)(U\psi) \quad (4)$$

$$\mathcal{L}' = \mathcal{L} + \gamma^\mu(-i\partial_\mu\alpha(x) - iqA'_\mu + iqA_\mu)\bar{\psi}\psi \quad (5)$$

and because the transformation of  $A^\mu$  is unspecified,  $\mathcal{L} = \mathcal{L}'$  whenever

$$A'_\mu = A_\mu - \frac{1}{q}\partial_\mu\alpha(x)$$

The above procedure demonstrated that beginning with the Lagrangian for a free fermion and imposing a local  $U(1)$  symmetry required the existence of a vector field  $A^\mu$ , and specified its transformation under the  $U(1)$  gauge group. The additional term in the derivative can be expanded to form a completely separate term in the Lagrangian,

$$\mathcal{L} = i\bar{\psi}\not{d}\psi - m\bar{\psi}\psi - (q\bar{\psi}\gamma^\mu\psi)A^\mu \quad (6)$$

and in this form it is clear that the  $A^\mu$  term has the exact form of the electromagnetic interaction. That is, this is the Lagrangian which reproduces the relativistic form of Maxwell's equations for a particle interacting with an electromagnetic field. It is natural to also introduce a term to the Lagrangian at this point to describe the free propagation of the vector  $A$  field, where the propagation of a vector field has the form of

$$-\frac{1}{16\pi}F^{\mu\nu}F_{\mu\nu} \quad \text{with} \quad F_{\mu\nu} = \partial_\mu A_\nu - \partial_\nu A_\mu \quad (7)$$

This then also describes the electromagnetic interactions in a vacuum and the propagation of a photon. The photon is an example of a gauge boson, a spin-0 particle required to exist by a gauge symmetry of the Lagrangian and one that corresponds to a force. In summary, requiring the  $U(1)$  symmetry was enough to recover all of electromagnetism and to predict the existence of a photon in the SM.

The interaction term that was placed into the Lagrangian by this procedure can be conveniently summarized with Feynman diagrams, which diagrammatically represent a transition from an initial state to a final state. All diagrams that start with the same initial state and end with the same final state must be considered, but more complicated diagrams can be built by linking together the simplest versions. A diagram that corresponds to the above term,  $(q\bar{\psi}\gamma^\mu\psi)A^\mu$ , is shown in Figure 1, for an interaction with a generic fermion.

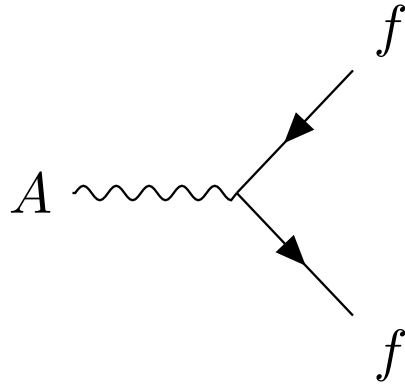


Figure 1: A Feynman diagram representing the interaction of the  $A$  field with a generic fermion,  $f$ .

743    2.2.1  $SU(2) \times U(1)$  AND THE ELECTROWEAK FORCE

744    The full picture of the electroweak section of the SM is more complicated than the  
 745    simplified explanation of the electromagnetic piece described above. In practice,  
 746    it is necessary to consider the entire  $SU(2) \times U(1)$  symmetry together, but the  
 747    procedure is the same. Enforcing the symmetry on the Lagrangian requires the  
 748    introduction of a covariant derivative, this time with four total distinct terms,  
 749    one for each of the generators of  $SU(2) \times U(1)$ . The result is a series of terms  
 750    in the Lagrangian which describe the interaction of a fermion with four vector  
 751    fields, the  $W_1$ ,  $W_2$ ,  $W_3$ , and  $B$  fields. These fields can mix in the quantum sense,  
 752    and linear combinations form the  $W^+$ ,  $W^-$ ,  $Z$ , and  $A$  fields that are considered  
 753    actual particles in the SM<sup>1</sup>.

754    2.2.2  $SU(3)$  AND THE STRONG FORCE

755    The same procedure can be applied starting with the  $SU(3)$  symmetry require-  
 756    ment, where eight additional fields must be introduced, one for each of the gen-  
 757    erators of  $SU(3)$ . The resulting Lagrangian describes quantum chromodynam-  
 758    ics (QCD) and predicts the existence of eight gauge bosons known collectively as  
 759    gluons.

760    2.3 NOETHER'S THEOREM, CHARGES, AND MATTER

761    Another direct consequence of the symmetries stipulated in the SM are a series  
 762    of conserved quantities, Noether charges, named after the mathematician and  
 763    physicist Emmy Noether. The charges arise as a direct consequence of Noether's  
 764    theorem, which can be informally stated as

---

<sup>1</sup> These states are the actual particles because they are mass eigenstates, but the full explanation of this will have to wait for the discussion of the Higgs mechanism.

765       *For every symmetry of the Lagrangian, there exists a corresponding phys-  
766       ical quantity whose value is conserved in time.*

767       Or, stated another way, symmetries of the Lagrangian mathematically require  
768       the conservation of specific quantities taken from the Lagrangian. This rela-  
769       tionship can also be thought of as operating in the other direction, the exis-  
770       tence of a conserved charge can be shown to generate the symmetry in the La-  
771       grangian. This theorem is actually quite striking in a somewhat unexpected re-  
772       lation between simple geometric symmetries and physically observable conser-  
773       vation laws. For example, the theorem connects the translation invariance of  
774       the Lagrangian in space to the conservation of momentum and the translation  
775       invariance in time to the conservation of energy.

776       In the context of the SM, the required symmetries of  $U(1) \times SU(2) \times SU(3)$   
777       correspond to the charges that are considered properties of all elementary par-  
778       ticles. The most familiar of these properties is the electric charge,  $Q$ , which is  
779       one of the conserved quantities of  $SU(2) \times U(1)$ . The remaining pieces of  
780        $SU(2) \times U(1)$  correspond to weak isospin,  $T$  and  $T_3$ , where  $T$  has only non-  
781       negative values and  $T_3$  can be positive and negative. The  $SU(3)$  symmetry is  
782       generated by the three colors of QCD, red, green, and blue, each with a corre-  
783       sponding opposite color, anti-red, anti-green, and anti-blue.

784       The matter in the observable universe consists of a collection of particles which  
785       carry these charges, in addition to spin and mass. The particles typically thought  
786       of as matter are all fermions: particles with spin-1/2. All of the fermions belong  
787       to one of two groups, quarks and leptons, and one of three generations. Each  
788       of the generations have similar properties but significantly different masses; the  
789       particles in consecutive generations have increasing mass. Quarks are distin-  
790       guished from leptons in that they carry color charge, in addition to electric charge  
791       and weak isospin. The particles in the SM are summarized in Figure 2, and the  
792       matter particles are the twelve types of fermions displayed on the left side of the  
793       graphic.

### 794       2.3.1 QUARKS

795       The three generations of quarks each have a particle with electric charge +2/3  
796       and one with charge -1/3. They are referred to us up and down, charm and  
797       strange, and top and bottom respectively, and these are referred to as the quark  
798       flavors. Although Figure 2 only shows these six flavors, there is a unique particle  
799       for each combination of the three colors and flavor. And each quark has an anti-  
800       particle with the opposite electric and color charge values.

801       However, individual quarks are never observed in nature, but instead form  
802       color-neutral bound states. One way to form a color neutral combination is a  
803       bound state of three quarks with three different color charges, called a baryon.  
804       Baryons are the most common type of quark configuration in conventional mat-  
805       ter, and include protons and neutrons. The other common configuration is a  
806       bound state of a quark and an anti-quark, called a meson, where the two quarks  
807       have the same type but opposite colors. The conservation of the various charges  
808       carried by quarks, along with the requirement that quarks appear in color-neutral

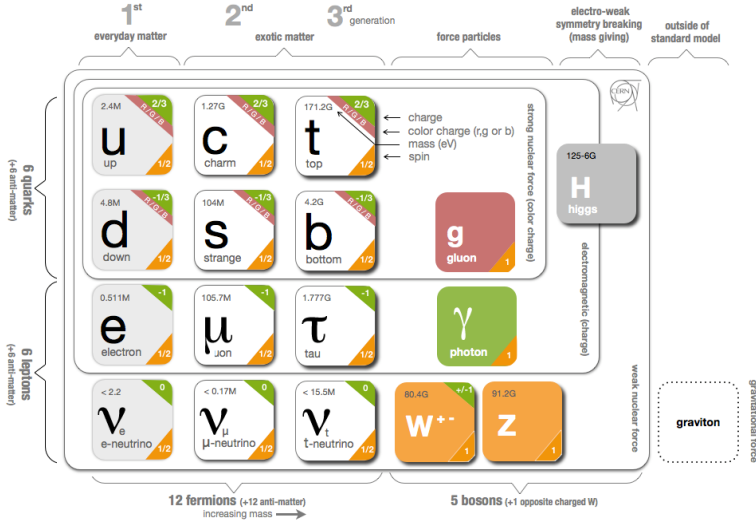


Figure 2: The particle content of the SM.

809 states, result in the observed conservation of baryon number,  $B$ , where baryons  
 810 have  $B = 1$  and mesons have  $B = 0$ .

### 811 2.3.2 LEPTONS

812 The remaining fermions, the leptons, do not carry color charge. Each generation  
 813 contains an electrically charged lepton, the electron, muon, and tau, and an elec-  
 814 trically neutral lepton called a neutrino. For the charged leptons, the flavors are  
 815 mass eigenstates, with the masses listed in Figure 2. The flavors of the neutrinos,  
 816 on the other hand, are not mass eigenstates: they propagate in mass eigenstates  
 817 and so can oscillate between different flavors. The absolute masses of the neu-  
 818 trinos are not currently known, but the phenomenon of oscillations shows that  
 819 they have three different mass values. Although there is no direct conservation  
 820 law resulting from the symmetries of the SM Lagrangian, no interactions have  
 821 been observed which alter lepton number,  $L$ , the difference in the number of lep-  
 822 tons and anti-leptons.

### 823 2.3.3 CHIRALITY

824 All of the fermions described above have two possible values of the magnitude  
 825 of weak isospin,  $T$ , either 0 or  $1/2$ . The fermions with  $T = 0$  are called right-  
 826 handed, while those with  $T = 1/2$  are called left-handed. For left-handed fermions,  
 827 each of the quark and lepton generations have one particle with  $T_3 = -1/2$  and  
 828 one with  $T_3 = +1/2$ . The neutrinos have  $T_3 = +1/2$ , while the charged leptons  
 829 have  $T_3 = -1/2$ . Similarly, the positively charged quarks have  $T_3 = +1/2$  and the  
 830 negatively charged quarks have  $T_3 = -1/2$ . Because the right-handed neutrinos  
 831 would have no charge of any type, it is not clear if they exist at all.

## 832 2.4 HIGGS MECHANISM AND MASS

833 The description of the electroweak forces above left out an important part of the  
 834 observed nature of the electroweak force. Many physical experiments observed  
 835 phenomena corresponding to the interaction of the weak bosons that were best  
 836 explained if they had significant masses. A large mass for the W and Z bosons  
 837 would explain the relative weakness of their interactions compared to the elec-  
 838 tromagnetic field. The Lagrangian's discussed above did not include a mass term  
 839 for the gauge bosons, and in fact such a term would not be allowed by the require-  
 840 ment of gauge invariance. This was a significant problem for the **SM**, and the  
 841 symmetry of the electroweak sector would have to be broken in order to allow  
 842 for non zero masses for some of the gauge bosons.

843 One mechanism to allow for this spontaneous symmetry breaking is the Higgs  
 844 mechanism, which posits the existence of an additional scalar field. It begins  
 845 with a  $SU(2) \times U(1)$  invariant Lagrangian of the form

$$\mathcal{L} = |D_\mu \phi|^2 - \frac{1}{2}\mu^2\phi^+\phi - \frac{1}{4}\lambda(\phi^+\phi)^2 \quad (8)$$

846 where  $\phi$  is the new scalar field and, importantly,  $\mu^2$  is negative. This leads to a  
 847 minimum value of the field at a non-zero value of  $\phi$ , specifically where

$$\langle \phi \rangle = \frac{1}{\sqrt{2}} \begin{pmatrix} 0 \\ v \end{pmatrix} \quad \text{with} \quad v = \frac{2\mu^2}{\lambda} \quad (9)$$

848 Expanding the original Lagrangian about its expectation value,

$$\langle \phi \rangle = \frac{1}{\sqrt{2}} \begin{pmatrix} 0 \\ v + H \end{pmatrix} \quad (10)$$

849 gives potential terms in the Lagrangian like

$$\mathcal{L}_H = -\frac{1}{2}m_H^2 H^2 - \sqrt{\frac{\lambda}{2}}m_H H^3 - \frac{1}{4}\lambda H^4 \quad (11)$$

850 where  $m_H = \sqrt{2}\mu$ . The form of this Lagrangian shows that the non-zero ex-  
 851 pectation value of the  $\phi$  field has introduced a massive scalar field  $H$  with self  
 852 interaction terms. It has an additional important consequence on the description  
 853 of the gauge bosons, through the expansion of the term involving the covariant  
 854 derivative:

$$|D_\mu \phi|^2 \supset \frac{1}{8} (g^2(W_{1\mu}W_1^\mu + W_{2\mu}W_2^\mu) + (g'B_\mu - gW_3\mu)^2) \quad (12)$$

855 where the  $W_i$  and  $B$  fields are the original  $SU(2) \times U(1)$  gauge fields men-  
 856 tioned previously. The above equation can be rearranged using linear combina-  
 857 tions of the fields to from mass terms for the gauge bosons, and the mass eigen-  
 858 states are exactly the  $W^\pm$ ,  $Z$ , and  $A$  fields. Only the  $A$  field, corresponding to

859 the photon, results in a zero mass, and the remaining three fields acquire masses.  
 860 Because the originally introduced Lagrangian, written in terms of  $\phi$ , was clearly  
 861 gauge invariant, this resulting configuration must also be gauge invariant.

862 This is the Higgs mechanism, where the introduction of a gauge invariant  
 863 scalar field with a non-zero expectation value can generate masses for the gauge  
 864 bosons without violating the underlying symmetries. The particle that is asso-  
 865 ciated with the perturbations of this field,  $H$ , is called the Higgs boson, and is  
 866 said to generate the masses of the remaining bosons. The resulting masses are  
 867 listed in Figure 2. Because this mechanism was so successful in describing the  
 868 observed properties of the  $W$  and  $Z$  bosons, it has been considered part of the  
 869 **SM** for decades, although the actual Higgs boson was only recently observed in  
 870 2012, confirming the theory.

871 The Higgs mechanism is also responsible for generating the masses of the  
 872 fermions. The original mass terms that were listed in the Lagrangian for fermions  
 873 are replaced with Yukawa coupling terms, which introduce interactions between  
 874 the  $\phi$  field and the fermions. Like with the gauge bosons, the non-zero expec-  
 875 tation value of the field yields mass terms, and the expansion about that value  
 876 introduces interaction terms between the fermions and the Higgs boson. The  
 877 masses are different between each fermion because each has a different Yukawa  
 878 coupling, which results in the masses listed in Figure 2.

## 879 2.5 PHENOMENOLOGY

880 The **SM** Lagrangian described above contains all of the information necessary  
 881 to describe particle physics through the path integral formulation. However, a  
 882 tremendous amount of complexity emerges from that description because of the  
 883 diverse allowed interactions between the ensemble of particles in the **SM**. A qual-  
 884 itative understanding of the phenomenology produced by those interactions is  
 885 immensely helpful in understanding the analysis of particle physics.

### 886 2.5.1 ELECTROWEAK PHYSICS

887 The masses of the  $W$  and  $Z$  bosons result in significantly different processes  
 888 for the weak fields than the electromagnetic field, despite their interactions be-  
 889 ing similar before symmetry breaking. The massless photon is stable, and can  
 890 propagate in a vacuum, resulting in the familiar long range interactions of elec-  
 891 tromagnetism. The  $W$  and  $Z$  bosons, however, are unstable, as they have large  
 892 enough masses to decay to fermions, such as the decays shown in Figure 3. For  
 893 this reason, photons can be observed directly, while the other bosons are suffi-  
 894 ciently short-lived that they can only be measured from their decay products.

895 Because the  $W$  and  $Z$  bosons interact with both quarks and leptons, they are  
 896 responsible for the production of leptons in proton-proton collisions.  $Z$  bosons  
 897 produce pairs of opposite sign, same flavor leptons.  $W$  bosons, on the other hand,  
 898 produce a single lepton and the corresponding neutrino.

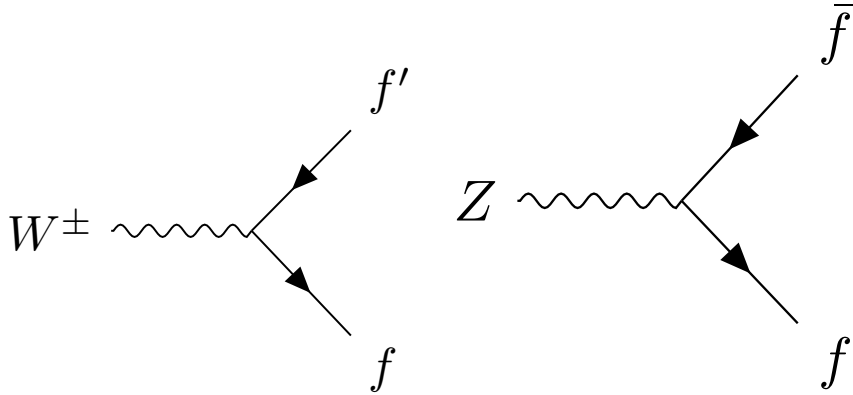


Figure 3: The Feynman diagrams representing the decays of the  $W$  and  $Z$  bosons to fermions. Here  $f$  indicates a generic fermion,  $\bar{f}$  its antiparticle, and  $f'$  the partner of that fermion in the same generation.

899 2.5.2 STRONG PHYSICS

900 The phenomenology of the strong sector differs significantly from the weak sec-  
 901 tor because the gluons are massless but color charged. Because of this, gluons  
 902 can interact with each other, and contributions from multiple gluon interactions  
 903 lead to a significant growth in the strength of the field at low energies. The depen-  
 904 dence of the field strength on the energy scale is described by renormalization,  
 905 and in [QCD](#) the coupling is only small at high energies. Above around the GeV  
 906 scale, the interactions of quarks become perturbative, similar to the electroweak  
 907 fields; this phenomenon is known as asymptotic freedom.

908 At lower energies, however, the strength of the strong interaction is so signif-  
 909 icant that the interactions of color-charged particles create additional particles  
 910 until they form neutral bound-states. This process is known as hadronization,  
 911 and explains why no quarks are observed isolated in nature: they all form bound  
 912 states of hadrons like protons, neutrons, and pions. The hadronization process  
 913 can produce a significant number of particles, so that a single energetic quark  
 914 recoiling against another quark can generate a cascade of dozens of hadrons.  
 915 Because of the initial boost of such an energetic configuration, the resulting  
 916 hadrons are collimated, and conical spray of particles often referred to as a jet.

917 2.5.3 PROTON-PROTON COLLISIONS

918 Proton-proton collisions are a convenient way to generate high energy interac-  
 919 tions to probe the [SM](#) and to search for new physics. At the energies that will be  
 920 discussed in this analysis, the substructure of the protons is very important to the  
 921 description of the resulting interactions. At lowest order, protons are composed  
 922 of two up quarks and one down quark, but this description is incomplete. The  
 923 actual bound state includes a chaotic sea of additional quarks and gluons, each of  
 924 which carries a variable fraction of the proton's energy. When a proton-proton

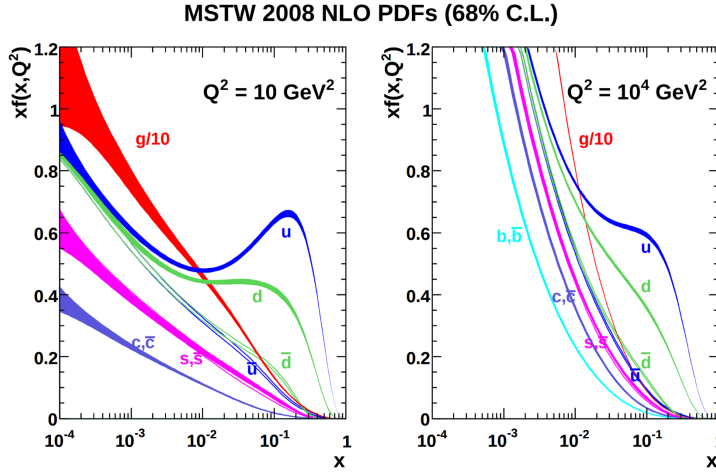


Figure 4: The PDFs for proton-proton collisions at  $Q^2 = 10 \text{ GeV}^2$  and  $Q^2 = 10^4 \text{ GeV}^2$ . Each shows the fraction of particles which carry a fraction  $x$  of the total proton energy at the specified scale [1].

925 collision takes place, it is these constituents that interact with each other, resulting  
 926 in a highly variable collision energy even when the proton-proton energy is  
 927 consistent.

928 The fraction of the energy carried by each constituent varies moment to moment,  
 929 but can be modelled probabilistically by PDFs. These are difficult to predict  
 930 theoretically, as the QCD calculations are extremely complex, and instead  
 931 are measured in hard-scattering experiments. They are usually represented by  
 932 how often a given type of particle carries a fraction  $x$  of the total proton energy.  
 933 Those fraction change significantly with the scale of the interaction; the PDFs of  
 934 proton-proton collisions at both  $Q^2 = 10 \text{ GeV}^2$  and  $Q^2 = 10^4 \text{ GeV}^2$  are shown  
 935 in Figure 4.

## 936 2.6 LIMITATIONS

937 Despite the great success of the relatively simple SM in describing such a broad  
 938 range of emergent phenomena, it is clear that the picture it presents of the interactions  
 939 of fundamental particles is incomplete. The SM contains concerning  
 940 coincidences that suggest a more ordered underlying substructure that is not ex-  
 941 pressed in the current form. It also fails to explain a number of cosmological  
 942 measurements of the nature of matter in the universe. These limitations suggest  
 943 the need for new, beyond the Standard Model (BSM) physics that would provide  
 944 a more complete description at higher energies.

### 945 2.6.1 THEORETICAL CONCERNs

946 There have been no successful integrations of the SM's description of the elec-  
 947 troweak and strong forces with the description of gravity, and it is still unclear  
 948 how to account for the effects of gravity at the Planck scale of approximately

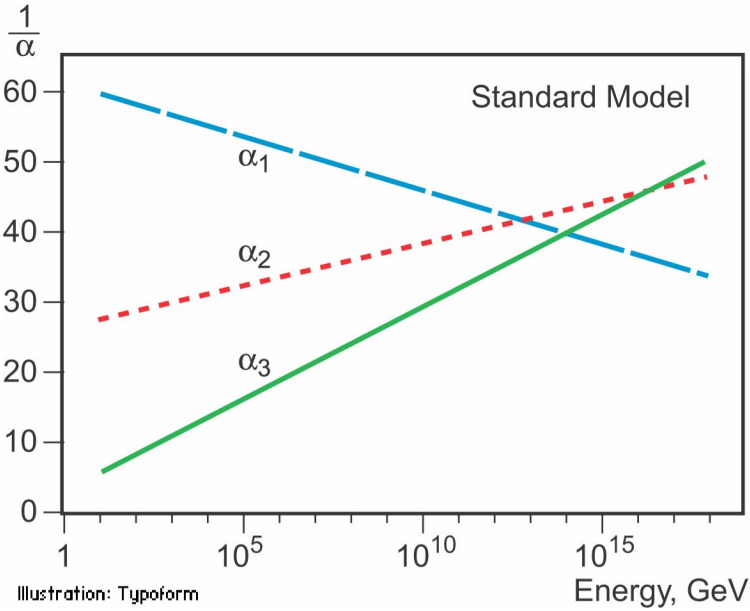


Figure 5: An approximation of the running of the coupling constants in the SM up to the Planck scale [unification\_plot].

949  $10^{19}$  GeV, where it can no longer be ignored. The Planck scale is an important  
 950 cutoff for the SM, as it is clear that the SM must break down somewhere between  
 951 the current highest energy tests of the SM, around 1 TeV, and the Planck scale.

952 One example of this is the Higgs mass, which is determined in the SM by a  
 953 sum of its bare mass and the interactions in the vacuum with all massive parti-  
 954 cles. As there must be new physics at the Planck scale to describe gravity, some  
 955 of those corrections would include contributions at a scale seventeen orders of  
 956 magnitude above the mass of the Higgs. Either the bare mass of the Higgs boson  
 957 precisely cancels those contributions to leave a remainder seventeen orders of  
 958 magnitudes smaller, or a new theory exists at a lower scale that shields the Higgs  
 959 mass from those terms. A theory where such a unlikely cancellation of free pa-  
 960 rameters occurs is called fine-tuned, and one that is free from such cancellations  
 961 is called natural. Theories where the mass of the Higgs is natural are usually pre-  
 962 ferred, as they suggest an underlying, coherent structure. The enormous differ-  
 963 ence in scales between the weak scale (including the Higgs mass), and the Planck  
 964 scale, is often referred to as the hierarchy problem.

965 There is also a compelling argument that the  $SU(3) \times SU(2) \times U(1)$  gauge  
 966 structure of the SM might originate from a single, unified gauge theory. For ex-  
 967 ample, it is possible to represent that gauge structure as a  $SU(5)$  gauge group  
 968 with only a few inconsistencies with the current implementation. This unifica-  
 969 tion is suggested by the scaling of the coupling constants for each of the forces  
 970 under renormalization; they come close to converging to a single value at higher  
 971 energies, as seen in Figure 5. An additional correction to the scaling of the cou-  
 972 pling constants from new physics above the TeV scale could cause them to merge  
 973 into a single value at high energies.

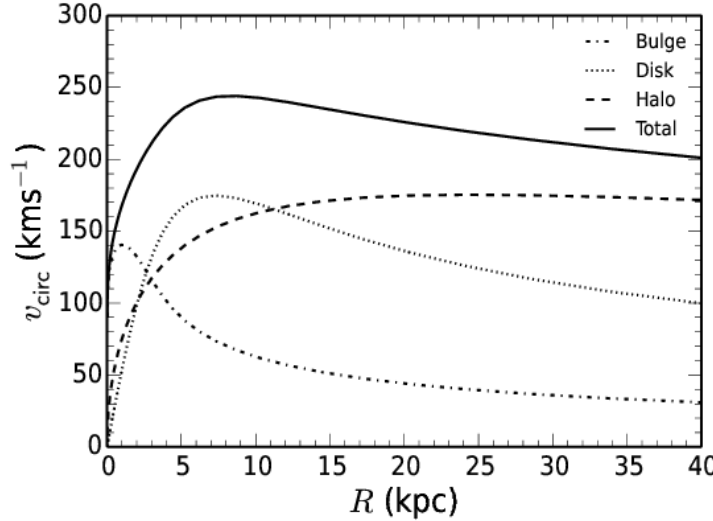


Figure 6: The distribution of velocities of stars as a function of the radius from the center of the galaxy. The contributions to the velocity from the various components of matter in the galaxy are shown [2].

#### 974 2.6.2 COSMOLOGICAL OBSERVATIONS

975 The SM contains a symmetry in the description of matter and antimatter that is  
 976 not reflected in cosmological observations. The process of the standard model  
 977 create or remove matter and antimatter in equal amounts, so a universe that be-  
 978 gins with an equal quantity of each should result in a universe with an approxi-  
 979 mate balance of matter and antimatter. However, cosmological observations of  
 980 the relative amount of each type clearly show that the directly observable mass  
 981 of the universe is overwhelmingly made of matter. As this difference is largely  
 982 a difference in the generation of baryons and anti-baryons, this discrepancy is  
 983 often referred to as the baryogenesis problem.

984 A number of astrophysical observations of large scale gravitational interac-  
 985 tions suggest the presence of a significant amount of non-luminous matter that  
 986 interacts with the normal matter only gravitationally. The first evidence of this  
 987 came from the observation of galactic rotation curves, the velocities of stars as  
 988 a function of the radius from the center of a galaxy. These can be directly pre-  
 989 dicted from the amount of matter contained within the sphere up to the radius  
 990 of the star. An estimate based only on the luminous matter in the galaxies would  
 991 predict a dependence that falls off with the radius, but the observed curves show  
 992 a mostly constant distribution of velocities [2], as seen in Figure 6. The higher  
 993 velocities than predicted by the luminous matter can be explained by a halo of  
 994 dark matter that extends significantly outside the galactic disk.

995 This dark matter accounts for a majority of the matter in the universe, and is  
 996 incompatible with the matter particles predicted by the SM. Many observations  
 997 support its existence, but there have been no direct detections of a particle which  
 998 could account for the large quantity of gravitationally interacting dark matter.  
 999 The SM would have to require a significant extension to include the particles

1000 needed to explain dark matter and the processes needed to explain the observed  
1001 matter-antimatter asymmetry.

1002

1003 SUPERSYMMETRY

---

1004 The theory of Supersymmetry ([SUSY](#)) presents an extension to the [SM](#) that solves  
 1005 a number of the outstanding issues. It is based on another proposed symmetry,  
 1006 one which introduces an equality between the fermionic particles and proposed  
 1007 bosonic partners. The symmetry is defined by extending spacetime into a super-  
 1008 space, which includes one dimension that describes a particle's spin: a transfor-  
 1009 mation in this space moves a fermion with spin-1/2 to a boson with spin-0 or  
 1010 vice-versa. Requiring the [SM](#) to be symmetrical under these transformations re-  
 1011 quires the existence of a bosonic partner for every current matter fermion in the  
 1012 [SM](#) and a fermionic partner for every boson. The partners are called superpar-  
 1013 ticles (sparticles), where quarks partner with squarks and leptons partner with  
 1014 sleptons, and each boson has a fermionic partner called a gaugino, such as the  
 1015 wino for the W boson. The superpartners, in the original form of the theory,  
 1016 should be identical to the original particle in every way except for spin; that is  
 1017 they would have the same quantum charges and the same mass.

1018 However, the simplest version of the theory, where the symmetry is unbroken,  
 1019 is incompatible with current observations of physics in a number of systems. For  
 1020 example, the existence of an electron with spin-0 would introduce a stable, elec-  
 1021 trically charged constituent of atoms that would not follow the Pauli exclusion  
 1022 principle and would thus significantly change atomic structure. Various high en-  
 1023 ergy physics measurements have also confirmed the spin of the W and Z bosons,  
 1024 for example, and a fermionic gaugino has never been produced at those masses.  
 1025 The solution to this incompatibility with observation is to conjecture that the  
 1026 symmetry exists but is broken, where the masses of the supersymmetric parti-  
 1027 cles are significantly larger than those of the current [SM](#) particles.

## 1028 3.1 STRUCTURE

1029 There are a number of ways to model [SUSY](#), but many of the resulting phenomena  
 1030 are similar, and a discussion of an example is sufficient describe the structure  
 1031 and results of the theory. The [MSSM](#) is one example of a complete description  
 1032 that includes the necessary symmetry breaking to result in the different masses  
 1033 between particles and sparticles. It is called minimal because it is designed to  
 1034 use the simplest possible extension to the [SM](#) that incorporateas [SUSY](#) and remains  
 1035 self consistent. The theory includes a sparticle partner for every standard model  
 1036 particle, which are listed in Table 1.

1037 To then provide the different masses for those sparticles, the [MSSM](#) introduces  
 1038 a second Higgs interaction. The resulting scalar field, along with the original  
 1039 Higgs field, generates five total particles,  $h^0$ , the original Higgs boson,  $A^0$ ,  $H^0$ ,  
 1040 and  $H^\pm$ , where the last two are electrically charged. These Higgs bosons can mix  
 1041 with the supersymmetric gauginos to form a series of mass eigenstates. These

Sector	Particles	Sparticles
Baryonic Matter	$(u, d)$	$(\tilde{u}, \tilde{d})$
	$(c, s)$	$(\tilde{c}, \tilde{s})$
	$(t, b)$	$(\tilde{t}, \tilde{b})$
Leptonic Matter	$(\nu_e, e)$	$(\tilde{\nu}_e, \tilde{e})$
	$(\nu_\mu, \mu)$	$(\tilde{\nu}_m u, \tilde{\mu})$
	$(\nu_\tau, \tau)$	$(\tilde{\nu}_\tau, \tilde{\tau})$
Higgs	$(H_u^+, H_u^0)$	$(\tilde{H}_u^+, \tilde{H}_u^0)$
	$(H_d^0, H_d^-)$	$(\tilde{H}_d^0, \tilde{H}_d^-)$
Strong	$g$	$\tilde{g}$
Electroweak	$(W^\pm, W^0)$	$(\tilde{W}^\pm, \tilde{W}^0)$
	$B^0$	$\tilde{B}^0$

Table 1: The particles in the **SM** and their corresponding superpartners in the **MSSM**.

1042 are usually referred to by the order of their masses, where the neutral gauginos  
 1043 (neutralinos) are labelled  $\tilde{\chi}_1^0, \tilde{\chi}_2^0, \tilde{\chi}_3^0$ , and  $\tilde{\chi}_4^0$ . The charged gauginos (charginos)  
 1044 are similarly labelled  $\tilde{\chi}_1^\pm$  and  $\tilde{\chi}_2^\pm$ .

1045 In addition to the new particle content, the **MSSM** introduces new interactions  
 1046 for the gauge bosons and gauginos. All interaction terms are added to the La-  
 1047 grangian which describe the interaction of a gauge boson or gaugino with a par-  
 1048 ticle or sparticle with the appropriate charge. Such terms include a few interac-  
 1049 tions which would violate the observed  $B - L$  symmetry that prevents proton  
 1050 decay. Either the couplings on these terms must be fine-tuned to match the ex-  
 1051 perimental limits on those decays, or an additional symmetry must be imposed  
 1052 to exclude the terms. The **MSSM** and several other **SUSY** models choose to intro-  
 1053 duce a new symmetry known as R-parity. Sparticles are R-parity odd while **SM**  
 1054 particles are R-parity even. And by requiring that each term in the supersymmet-  
 1055 ric Lagrangian conserves R-parity, it is enforced that sparticles are produced in  
 1056 pairs.

1057 The conservation of R-parity removes the  $B - L$  violating terms naturally  
 1058 from the Lagrangian. The remaining terms include all of the interactions of the  
 1059 **SM** where two of the particles are replaced with their **SUSY** partners, so that R-  
 1060 parity is conserved in the interactions. This also has an important significance in  
 1061 making the **LSP**, the  $\tilde{\chi}_1^0$ , stable, as it cannot decay to only **SM** particles without vi-  
 1062 olating the conservation of R-parity. The heavier sparticles then decay in chains,  
 1063 emitting an **SM** particle in each step, and leaving behind the **LSP** at the end of the  
 1064 chain.

### 1065 3.1.1 SIMPLIFIED MODELS

1066 The **MSSM** is just one example of a large suite of **SUSY** models with similar results.  
 1067 Each of those models can have hundreds of individual parameters that ultimately  
 1068 determine the masses and interactions of the supersymmetric particles. To avoid

1069 this complexity in making experimental measurements, the analyses of high en-  
 1070 ergy collisions often rely on simplified models. These models produce events  
 1071 from a single process, and the observable parameters such as the mass of the par-  
 1072 ticles and their lifetimes are controlled directly, rather than tuning the hundreds  
 1073 of underlying parameters.

1074 Experimental analyses use these models to search for new physics and to set  
 1075 limits on the production rates for a given type of process with working points  
 1076 of a few observable parameters. As one example, a simplified model may specify  
 1077 pair production of gluinos where the free parameters are the mass of the gluino  
 1078 and the types and masses of the particles it can decay into. The small number of  
 1079 parameters allows the phase space to be searched in a grid by simulating events  
 1080 with a few examples for the parameters and interpolating between them. The  
 1081 resulting analysis can set cross sectional limits as a function of the simplified  
 1082 parameters, and this allows for an easy interpretation of the result in a number  
 1083 of **SUSY** models.

## 1084 3.2 MOTIVATION

1085 **SUSY** models, including The **MSSM**, ameliorate many of the issues in the **SM** dis-  
 1086 cussed in Section 2.6. The first, a solution to the hierarchy problem, comes as a  
 1087 direct consequence of the introduction of massive superpartners for each **SM** par-  
 1088 ticle. The contributions to the Higgs mass from the much higher energy Planck  
 1089 scale come from a series of loop diagrams in the **SM**, where each massive **SM** parti-  
 1090 cle has a loop contribution. The introduction of superpartners generates a series  
 1091 of corresponding diagrams for correction to the Higgs mass, with opposite sign  
 1092 contributions because the superpartners have different spins. Those oppostie  
 1093 sign contributions cancel the correction terms at high energies, leaving behind a  
 1094 correction to the Higgs mass that is at the same scale as the masses of the super-  
 1095 partners. If the superpartners exist at the TeV scale, then the Higgs mass of 125  
 1096 GeV can be explained without significant fine-tuning, and the theory becomes  
 1097 natural.

1098 **SUSY** also has the potential to precisely enable the unification of the coupling  
 1099 constants at high energy. Without supersymmetric contributions, the coupling  
 1100 constants come close to a single value near the Planck scale, as shown in Fig-  
 1101 ure 5, but they do not exactly merge. With the addition of the **MSSM**, they join  
 1102 precisely at a single point, suggesting a unification into a single gauge theory at  
 1103 high energy, as shown in Figure 7. This precise unification, like the naturalness  
 1104 argument, also requires that the masses of the superpartners be near the TeV  
 1105 scale.

1106 The presence of R-parity in a **SUSY** model also provides an explanation for  
 1107 dark matter. The **LSP**, as discussed in Section 3.1, is a massive, neutral, and stable  
 1108 particle as long as R-parity is conserved. In the early universe, when the energy  
 1109 density was extremely high, **LSPs** could be spontaneously produced just as often  
 1110 as other particles like photons, and would result in a thermal equilibrium. Then,  
 1111 as the universe cooled, the average energy would be too low to create additional  
 1112 **LSPs**, and they would be left behind and only interact with the remaining matter

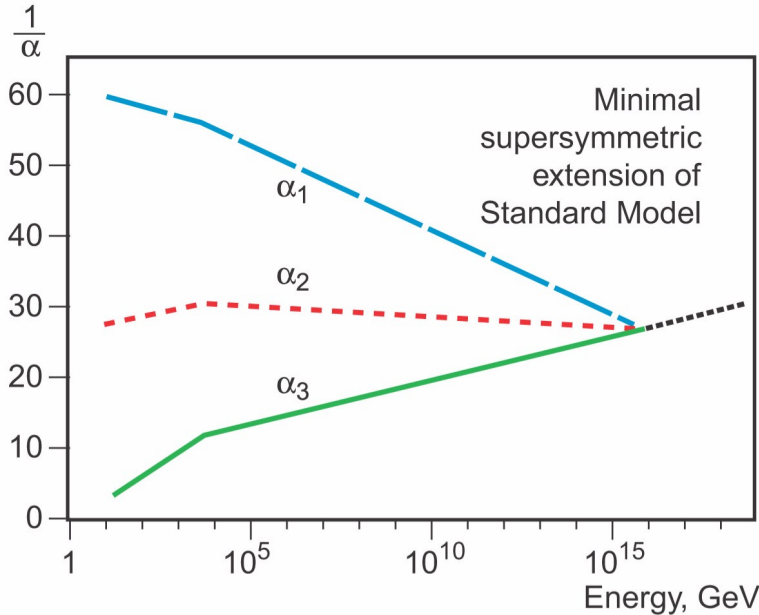


Figure 7: An approximation of the running of the coupling constants in the SM up to the Planck scale [[unification\\_plot](#)].

gravitationally, a process called freeze out. Since those particles are stable, they would remain indefinitely. With the existence of an LSP at around the TeV scale, this process can explain the observed amount of dark matter in the universe.

Together, this variety of solutions to existing problems provides strong theoretical support for the existence of SUSY near the TeV scale. The LHC is the first collider experiment to be able to probe into TeV scale interactions, making it an exciting time to look for this extension to the SM. A range of models have begun to be excluded with masses above 1 TeV [3], leading to a motivation to explore a wider variety of models with phenomena that may have been missed by the most direct search strategies.

### 3.3 LONG-LIVED PARTICLES

Some proposed SUSY models can produce Long-Lived Particles (LLPs) other than just the LSP. The most direct search strategies for SUSY often assume that the various non-stable sparticles decay promptly, rather than propagating through some fraction of the detector. Although the processes involved are very similar, the long-lifetime of the produced particles can lead to very different experimental signatures, and often require separate dedicated searches. It is important to design and execute search strategies for LLPs in order to completely cover possible production of new physics.

There are a few ways to generate long lifetimes for the massive SUSY particles, depending on the specific model. In examples like Spread Supersymmetry [4] and Split Supersymmetry [5, 6], the introduction of a split between two mass scales suppresses the decay of gluinos. In these and similar models, the squarks are much heavier than the gluino, and the gluino must decay through the production

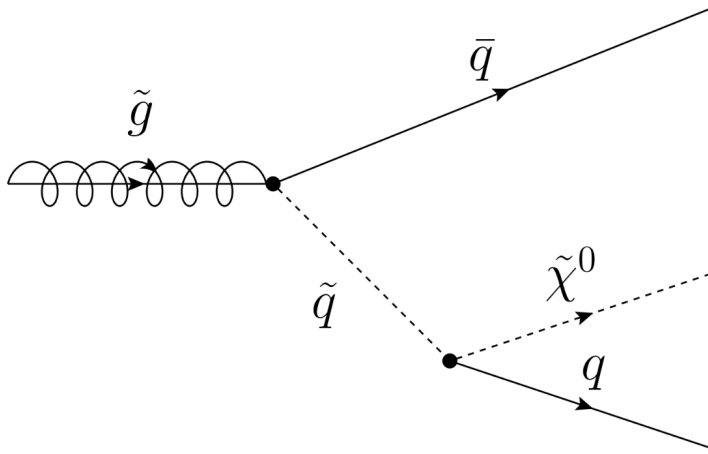


Figure 8: The decay of a gluino to quarks and an LSP, which precedes through a squark.

of a virtual squark, as shown in the diagram of Figure 8. The large mass of the squarks in the split models suppresses the decay rate, and can result in lifetimes of the order of 1 ns [4].

Nearly degenerate particles is another mechanism that results in long lifetimes, again by suppressing decay rates. When a particle must decay to another particle with nearly the same mass, the phase space factor in the decay results in a low decay rate. For example, a neutron has a lifetime of roughly fifteen minutes because its mass is so close to the proton. Models which result in a nearly degenerate chargino and LSP provide a long-lived chargino as well.

Again, because of the wide variety of models which can produce LLPs and the large number of parameters which determine their masses and lifetimes, the analysis presented here relies on simplified models. The models directly specify the decay mode of the LLPs as well as their masses and lifetimes, using a grid of values. The results of searches using these simplified models can be interpreted over a very wide range of models that predict LLPs, even including non-supersymmetric extensions to the SM.

1153

## PART III

1154

### EXPERIMENTAL STRUCTURE AND RECONSTRUCTION

1155

You can put some informational part preamble text here.

1156

1157 THE LARGE HADRON COLLIDER

---

1158 The LHC, a two-ring superconducting hadron accelerator, provides high energy  
1159 proton-proton collisions for several large experiments at European Organiza-  
1160 tion for Nuclear Research (CERN) in Geneva, Switzerland [7, 8]. It is the largest,  
1161 highest-luminosity, and highest-energy proton collider ever built, and was con-  
1162 structed by a collaboration of more than 10,000 scientists from the more than  
1163 100 countries that contribute to CERN. The original design of the LHC focused on  
1164 providing collision energies of up to 14 TeV and generating enough collisions to  
1165 reveal physics beyond the SM which is predicted to exist at higher energy scales.

1166 The LHC was installed in an existing 27 km tunnel at CERN which was orig-  
1167 inally designed to house the Large Electron Positron collider (LEP) [9]. This al-  
1168 lows the collider to use existing accelerators at the same complex to provide the  
1169 initial acceleration of protons up to 450 GeV before injecting into LHC. The in-  
1170 jected hadrons are accelerated up to as much as 14 TeV while being focused into  
1171 two beams traveling in opposite directions. During this process the protons cir-  
1172 culate around the tunnel millions of times, while the beams are intermittently  
1173 crossed at the four locations of the experiments to provide collisions. These col-  
1174 lision points correspond to the four major LHC experiments: ATLAS, Compact  
1175 Muon Solenoid (CMS), Large Hadron Collider beauty experiment (LHCb), and  
1176 A Large Ion Collider Experiment (ALICE), and Figure 9 shows the layout of the  
1177 experiments both on the surface and below. ATLAS and CMS are both general  
1178 purpose, high-luminosity detectors which search for a wide range of new types  
1179 of physics [10, 11]. LHCb studies the interactions of b-hadrons to explore the  
1180 asymmetry between matter and antimatter [12]. ALICE focuses on the collisions  
1181 of lead ions, which the LHC also provides, in order to study the properties of  
1182 quark-gluon plasma [13].

1183 During the first five years of continued operation, after the LHC turned on in  
1184 2010, the LHC has provided four major data collecting periods. In 2010 the LHC  
1185 generated collisions at several energies, starting at 900 GeV. It increased the  
1186 energy from 900 GeV to 2.76 TeV and then subsequently to 7 TeV, with a peak  
1187 luminosity of  $2 \times 10^{32} \text{ cm}^{-2}\text{s}^{-1}$ , and a total delivered luminosity of  $50 \text{ pb}^{-1}$ .  
1188 The next run, during 2011, continued the operation at 7 TeV and provided an  
1189 additional  $5 \text{ fb}^{-1}$  with a peak luminosity of  $4 \times 10^{33} \text{ cm}^{-2}\text{s}^{-1}$ . The energy was  
1190 then increased to 8 TeV for the data collection during 2012, which provided  $23 \text{ fb}^{-1}$   
1191 with a peak luminosity of  $7.7 \times 10^{33} \text{ cm}^{-2}\text{s}^{-1}$ . After the first long shutdown  
1192 for 2013 and 2014, the LHC resumed operation and increased the energy to 13  
1193 TeV in 2015, where it delivered  $4.2 \text{ fb}^{-1}$  with a peak luminosity of  $5.5 \times 10^{33} \text{ cm}^{-2}\text{s}^{-1}$ .  
1194 The LHC is currently providing additional 13 TeV collisions in 2016 with higher  
1195 luminosities than during any previous data collection periods. These  
1196 running periods are summarized in Figure 10, which shows the total delivered

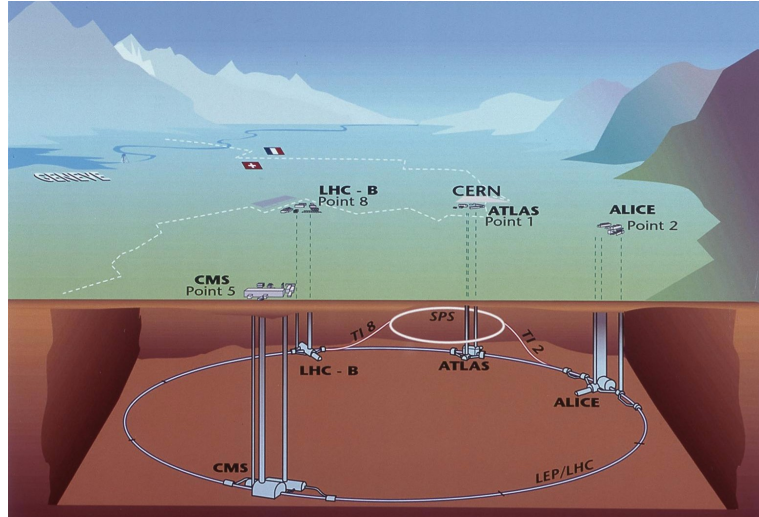


Figure 9: The four collision points and corresponding experiments of the [LHC](#). The image includes the location of the nearby city of Geneva as well as the border of France and Switzerland.

1197 luminosity over time for the [ATLAS](#) experiment during each of the four years of  
 1198 data collection since 2011.

## 1199 4.1 INJECTION CHAIN

1200 The [LHC](#) takes advantage of the presence of previously built accelerators at [CERN](#)  
 1201 to work up to the target energy in consecutive stages. The series of accelerators  
 1202 that feed into the [LHC](#) are known collectively as the injection chain, and together  
 1203 with the [LHC](#) form the accelerator complex. The full complex is illustrated in  
 1204 Figure 11, which details the complex series required to reach collisions of 13 or  
 1205 14 TeV.

1206 Protons at the [LHC](#) begin as hydrogen atoms in the Linac 2, a linear accelerator  
 1207 which replaced Linac 1 as the primary proton accelerator at [CERN](#) in 1978. In  
 1208 Linac 2, the hydrogen atoms are stripped of their electrons by a strong magnetic field,  
 1209 and the resulting protons are accelerated up to 50 MeV by cylindrical con-  
 1210 ductors charged by radio frequency cavities. The protons are then transferred  
 1211 to the Proton Synchrotron Booster ([PSB](#)), which uses a stack of four synchrotron  
 1212 rings to accelerate the protons up to 1.4 GeV. Then the protons are injected  
 1213 into the Proton Synchrotron ([PS](#)) which again uses synchrotron rings to bring  
 1214 the energy up to 25 GeV. The intermediate step between Linac 2 and the [PS](#) is  
 1215 not directly necessary, as the [PS](#) can accelerate protons starting from as low as  
 1216 50 MeV. The inclusion of the [PSB](#) allows the [PS](#) to accept a higher intensity of  
 1217 injection and so increases the deliverable luminosity in the [LHC](#). The penulti-  
 1218 mate stage of acceleration is provided by the Super Proton Synchrotron ([SPS](#)), a  
 1219 large synchrotron with a 7 km circumference that was commissioned at [CERN](#)  
 1220 in 1976. During this step the protons increase in energy to 450 GeV, after which  
 1221 they can be directly injected into the [LHC](#).

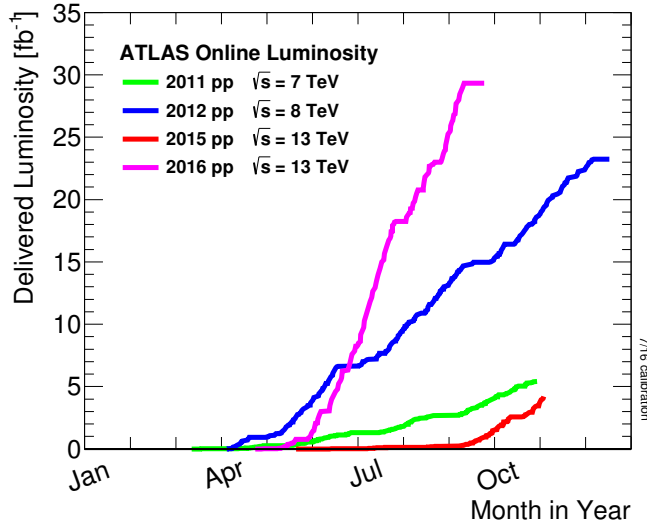


Figure 10: The cumulative luminosity over time delivered to the [ATLAS](#) experiment from high energy proton-proton collisions since 2011. The energies of the collisions are listed for each of the data-taking periods.

1222      The final step is the [LHC](#) itself, which receives protons from the [SPS](#) into two  
 1223      separate beam pipes which circulate in opposite directions. The filling process  
 1224      at this steps takes approximately 4 minutes, and the subsequent acceleration to  
 1225      the final energy (6.5 TeV during 2015 and up to 7 TeV by design) takes approxi-  
 1226      mately half an hour. At this point the protons circulate around the circumference  
 1227      tens of thousands of times a second and continue for up to two hours.

## 1228      4.2 DESIGN

### 1229      4.2.1 LAYOUT

1230      Many of the aspects of the [LHC](#) design are driven by the use of the existing [LEP](#)  
 1231      tunnel. This tunnel slopes gradually, with a 1.4% decline, with 90% of its length  
 1232      built into molasse rock which is particularly well suited to the application. The  
 1233      circumference is composed of eight 2987 meter arcs and eight 528 meter straight  
 1234      sections which connect them; this configuration is illustrated in Figure 12. The  
 1235      tunnel diameter is 3.7 m throughout its length.

The design energy is directly limited by the size of this tunnel, with its radius of curvature of 2804 m. A significant magnetic field is required to curve the protons around that radius of curvature; the relationship is given by

$$p \simeq 0.3BR \quad (13)$$

1236      where  $p$  is the momentum of the particle in GeV,  $B$  is the magnetic field in Tesla,  
 1237      and  $R$  is the radius of curvature in meters. From the target design energy of  
 1238      14 TeV, or 7 TeV of momentum for protons in each beam, the required mag-  
 1239      netic field is 8.33 Tesla. This is too large a field strength to be practical with  
 1240      iron electromagnets, because of the enormous power required and the resulting

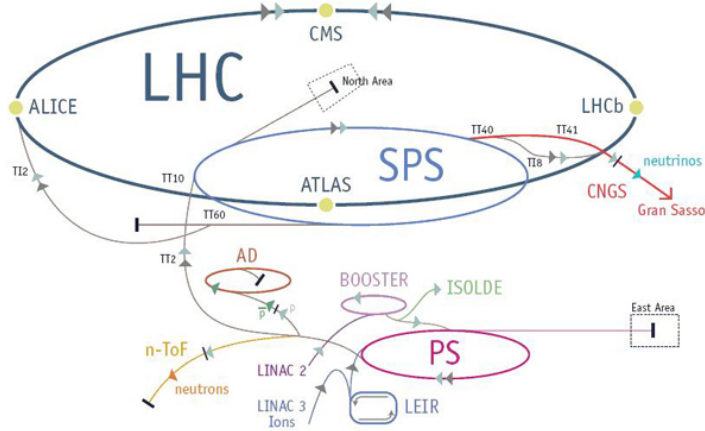


Figure 11: The accelerator complex that builds up to the full design energies at the LHC. The protons are passed in order to Linac 2, the PSB, the PS, the SPS and then the LHC.

1241 requirements for cooling. Because of these constraints, the LHC uses supercon-  
 1242 ducting magnets which can maintain that field strength with significantly less  
 1243 power consumption.

#### 1244 4.2.2 MAGNETS

1245 The magnets chosen were Niobium and Titanium (NbTi) which allow for field  
 1246 strengths as high as 10 Tesla when cooled down to 1.9 K. Reaching the target  
 1247 temperature of 1.9 K for all of the magnets requires superfluid helium and a large  
 1248 cryogenic system along the entire length of the tunnel. During normal operation,  
 1249 the LHC uses 120 tonnes of helium within the magnets, and the entire system is  
 1250 cooled by eight cryogenic helium refrigerators. The temperature increase that  
 1251 occurs during transit from the refrigerator along the beam necessitates that the  
 1252 refrigerators cool the helium down to 1.8 K. Any significant increase above this  
 1253 temperature range can remove the superconductive properties of the magnets,  
 1254 which in turn generates drastically larger heat losses from the current within the  
 1255 magnets and causes a rapid rise in temperature called a quench.

1256 There are approximately 8000 superconducting magnets distributed around  
 1257 the LHC. The 1232 bending magnets, which keep the protons curving along the  
 1258 length of the beam, are twin bore cryodipoles, which allow both proton beams  
 1259 to be accommodated by one magnet and all of the associated cooling structure.  
 1260 Figure 13 shows the cross section of the design for these dipoles. The magnets  
 1261 are very large, 16.5 m long with a diameter of 0.57 meters and a total weight of 28  
 1262 tonnes. They are slightly curved, with an angle of 5.1 mrad, in order to carefully  
 1263 match the beam path. The twin bore accommodates both magnets inside the  
 1264 two 5 cm diameter holes which are surrounded by the superconducting coils.  
 1265 The coils require 12 kA of current in order to produce the required magnetic  
 1266 field. These coils are comprised of NbTi cable wound in two layers; the wire in

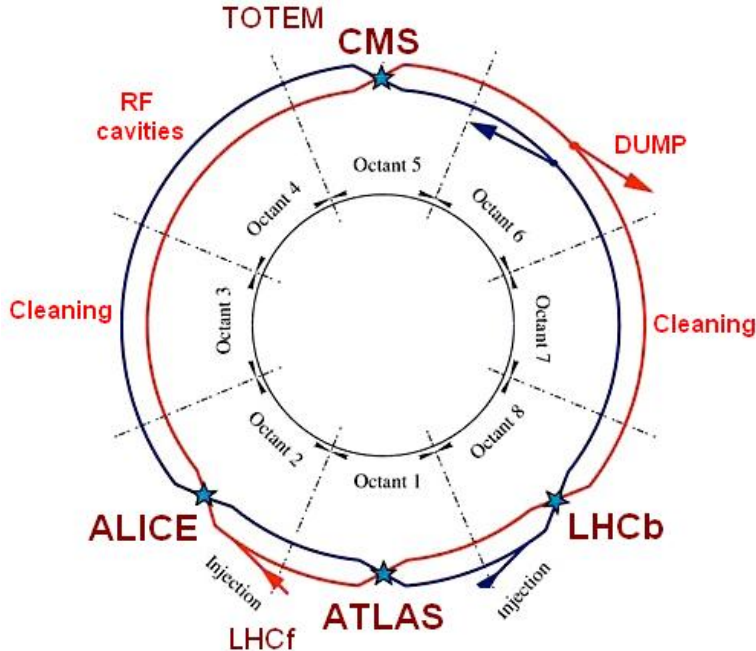


Figure 12: A schematic of the layout of the LHC, not to scale. The arched and straight sections are illustrated at the bottom of the schematic, and all four crossing sites are indicated with their respective experiments.

1267 the inner layer has a diameter of 1.065 mm while the wire in the outer layer has  
1268 a diameter of 0.825 mm.

1269 The large currents in the wires, along with the magnetic field produced, result  
1270 in forces on the magnets which would tend to push them apart with over 10,000  
1271 Newtons per meter. Constraining the magnets requires a significant amount of  
1272 structure including non-magnetic stainless steel collars. Both the presence of  
1273 these electromagnetic forces and the varying thermal contraction coefficient of  
1274 the pieces of the magnet produce significant forces on the cold mass structure.  
1275 The cold mass is carefully engineered to so that these stresses do not significantly  
1276 alter the magnetic field shape, which must be maintained between magnets to a  
1277 precision of approximately  $10^{-4}$  for successful operation.

1278 The remaining 6800 magnets are a variety of quadrupole, sextapole, octopole,  
1279 and single bore dipole magnets. These are used to damp oscillations, correct  
1280 beam trajectories, focus the beams during circulation, and to squeeze the beams  
1281 before collisions.

#### 1282 4.2.3 RF CAVITIES

1283 Sixteen RF cavities produce the actual acceleration of the proton beam up to the  
1284 design energy. These RF cavities are tuned to operate at 400 MHz, and are pow-  
1285 ered by high-powered electron beams modulated at the same frequency, called  
1286 klystrons. The resonance within the cavity with the oscillating electric field  
1287 establishes a voltage differential of 2 MV per cavity. The sixteen cavities are  
1288 split between the two beams, so combined the cavities provide 16 MV per beam,

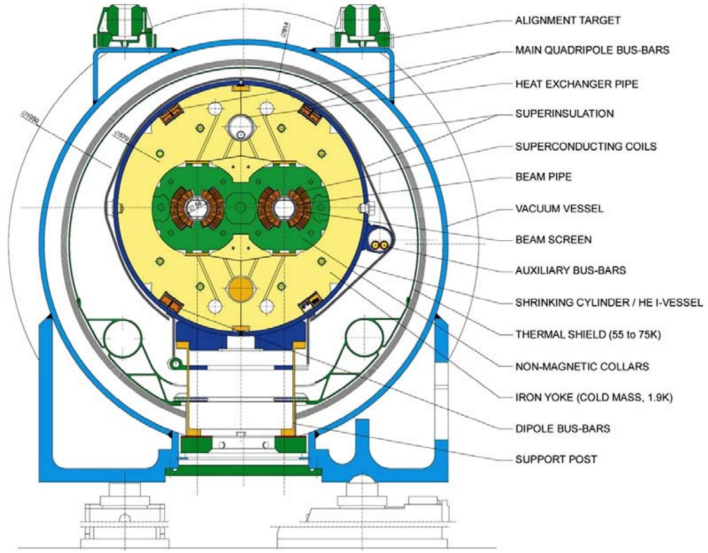


Figure 13: A cross section of the the cryodipole magnets which bend the flight path of protons around the circumference of the LHC. The diagram includes both the superconducting coils which produce the magnetic field and the structural elements which keep the magnets precisely aligned.

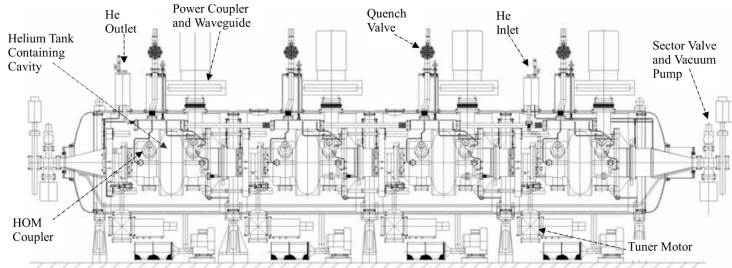


Figure 14: The arrangement of four RF cavities within a cryomodule.

1289 which accelerate the protons on each consecutive pass through the cavity. This  
 1290 acceleration is also necessary during circulation even after the target energy has  
 1291 been reach in order to compensate for losses from synchrotron radiation.

1292 The cavities are arranged in cryomodules which contain four cavities, with  
 1293 two cryomodules per beam; this arrangement is illustrated in Figure 14. These  
 1294 cryomodules are necessary to maintain the superconducting state of the cavities,  
 1295 which are also constructed from niobium. The RF cavities use niobium along  
 1296 with copper to allow for low power losses in the superconductors. The copper  
 1297 provides a reduced susceptibility to quenching, as it rapidly conducts away heat  
 1298 generated by imperfections in the niobium, as well as natural shielding from the  
 1299 earth's magnetic field which can interfere with the RF system.

1300 The nature of the radio frequency oscillations tends to group protons together  
 1301 into buckets. A proton traveling exactly in phase with the RF oscillations will not  
 1302 be displaced at all during a single circulation, and those slightly ahead or behind  
 1303 of that phase will slightly decelerate or accelerate, respectively. This produces

1304 separate clusters of protons which arrive in phase to the cavities every 2.5 ns,  
 1305 corresponding to the 400 MHz frequency.

1306 4.2.4 BEAM

1307 The beams of protons circulate within 54 km of 5 cm diameter beam pipe. This  
 1308 entire structure is kept under vacuum at 1.9 K to prevent interactions between  
 1309 the beam pipe and the magnets as well as to prevent any interactions between the  
 1310 circulating protons and gas in the pipe. The vacuum within the pipe establishes  
 1311 a pressure as low as  $10^{-9}$  mbar before the protons are introduced.

1312 Because of the very high energies of the circulating protons, synchrotron ra-  
 1313 diation is not negligible in the bending regions. The protons are expected to  
 1314 radiate 3.9 kW per beam at 14 TeV, with 0.22 W/m, which is enough power to  
 1315 heat the liquid helium and cause a quench were it absorbed by the magnets. To  
 1316 prevent this, a copper screen is placed within the vacuum tube that absorb the  
 1317 emitted photons. This screen is kept between 5 and 20 K by the liquid helium  
 1318 cooling system.

1319 4.3 LUMINOSITY PARAMETERS

In addition to the high energy of the collisions, the rate of collisions is extremely important to enabling the discovery of new physics. Many measurements and searches require a large number of events in order to be able to make statistically significant conclusions. The rate of collisions is measured using luminosity, the number of collisions per unit time and unit cross section for the proton-proton collisions. From the beam parameters, luminosity is given by

$$\mathcal{L} = \frac{N_b^2 n_b f_{rev} \gamma}{4\pi\epsilon_n \beta^*} F \quad (14)$$

1320 where  $N_b$  is the number of protons per bunch,  $n_b$  is the number of bunches per  
 1321 beam,  $f_{rev}$  is the frequency of revolution,  $\gamma$  is the Lorentz factor for the protons  
 1322 at the circulating energy,  $\epsilon_n$  is the emittance,  $\beta^*$  is the amplitude function at the  
 1323 collision point, and  $F$  is a geometric factor that accounts for the crossing angle of  
 1324 the beams at the collision point. The emittance measures the average spread of  
 1325 particles in both position and momentum space, while the amplitude function  
 1326 is a beam parameter which measures how much the beam has been squeezed.  
 1327 Together  $\epsilon_n$  and  $\beta^*$  give the size of the beam in the transverse direction,  $\sigma =$   
 1328  $\sqrt{\epsilon\beta^*}$ .  $\beta$  changes over the length of the beam as the accessory magnets shape the  
 1329 distribution of protons, but only the value at the point of collisions,  $\beta^*$ , affects  
 1330 the luminosity.

1331 The luminosity is maximized to the extent possible by tuning the parameters  
 1332 in Equation 14. A number of these are constrained by the design decisions. The  
 1333 revolution frequency is determined entirely by the length of the tunnel, as the  
 1334 protons travel at very close to the speed of light. The geometric factor  $F$  is de-  
 1335 termined by the crossing angle of the beams at the collision points, again a com-

Parameter	Unit	Injection	Nominal
Beam Energy	TeV	0.450	7
Peak Instantaneous Luminosity	$\text{cm}^{-2}\text{s}^{-1}$	-	$10^{34}$
Bunch Spacing	ns	25	25
Number of Filled Bunches	-	2808	2808
Normalized Transverse Emittance	$\mu\text{m}$	3.75	3.75
Frequency	MHz	400.789	400.790
RF Voltage/Beam	MV	8	16
Stored Energy	MJ	-	362
Magnetic Field	T	0.54	8.33
Operating Temperature	K	1.9	1.9

Table 2: The design parameters of the [LHC](#) beam that determines the energy of collisions and the luminosity, for both the injection of protons and at the nominal circulation.

ponent of the tunnel design; this angle is already very small at  $285 \mu\text{rad}$ , which helps to maximize the geometric factor.

The major pieces that can be adjusted are the number of protons per bunch,  $N_b$ , the number of bunches in the beam,  $n_b$ , and the amplitude function  $\beta$ . Increasing either  $N_b$  or  $n_b$  increases the amount of energy stored in the beam, which presents a danger if control of the beam is lost. At design specifications, the beam stores 362 MJ, which is enough energy to damage the detectors or accelerator if the beam were to wander out of the beam pipe. So, the luminosity is primarily controlled at the [LHC](#) by adjusting  $\beta^*$ , where lowering  $\beta^*$  increases the luminosity.  $\beta^*$  is tuned to provide the various values of luminosity used at the [LHC](#) which can be raised to as much as  $10^{34}$ .

The nominal bunch structure consists of 3654 bunches, each holding  $10^{11}$  protons, which cross a collision point in 25 ns. These are further subdivided into the buckets mentioned in Section 4.2.3 by the clustering properties of the RF cavities. The bunches are further grouped into trains of 72 bunches which are separated by a gap which would otherwise hold 12 bunches. At nominal operation 2808 of the bunches will actually be filled with protons, while the remainder are left empty to form an abort gap that can be used in case the beam needs to be dumped.

The various beam parameters are summarized in Table 2 for the designed operation. In practice, the beam has operated at lower energies and lower luminosities than the design values for the majority of its lifetime, but the [LHC](#) has begun to operate at full design values during Run 2.

#### 4.4 DELIVERED LUMINOSITY

During the data collection of 2015, the [LHC](#) operated at luminosities as large as  $5 \times 10^{33} \text{ cm}^{-2}\text{s}^{-1}$ . It is convenient to refer to the integrated luminosity, the inte-

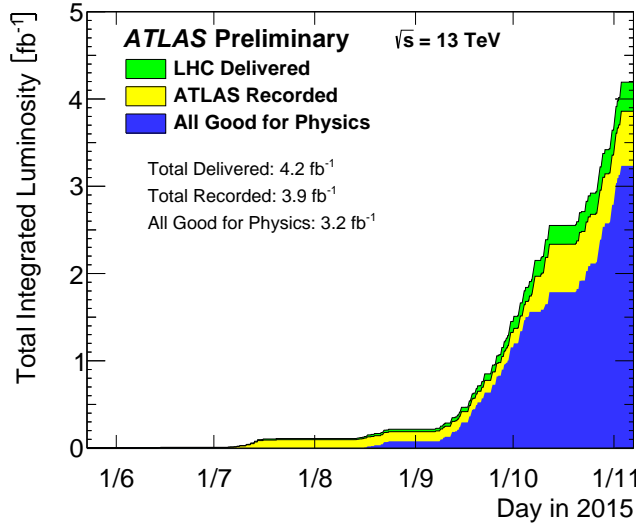


Figure 15: The cumulative luminosity versus time delivered to ATLAS (green), recorded by ATLAS (yellow), and certified to be good quality data (blue) during stable beams for pp collisions at 13 TeV in 2015.

gral of the instantaneous luminosity, which corresponds directly to the number of delivered events for a given process.

$$N = \sigma \times \int \mathcal{L}(t) dt$$

where  $\sigma$  is the cross section for the process of interest. The integrated luminosity over time is shown in Figure 15. This includes the luminosity delivered by the LHC as well as the luminosity that was recorded by ATLAS. ATLAS only records collisions when the LHC reports that the beam conditions are stable, so some of the delivered luminosity is not recorded. The figure also includes the amount of luminosity marked as good for physics, which includes additional requirements on the operation of the detector during data collection that are necessary for precise measurements.

Because the beam circulates and collides bunches of protons, it is possible for a single crossing to produce multiple proton-proton collisions. As the instantaneous luminosity is increased, the average number of collisions generated per bunch crossing increases. An event refers to the entire collection of interactions during a single bunch crossing, while interactions refer to the individual proton-proton collisions. The additional interactions produced during each bunch crossing are referred to as pileup, which can be more precisely defined quantified using the average number of additional proton-proton interactions per crossing, often denoted  $\mu$ . Figure 16 shows the luminosity-weighted distribution of the mean number of interactions for events collected in 2015. The presence of as many as twenty interactions in a single collision provides a significant challenge in reconstructing events and isolating the targeted physical processes.

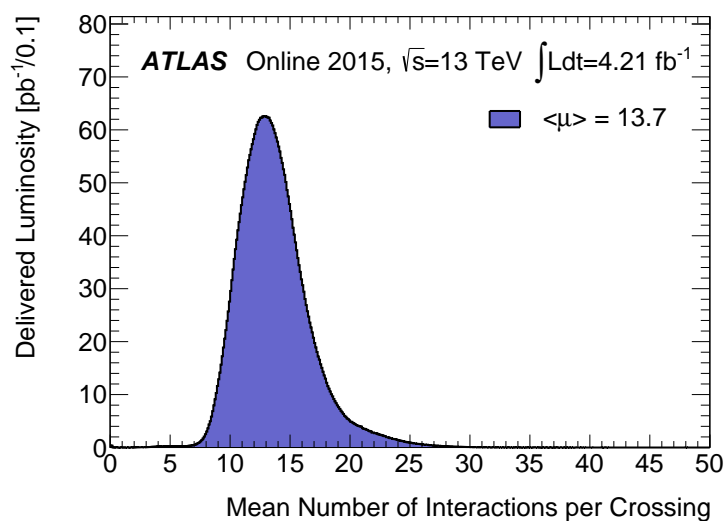


Figure 16: The luminosity-weighted distribution of the mean number of interactions per crossing for the 2015 pp collision data at 13 TeV.

1380

1381 THE ATLAS DETECTOR

---

1382 The four major LHC experiments at CERN seek to use the never before matched  
 1383 energies and luminosities of the new collider to explore the boundaries of par-  
 1384 ticle physics and to gain insight into the fundamental forces of nature. Two of  
 1385 these experiments, ATLAS and CMS, are general purpose detectors that seek to  
 1386 measure a variety of processes in the up to 13 TeV proton-proton collisions that  
 1387 occur as much as 800 million times per second at the LHC at the design lumi-  
 1388 nosity of  $10^{34} \text{ cm}^{-2}\text{s}^{-1}$ . ATLAS employs a hermetic detector design, one which  
 1389 encloses the particle collisions as completely as possible with detecting elements,  
 1390 that allows it to study a wide range of physics from SM and Higgs measurements  
 1391 to searches for new physics in models like SUSY [10].

1392 Accommodating this wide variety of goals is a challenge for the design of the  
 1393 detector. The wide range of energies involved requires high measurement pre-  
 1394 cision over several orders of magnitude, and the numerous physics processes  
 1395 require an ability to measure a variety of particle types. At the time of the con-  
 1396 struction of ATLAS, the Higgs boson had yet to be discovered, but the diphoton  
 1397 decay mode was (correctly) expected to be important and necessitated a high  
 1398 resolution photon measurement. The potential for decays of new heavy gauge  
 1399 bosons,  $W'$  and  $Z'$ , required a similarly high momentum resolution for leptons  
 1400 with momentum up to several TeV. Hadronic decay modes of several possible  
 1401 new high energy particles could result in very energetic jets, again up to several  
 1402 TeV, and reconstructing the decay resonances would again require good energy  
 1403 resolution. Several models, such as SUSY or Extra Dimensions, predict the exis-  
 1404 tence of particles which would not interact with traditional detecting elements.  
 1405 However these particles can still be observed in a hermetic detector by accurately  
 1406 measuring the remaining event constituents to observe an imbalance in energy  
 1407 called missing energy or  $E_T^{\text{miss}}$ . Measuring  $E_T^{\text{miss}}$  implicitly requires a good res-  
 1408 olution on all SM particles that can be produced. And at the lower end of the  
 1409 energy spectrum, precision SM measurements would require good resolution of  
 1410 a variety of particle types at energies as low as a few GeV, so the design needs to  
 1411 accommodate roughly three orders of magnitude.

1412 This broad spectrum of measurements requires a variety of detector systems  
 1413 working together to form a cohesive picture of each collision. Two large mag-  
 1414 net systems produce magnetic fields that provide a curvature to the propaga-  
 1415 tion of charged particles and allows for precision momentum measurements by  
 1416 other systems. The inner detector uses a combination of tracking technologies  
 1417 to reconstruct particle trajectories and vertices for charged particles. A variety  
 1418 of calorimeters measure the energies of hadrons, electrons, and photons over a  
 1419 large solid angle. A large muon spectrometer identifies muons and uses the sec-  
 1420 ond magnet system to provide an independent measurement of their momentum

1421 from the inner detector and improve the resolution. The layout of all of these  
 1422 systems is shown in Figure 17.

1423 The performance goals needed to achieve the various targeted measurements  
 1424 and searches discussed above can be summarized as resolution and coverage re-  
 1425 quirements on each of these systems. Those requirements are listed in Table 3.

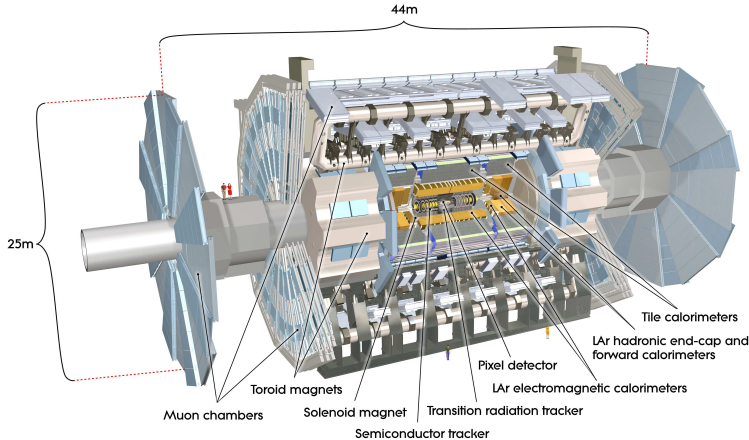


Figure 17: A cut-away schematic of the layout of the [ATLAS](#) detector. Each of the major subsystems is indicated.

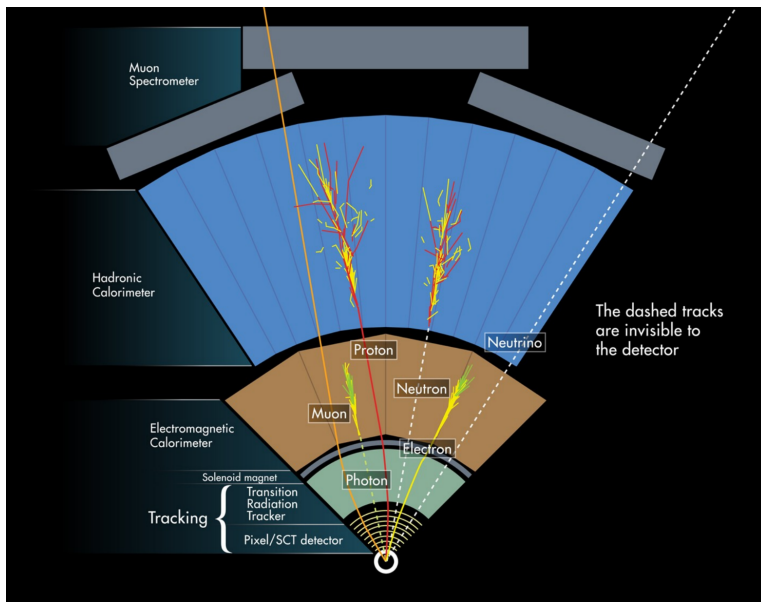


Figure 18: A cross-sectional slice of the [ATLAS](#) experiment which illustrates how the various SM particles interact with the detector systems.

1426 Incorporating these various pieces into a single detector is a significant tech-  
 1427 nical challenge. The resulting detector has a diameter of 22 m, is 46 m long,  
 1428 and weighs 7,000 tons; it is the largest volume particle detector ever constructed.  
 1429 The various detector elements need to be constructed and assembled with pre-  
 1430 cision as low as micrometers. These systems all need to function well even after  
 1431 exposure to the significant radiation dose from the collisions. Designing, con-

Detector Component	Required Resolution	$ \eta $ Coverage	
		Measurement	Trigger
Tracking	$\sigma_{p_T}/p_T = 0.05\% p_T + 1\%$	2.5	-
EM Calorimetry	$\sigma_E/E = 10\%/\sqrt{E} + 0.7\%$	3.2	2.5
Hadronic Calorimetry			
Barrel and Endcap	$\sigma_E/E = 50\%/\sqrt{E} + 3\%$	3.2	3.2
Forward	$\sigma_E/E = 100\%/\sqrt{E} + 10\%$	3.1 – 4.9	3.1 – 4.9
Muon Spectrometer	$\sigma_{p_T}/p_T = 10\% \text{ at } p_T = 1 \text{ TeV}$	2.7	2.4

Table 3: The performance goals for each of the subsystems of the [ATLAS](#) detector. The  $|\eta|$  coverage specifies the range where the subsystem needs to be able to provide measurements with the specified resolution. The resolutions include a  $p_T$  or  $E$  dependence that is added in quadrature with a  $p_T/E$  independent piece.

1432 structing, and installing the detector took the combined effort of more than 3000  
1433 scientists from 38 countries over almost two decades.

## 1434 5.1 COORDINATE SYSTEM

1435 The coordinate system defined for the [ATLAS](#) detector is used throughout all of  
1436 the sections of this thesis. The system begins with the choice of a  $z$  axis along  
1437 the beamline. The positive  $z$  side of the detector is commonly referred to  
1438 as the  $A$ -side, and the negative  $z$  side is referred to as the  $C$ -side. The  $x - y$   
1439 plane is then the plane transverse to the beam direction, with the  $x$  direction  
1440 defined as pointing from the interaction point to the center of the [LHC](#) ring and  
1441 the  $y$  direction defined as pointing upwards. The nominal interaction point is  
1442 the origin of this system.

1443 It is more convenient in practice to use a cylindrical coordinate system; this  
1444 choice of coordinate system reflects the cylindrical symmetry of the [ATLAS](#) de-  
1445 tector. The distance from the beamline is the radius,  $r'$ , and the angle from the  
1446  $z$ -axis is  $\theta$ . The azimuthal angle uses the usual definition, with  $\phi$  running around  
1447 the  $z$ -axis and  $\phi = 0$  corresponding to the  $x$ -axis. Many aspects of the detector  
1448 are independent of the this coordinate to first order. The  $\theta$  direction is typically  
1449 specified using rapidity or pseudorapidity, where rapidity is defined as

$$y = \frac{1}{2} \ln \frac{E + p_z}{E - p_z} \quad (15)$$

1450 Rapidity is particularly useful to indicate the component along the  $z$  direction  
1451 because differences in rapidity are invariant to boosts along the  $z$ -direction. A  
1452 similar quantity which depends only the  $\theta$  is pseudorapidity,

$$\eta = -\ln \tan \frac{\theta}{2} \quad (16)$$

1453 which is the same as rapidity when the particle is massless and in the limit where  
 1454 the energy is much larger than the particle's mass. It is often useful to refer to  
 1455 differences in solid angle using the pseudorapidity and the azimuthal angle:

$$\Delta R = \sqrt{\Delta\phi^2 + \Delta\eta^2} \quad (17)$$

1456 The pseudorapidity is also invariant to boosts along the  $z$ -axis for high mo-  
 1457 mentum particles, and is preferable to rapidity because it does not depend on  
 1458 the specific choice of particle. Pseudorapidity is also preferable to  $\theta$  because par-  
 1459 ticle production is roughly uniform in equal-width intervals of  $\eta$  up to about  
 1460  $\eta = 5.0$ . A particle traveling along the beampipe has  $\eta = \text{inf}$  and a particle  
 1461 traveling perpendicular to the beampipe has  $\eta = 0$ . The extent of the tracker,  
 1462  $|\eta| < 2.5$ , corresponds to approximately  $0.05\pi < \theta[\text{rad}] < 0.95\pi$  and the  
 1463 extent of the calorimeters,  $|\eta| < 4.9$  corresponds to approximately  $0.005\pi <$   
 1464  $\theta[\text{rad}] < 0.995\pi$ . Many detector components are broken into multiple subsys-  
 1465 tems to provide coverage at greater  $|\eta|$ . The lower  $|\eta|$  region is referred to as the  
 1466 barrel, typically with  $|\eta| \lesssim 2$ , and the greater  $|\eta|$  region is often referred to as the  
 1467 endcap.

1468 The initial energy and momentum of a proton-proton collision along the  $z$  di-  
 1469 rection is unknown in hadron colliders because different energies and momenta  
 1470 can be carried by the partons. Along the transverse plane, however, the vector  
 1471 sum of momentum will be zero. For this reason, many physical quantities are  
 1472 quantified in terms of their projection onto the transverse plan, such as  $p_T$  or  
 1473  $E_T$ . In addition,  $p_T$  alone determines the amount of curvature in the magnetic  
 1474 field, and can be measured independently by measuring the curvature of a parti-  
 1475 cle's propagation.

## 1476 5.2 MAGNETIC FIELD

1477 The magnet system used in [ATLAS](#) is designed to provide a substantial magnetic  
 1478 field in the two regions where the trajectory of particles is measured, the inner  
 1479 detector and the muon spectrometer. The magnetic field provides a curvature to  
 1480 the trajectory of charged particles and allows the precision tracking elements to  
 1481 make high resolutions measurements of  $p_T$ . To provide a magnetic field in these  
 1482 regions, [ATLAS](#) uses a hybrid system with four separate, superconducting mag-  
 1483 nets. A single solenoid provides a 2 T axial, uniform magnetic field for the inner  
 1484 detector, while a barrel toroid and two endcap toroids produce a non-uniform  
 1485 magnetic field of 0.5 and 1 T, respectively, for the muon detectors. This geom-  
 1486 etry is illustrated in Figure 19, and the parameters of the three magnet systems  
 1487 are summarized in Table 4.

1488 The central solenoid uses a single-layer coil with a current of 7.730 kA to gen-  
 1489 erate the 2 T axial field at the center of the magnet. The single-layer coil design  
 1490 enables a minimal amount of material to be used in the solenoid's construction,  
 1491 which is important because the solenoid is placed between the inner detector  
 1492 and the calorimeters. At normal incidence the magnet has only 0.66 radiation  
 1493 lengths worth of material, where one radiation length is the mean distance over

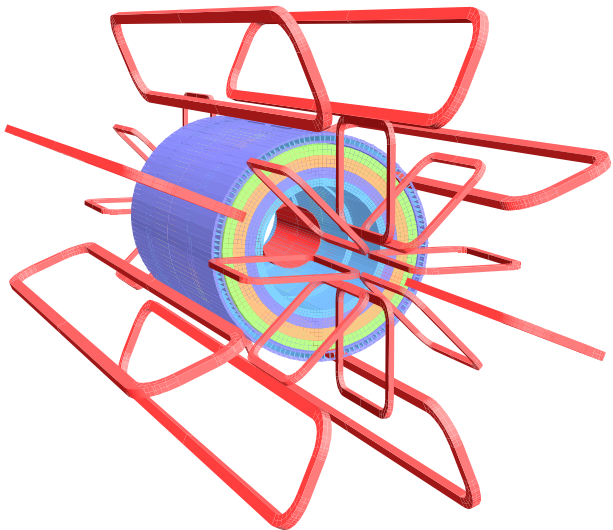


Figure 19: The layout of the four superconducting magnets in the [ATLAS](#) detector.

Parameter	Unit	Solenoid	Barrel Toroid	Endcap Toroids
Inner Diameter	m	2.4	9.4	1.7
Outer Diameter	m	2.6	20.1	10.7
Axial Length	m	5.3	25.3	5.0
Weight	tons	5.7	830	239
Conductor Size	mm <sup>2</sup>	30×4.25	57×12	41×4.25
Peak Field	T	2.6	3.9	4.1
Heat Load	W	130	990	330
Current	kA	7.7	20.5	20.0
Stored Energy	MJ	38	1080	206

Table 4: A summary of the parameters of each of the three magnet systems on [ATLAS](#).

1494 which a high-energy electron loses all but  $1/e$  of its energy through material in-  
 1495 teractions [3]. The coil is made of a high-strength aluminum stabilized NbTi  
 1496 superconductor which was optimized to achieve a high field with minimal thick-  
 1497 ness. The axial magnetic field produced by the solenoid bends charged particles  
 1498 in the  $\phi$  direction, following a circular path with a radius specified by Maxwell's  
 1499 equations (see Equation 13).

1500 The barrel toroid consists of eight coils which generate a 0.5 T magnetic field,  
 1501 on average, in the cylindrical region around the calorimeters with an approxi-  
 1502 mately 20 kA current. The coils are separated only by air to reduce the scatter-  
 1503 ing of muons as they propagate through the region. The coils are made of an  
 1504 aluminum stabilized NbTiCu superconductor and each is separately housed in a  
 1505 vacuum and cold chamber. This magnetic configuration produces a field in the  
 1506  $\phi$  and so curves muons traversing the volume primarily in the  $\eta$  direction.

1507 The endcap toroids follow a similar design to the barrel toroid and produce a  
 1508 1.0 T magnetic field, on average. Each has eight separate NbTiCu coils, and in  
 1509 this case all eight are housed within a single cold mass. This extra structure is  
 1510 necessary to withstand the Lorentz forces exerted by the magnets. These mag-  
 1511 nets are rotated 22.5% relative to the barrel toroid to provide a uniform field in  
 1512 the transition between the two systems. The endcap toroids also produce a field  
 1513 in the  $\phi$  direction and curve muons primarily in the  $\eta$  direction.

### 1514 5.3 INNER DETECTOR

1515 The ATLAS inner detector provides excellent momentum resolution as well as  
 1516 accurate primary and secondary vertex measurements through robust pattern  
 1517 recognition that identifies tracks left by charged particles. These tracks fulfill a  
 1518 number of important roles in the ATLAS measurement system: they measure the  
 1519 momentum of charged particles including electrons and muons, they can iden-  
 1520 tify electrons or photon conversions, they assign various particles and jets to dif-  
 1521 ferent vertices, and they provide a correction to  $E_T^{\text{miss}}$  measurements from low  
 1522 energy particles. The system has to be accurate enough to separate tracks from  
 1523 dozens of vertices, to resolve each vertex individually, and to measure the  $p_T$  of  
 1524 very high momentum tracks which curve very little even in the large magnetic  
 1525 field. This is accomplished by several independent layers of tracking systems.  
 1526 Closest to the interaction point is the very high granularity Pixel detector, in-  
 1527 cluding the newly added Insertible B-Layer, which is followed by the SCT layers.  
 1528 These silicon subdetectors both use discrete space-points to reconstruct track  
 1529 patterns. The final layer, the Transition Radiation Tracker (TRT), uses many lay-  
 1530 ers of straw tube elements interleaved with transition radiation material to pro-  
 1531 vide continuous tracking. The arrangement of these subdetectors is shown in  
 1532 Figure 20. To provide the desired hermetic coverage, the subdetectors are di-  
 1533 vided into barrel and endcap geometries. Figure 21 shows the layout of the sub-  
 1534 detectors in more detail, and illustrates how tracks at various pseudorapidities  
 1535 can traverse the subdetectors; tracks with  $\eta > 1.1$  begin to traverse the endcap  
 1536 subdetectors rather than those in the barrel, and tracks with  $\eta > 1.7$  use primar-

ily endcap elements. The IBL was not present during the original commissioning of the inner detector and is not shown in this figure.

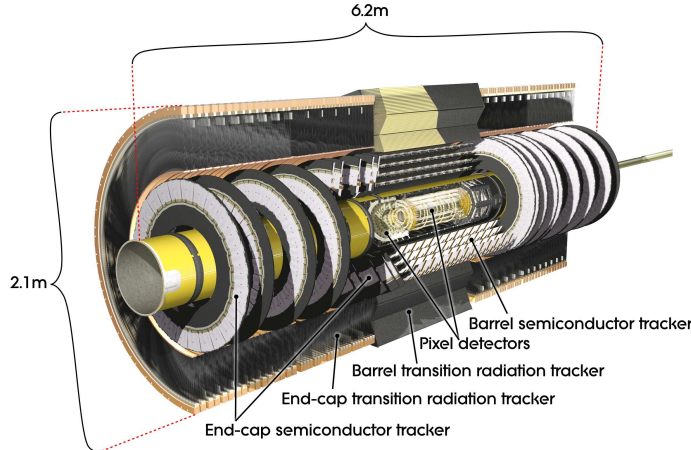


Figure 20: The arrangement of the subdetectors of the ATLAS inner detector. Each of the subdetectors is labeled in the cut-away view of the system.

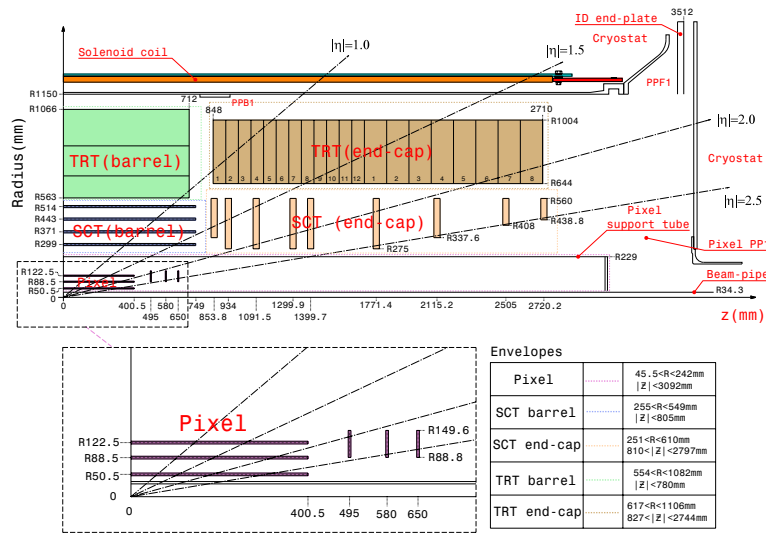


Figure 21: A quarter section of the ATLAS inner detector which shows the layout of each of the subdetectors in detail. The lower panel shows an enlarged view of the pixel detector. Example trajectories for a particle with  $\eta = 1.0, 1.5, 2.0, 2.5$  are shown. The IBL, which was added after the original detector commissioning, is not shown.

Figure 22 shows a computer generated three-dimensional view of the inner detector along the beam axis, which emphasizes the straw tube structure of the TRT as well as the overlapping geometry of the SCT. This figure also includes the IBL, which was added during the long shutdown and provides an additional measurement layer in the Pixel detector as of the beginning of Run 2. Figure 23 shows an alternative computer generated three-dimensional view transverse to the beam axis which emphasizes the endcap structures of the SCT and TRT.

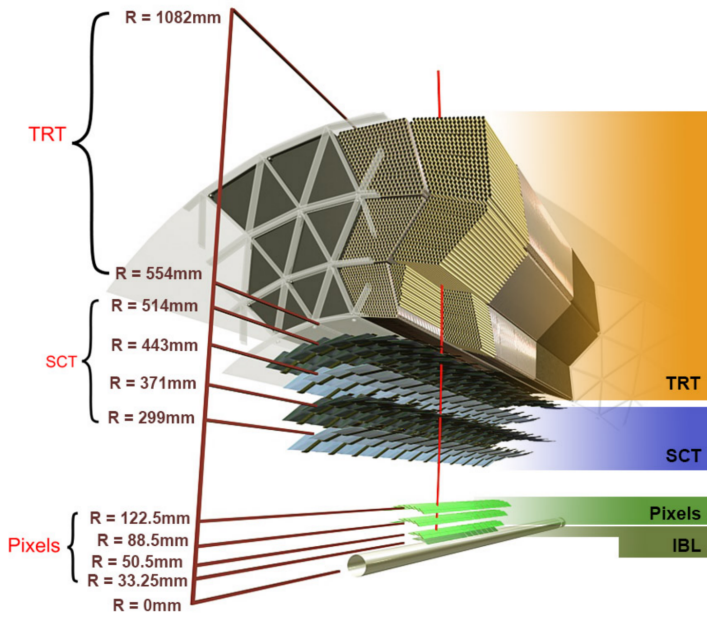


Figure 22: A computer generated three-dimensional view of the inner detector along the line of the beam axis. The subdetectors and their positions are labeled.

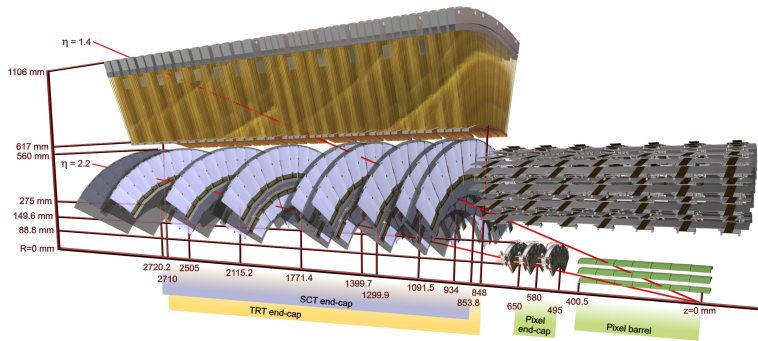


Figure 23: An alternative computer generated three-dimensional view of the inner detector transverse to the beam axis. The subdetectors and their positions are labeled.

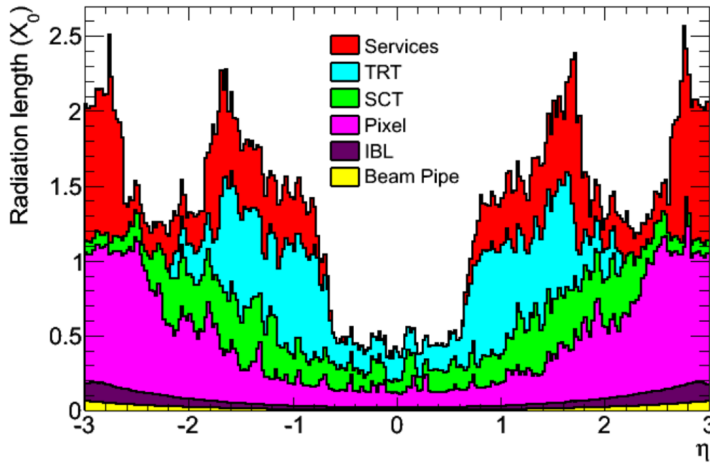


Figure 24: The integrated radiation lengths traversed by a straight track at the exit of the ID envelope, including the services and thermal enclosures. The distribution is shown as a function of  $|\eta|$  and averaged over  $\phi$ . The breakdown indicates the contributions of individual sub-detectors, including services in their active volume.

As the closest system to the interaction point, it is crucial for the inner detector to use as little material as possible to avoid scattering of charged particles or photon conversions before they reach the remaining subdetectors. The various components, including the readout electronics, cooling infrastructure, gas volumes, and support structures, were designed to accommodate this need for minimal components. Even with these optimizations, the combination of stringent performance requirements and the harsh radiation environment in the inner detector requires a significant amount of material. This material causes many electrons to lose most of their energy before reaching the electromagnetic calorimeter and approximately 40% of photons convert into an electron-positron pair while traversing the inner detector. Figure 24 shows the integrated radiation lengths traversed by a straight track in the inner detector as a function of  $\eta$ , grouped by subdetector. There is a large increase in the amount of material for support structures around  $|\eta| = 1.7$ , where the inner detector transitions from barrel to endcap.

The inner detector is designed to work as a cohesive unit to provide complete tracking information for charged particulars, and the subdetectors are complementary. Table 5 summarizes the parameters of each of the subdetectors as well as the parameters of the combined inner detector. Table 6 summarizes the expected performance that can be achieved by the inner detector as a whole.

### 5.3.1 PIXEL DETECTOR

The Pixel detector is the closest detector to the interaction point and therefore is designed to provide extremely high granularity while simultaneously handling a very large dose of radiation from collisions. It consists of four layers of silicon pixel modules, each of which provides a precision measurement on the trajectory

Parameter	Inner Detector	Pixel	SCT	TRT
Inner Radius	3.1 cm	3.1 cm	30 cm	56 cm
$ \eta $ Coverage	-	2.5	2.5	2.0
Cell Width	-	50 $\mu\text{m}$	80 $\mu\text{m}$	4 mm
Cell Length	-	400 $\mu\text{m}$	12 cm	70 cm
Material at $ \eta  = 0.0$	0.3 $X/X_0$			
Material at $ \eta  = 1.7$	1.2 $X/X_0$			
Material at $ \eta  = 2.5$	0.5 $X/X_0$			
Number of Hits	48	4	8	36
Channels	99 M	92 M	6.3 M	350 k

Table 5: A summary of the parameters of the inner detector and each of the subdetectors [10].

of any charged particle. In the barrel region, the four layers are located at radial distances of 31 mm, 51 mm, 89 mm, and 123 mm. The three outer layers also include endcap elements, illustrated in Figure 21, which are located at 495 mm, 580 mm, and 650 mm away from the interaction point.

The pixel sensor technology uses a p-n junction of n-type bulk that contains both p<sup>+</sup> and n<sup>+</sup> impurities. This combination is crucial in maintaining performance after a significant radiation dose, as the n<sup>+</sup> implants allow the sensor to continue function after the n-type bulk has been converted to a p-type bulk by the accumulation of radiation. In either configuration, when a charged particle passes through the bulk, it ionizes thousands of electron-hole pairs. The electrons and holes are pulled in opposite directions by the electric field established between the anode and cathode of the junction, which then produces a current that can be measured and recorded by readout electronics.

The size of the pixels in the original three layers are 50  $\mu\text{m}$  x 400  $\mu\text{m}$  in the  $r - \phi$  and  $z$  directions, respectively. Those pixels are bump-bonded to front-end readout chips, the FE-I3, which contains a total of 2880 pixels per chip. In the three original pixel layers, the chips are grouped into modules composed of 16 chips each with 46,080 pixels per module and a total size of 20 mm x 60 mm x 250  $\mu\text{m}$ . The modules are further arranged into long rectangular structures that run parallel to the beamline called staves. By tiling several staves with an offset of 20°, the stave geometry provides full azimuthal coverage in the barrel region while accommodating the readout and cable systems. The endcap regions are instead arranged into petals and then into wheels. This arrangement can be seen in Figure 25 which shows a computer-generated, cut-away image of the outer three layers of the pixel detector. Together these three layers contain 1744 modules between the barrel and two endcap sections.

The innermost layer, the IBL, was added during the long shutdown before Run 2, and provides the fourth track measurement. It was inserted directly into the existing pixel detector by removing the existing beam pipe and replacing it with a significantly smaller version. This insertion can be seen in action in Figure 26,

Parameter	Particle	Value
Reconstruction Efficiency	Muon, $p_T = 1 \text{ GeV}$	96.8%
	Pion, $p_T = 1 \text{ GeV}$	84.0%
	Electron, $p_T = 5 \text{ GeV}$	90.0%
Momentum Resolution	$p_T = 1 \text{ GeV},  \eta  \approx 0$	1.3%
	$p_T = 1 \text{ GeV},  \eta  \approx 2.5$	2.0%
	$p_T = 100 \text{ GeV},  \eta  \approx 0$	3.8%
	$p_T = 100 \text{ GeV},  \eta  \approx 2.5$	11%
Transverse IP Resolution	$p_T = 1 \text{ GeV},  \eta  \approx 0$	$75 \mu\text{m}$
	$p_T = 1 \text{ GeV},  \eta  \approx 2.5$	$200 \mu\text{m}$
	$p_T = 1000 \text{ GeV},  \eta  \approx 0$	$11 \mu\text{m}$
	$p_T = 1000 \text{ GeV},  \eta  \approx 2.5$	$11 \mu\text{m}$
Longitudinal IP Resolution	$p_T = 1 \text{ GeV},  \eta  \approx 0$	$150 \mu\text{m}$
	$p_T = 1 \text{ GeV},  \eta  \approx 2.5$	$900 \mu\text{m}$
	$p_T = 1000 \text{ GeV},  \eta  \approx 0$	$90 \mu\text{m}$
	$p_T = 1000 \text{ GeV},  \eta  \approx 2.5$	$190 \mu\text{m}$

Table 6: A summary of the expected performance of the combined inner detector [14]. Included are the reconstruction efficiencies for multiple particle types as well as the momentum and IP resolution for various momenta.

which emphasizes the extreme precision required to place the the 70 cm long layer with only 2 mm of clearance. The IBL was commissioned to provide continued tracking robustness and high precision in the higher luminosity environment of Run 2 [15]. The proximity of this layer to the collisions necessitated an even higher granularity and better radiation hardness than the other pixel layers. And the strict space requirements to add an active sensing layer so close to the interaction point required a sensor chip with a much higher active area and a larger overall area per chip. These requirements led to the development of a new chip type, the FE-I4 (compared to the FE-I3 chips used in the original pixel detector) with improved radiation hardness and a larger active footprint of 90%. The IBL is comprised of 448 of these individual chips arranged in 14 staves, with 26,880 pixels per chip and a chip size of 18.5 mm x 41.3 mm x 200  $\mu\text{m}$ . The staves, like in the other layers of the pixel detector, are offset by 14° to provide full azimuthal coverage. This arrangement can be seen in Figure 27, which shows two computer-generated images of the IBL geometry and includes the some of the remaining pixel layers.

### 5.3.2 SEMICONDUCTOR TRACKER

The SCT, the subdetector which immediately surrounds the Pixel detector, provides additional discrete measurements of the trajectory of a charged particle. Because the SCT is further away from the interaction point, the spatial resolution

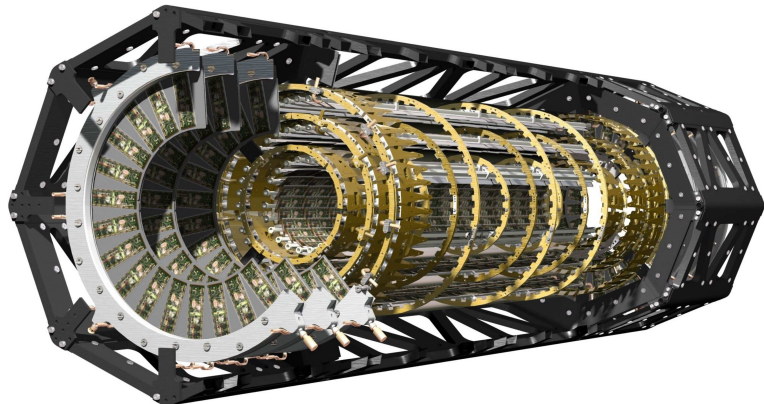


Figure 25: A cut away image of the outer three layers of the pixel detector.

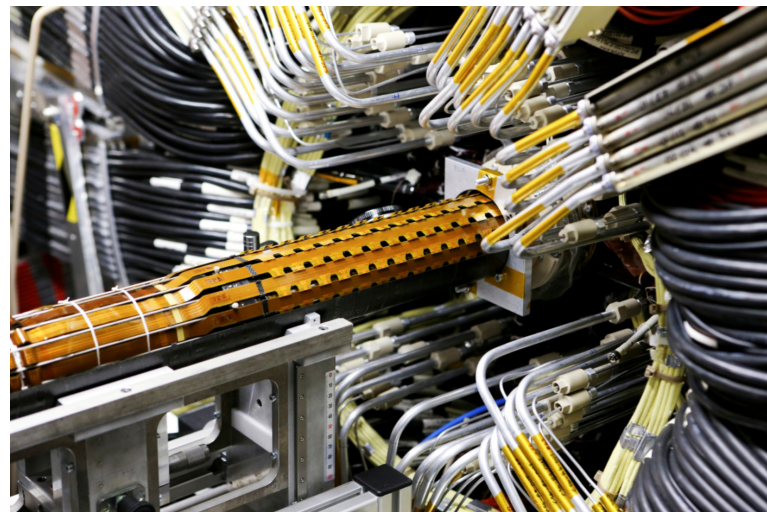


Figure 26: An image of the insertion of the IBL into the current pixel detector.

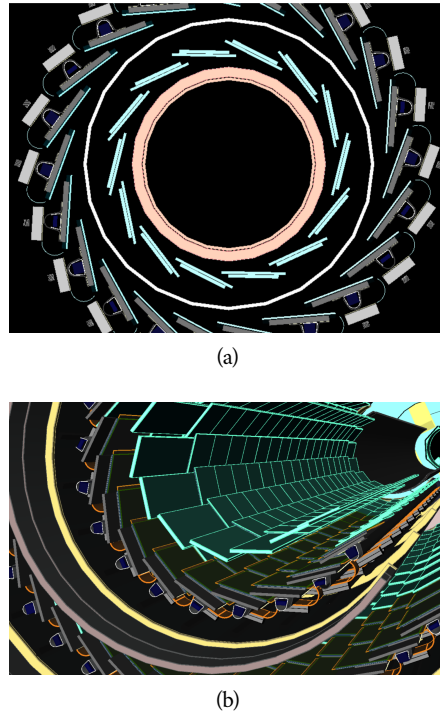


Figure 27: A three-dimensional computer-generated image of the geometry of the **IBL** with a view (a) mostly transverse to the beam pipe (b) mostly parallel to the beam pipe.

1621 does not need to be as high as in the pixel detector, and so the **SCT** uses micro-  
 1622 strips instead of pixels. Although pixels provide a more accurate measurement,  
 1623 the number of pixels and readout channels required to cover the cylindrical area  
 1624 at the radius of the **SCT** layers would be prohibitively complicated and expensive.

1625 Each individual silicon strip sensor contains 768 individual readout strips  
 1626 with a total area of  $6.36 \text{ cm} \times 6.40 \text{ cm}$  and a pitch of  $80 \mu\text{m}$ . Pairs of these sen-  
 1627 sors are then bonded together to form a combined strip with a length of 12.8 cm.  
 1628 Two of these combined strips are then placed back to back with a relative tilt of  
 1629 40 mrad. This geometry is illustrated in an expanded view in Figure 28. The pur-  
 1630 pose of angular offset of the consecutive layers is to allow the strip sensor areas  
 1631 to more accurately measure the position of a particle by comparing the overlap  
 1632 of the two strips which were traversed by a track.

1633 Four of these double layers are placed in the barrel region, with radii of 284  
 1634 mm, 355 mm, 427 mm, and 498 mm. Together these layers provide eight addi-  
 1635 tional measurements for each track that traverses the central  $|\eta|$  region. In the  
 1636 endcap region, the layers are arranged in wheels, with the double layers simi-  
 1637 larly offset to provide improved resolution. With these configurations, the **SCT**  
 1638 achieves a spatial resolution of  $17 \mu\text{m}$  in the  $r - \phi$  direction and  $580 \mu\text{m}$  in the  
 1639  $z$  direction.

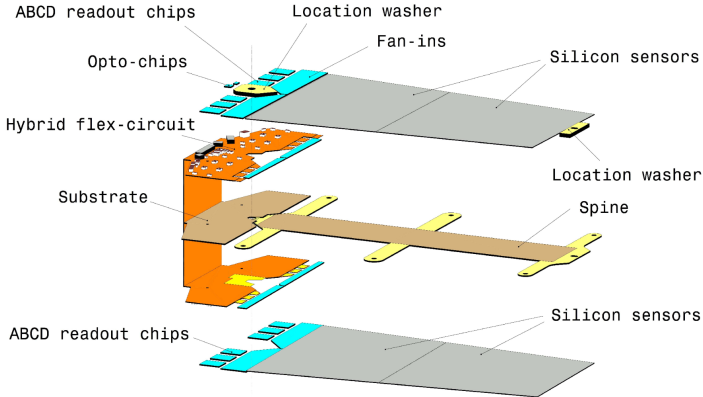


Figure 28: An expanded view of the geometry of the **SCT** double layers in the barrel region.

### 1640 5.3.3 TRANSITION RADIATION TRACKER

1641 The final component of the inner detector, the **TRT**, provides continuous track-  
 1642 ing using straw drift tubes. The tubes are made of Kapton and aluminum with  
 1643 a diameter of 4 mm and are filled with a gas mixture of 70% Xe, 27% CO<sub>2</sub>, and  
 1644 3% O<sub>2</sub>. At the center of each tube is a gold-plated anode tungsten wire 30  $\mu\text{m}$  in  
 1645 diameter. When a charged particle passes through these tubes, it ionizes the gas  
 1646 within. The ions produced drift in the electric field established between the wire  
 1647 and the tube wall, and the large electric field near the wire produces avalanche  
 1648 multiplication and results in an electric current on the wire that is read out by  
 1649 the electronics and provides a track measurement. The time it takes the ioniza-  
 1650 tion to drift to the wire can be used to estimate the distance from the wire that  
 1651 the particle passed through the tube; this gives a resolution on the distance of ap-  
 1652 proximately 130  $\mu\text{m}$ . Combining several such measurements between consecu-  
 1653 tive hits in the **TRT** tubes allows the trajectory of the particle to be reconstructed  
 1654 with much better resolution than is available in each individual tube.

1655 In addition to the continuous tracking, the detector can use transition radia-  
 1656 tion produced when a particle passes between the layers to distinguish between  
 1657 electrons and heavier charged particles. The space between the tubes is filled  
 1658 with CO<sub>2</sub>, and so has a different dielectric constant than the gas within the tubes  
 1659 which contains Xe. At the transition between those media, a relativistic par-  
 1660 ticle emits radiation proportional to  $\gamma$ , so inversely proportional to mass at a  
 1661 fixed momentum. The photons produced in this transition then produce an  
 1662 ionization cascade which is significantly larger than the signal for the minimally-  
 1663 ionizing charged particles. To distinguish between these two cases, the **TRT** de-  
 1664 fines two signal thresholds, a low threshold for the typical signal produced by a  
 1665 minimally ionizing particle (**MIP**) and a high threshold for the the signal produced  
 1666 by transition radiation. A high momentum electron is expected to produce ap-  
 1667 proximately 7 to 10 high threshold hits as it traverses the **TRT**, and thus these hits  
 1668 provide a way to distinguish electrons from other charged particles.

1669     The [TRT](#) contains 351,000 tubes in total, divided between the barrel and end-  
 1670     cap regions. In the barrel region, the tubes are 144 cm long and arranged in 73  
 1671     layers parallel to the beampipe. In the endcap region, the tubes are 37 cm long  
 1672     and arranged in 160 layers transverse to the beampipe. These configurations  
 1673     can be seen in [Figure 22](#) and [Figure 23](#). With this geometry the [TRT](#) achieves a  
 1674     resolution of 130  $\mu\text{m}$  in the  $r - \phi$  direction.

1675     

## 5.4 CALORIMETRY

1676     The combination of calorimeter systems used in [ATLAS](#) can measure the energy  
 1677     of electrons, photons, hadrons, and hadronic jets with complete coverage up to  
 1678      $|\eta| < 4.9$  and across  $\phi$ . Unlike the inner detector, the calorimeters are capable  
 1679     of measuring neutral particles. To accomplish precision measurements of these  
 1680     particle types, the [ATLAS](#) calorimeter system uses four individual calorimeters,  
 1681     a [LAr](#) electromagnetic calorimeter in the barrel region, a tile hadronic calorime-  
 1682     ter in the barrel region, a [LAr](#) hadronic endcap calorimeter, and a [LAr](#) forward  
 1683     calorimeter. Together these provide hermetic coverage for the [ATLAS](#) detector.  
 1684     The configuration of these calorimeters is illustrated in [Figure 29](#). **Note: I could  
 1685     make this section much longer. It might be nice to include a more com-  
 1686     plete description of showers for example. I will extend this section if there  
 1687     is space at the end.**

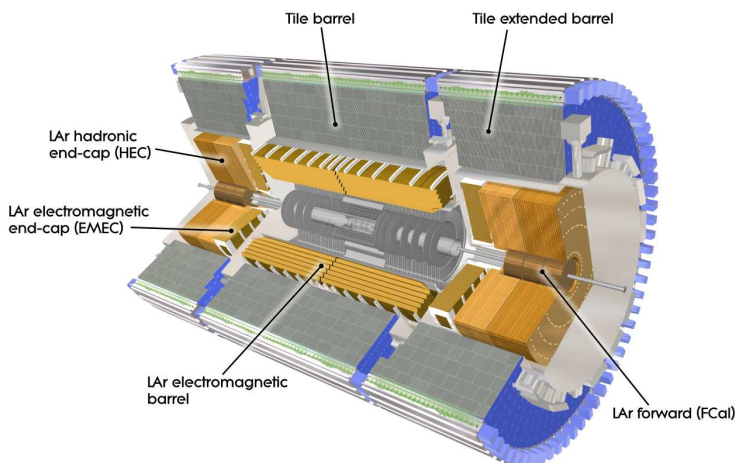


Figure 29

1688     The calorimeters are designed to absorb and measure the energy carried by  
 1689     a particle, and completely stop the particle's propagation in the process. This  
 1690     requires a significant amount of material to provide interactions. These interac-  
 1691     tions then produce secondary particles, which can produce secondary particles  
 1692     in turn, and thus form a cascade of particles called an electromagnetic ([EM](#)) or  
 1693     hadronic shower, depending on the governing mechanism. Electromagnetic and  
 1694     hadronic showers have very different properties and require different technolo-  
 1695     gies to measure them accurately. All of the calorimeters in the [ATLAS](#) calorimeter  
 1696     system are sampling calorimeters: they use alternating layers of absorbing and

active material. The dense absorbing layers initiate the showers while the active layers measure the energy of the produced particles. A fraction of the energy is lost in the inactive layers, so the energy measurement from the active layers has to be corrected to estimate the actual energy of the particle.

The EM calorimeter provides around 20 radiation lengths ( $X_0$ ) while the hadronic calorimeter provides around 10 interaction lengths ( $\lambda_0$ ). As mentioned previously, radiation lengths measure the distance over which an electromagnetically interacting particle loses a characteristic fraction of its energy. Interaction lengths, on the other hand, measure the mean distance traveled by a hadronic particle before undergoing a nuclear interaction [3]. Figure 30 show the radiation lengths in the layers of the EM calorimeter in the barrel region as well as the interaction lengths for all calorimeters.

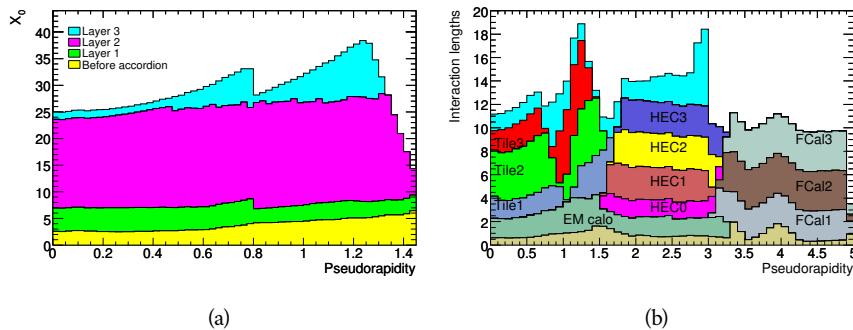


Figure 30: The depth of (a) the electromagnetic barrel calorimeter in radiation lengths and (b) all calorimeters in interaction lengths as a function of pseudorapidity.

#### 5.4.1 ELECTROMAGNETIC CALORIMETER

The electromagnetic calorimeters use alternating layers of liquid argon and lead in an accordion shape. The accordion shape provides complete coverage in the  $\phi$  direction while also providing many alternating layers for the a particle to pass through. The configuration is detailed in Figure 31. When an electron or photon passes through the lead, it produces an electromagnetic shower. The particles produced in those showers then pass into and ionize the liquid argon; the ions produced can then be collected by an electrode in the liquid argon layer to provide the actual energy measurement.

The barrel region is covered by a presampler and three separate sampling layers with decreasing segmentation. The presampler is a thin layer of liquid argon which measures the energy of any electromagnetic showers which are initiated before the particle reaches the calorimeter due to interactions with the detector material. The first layer is the strip layer, which has fine segmentation in  $\eta$  to enhance the identification of shower shapes and to provide a precise  $\eta$  measurement for reconstructing photons and electrons. The strip layer has only 4 radiation lengths worth of material, and has a segmentation of  $\Delta\eta = 0.003$  and  $\Delta\phi = 0.1$ . The second layer is also finely segmented, with a segmentation of  $\Delta\eta = 0.025$  and  $\Delta\phi = 0.025$ , and a thickness of 16  $X_0$ . This layer is designed

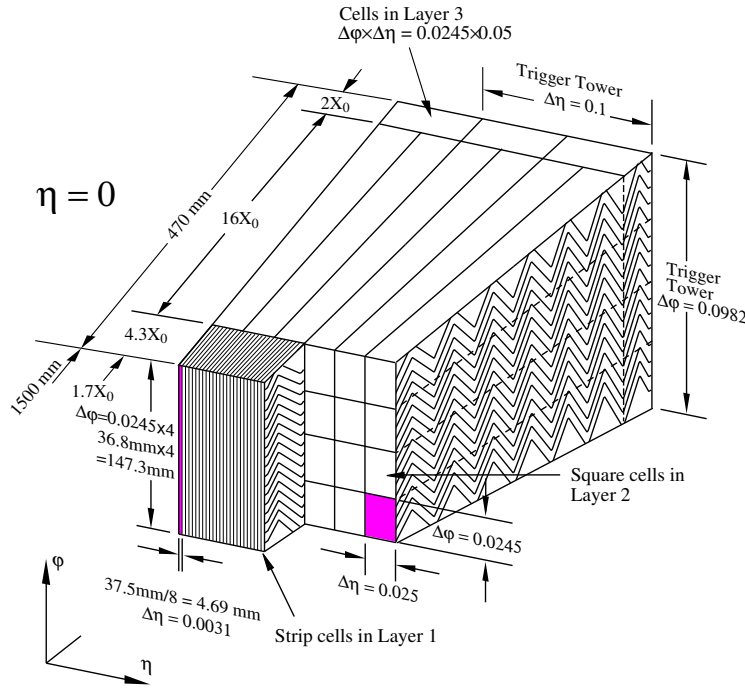


Figure 31: A schematic of the LAr calorimeter in the barrel region, highlighting the accordion structure.

1728 to contain an electromagnetic shower and to measure the majority of the energy  
 1729 for photons and electrons. The third layer is only  $2 X_0$  thick and measures the  
 1730 energy of electromagnetic showers which leak out of the second layer, and helps  
 1731 to separate electromagnetic showers from hadronic showers. The structure of  
 1732 the LAr endcap calorimeter is similar except that the layers are arranged parallel  
 1733 to the beampipe to measure energy deposits from high  $\eta$  particles.

#### 1734 5.4.2 HADRONIC CALORIMETERS

1735 The hadronic calorimeters use a few different technologies to satisfy the resolu-  
 1736 tion demands in the different areas of the detector, and together they cover the  
 1737 region  $|\eta| < 2.7$ . In the barrel region, for  $|\eta| < 1.7$ , the hadronic calorimeters  
 1738 are constructed of alternating tiles of steel and plastic scintillator. Like in the  
 1739 electromagnetic calorimeter, the dense layer initiates a shower (in this case the  
 1740 dense layer is the steel and the shower is hadronic) of particles which pass into  
 1741 and ionize the following layer. The ionization in the plastic scintillator instead  
 1742 produces a light signal proportional to the amount of ionization produced by the  
 1743 shower, and this signal is measured using photomultipliers and provides the ac-  
 1744 tual energy measurement. The construction of a tile in the calorimeter is shown  
 1745 Figure 32, which highlights the alternating layers of steel and scintillator.

1746 This tile calorimeter, as well as the remaining hadronic calorimeters, have a  
 1747 much coarser granularity than the electromagnetic calorimeters. The high gran-  
 1748 ularity is not needed for an accurate energy measurement, and the hadronic  
 1749 calorimeters are not designed to distinguish particle types like the electromag-

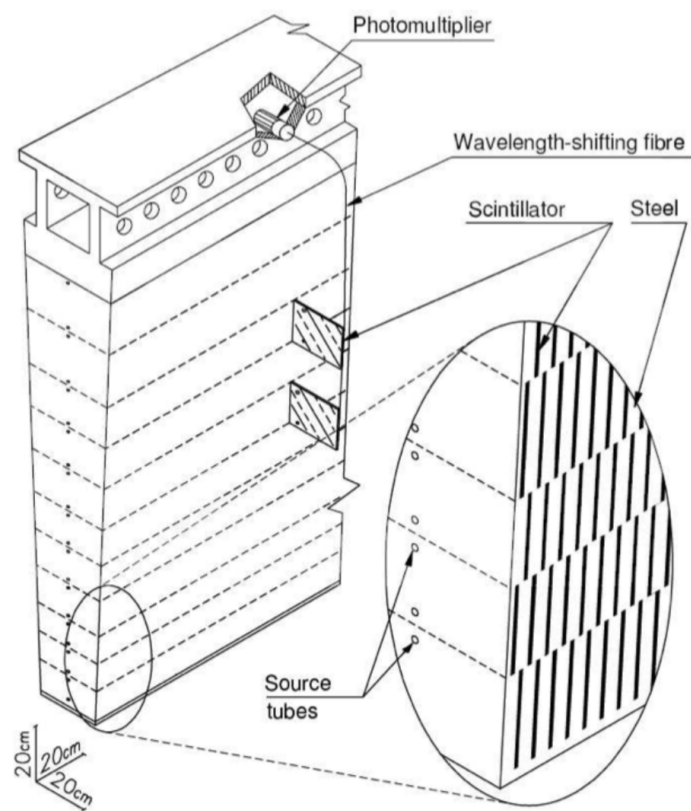


Figure 32: A schematic of a hadronic tile module which shows the alternating layers of steel and plastic scintillator.

netic calorimeters. The tile granularity is approximately  $\Delta\eta = 0.1$  and  $\Delta\phi = 0.1$ , and the segmentation in depth and  $\eta$  is shown in Figure 33.

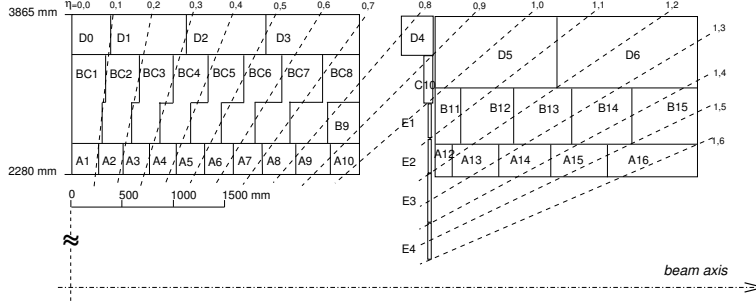


Figure 33: The segmentation in depth and  $\eta$  of the tile-calorimeter modules in the central (left) and extended (right) barrels.

The remaining hadronic calorimeters all use the same alternating sampling structure but with different active and inactive materials. The hadronic endcap calorimeter covers the range of  $1.5 < |\eta| < 3.2$  and uses an inactive layer of copper and an active layer of liquid argon. The forward calorimeter covers the range of  $3.1 < |\eta| < 4.9$  and uses a dense matrix of copper and tungsten filled with liquid argon.

## 5.5 MUON SPECTROMETER

Among SM particles, only muons and neutrinos consistently pass through the calorimeters. Because the neutrinos are also electrically neutral, there is no feasible option to measure them directly in ATLAS. The muons, on the other hand, are charged and are thus already measured as a track in the inner detector. The muon spectrometer provides a way to consistently identify muon tracks and also a way to provide an additional measurement of their momentum.

The muon spectrometer contains four subdetectors that cover the barrel and endcap regions. In the barrel region, the muon spectrometer uses a combination of Resistive Plate Chambers (RPCs) and MDTs to provide both a coarse, fast measurement for triggering and a precise momentum measurement for offline event reconstruction. Similarly, in the endcap region, the TGCs, MDTs, and CSCs allow for both triggering and precise measurements. The CSCs are used only in the innermost layer of the endcap region between  $2.0 < |\eta| < 2.7$  where the particle flux is too large for the MDTs to provide accurate measurements. The overall layout of the muon systems are shown in the cut-away diagram in Figure 34, and Figure 35 shows a precise schematic of the layout of each of the detecting elements. The geometric arrangement shown provides consistent coverage for muons produced up to  $|\eta| < 2.7$ , and takes full advantage of the bending of the muons in the toroidal magnetic field, described in Section 5.2, to measure their momentum. Figure 36 shows a cross-section of the arrangement of the muon spectrometer in the barrel; the layers are divided into eight small and eight large chambers that are overlapped to provide complete coverage in  $\phi$ .

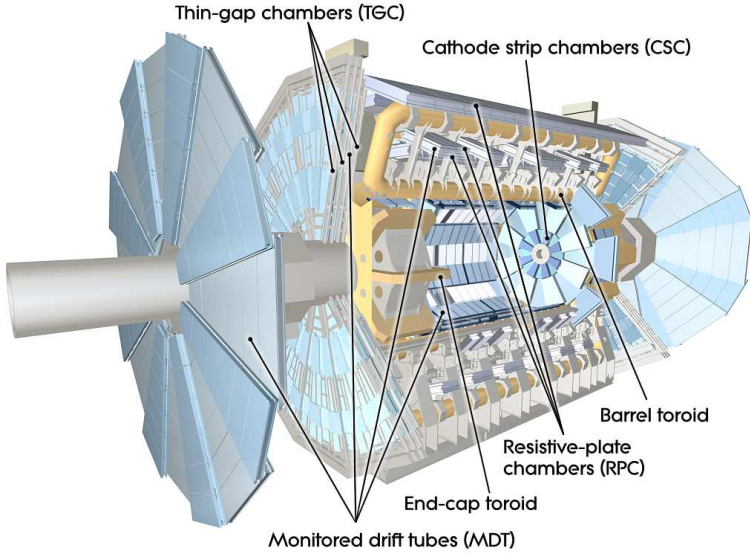


Figure 34: A cut-away diagram of the muon systems on [ATLAS](#).

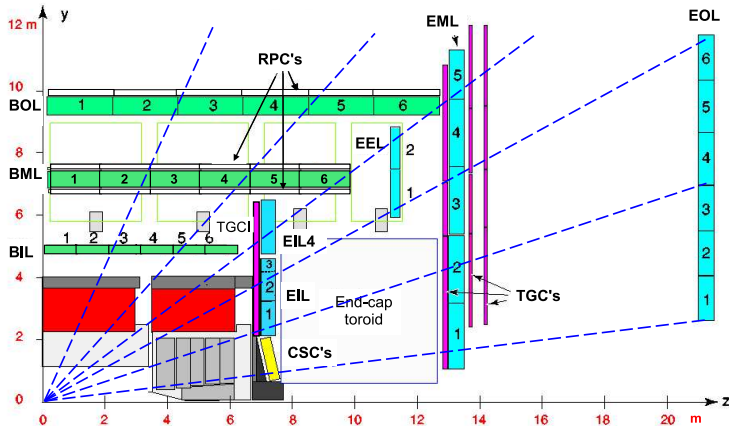


Figure 35: A quarter view of the muon spectrometer which highlights the layout of each of the detecting elements. The BOL, BML, BIL, EML, EIL, and EOL are all [MDT](#) elements, where the acronyms encode their positions.

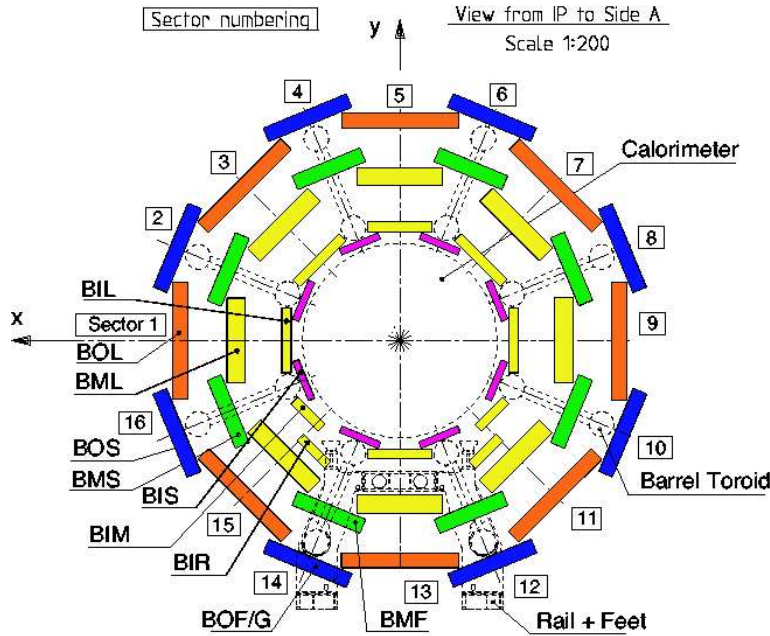


Figure 36: A schematic of the cross-section of the muon spectrometer in the barrel region.

#### 1781 5.5.1 MONITORED DRIFT TUBE

1782 The momentum measurements in the barrel region are provided by three consecutive layers of MDT elements, located at approximately 5 m, 7 m, and 9 m from  
 1783 the interaction point. Each of these layers is a composite of two multilayers of  
 1784 drift tubes: two layers of three to four layers of tubes, as shown in Figure 37.  
 1785 These aluminum tubes are 3 cm in diameter, with lengths between 0.9 and 6.2 m,  
 1786 and are filled with a mixture of ArCO<sub>2</sub> kept at 3 bar absolute pressure. A central  
 1787 tungsten-rhenium wire with a diameter of 50  $\mu\text{m}$  runs along the length of the  
 1788 tube, and is kept at a potential of 3080 V.  
 1789

1790 A muon traversing these tubes ionizes the gas, and the ionization electrons  
 1791 then drift in the electric field toward the central wire. Close to the wire, the  
 1792 electric field is strong enough to cause the original ionization electrons to ionize  
 1793 additional electrons, producing an avalanche that can be measured as a current  
 1794 along the wire. The time of arrival of that current depends on how far the muon  
 1795 entered from the wire, and can be used to achieve a position resolution of 80  $\mu\text{m}$   
 1796 in an individual tube. The combination of the measurements in the consecutive  
 1797 layers of tubes improves this position resolution to 35  $\mu\text{m}$  transverse to the tubes,  
 1798 with a resolution of 1 m along the tube direction.

1799 To achieve a good resolution over the entire length of a muon track, the rel-  
 1800 ative positions of the tubes of the muon spectrometer must be known to an ac-  
 1801 curacy of 30  $\mu\text{m}$ . This is achieved by an optical laser alignment system placed in  
 1802 each of the individual chambers and throughout the cavern. These monitor any  
 1803 changes in position or alignment due to effects like gravitational sag, tem-  
 1804 perature shifts, and the magnetic field. The configuration of the alignment system  
 1805 within an individual chamber is also shown in Figure 36.

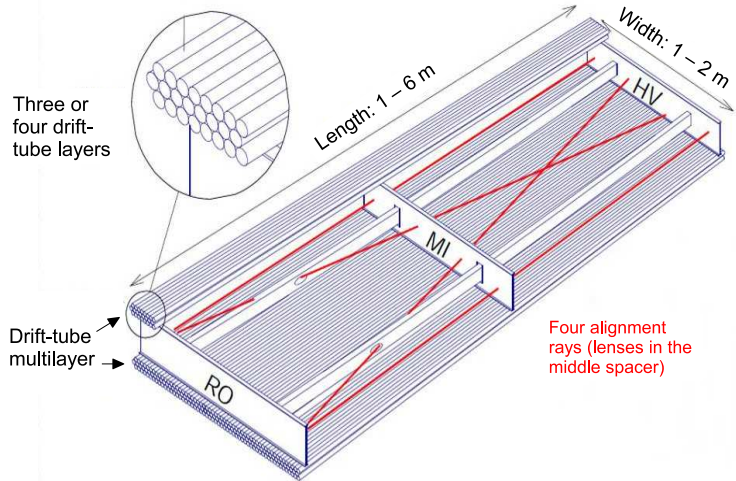


Figure 37: A schematic of a single **MDT** chamber, which shows the multilayers of drift tubes as well as the alignment system.

### 1806 5.5.2 RESISTIVE PLATE CHAMBER

1807 The **RPC** is the outermost detecting layer in the muon spectrometer in the barrel  
 1808 region, and provides a fast measurement of the  $\phi$  position of muons for triggering.  
 1809 The speed of the measurement, with a time resolution of just a few tens of  
 1810 nanoseconds, requires a poor spatial resolution of approximately 1 cm. There  
 1811 are three **RPCs** layers in the muon spectrometer, two located on either side of  
 1812 the central **MDT** layer and one located outside the final **MDT** layer, as shown in  
 1813 Figure 35. The **RPCs** consist of two layers of parallel plates filled with a gas mix-  
 1814 ture of  $C_2H_2F_4$ . A muon passing through these systems ionizes the gas, like in  
 1815 the **MDT**, which causes an avalanche of ionization electrons in the electric field  
 1816 maintained between the plates. Metal strips on the outside of the chamber ca-  
 1817 pacitively couple to the accumulated charge, and are read out to measure the  $\eta$   
 1818 and  $\phi$  positions of the muon track.

### 1819 5.5.3 CATHODE STRIP CHAMBER

1820 The majority of the momentum measurements in the endcap region are provided  
 1821 by the **MDTs**. In the most forward region of the muon spectrometer, between  
 1822  $2.0 < \eta < 2.7$ , the particle flux is very high due to contributions from low energy  
 1823 photons and neutrons. The **MDT** can only sustain a hit rate of approximately 150  
 1824 Hz/cm<sup>2</sup> because of limitations in the drift times of the gas and the capacity of  
 1825 the readout electronics. The **CSCs** were designed to handle higher hit rates, up to  
 1826 1000 Hz/cm<sup>2</sup>, and provide the necessary coverage in that high flux region.

1827 The **CSC** consists of several multiwire proportional chambers, where the wires  
 1828 are oriented in the radial direction out from the beampipe. There are eight large  
 1829 and eight small chambers, arranged to partially overlap in the  $\phi$  direction, as  
 1830 shown in Figure 38. Like in the **MDT**, a muon traversing the system produces  
 1831 ionization in the gas; here, however, the ionization is collected on a number of

wires. These wires couple to cathodes on the chambers which are segmented into strips in two directions. The relative amount of charge on each of the neighboring strips can be used to interpolate to the position of the muon in both  $\eta$  and  $\phi$ .

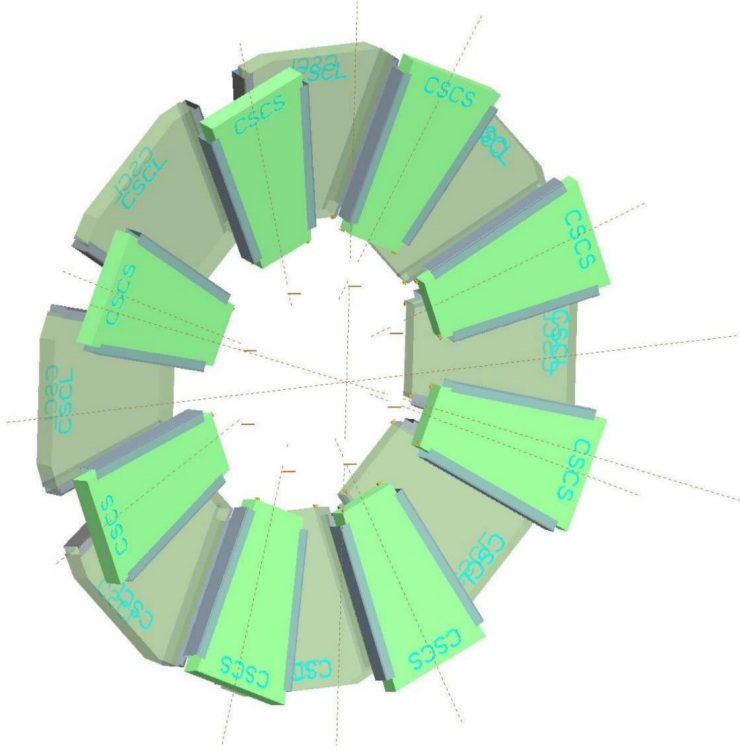


Figure 38: A schematic of the [CSC](#) endcap, showing the overlapping arrangement of the eight large and eight small chambers.

#### 5.5.4 THIN GAP CHAMBER

Like in the barrel region, a separate, fast detector is required to provide position measurements of muons for trigger in the endcap region. This is provided by the [TGC](#) which consists of seven layers in the middle station of the endcap, two doublet layers and one triplet layer, and a single doublet layer in the inner endcap station. Figure 39 shows the arrangement of the triple and doublet layers of the [TGCs](#).

Like the [CSCss](#), the [TGCs](#) are multiwire proportional chambers with a wire-to-cathode distance of 1.4 mm and a wire-to-wire distance of 1.8 mm. Readout strips on the outside of the chambers run perpendicular to the wires, and couple to the charge collected on the wires to provide a position measurement in the  $\eta$  direction. The current induced on the wires is also readout to provide a position measurement in the  $\phi$  direction. The high electric field and small wire-to-wire distance give it the required good time resolution to be used for triggering events.

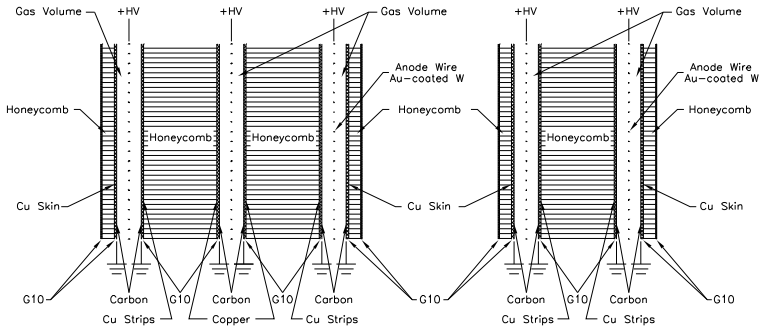


Figure 39: A schematic of the TGC doublet and triplet layers.

## 1850 5.6 TRIGGER

1851 It is not possible for the detector and the associated computing systems to record  
 1852 the terabytes of data that the 40 MHz event rate produces every second. Instead,  
 1853 a small fraction of these events are selected by the trigger system to be recorded  
 1854 and later analyzed. Selecting interesting events at such a high rate poses a sig-  
 1855 nificant challenge for the both the detector design and the implementation of a  
 1856 trigger decision and data acquisition system. The trigger must balance the time  
 1857 needed to decide to keep an event, to avoid losing information, with the filtering  
 1858 accuracy to consistently select a full menu of physics events that can be used for  
 1859 the wide array of searches and measurements targeted by [ATLAS](#).

1860 The [ATLAS](#) trigger system, as of Run 2, consists of two levels of decision mak-  
 1861 ing. The first level, referred to as L1, is hardware based and uses inputs from  
 1862 a subset of the detector elements to narrow the considered event rate from the  
 1863 original 40 MHz down to 100 kHz. The 100 kHz rate is the maximal rate that the  
 1864 event information can be transferred from the detector. The second, software-  
 1865 based level, referred to as the [HLT](#), makes the final decisions on which events to  
 1866 keep for analysis and selects a rate of around 1 kHz. The collection of selection  
 1867 criteria used to make the L1 decisions feed into subsequent selection criteria in  
 1868 the [HLT](#), and the set of these combinations of L1 and [HLT](#) criteria from the trig-  
 1869 ger menu which defines exactly what events are recorded on [ATLAS](#). The trigger  
 1870 menu used for 2015 data collection is shown in Table 7, which summarizes the  
 1871 selection requirements at both levels and additionally shows the peak measured  
 1872 rates contributed by each.

1873 At L1, the trigger system uses information primarily from the calorimeters  
 1874 and muon spectrometer to select high  $p_T$  jets, electrons, photons, and muons.  
 1875 The electromagnetic calorimeter uses reduced granularity energy measurements  
 1876 as well as isolation requirements to select electrons and photons. The hadronic  
 1877 calorimeter also uses a combination of reduced granularity energy measurements  
 1878 and isolation to select high momentum jets and hadronically decaying tau lep-  
 1879 tons.

1880 The calorimeters are also used to provide triggers based on missing energy:  
 1881 the coarse granularity energy measurements are used to calculate a directional  
 1882 sum of energies and to trigger on a significant imbalance. Only the [RPCs](#) and

Trigger	Typical offline selection	Trigger Selection		Level-1 Peak Rate (kHz)	HLT Peak Rate (Hz)
		Level-1 (GeV)	HLT (GeV)		
Single leptons	Single iso $\mu$ , $p_T > 21$ GeV	15	20	7	130
	Single $e$ , $p_T > 25$ GeV	20	24	18	139
	Single $\mu$ , $p_T > 42$ GeV	20	40	5	33
	Single $\tau$ , $p_T > 90$ GeV	60	80	2	41
Two leptons	Two $\mu$ 's, each $p_T > 11$ GeV	$2 \times 10$	$2 \times 10$	0.8	19
	Two $\mu$ 's, $p_T > 19, 10$ GeV	15	18, 8	7	18
	Two loose $e$ 's, each $p_T > 15$ GeV	$2 \times 10$	$2 \times 12$	10	5
	One $e$ & one $\mu$ , $p_T > 10, 26$ GeV	20 ( $\mu$ )	7, 24	5	1
	One loose $e$ & one $\mu$ , $p_T > 19, 15$ GeV	15, 10	17, 14	0.4	2
	Two $\tau$ 's, $p_T > 40, 30$ GeV	20, 12	35, 25	2	22
	One $\tau$ , one $\mu$ , $p_T > 30, 15$ GeV	12, 10 (+jets)	25, 14	0.5	10
Three leptons	One $\tau$ , one $e$ , $p_T > 30, 19$ GeV	12, 15 (+jets)	25, 17	1	3.9
	Three loose $e$ 's, $p_T > 19, 11, 11$ GeV	15, $2 \times 7$	17, $2 \times 9$	3	< 0.1
	Three $\mu$ 's, each $p_T > 8$ GeV	$3 \times 6$	$3 \times 6$	< 0.1	4
	Three $\mu$ 's, $p_T > 19, 2 \times 6$ GeV	15	18, $2 \times 4$	7	2
	Two $\mu$ 's & one $e$ , $p_T > 2 \times 11, 14$ GeV	$2 \times 10$ ( $\mu$ 's)	$2 \times 10, 12$	0.8	0.2
	Two loose $e$ 's & one $\mu$ , $p_T > 2 \times 11, 11$ GeV	$2 \times 8, 10$	$2 \times 12, 10$	0.3	< 0.1
	One photon	one $\gamma$ , $p_T > 125$ GeV	22	120	8
Two photons	Two loose $\gamma$ 's, $p_T > 40, 30$ GeV	$2 \times 15$	35, 25	1.5	12
	Two tight $\gamma$ 's, $p_T > 25, 25$ GeV	$2 \times 15$	$2 \times 20$	1.5	7
Single jet	Jet ( $R = 0.4$ ), $p_T > 400$ GeV	100	360	0.9	18
	Jet ( $R = 1.0$ ), $p_T > 400$ GeV	100	360	0.9	23
$E_T^{\text{miss}}$	$E_T^{\text{miss}} > 180$ GeV	50	70	0.7	55
Multi-jets	Four jets, each $p_T > 95$ GeV	$3 \times 40$	$4 \times 85$	0.3	20
	Five jets, each $p_T > 70$ GeV	$4 \times 20$	$5 \times 60$	0.4	15
	Six jets, each $p_T > 55$ GeV	$4 \times 15$	$6 \times 45$	1.0	12
$b$ -jets	One loose $b$ , $p_T > 235$ GeV	100	225	0.9	35
	Two medium $b$ 's, $p_T > 160, 60$ GeV	100	150, 50	0.9	9
	One $b$ & three jets, each $p_T > 75$ GeV	$3 \times 25$	$4 \times 65$	0.9	11
	Two $b$ & two jets, each $p_T > 45$ GeV	$3 \times 25$	$4 \times 35$	0.9	9
$b$ -physics	Two $\mu$ 's, $p_T > 6, 4$ GeV plus dedicated $b$ -physics selections	6, 4	6, 4	8	52
Total				70	1400

Table 7: The trigger menu for the 2015 data collection with  $L = 5 \times 10^{33} \text{ cm}^{-2} \text{s}^{-1}$ . Both the L1 and HLT selection requirements and their trigger rates are shown measured at the specified luminosity are shown. The typical offline selections represent a typical set of offline requirements imposed after the trigger in an analysis.

1883 TGCs muon subdetectors contribute to the decision at L1, and are used to identify  
 1884 high momentum muons. The contributions to the triggering rate of the various  
 1885 types of L1 triggers are shown in Figure 40. The total rate is indicated in black  
 1886 and is lower than the sum of individual rates because their is significant overlap  
 1887 between different trigger channels. The majority of the rate comes from lepton  
 1888 and photon triggers.

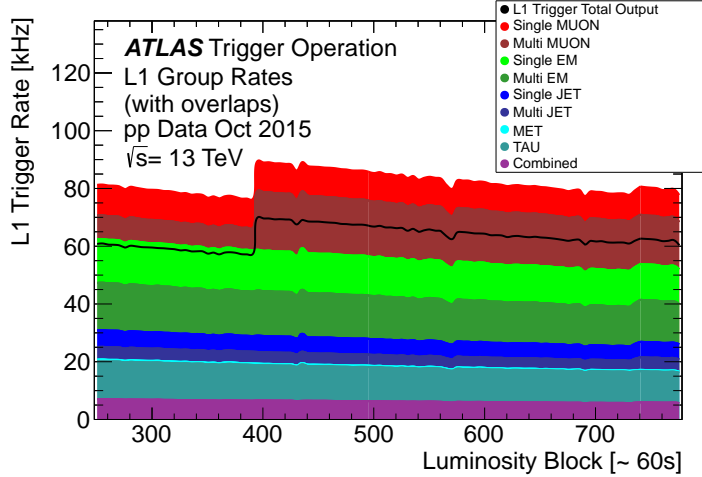


Figure 40: The L1 Trigger rate broken down into the types of triggers as a function of the luminosity block for the 2015 data collection period.

1889 After an event is chosen by the L1 trigger, the detector measurements from the  
 1890 bunch crossing which fired the trigger is read out from the front-end electronics  
 1891 and stored on read-out boards. This inclusive information is necessary to make  
 1892 more the more precise event selections than is possible with the reduced infor-  
 1893 mation at L1. The HLT then uses this information with software algorithms to  
 1894 decide whether or not to permanently record the event. The L1 trigger also for-  
 1895 wards which decision was made and Region of Interests (RoIs) to the HLT, which  
 1896 allows the HLT to focus on particular algorithms and particular sections of the  
 1897 detector to greatly improve the algorithmic selection speed. The additional in-  
 1898 formation available to the HLT allows it to implement additional trigger targets,  
 1899 such as identified jets from the decays of b-hadrons. The contributions to the  
 1900 triggering rate of the various types of HLT triggers are shown in Figure 41.

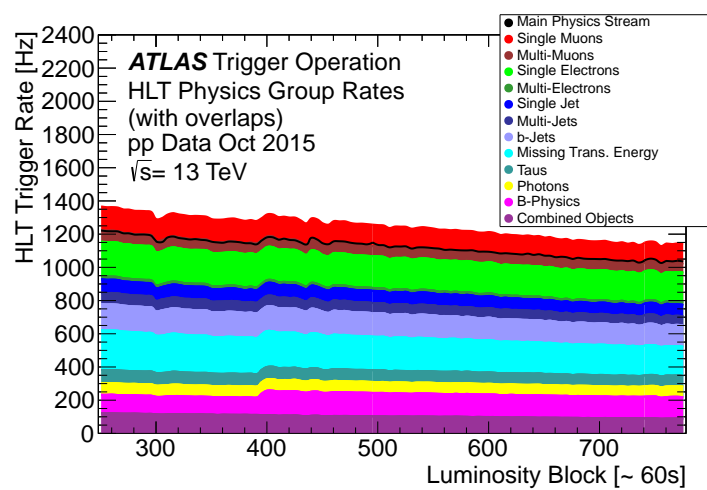


Figure 41: The HLT Trigger rate broken down into the types of triggers as a function of the luminosity block for the 2015 data collection period.

1901

1902 EVENT RECONSTRUCTION

---

1903 The ATLAS experiment combines measurements in the subdetectors to form a  
 1904 cohesive picture of each physics event. The majority of particles that traverse  
 1905 the detector leave behind some combination of ionization hits in the tracking  
 1906 detectors or energy deposits in the calorimeters, and these measurements can  
 1907 be used to reconstruct physical quantities like the particle's energy, momentum,  
 1908 or trajectory. Even the type of the particle can be distinguished by comparing  
 1909 the various ways that different species of stable particles interact with the sub-  
 1910 detectors. Reconstruction is the series of algorithms which take the electronic  
 1911 outputs of the detector and assigns them into individual physics objects. The  
 1912 physics objects summarize the properties of particles produced by the collision  
 1913 or subsequent decays, either for individual isolated particles like leptons, or for  
 1914 a collection of the cascade of products produced in the decay of an energetic  
 1915 hadron, called a jet. These are the objects and quantities most often used in anal-  
 1916 ysis to make measurements of SM processes or to search for new physics.

## 1917 6.1 CHARGED PARTICLES

1918 As described in Section 5.3, charged particles that traverse the inner detector  
 1919 leave behind hits in the subdetectors. Each of these hits translates into a position  
 1920 measurement along the trajectory of that particle, with position resolutions de-  
 1921 pending on the subdetector that provided the measurement. Track reconstruc-  
 1922 tion uses these position measurements to collect hits in consecutive layers of  
 1923 the detector into a trajectory consistent with a particle curving in a magnetic  
 1924 field [16, 17]. This reconstructed trajectory is called a track. The number of hits  
 1925 in the inner detector for each event makes a combinatorial method completely  
 1926 infeasible: the algorithms that form tracks must be significantly more intelligent  
 1927 so that event reconstruction does not exhaust computing resources.

1928 The first and primary algorithm employed in track reconstruction is called  
 1929 the inside-out method, which begins with the assumption that the track orig-  
 1930 inated from the interaction point. Its purpose is to identify primary particles,  
 1931 those which originate in the proton-proton collisions and with a lifetime long  
 1932 enough to reach the inner detector. Combinations of three hits are considered  
 1933 from measurements in the Pixel detector and the SCT, and form the seed for a  
 1934 track. Specifically, the seeding algorithm looks for a seed using three pixel hits,  
 1935 two pixel hits and one SCT hit, or three SCT hits. The seed is then extrapolated  
 1936 forwards and backwards into the Pixel and SCT detectors depending on the seed  
 1937 location, and hits in each layer are considered to be added to the track using a  
 1938 combinatorial Kalman filter [17]. After all of the silicon layers have been consid-  
 1939 ered, tracks are filtered to reduce ambiguities from other nearby tracks or from  
 1940 combinatorial coincidences. Then the tracks are extended outwards into the TRT

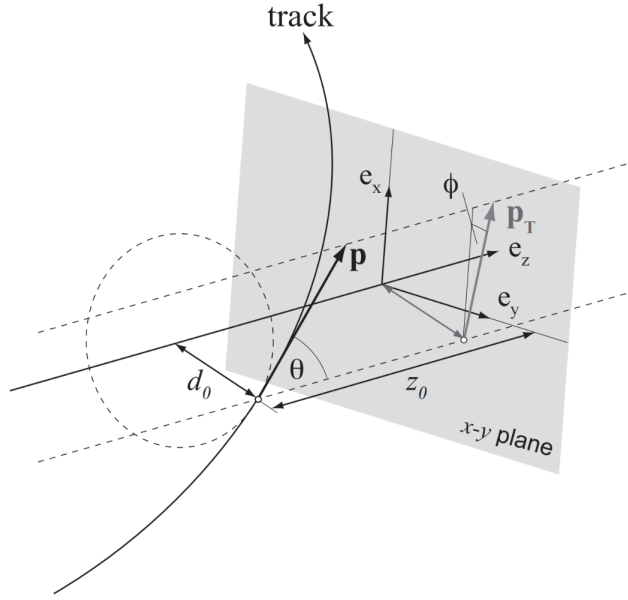


Figure 42: An illustration of the perigee representation of track parameters for an example track. The charge is not directly shown, but is indicated by the direction of curvature of the track [18].

in the same way. This algorithm is how the hits are chosen to be incorporated into a single track. Once the hits are collected, a fitting algorithm calculates the track parameters which best model the locations of the hits and their resolutions. The fitting uses five parameters,  $(d_0, z_0, \phi, \theta, q/p)$ , to specify a track in a perigee representation:  $d_0$  and  $z_0$  are the transverse and longitudinal impact parameters at the closest approach to the nominal beam axis,  $\phi$  and  $\theta$  are the usual angular coordinates, and  $q/p$  is the charge divided by the momentum. These parameters are illustrated in Figure 42. Those parameters directly determine the direction and momentum of the particle which produced the track.

This inside-out algorithm is complemented by an outside-in algorithm, which is used to find tracks from secondary particles, those produced in the decays or interactions of the primary particles inside the detector. As the name indicates, the outside-in algorithm begins by seeding tracks in the outermost layers of the inner detector, in the TRT. The seed in this case is formed by a segment in the TRT, and the track is propagated backwards into the SCT before being refitted to use all the included points. Some tracks are found with TRT segments only, which can result from interactions with the detector following the SCT. Figure 43 shows an example of the geometry of tracks formed by both algorithms, where the hits belonging to tracks found using the inside-out algorithm are highlighted in red, and the hits belonging to the tracks found using the outside-in algorithm are circled in black. The figure highlights the presence of a large number of both primary and secondary tracks in a single event, as well as the overall large number of hits present in the inner detector.

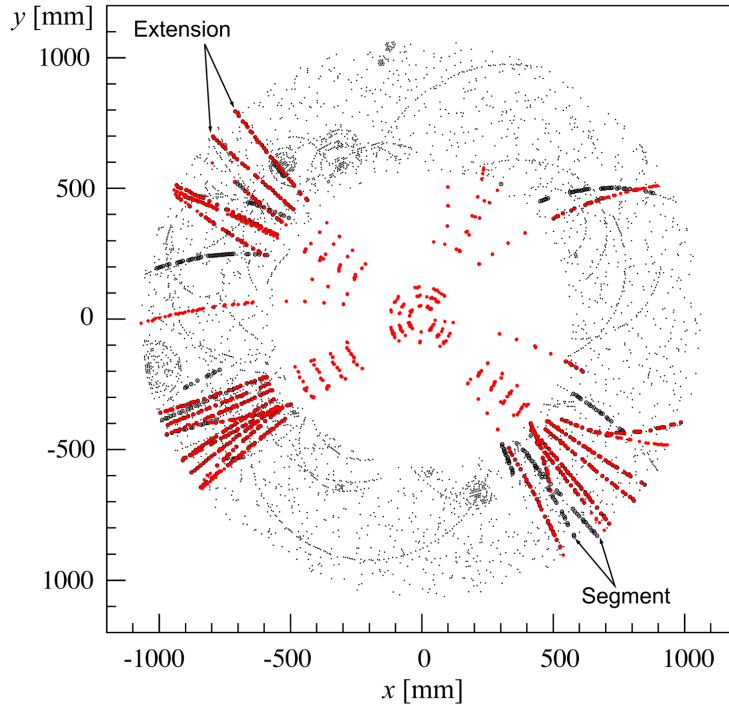


Figure 43: The  $x$  and  $y$  locations of the hits generated in a simulated  $t\bar{t}$  event in the inner detector. The hits which belong to tracks formed using the inside-out algorithm are highlighted in red, while the hits which belong to tracks formed using the outside-in algorithm are circled in black.

1964      The tracks resulting from these algorithms can be contaminated by nearby  
 1965      particles confusing the tracking algorithm in a high luminosity environment.  
 1966      For example, enough hits present in the inner detector can lead to fake tracks  
 1967      from combinations of hits from multiple individual tracks. Therefore, after the  
 1968      tracks are formed and fitted, additional quality requirements are imposed in  
 1969      order to reduce such backgrounds. Most tracking applications require at least  
 1970      seven silicon hits, that is, seven hits between the Pixel detector and **SCT**. Then the  
 1971      tracks are required to have at most two holes in the Pixel detector, where holes  
 1972      are non-existing but expected measurements in a layer of the subdetector. If the  
 1973      missing hit corresponds to an inactive module, however, it is not counted as a  
 1974      hole but instead as a hit for tracking as the lack of a measurement is expected in  
 1975      that case.

1976    6.1.1 PIXEL NEURAL NETWORK

1977      The hits in the Pixel detector are not typically confined to a single pixel, but  
 1978      rather the charge is spread over several pixels per layer which are grouped to-  
 1979      gether into clusters. The clustering of these pixels for isolated tracks is relatively  
 1980      straightforward, but complications can arise in the high occupancy environment  
 1981      where hits from multiple particles can overlap in a single cluster. Figure 44  
 1982      shows examples of clusters generated by a single isolated particle, two nearly  
 1983      overlapping particles, and a particle which emits a  $\delta$ -ray. A  $\delta$ -ray is a secondary

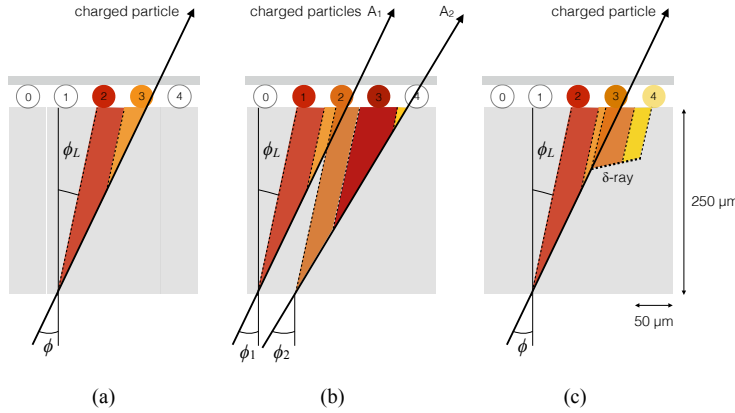


Figure 44: Examples of the clusters formed in a single layer of the pixel detector for (a) a single isolated particle, (b) two nearly-overlapping particles, and (c) a particle which emits a  $\delta$ -ray [19].

1984 electron which is generated with enough energy to escape a significant distance  
1985 away from the original particle and to generate additional ionization.

1986 A series of neural-networks analyzes the shape of the clusters to determine  
1987 how many particles produced the cluster and to estimate the positions of each  
1988 of the particles within the cluster. These allow for an identification of clusters  
1989 caused by more than one particle or by a particle that emits a  $\delta$ -ray. In a high-  
1990 density tracking environment, the multiple position outputs can be used as the  
1991 locations of individual hits to allow reconstruction of tracks which almost over-  
1992 lap and with a much better separation than is possible without the splitting of  
1993 individual clusters.

#### 1994 6.1.2 PIXEL DE/DX

1995 A hit in the Pixel detector corresponds to the voltage generated from ionization  
1996 current rising above a threshold value that is tuned to consistently record the  
1997 passing of MIPs. A larger amount of charge deposited results in a larger voltage,  
1998 and a larger signal remains above the threshold for a longer period of time. The  
1999 time over threshold (ToT) is read out of the Pixel detector, and can be used to  
2000 provide a measurement of the charge deposited in each pixel. The charge mea-  
2001 surements from each of the pixels included in a pixel cluster are summed to form  
2002 one charge measurement per layer of the pixel detector. That charge measure-  
2003 ment, combined with the angle of incidence of the track and the known sizes of  
2004 each detector element, can be converted into a measurement of  $dE/dx$ , the ion-  
2005 ization energy deposited per unit distance, measured in  $\text{MeVg}^{-1}\text{cm}^2$ . The IBL  
2006 only has sixteen available values (4 bits) of ToT to readout, compared to the 256  
2007 available values (8 bits) in the remaining pixel layers. To help alleviate this lack  
2008 of range, the IBL also records if it is in overflow: when the ionization is sufficient  
2009 to generate a ToT above the largest value that can be recorded in the 4 bits.

2010     The measurements across multiple layers are combined to form an average  
 2011    value of  $dE/dx$  for the track as a whole. Depending on where a charge particle  
 2012    is produced, it will traverse four Pixel layers and create four clusters on average.  
 2013    It can produce as few as two clusters in the Pixel detector if it passes through in-  
 2014    active modules, and as many as five if it is in a region of the detector where multiple  
 2015    modules overlap. To reduce the influence of the typical long Landau tails of the  
 2016    distribution of  $dE/dx$  deposits [3], the average is calculated as a truncated mean  
 2017    of these clusters. The value measured in the IBL is removed if it is in overflow, as  
 2018    the measured value is not reliable in that case. If a track has five measurements  
 2019    in the pixel detector, the two highest cluster values are removed. If a track has  
 2020    two, three, or four measurements in the pixel detector, only the single highest  
 2021    cluster value is removed. The remaining values are averaged to form the pixel  
 2022     $dE/dx$ .

2023    6.1.3 VERTEX RECONSTRUCTION

2024    A vertex represents the intersection of multiple tracks and corresponds to the  
 2025    location of an interaction. If at least two charged particles result from the in-  
 2026    teraction, the intersection of their resulting tracks reveals its position with high  
 2027    precision. Vertices are divided into two groups, primary vertices which corre-  
 2028    spond to the actual proton-proton collisions, and secondary vertices which cor-  
 2029    respond to decays of short-lived particles or interactions with the detector. Pri-  
 2030    mary vertices are particularly important, as they can provide a precise location  
 2031    for the interaction which generated the observed particles. Understanding that  
 2032    location is crucial in understanding the geometry of the event.

2033    Primary vertices are reconstructed by iteratively identifying seeds from recon-  
 2034    structed tracks [20]. Each track's extrapolated  $z$  position at the beamline forms a  
 2035    seed, and nearby tracks are fitted using that position as a point along their trajec-  
 2036    tory. The goodness of fit with that vertex is considered for each track, measured  
 2037    in  $\chi^2$ . The final position of the vertex is determined by a fit to all of the con-  
 2038    sidered tracks, where the contribution from each track is weighted according to  
 2039    the  $\chi^2$  compatibility with that vertex. Any tracks from this procedure that are  
 2040    displaced by more than  $7\sigma$  from that vertex are removed from the fit and used  
 2041    to seed a new vertex. This procedure is iterated until no additional vertices can  
 2042    be found.

2043    This procedure is typically performed twice. The first set of vertices is used  
 2044    to fit a profile for the beamspot, which indicates the position of the intersection  
 2045    of beams in that particular bunch crossing. The fitted beamspot then provides  
 2046    a constraint for the second attempt to locate primary vertices, where both the  
 2047    track fitting and seeding of vertices are required to be consistent with interac-  
 2048    tions occurring within the beamspot.

2049    6.2 ELECTRONS AND PHOTONS

2050    Electrons are measured as both a charged particle track and energy deposits in  
 2051    the electromagnetic calorimeter. Photons, on the other hand, leave energy de-

2052 posits in the electromagnetic calorimeter but do not produce a corresponding  
 2053 track. Because the electromagnetic interactions with the calorimeter of both  
 2054 photons and electrons produces more photons and electrons, the behavior in the  
 2055 calorimeter is very similar and there is significant overlap in the reconstruction  
 2056 techniques for each.

2057 The reconstruction of a photon or an electron in the calorimeter is based on  
 2058 clustering algorithms which identify groups of energy deposits [21–23]. For this  
 2059 purpose, the entire electromagnetic calorimeter is subdivided into a grid of 200  
 2060 by 256 towers in the  $\eta$  and  $\phi$  directions, respectively, where the individual grid  
 2061 units have a size of  $\Delta\eta = 0.025$  and  $\Delta\phi = 0.025$ . These towers correspond to  
 2062 individual cells in the middle, coarsest layer of the EM calorimeter, and in the re-  
 2063 maining layers the cells are grouped together cover the same area in  $\eta - \phi$  space.  
 2064 The clustering begins by finding seeds with a sliding-window algorithm based  
 2065 on the towers: a window of 3 by 5 towers is formed and translated until the sum  
 2066 of the energy within the window is maximized. If that energy is above 2.5 GeV,  
 2067 then that region becomes a seed. The choice of 2.5 GeV was chosen to com-  
 2068 promise between maximizing reconstruction efficiency while minimizing fake  
 2069 electron seeds from electronic noise or soft hadrons from additional interactions.  
 2070 The seeds are rejected if the energy measured in the hadronic calorimeter behind  
 2071 the seed is large, as this typically indicates a hadron rather than an electron or  
 2072 photon.

2073 Next, the inner detector tracks within a cone of  $\Delta R = 0.3$  are compared to  
 2074 the location and energy of the seed. Tracks are matched to the cluster if the ex-  
 2075 trapolation of the track to the energy-weighted center in the middle layer of the  
 2076 EM calorimeter falls within  $\Delta\phi < 0.2$  in the direction of the curvature of the  
 2077 track or  $\Delta\phi < 0.05$  in the direction opposite of the curvature of the track. If the  
 2078 seed matches with a track that originated from a primary vertex, the combina-  
 2079 tion of track and electromagnetic cluster is reconstructed as an electron. If the  
 2080 seed matches with a track that did not originate from a primary vertex, then the  
 2081 electromagnetic cluster is reconstructed as a converted photon. And if there is  
 2082 no corresponding track in the inner detector, then the cluster is reconstructed  
 2083 as a photon.

2084 After classification, the final clustering of the energy in the EM calorimeter  
 2085 calorimeter is performed. The classification must be done first, as the expected  
 2086 size of the energy deposits in the calorimeter are different for electrons and pho-  
 2087 tons. In the barrel region, the final clusters for electrons are formed in rectangles  
 2088 of 3 towers in the  $\eta$ -direction and 7 towers in the  $\phi$ -direction. This asymmetric  
 2089 window accounts for the curving of the produced charged particles only in the  
 2090  $\phi$  direction. For photons, the size of the rectangle is 3 towers by 5 towers. In the  
 2091 endcap region, all object types are clustered in rectangles of 5 towers by 5 tow-  
 2092 ers, as the effect of the magnetic field curvature is less pronounced in this region.  
 2093 The sum of the energies in these clusters provide the final energy measurement  
 2094 for the electron or photon.

## 2095 6.2.1 PHOTON IDENTIFICATION

2096 The original requirement for constructing a photon cluster, a significant energy  
 2097 deposit in the electromagnetic calorimeter without a corresponding track or en-  
 2098 ergy deposits in the hadronic calorimeter, is already effective in identifying pho-  
 2099 tons. However, there is a significant background for prompt photon production  
 2100 from the decays of pions,  $\pi^0 \rightarrow \gamma\gamma$ . These can be identified using the shape of  
 2101 the cluster in the narrow  $\eta$  granularity in the first layer of the EM calorimeter.

## 2102 6.2.2 ELECTRON IDENTIFICATION

2103 Prompt electrons have a number of backgrounds, such as secondary electrons  
 2104 from hadron decays or misidentified hadronic jets, that can be rejected using ad-  
 2105 dditional information from the EM calorimeter and the inner detector. The most  
 2106 basic level of electron identification, referred to as Loose, makes requirements  
 2107 on the shower shapes in the high granularity first layer of the EM calorimeter  
 2108 as well as the quality of the inner detector track. It also requires a good match  
 2109 between the track and the calorimeter energy deposits and a small fraction of  
 2110 energy in the hadronic calorimeter behind the electromagnetic cluster. ATLAS  
 2111 defines several additional working points, including Medium and Tight, which  
 2112 provide progressively lower background rates for electrons by imposing addi-  
 2113 tionally strict requirements on the above variables as well as new requirements  
 2114 like the impact parameter of the inner detector track or the comparison of the  
 2115 cluster energy to the momentum in the inner detector.

## 2116 6.3 MUONS

2117 Muons produced in ATLAS first traverse the inner detector and leave behind a  
 2118 track as described in Section 6.1. The muon then passes through the calorimeter,  
 2119 leaving behind a small, characteristic amount of energy, and then passes through  
 2120 the muon spectrometer where it produces hits in the MDTs or CSCs. Muon tracks  
 2121 are formed from local segments of hits in each layer of the MDTs or CSCs, and  
 2122 then the final muon spectrometer track is formed by combining the two local  
 2123 segments [24]. When a track is reconstructed in both the inner detector and  
 2124 the muon spectrometer, the track is refitted to include the hits in both the inner  
 2125 detector and the muon spectrometer, and forms a combined muon.

2126 In a few regions of the detector, a muon may fail to leave behind both a com-  
 2127 plete inner detector and muon system track. For a very small fraction of the  
 2128 acceptance of the muon system, there is only one layer of muon chambers and a  
 2129 global muon system track is not formed. In this case, as long as the track in the  
 2130 inner detector exists and geometrically matches to a segment, a segment-tagged  
 2131 muon is formed using momentum measurements from the inner detector. In  
 2132 the region where the muon system has coverage but the inner detector does not,  
 2133  $2.5 < |\eta| < 2.7$ , a stand-alone muon is formed which uses only information  
 2134 from the muon system. And for muons produced within one of the few holes in  
 2135 the muon system, including  $|\eta| < 0.1$ , the characteristic energy deposits in the

2136 calorimeter can be used to tag an inner detector track as a calo-tag muon. These  
 2137 additional categories are used to achieve high efficiency over a larger range of  
 2138 acceptance, but the combined muons are the most reliable.

### 2139 6.3.1 MUON IDENTIFICATION

2140 The various types of muons are incorporated into three working points: Loose,  
 2141 Medium, and Tight, which reflect the increasing muon purity for each of the  
 2142 selections definitions. Tight muons include only combined muons with a good  
 2143 track fit quality and momentum resolution and at least two hits in a precision  
 2144 muon system layer. Medium muons include those in tight as well as combined  
 2145 muons with one precision hit and one precision hole, where hole is defined in  
 2146 the same way as in Section 6.1. The medium working point also includes stand-  
 2147 alone muons with  $|\eta| > 2.5$  and at least two hits in precision layers. And finally  
 2148 the loose working point includes both medium and tight muons, but additional  
 2149 includes segment-tagged and calo-tagged muons in the region  $|\eta| < 0.1$ .

## 2150 6.4 JETS

2151 A jet does not directly correspond to a physical particle, unlike all of the recon-  
 2152 structed objects described above, but instead tries to capture the conical cascade  
 2153 of particles produced in the hadronization of a quark or gluon from the proton-  
 2154 proton collision. The hadronization process creates a very large number of col-  
 2155 limated particles, with a high enough density that individually reconstructing all  
 2156 of the produced particles in the calorimeter is not possible within ATLAS. How-  
 2157 ever most analyses are interested only in the kinematics of the particle which  
 2158 produced the cascade, rather than the individual products. Therefore, jets are  
 2159 a useful tool to measure the combined energy and direction of the ensemble of  
 2160 products and thus represents the kinematics of the original. Jet algorithms are  
 2161 very generic and can be used to group together a number of types of objects to  
 2162 form aggregate representations. For example, truth particles in simulation can  
 2163 be grouped in truth jets, or tracks from the inner detector can be grouped to-  
 2164 gether to form track jets. This section, however, will focus on calorimeter jets  
 2165 which take topoclusters of energy deposits in the calorimeter as inputs and pro-  
 2166 duce a combined object which represents the energy measured by the calorime-  
 2167 ter and the location where it was deposited.

### 2168 6.4.1 TOPOLOGICAL CLUSTERING

2169 Hadrons often deposit their energy into multiple individual cells in both the elec-  
 2170 tromagnetic and hadronic calorimeters. The purpose of topological clustering is  
 2171 to group cells in all three dimensions into clusters that represent a single energy  
 2172 deposit. The procedure must be robust enough to reject noise fluctuations in  
 2173 the cell energy measurements that can come from both electronic noise and ad-  
 2174 dditional low energy particles produced in pileup activity. The background level

2175 of calorimeter noise is called  $\sigma_{\text{noise}}$ , and is an important component of the topo-  
 2176 logical clustering.

2177 The topological clusters are formed in a three step process called the 4-2-0  
 2178 threshold scheme, which uses three energy thresholds to build up a cluster from  
 2179 cells [25]. First, any cells with a measured energy above  $4\sigma_{\text{noise}}$  are identified  
 2180 as seed cells. The cells adjacent to the seed cells with a measured energy above  
 2181  $2\sigma_{\text{noise}}$  are called secondary cells. All of the cells which are adjacent to a sec-  
 2182 ondary cell with  $E_{\text{cell}} > 2\sigma_{\text{noise}}$  are also labeled secondary cells. Tertiary cells  
 2183 are those immediately adjacent to a seed or secondary cell with a measured en-  
 2184 ergy above zero. Adjacency in this sense is defined in three dimensions, cells are  
 2185 adjacent if they are neighbors within a layer but also if they have the same  $\eta - \phi$   
 2186 coordinates but are in adjacent layers or even in an adjacent layer in another  
 2187 calorimeter.

2188 From these definitions, clusters are built by resolving the seeds in order of  
 2189 significance, the ratio  $E_{\text{cell}}/\sigma_{\text{noise}}$ . All adjacent secondary cells to the highest  
 2190 significance seed are added to that seed's topocluster, and any of those cells which  
 2191 would also have qualified as seeds are removed from the list of seeds. Once all  
 2192 of the secondary cells have been added, the tertiary cells are then added to that  
 2193 cluster as well. This procedure is then iterated until no seeds remain, forming  
 2194 the first round of topoclusters.

2195 It is also useful to split topoclusters into multiples if local maxima are present  
 2196 within the topocluster, as clusters produced by multiple nearby particles can  
 2197 merge. The splitting process begins by finding local maxima cells in the middle  
 2198 layer of the calorimeters with a minimum energy of 500 MeV and at least four  
 2199 neighboring secondary cells. These requirements reduce the likelihood to split  
 2200 a cluster due to random fluctuations, as the middle layers provide the most reli-  
 2201 able energy measurements. Cells between two local maxima can then be shared  
 2202 between two clusters to account for overlapping contributions from two parti-  
 2203 cles. The energy sharing is weighted by the energy of each cluster as well as the  
 2204 distance of the cell to the centroid of that cluster.

2205 The energies of all the cells in the cluster are then summed together to form  
 2206 the energy of that cluster. The energy needs to be corrected for the various losses  
 2207 expected in the calorimeter, as described in Section 5.4. The simplest correction,  
 2208 scaling the measured energy by the sampling fraction, brings the cluster energies  
 2209 to the EM scale. It is called the EM scale because it accurately describes the energy  
 2210 of electromagnetic showers.

2211 Another scale is defined to improve accuracy for hadronic processes, the local  
 2212 cluster weighted (LCW) scale, that helps to correct for the expected variations in  
 2213 hadronic energy deposits. The LCW correction first determines if the shower is  
 2214 hadronic or electromagnetic, based on the depth of the shower and the cluster  
 2215 energy density. For hadronic showers, the energy is corrected for calorimeter  
 2216 non-compensation, an effect which reduces the measured energy of hadronic  
 2217 showers because some of the energy goes into invisible processes like the break  
 2218 up of nuclei. All clusters are then corrected for energy that may be deposited in  
 2219 uninstrumented regions in that cluster's location in the calorimeter, and they are

2220 also corrected with an estimate of how much energy falls outside the extent of  
 2221 the cluster based on its shape and the deposit type.

2222 6.4.2 JET ALGORITHMS

2223 Using the topological clusters as inputs, a jet algorithm groups them together  
 2224 into a collection of adjacent energy deposits that is intended to correspond to  
 2225 a single process [26]. Jet algorithms need a few key characteristics to be usable  
 2226 for physics analysis. First, the jets produced by the algorithm should have little  
 2227 dependence on the addition of soft particles to the event (infrared safety), as a  
 2228 negligible addition of energy should not significantly modify the event topology.  
 2229 Similarly, the jets produced by the algorithm should also not significantly depend  
 2230 on mostly collinear splitting of an input particle (collinear safety); that is, a single  
 2231 quark replaced by two, parallel quarks with half the original's momentum should  
 2232 not change the resulting jets, which are intended to capture only the properties  
 2233 of the aggregate and not those of individual particles. And finally the algorithm  
 2234 needs to be sufficiently simple and fast to be used for the large rate of collected  
 2235 proton-proton collisions on [ATLAS](#).

2236 The most commonly used algorithm on [ATLAS](#) that satisfies these requirements  
 2237 is called the anti- $k_t$  algorithm, and is discussed in further detail in Reference [27].  
 2238 The anti- $k_t$ , in brief, relies on iteratively combining the input objects that are  
 2239 closest together, where closest is defined by a particular distance metric,  $d_{i,j}$ ,  
 2240 where the index  $i$  represents the combination constructed so far and  $j$  is an ad-  
 2241 ditional object being considered. The combinations stop when the closest re-  
 2242 maining object is the beam itself, where the distance to the beam is called  $d_{i,B}$ .  
 2243 An entire class of algorithms follows this procedure with the following distance  
 2244 metrics

$$d_{i,j} = \min(k_{ti}^{2p}, k_{tj}^{2p}) \frac{\Delta_{ij}^2}{R^2} \quad (18)$$

$$d_{i,B} = k_{ti}^{2p} \quad (19)$$

2245 where  $\Delta_{ij} = (y_i - y_j)^2 + (\phi_i - \phi_j)^2$ ,  $k_{ti}$  is the transverse momentum of the  
 2246 object,  $y$  is the rapidity, and  $p$  is a parameter of the algorithm. Anti- $k_t$  is the  
 2247 particular case where  $p = -1$ , and is a choice that results in an algorithm that is  
 2248 both infrared and collinear safe.

2249 The algorithm is repeated until there are no input objects remaining, which  
 2250 results in a series of jets. Each jet has a complete four momentum from the com-  
 2251 bination of its input clusters, where the combinations assume a mass of zero.  
 2252 The jet energies then need to be calibrated to attempt to match the energy of the  
 2253 object which produced the jet.

2254 6.4.3 JET ENERGY SCALE

2255 Though the [LCW](#) scheme attempts to correct the topoclusters to reflect the true  
 2256 deposited energy, the correction does not fully account for energy lost within

the calorimeters. Because of these effects, the original reconstructed jet energy does not reflect the true energy of the particle which initiated the jet. Therefore it is necessary to additionally correct the reconstructed jet itself, in addition to the corrections on the inputs. This correction is referred to as the **JES**, which combines several individual steps of calibration [28].

The first calibration step corrections the direction of the jet to ensure that it points back to the primary vertex. Next, the energy of the jet is corrected for pileup by subtracting the expected contribution from pileup based on the momentum,  $\eta$ , and area of the jet as well as the number of reconstructed vertices and expected number of interactions per crossing. The largest single correction is the absolute  $\eta$  and scale correction, where the jet energy and pseudorapidity is corrected to attempt to match the energy and pseudorapidity of the parton which produced it. This correction is measured in simulation by comparing the reconstructed jet energies to the energy of the truth particle which produced it. However the simulation is not relied on alone to estimate this correction, and an additional step applies an additional energy correction based on in-situ measurements in data. These corrections come from various techniques which measure jet energies indirectly by balancing them with other, well-measured objects. In the central region ( $|\eta| < 1.2$ ), jets are balanced against photons and the leptonic decays of Z bosons and high momentum jets ( $p_T > 210$  GeV) are also balanced against multiple smaller jets in multijet events. Jets at larger pseudorapidities, above  $|\eta| = 1.2$ , are calibrated by balancing with lower pseudorapidity jets.

These steps introduce a number of systematic uncertainties, referred to as the **JES** uncertainty. The largest of these comes from the in-situ measurements, which are statistically limited in measuring high momentum and high pseudorapidity jets. The total, fractional **JES** uncertainty is shown as a function of  $p_T$  in Figure 45. The uncertainty falls to a minimum value of just over 1.0% around a few hundred GeV, and rises again at high momentum because of the difficulty of measuring jet balance in data above 2-3 TeV. The uncertainty is also minimized at low  $|\eta|$ , and grows at large  $|\eta|$  again where making in-situ measurements is difficult. This technique does not actually provide a measurement of the uncertainty for the highest energy jets, above 3 TeV, because there are not enough measured data events to provide them. An alternative method for deriving the **JES** and **JES** uncertainty that can be used even for very high  $p_T$  jets will be discussed in Chapter 8.

## 6.5 MISSING TRANSVERSE ENERGY

Among stable **SM** particles, only the neutrino cannot be directly measured in the **ATLAS** detector. Because the neutrino carries neither electric nor color charge, it is very unlikely to interact with the tracking detectors or the calorimeters, and instead passes through the detector completely unobserved. Some particles which have been conjectured to exist, like the **LSP** in many **SUSY** models, would also have the same behavior. Therefore, it is important for **ATLAS** to provide some way to assess the momentum carried away by a neutral, colorless particle. This can be accomplished through a measurement of missing energy in the transverse

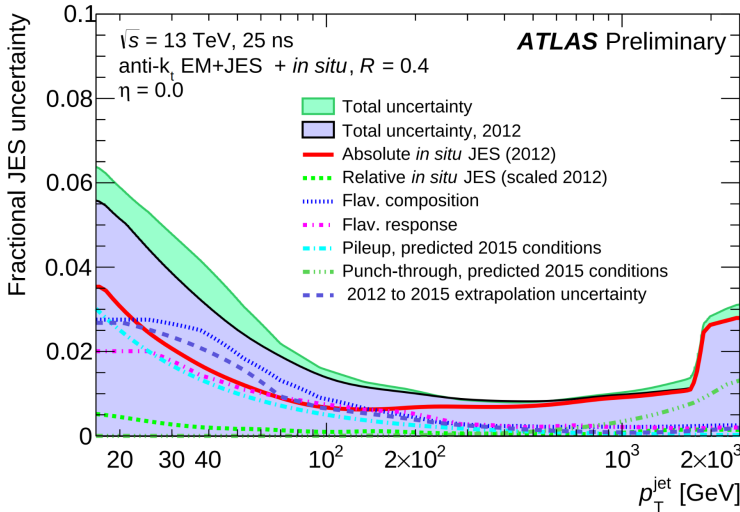


Figure 45: The total, fractional JES uncertainties estimated for 2015 data as a function of jet  $p_T$ .

direction, or  $E_T^{\text{miss}}$ , which quantifies the momentum imbalance of the observed particles. From the conservation of momentum and the lack of the initial momentum in the transverse plane in the proton-proton collisions, any imbalance of momentum can be inferred to be carried away by an unmeasured particle.

$E_T^{\text{miss}}$  is more precisely defined as the magnitude of the vector sum of the  $(p_x, p_y)$  components of each observed object's momentum. The definition is simple, but there can be significant complexity in defining the inputs. As of Run 2, ATLAS uses a common algorithmic approach to carefully calculate missing energy, but each analysis is free to define its own inputs. For the analysis discussed throughout this thesis, the missing energy inputs consist of the electrons, photons, muons, and jets discussed in the previous sections, in addition to a track-based soft term.

To produce the most precise measurement of  $E_T^{\text{miss}}$ , it is important to use the best representation of the momentum of each of the input objects, which can often be reconstructed as multiple different types in a single event. For example, an electron can be reconstructed separately as an electron (Section 6.2) and a jet (Section 6.4), but the electron representation has the highest precision for reconstructing the true electron momentum. To ensure no duplications in the  $E_T^{\text{miss}}$  definition, the inputs are collectively considered for overlap removal. Only the most precise object type is kept for objects that fall within a cone of  $\Delta R < 0.2$  for pairs of electrons and jets and a cone of  $\Delta R < 0.4$  for other pair types.

The fully reconstructed objects do not include all of the energy within the events, as some clusters do not enter into a jet and some tracks are not classified as electrons or muons. These momentum carried by these objects is accounted for in a soft-term, which tallies all of the energy carried by the particles too soft to form separate objects. The track soft term uses only tracking information to estimate the contribution of soft objects, and does so by vectorially summing the momentum of all well-reconstructed tracks with momentum above 400 MeV.

2329 All of these contributions together give a single  $E_T^{\text{miss}}$  value for a given event.  
2330 The direction of that missing energy is taken as opposite the vector sum of all the  
2331 constituents, to correspond to the momentum an invisible particle would have to  
2332 have to make the event balanced. Depending on the context, this missing energy  
2333 can be considered the energy of a neutrino or an LSP, with a large missing energy  
2334 being a common signal criteria for searches for new physics.

2335

## PART IV

2336

### CALORIMETER RESPONSE

2337

You can put some informational part preamble text here.

2338

2339 RESPONSE MEASUREMENT WITH SINGLE HADRONS

---

2340 As discussed in Section 6.4, colored particles produced in collisions hadronize  
 2341 into jets of multiple hadrons. One approach to understanding jet energy mea-  
 2342 surements in the ATLAS calorimeters is to evaluate the calorimeter response to  
 2343 those individual hadrons; measurements of individual hadrons can be used to  
 2344 build up an understanding of the jets that they form. The redundancy of the  
 2345 momentum provided by the tracking system and the energy provided by the  
 2346 calorimeter provides an opportunity to study calorimeter response using real  
 2347 collisions, as described further in Section 7.2.

2348 Calorimeter response includes a number of physical effects that can be ex-  
 2349 tracted to provide insight into many aspects of jet modeling. First, many charged  
 2350 hadrons interact with the material of the detector prior to reaching the calorime-  
 2351 ters and thus do not deposit any energy. Comparing this effect in data and simu-  
 2352 lation is a powerful tool in validating the interactions of particles with the mate-  
 2353 rial of the detector and the model of the detector geometry in simulation, see Sec-  
 2354 tion 7.2.2. The particles which do reach the calorimeter deposit their energy into  
 2355 several adjacent cells, which are then clustered together. The energy of the clus-  
 2356 ter is then the total energy deposited by that particle. Comparing the response of  
 2357 hadrons in data to that of simulated hadrons provides a direct evaluation of the  
 2358 showering of hadronic particles and the energy deposited by particles in matter  
 2359 (Section 7.2.4).

2360 The above studies all use an inclusive selection of charged particles, which are  
 2361 comprised predominantly of pions, kaons, and (anti)protons. It is also possible to  
 2362 measure the response to various identified particle types separately to evaluate  
 2363 the simulated interactions of each particle, particularly at low energies where  
 2364 differences between species are very relevant. Pions and (anti)protons can be  
 2365 identified through decays of long-lived particles, in particular  $\Lambda$ ,  $\bar{\Lambda}$ , and  $K_S^0$ , and  
 2366 then used to measure response as described above. This is discussed in detail in  
 2367 Section 7.3.

2368 The results in this chapter use data collected at 7 and 8 TeV collected in 2010  
 2369 and 2012, respectively. Both are included as the calorimeter was repaired and  
 2370 recalibrated between those two data-taking periods. Both sets of data are com-  
 2371 pared to an updated simulation that includes new physics models provided by  
 2372 Geant4 [29] and improvements in the detector description [30, 31]. The present  
 2373 results are published in European Physical Journal C (EPJC) [32] and can be com-  
 2374 compared to a similar measurement performed in 2009 and 2010 [33], which used  
 2375 the previous version of the simulation framework [34].

## 2376 7.1 DATASET AND SIMULATION

## 2377 7.1.1 DATA SAMPLES

2378 The two datasets used in this chapter are taken from dedicated low-pileup runs  
 2379 where the fraction of events with multiple interactions was negligible. These  
 2380 datasets are used rather than those containing full-pileup events to facilitate mea-  
 2381 surement of isolated hadrons. The 2012 dataset at  $\sqrt{s} = 8$  TeV contains 8 mil-  
 2382 lion events and corresponds to an integrated luminosity of  $0.1 \text{ nb}^{-1}$ . The 2010  
 2383 dataset at  $\sqrt{s} = 7$  TeV contains 3 million events and corresponds to an inte-  
 2384 grated luminosity of  $3.2 \text{ nb}^{-1}$ . The latter dataset was also used for the 2010 re-  
 2385 sults [33], but it has since been reanalyzed with an updated reconstruction in-  
 2386 cluding the final, best understanding of the detector description for the material  
 2387 and alignment from Run 1.

## 2388 7.1.2 SIMULATED SAMPLES

2389 The two datasets above are compared to simulated single-, double-, and non-  
 2390 diffractive events generated with Pythia8 [35] using the A2 configuration of  
 2391 hadronization [36] and the MSTW 2008 parton-distribution function set [37,  
 2392 38]. The admixture of the single-, double-, and non-diffractive events uses the  
 2393 default relative contributions from Pythia8. The conditions and energies for  
 2394 the two simulations are chosen so that they match those of the corresponding  
 2395 dataset.

2396 To evaluate the interaction of hadrons with detector material, the simulation  
 2397 uses two different collections of hadronic physics models, called physics lists, in  
 2398 Geant4 9.4 [39]. The first, QGSP\_BERT, combines the Bertini intra-nuclear  
 2399 cascade [40–42] below 9.9 GeV, a parametrized proton inelastic model from 9.5  
 2400 to 25 GeV [43], and a quark-gluon string model above 12 GeV [44–48]. The  
 2401 second, FTFP\_BERT, combines the Bertini intra-nuclear cascade [40–42] below  
 2402 5 GeV and the Fritiof model [49–52] above 4 GeV. In either list, Geant4 en-  
 2403 forces a smooth transition between models where multiple models overlap.

## 2404 7.1.3 EVENT SELECTION

2405 The event selection for this study is minimal, as the only requirement is selecting  
 2406 good-quality events with an isolated track. Such events are triggered by requir-  
 2407 ing at least two hits in the minimum-bias trigger scintillators. After trigger, each  
 2408 event is required to have exactly one reconstructed vertex, and that vertex is re-  
 2409 quired to have four or more associated tracks.

2410 The particles which are selected for the response measurements are first iden-  
 2411 tified as tracks in the inner detector. The tracks are required to have at least 500  
 2412 MeV of transverse momentum. To ensure a reliable momentum measurement,  
 2413 these tracks are required to have at least one hit in the pixel detector, six hits in  
 2414 the SCT, and small longitudinal and transverse impact parameters with respect  
 2415 to the primary vertex [33]. For the majority of the measurements in this chapter,

2416 the track is additionally required to have 20 hits in the TRT, which significantly  
 2417 reduces the contribution from tracks which undergo nuclear interactions. This  
 2418 requirement and its effect is discussed in more detail in Section 7.2.5. In addition,  
 2419 tracks are rejected if there is any other reconstructed track which extrapolates  
 2420 to the calorimeter within a cone of  $\Delta R = \sqrt{(\Delta\phi)^2 + (\Delta\eta)^2} < 0.4$ . This require-  
 2421 ment guarantees that the contamination of energy from nearby charged particles  
 2422 is negligible [33].

## 2423 7.2 INCLUSIVE HADRON RESPONSE

2424 The calorimeter response is more precisely defined as the ratio of the measured  
 2425 calorimeter energy to the true energy carried by the particle, although this true  
 2426 energy is unknown. For charged particles, however, the inner detector provides  
 2427 a very precise measurement of momentum (with uncertainty less than 1%) that  
 2428 can be used as a proxy for true energy. The ratio of the energy deposited by  
 2429 the charged particle in the calorimeter,  $E$ , to its momentum measured in the  
 2430 inner detector  $p$ , forms the calorimeter response measure called  $E/p$ . Though  
 2431 the distribution of  $E/p$  contains a number of physical features, this study focuses  
 2432 on the trends in two aggregated quantities:  $\langle E/p \rangle$ , the average of  $E/p$  for the  
 2433 selected tracks, and the zero fraction, the fraction of tracks with no associated  
 2434 energy in the calorimeter for those tracks.

2435 The calorimeter energy assigned to a track is defined using clusters. The clus-  
 2436 ters are formed using a 4–2–0 algorithm [53] that begins with seeds requiring  
 2437 at least 4 times the average calorimeter cell noise. The neighboring cells with  
 2438 at least twice that noise threshold are then added to the cluster, and all bound-  
 2439 ing cells are then added with no requirement. This algorithm minimizes noise  
 2440 contributions through its seeding process, and including the bounding cells im-  
 2441 proves the energy resolution [54]. The clusters are associated to a given track  
 2442 if they fall within a cone of  $\Delta R = 0.2$  of the extrapolated position of the track,  
 2443 which includes about 90% of the energy on average [33].

### 2444 7.2.1 E/P DISTRIBUTION

2445 The  $E/p$  distributions measured in both data and simulation are shown in Fig-  
 2446 ure 46 for two example bins of track momentum and for tracks in the central  
 2447 region of the detector. These distributions show several important features of  
 2448 the  $E/p$  observable. The large content in the bin at  $E = 0$  comes from tracks that  
 2449 have no associated cluster, which occurs due to interactions with detector mate-  
 2450 rial prior to reaching the calorimeter or the energy deposit being insuffi-  
 2451 ciently large to generate a seed, and are discussed in Section 7.2.2. The small negative  
 2452 tail also comes from tracks that do not deposit any energy in the calorimeter but  
 2453 are randomly associated to a cluster with an energy below the noise threshold.  
 2454 The long positive tail above 1.0 comes from the contribution of neutral parti-  
 2455 cles. Nearby neutral particles deposit (sometimes large) additional energy in the  
 2456 calorimeter but do not produce tracks in the inner detector, so they cannot be  
 2457 rejected by the track isolation requirement. Additionally the peak and mean of

2458 the distribution falls below 1.0 because of the loss of energy not found within  
 2459 the cone as well as the non-compensation of the calorimeter.

2460 The data and simulation share the same features, but the high and low tails  
 2461 are significantly different. The simulated events tend to overestimate the con-  
 2462 tribution of neutral particles to the long tail, an effect which can be isolated and  
 2463 removed as discussed in Section 7.2.3. Additionally, the simulated clusters have  
 2464 less noise on average, although this is a small effect on the overall response.

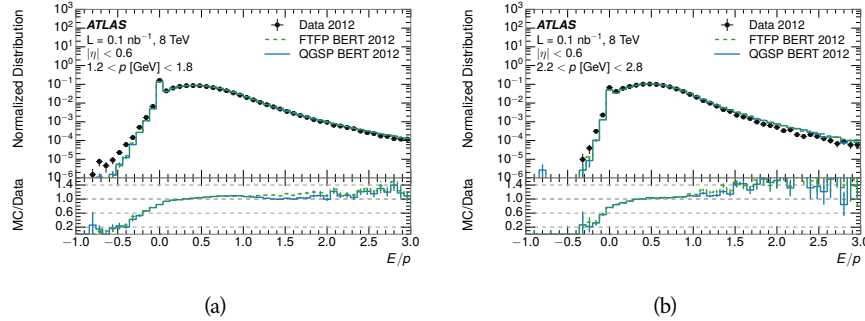


Figure 46: The  $E/p$  distribution and ratio of simulation to data for isolated tracks with  
 (a)  $|\eta| < 0.6$  and  $1.2 < p/\text{GeV} < 1.8$  and (b)  $|\eta| < 0.6$  and  $2.2 < p/\text{GeV} < 2.8$ .

## 2465 7.2.2 ZERO FRACTION

2466 The fraction of particles with no associated clusters, or similarly those with  $E \leq$   
 2467 0, reflects the modeling of both the detector geometry and hadronic interactions.  
 2468 The zero fraction is expected to rise as the amount of material a particle traverses  
 2469 increases, while it is expected to decrease as the particle energy increases. This  
 2470 dependence can be seen in Figure 47, where the zero fraction in data and simula-  
 2471 tion is shown as a function of momentum and the amount of material measured  
 2472 in interaction lengths. The trends are similar between 2010 and 2012 and for  
 2473 positively and negatively charged particles. The zero fraction decreases with  
 2474 energy as expected. The absolute discrepancy in zero fraction between data and  
 2475 simulation decreases with momentum from 5% to less than 1%, but this becomes  
 2476 more pronounced in the ratio as the zero fraction shrinks quickly with increas-  
 2477 ing momentum. The amount of material in the detector increases with  $\eta$ , which  
 2478 is used to obtain results for interaction lengths ranging between 0.1 and 0.65  $\lambda$ .  
 2479 As the data and simulation have significant disagreement in the zero fraction  
 2480 over a number of interaction lengths, the difference must be primarily from the  
 2481 modeling of hadronic interactions with detector material and not just the detec-  
 2482 tor geometry. Although two different hadronic interaction models are shown  
 2483 in the figure, they have very similar discrepancies to data because both use the  
 2484 same description (the BERT model) at low momentum.

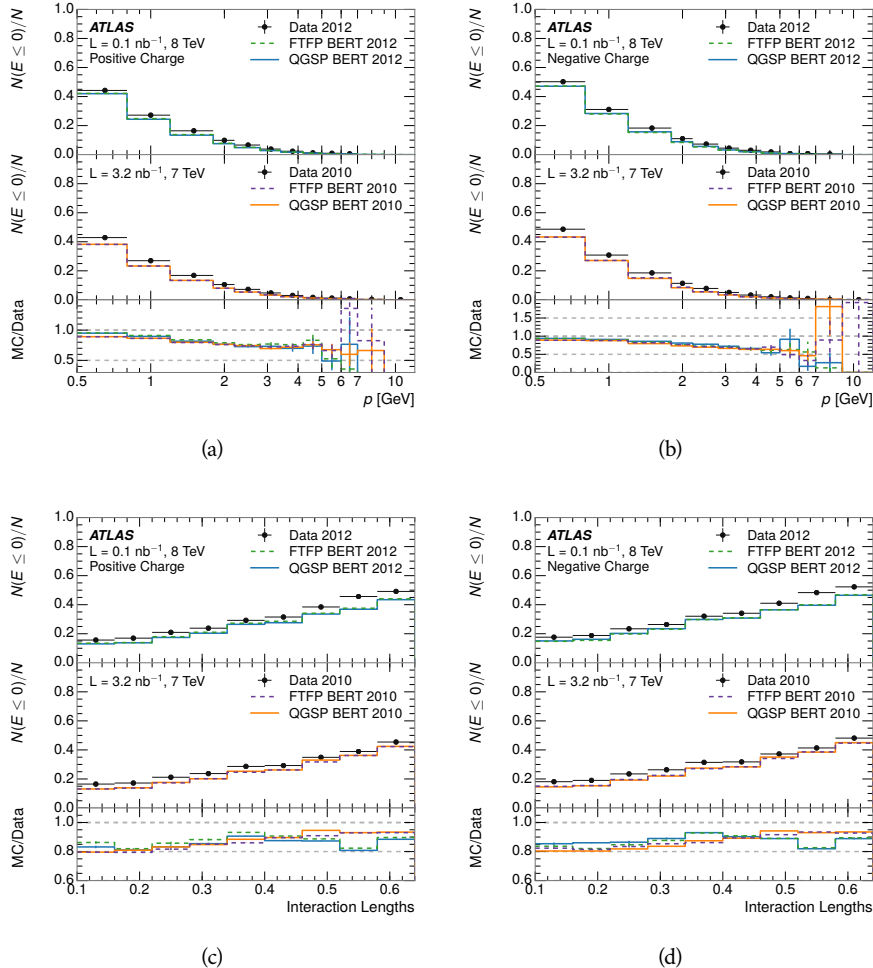


Figure 47: The fraction of tracks as a function (a, b) of momentum, (c, d) of interaction lengths with  $E \leq 0$  for tracks with positive (on the left) and negative (on the right) charge.

## 2485 7.2.3 NEUTRAL BACKGROUND SUBTRACTION

2486 The isolation requirement on hadrons is only effective in removing an energy  
 2487 contribution from nearby charged particles. Nearby neutral particles, predomi-  
 2488 nantly photons from  $\pi^0$  decays, also add their energy to the calorimeter clusters,  
 2489 but mostly in the electromagnetic calorimeter. The arrangement of energy de-  
 2490 posits is shown in Figure 48, which illustrates both energy deposits from the  
 2491 hadronic particle and additional deposits from neutral particles. It is possible to  
 2492 measure this contribution, on average, using late-showering hadrons that min-  
 2493 imally ionize in the electromagnetic calorimeter. Such particles are selected by  
 2494 requiring that they deposit less than 1.1 GeV in the EM calorimeter within a  
 2495 cone of  $\Delta R < 0.1$  around the track. To ensure that these particles are well mea-  
 2496 sured, they are additionally required to deposit between 40% and 90% of their  
 2497 energy in the hadronic calorimeter within the same cone.

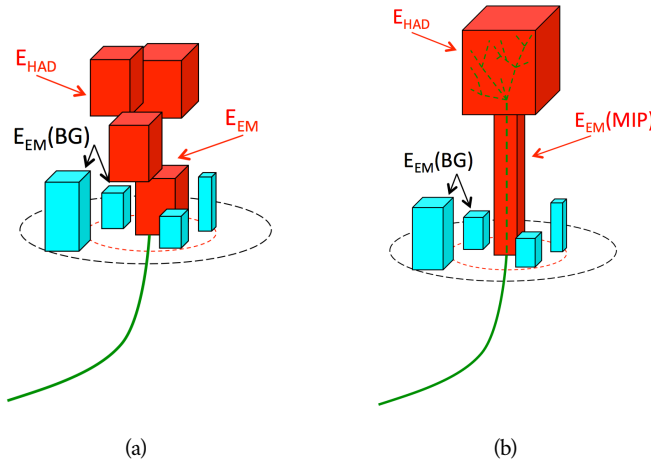


Figure 48: An illustration (a) of the geometry of energy deposits in the calorimeter. The red energy deposits come from the charged particle targeted for measurement, while the blue energy deposits are from nearby neutral particles and must be subtracted. The same diagram (b) for the neutral-background selection, described in Section 7.2.3.

2498 These particles provide a clean sample to measure the nearby neutral back-  
 2499 ground because they do not deposit energy in the area immediately surround-  
 2500 ing them in the EM calorimeter, as shown in Figure 48. So, the energy deposits in the  
 2501 region  $0.1 < \Delta R < 0.2$  can be attributed to neutral particles alone. To estimate  
 2502 the contribution to the whole cone considered for the response measurement,  
 2503 that energy is scaled by a geometric factor of  $4/3$ . This quantity,  $\langle E/p \rangle_{BG}$ , mea-  
 2504 sured in aggregate over a number of particles, gives the contribution to  $\langle E/p \rangle$   
 2505 from neutral particles in the EM calorimeter. Similar techniques were used in  
 2506 the individual layers of the hadronic calorimeters to show that the background  
 2507 from neutrals is negligible in those layers [33].

2508 The distribution of this background estimate is shown in Figure 49 for data  
 2509 and simulation with the two different physics lists. The contribution from neu-

tral particles falls from 0.1 at low momentum to around 0.03 for particles above 7 GeV. Although the simulation captures the overall trend, it significantly overestimates the neutral contribution for tracks with momentum between 2 and 8 GeV. This effect was also seen in the tails of the  $E/p$  distributions in Figure 46. This difference is likely due to modeling of coherent neutral particle radiation in Pythia8 that overestimates the production of  $\pi^0$  near the production of the charged particles. The discrepancy does not depend on  $\eta$  and thus is unlikely to be a mismodeling of the detector. This difference can be subtracted to form a corrected average of  $E/p$ .

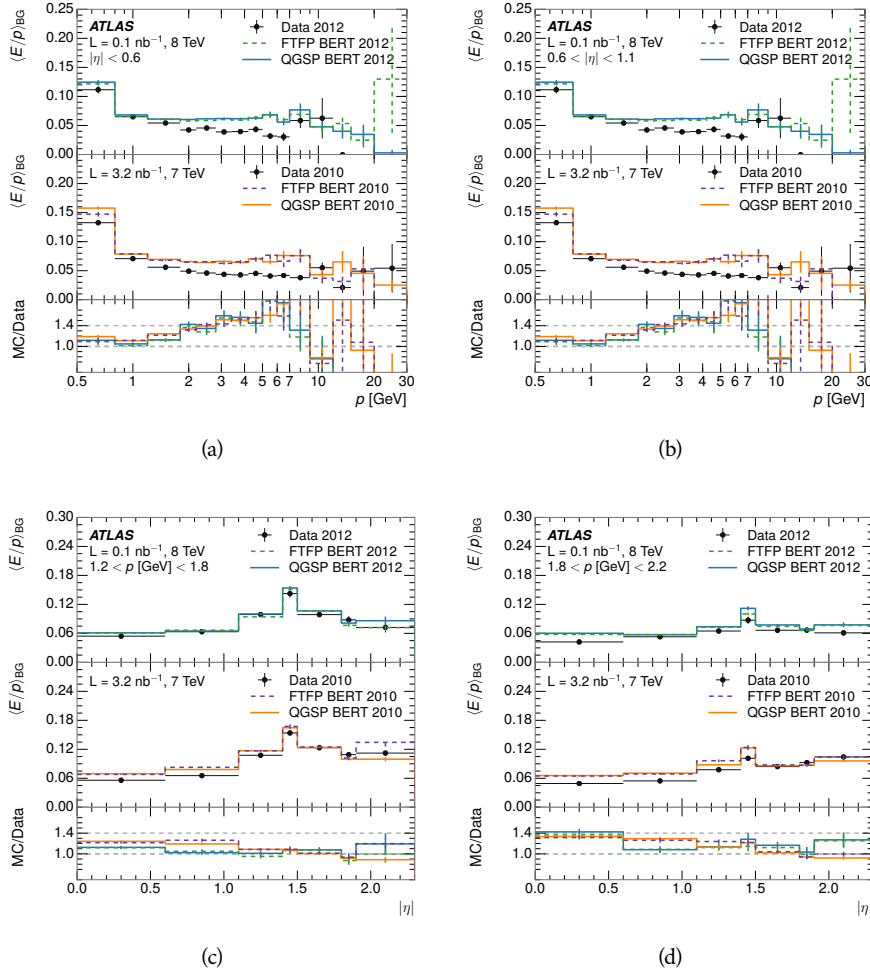


Figure 49:  $\langle E/p \rangle_{BG}$  as a function of the track momentum for tracks with (a)  $|\eta| < 0.6$ , (b)  $0.6 < |\eta| < 1.1$ , and as a function of the track pseudorapidity for tracks with (c)  $1.2 < p/\text{GeV} < 1.8$ , (d)  $1.8 < p/\text{GeV} < 2.2$ .

#### 7.2.4 CORRECTED RESPONSE

Figure 50 shows  $\langle E/p \rangle_{COR}$  as a function of momentum for several bins of pseudorapidity. This corrected  $\langle E/p \rangle_{COR} \equiv \langle E/p \rangle - \langle E/p \rangle_{BG}$  measures the average calorimeter response without the contamination of neutral particles. It is the

most direct measurement of calorimeter response in that it is the energy measured for fully isolated hadrons. The correction is performed separately in data and simulation, so that the mismodeling of the neutral background in simulation is removed from the comparison of response. The simulation overestimates the response at low momentum by about 5%, an effect that can be mostly attributed to the underestimation of the zero fraction mentioned previously. For  $|\eta| < 0.6$ , the data-simulation agreement has a larger discrepancy by about 5% for 2010 than 2012, although this is not reproduced in at higher pseudorapidity.

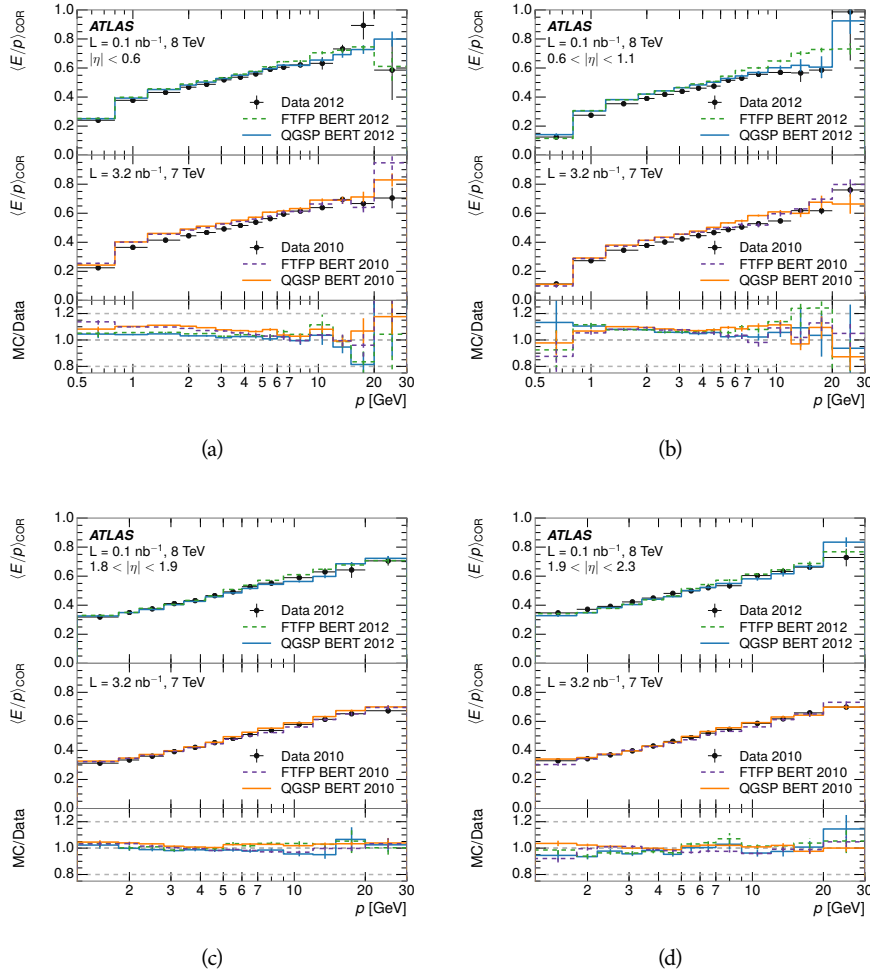


Figure 50:  $\langle E/p \rangle_{\text{COR}}$  as a function of track momentum, for tracks with (a)  $|\eta| < 0.6$ , (b)  $0.6 < |\eta| < 1.1$ , (c)  $1.8 < |\eta| < 1.9$ , and (d)  $1.9 < |\eta| < 2.3$ .

The response measurement above used topological clustering at the EM scale, that is clusters were formed to measure energy but no corrections were applied to correct for expected effects like energy lost outside of the cluster or in uninstrumented material. It is also interesting to measure  $\langle E/p \rangle_{\text{COR}}$  using LCW energies, which accounts for those effects by calibrating the energy based on the properties of the cluster such as energy density and depth in the calorimeter. Figure 51 shows these distributions for tracks with zero or more clusters and separately for tracks with one or more clusters. The calibration moves the mean

value of  $\langle E/p \rangle_{\text{COR}}$  significantly closer to 1.0 as desired, but the discrepancy between data and simulation remains in the comparison that includes tracks with zero associated clusters. The agreement between data and simulation improves noticeably when at least one cluster is required, as this removes the contribution from the mismodeling of the zero fraction.

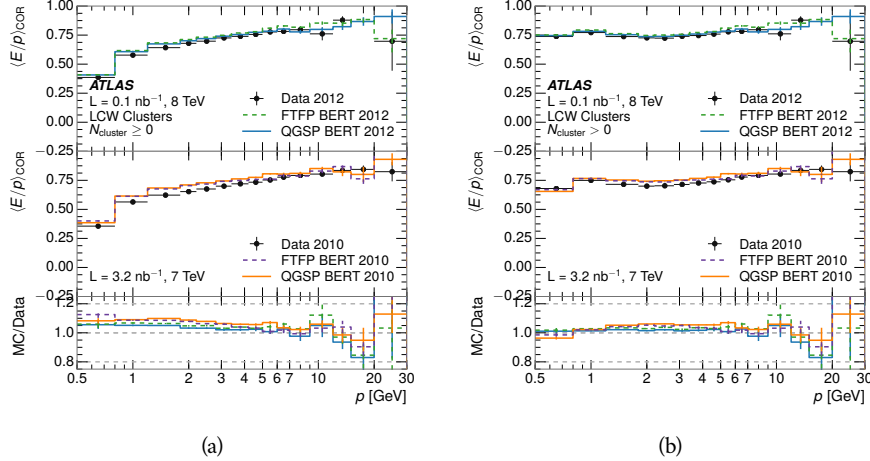


Figure 51:  $\langle E/p \rangle_{\text{COR}}$  calculated using LCW-calibrated topological clusters as a function of track momentum for tracks with (a) zero or more associated topological clusters or (b) one or more associated topological clusters.

## 7.2.5 ADDITIONAL STUDIES

As has been seen in several measurements in previous sections, the simulation does not correctly model the chance of a low momentum hadron to reach the calorimeter. Because of the consistent discrepancy across pseudorapidity and interaction lengths, this can be best explained by incomplete understanding of hadronic interactions with the detector [32]. For example, a hadron that scatters off of a nucleus in the inner detector can be deflected through a significant angle and not reach the expected location in the calorimeter. In addition, these interactions can produce secondary particles that are difficult to model.

The requirement used throughout the previous sections on the number of hits in the TRT reduces these effects by preferentially selecting tracks that do not undergo nuclear interactions. It is interesting to check how well the simulation models tracks with low numbers of TRT hits, which selects tracks that are more likely to have undergone a hadronic interaction. Figure 52 compares the distributions with  $N_{\text{TRT}} < 20$  to  $N_{\text{TRT}} > 20$  for real and simulated particles<sup>1</sup>. As expected, the tracks with fewer hits are poorly modeled in the simulation as  $\langle E/p \rangle_{\text{COR}}$  differs by as much as 25% at low momentum. They also have significantly lower  $\langle E/p \rangle_{\text{COR}}$  on average, because they are much less likely to have an associated cluster.

<sup>1</sup> The distribution with  $N_{\text{TRT}} > 20$  is the same as shown in Figure 50 (a) and is included again here for the comparison.

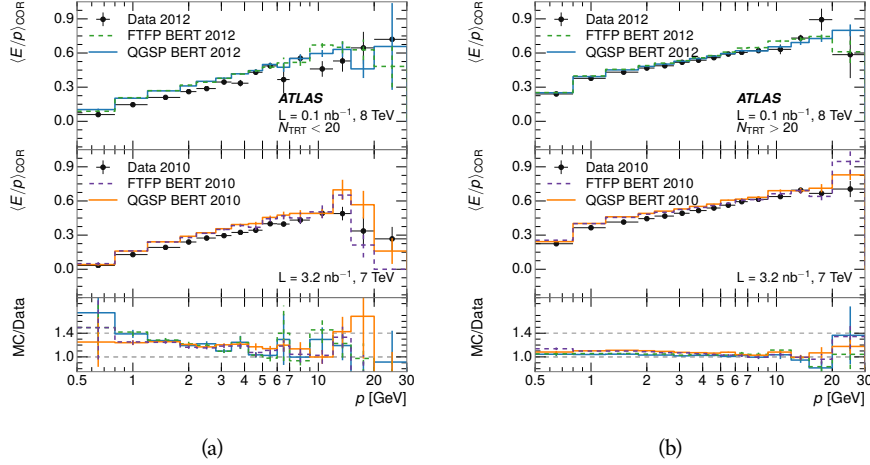


Figure 52: Comparison of the  $\langle E/p \rangle_{\text{COR}}$  for tracks with (a) less than and (b) greater than 20 hits in the TRT.

Another interesting aspect of the simulation is the description of antiprotons at low momentum, where QGSP\_BERT and FTFP\_BERT have significant differences. This can be seen to have an effect in the inclusive response measurement when separated into positive and negative charge. The  $\langle E/p \rangle_{\text{COR}}$  distributions for positive and negative particles are shown in Figure 53, where a small difference between QGSP\_BERT and FTFP\_BERT can be seen in the distribution for negative tracks. The figure also includes data, and the simulation overestimates  $\langle E/p \rangle_{\text{COR}}$  mostly due to an underestimation in zero fraction. There is an approximately 5% difference between the 2010 and 2012 simulated events. The difference between positive and negative particles is demonstrated more clearly in Figure 54, which shows the  $E/p$  distribution in the two simulations separated by charge. There is a small difference around  $E/p > 1.0$ , which can be explained by the additional energy deposited by the annihilation of the antiproton in the calorimeter that is modeled well only in FTFP\_BERT. This is also explored with data using identified antiprotons in Section 7.3.

The  $\langle E/p \rangle$  results in previous sections have considered the electromagnetic and hadronic calorimeters together as a single energy measurement, to emphasize the total energy deposited for a given particle. However, the deposits in each calorimeter are measured separately and  $\langle E/p \rangle$  can be constructed for each layer separately. As the layers are composed of different materials and are modeled separately in the detector geometry, confirmation that the simulation matches the data well in each layer adds confidence in both the description of hadronic interactions with the two different materials and also the geometric description of each.

The technique discussed in Section 7.2.3 for selecting MIPs in the electromagnetic calorimeter is also useful in studying deposits in the hadronic calorimeter. The tracks selected with the MIP requirements deposit almost all of their energy exclusively in the hadronic calorimeter. Figure 55 shows  $\langle E/p \rangle_{\text{Had}}^{\text{RAW}}$ , where RAW indicates that no correction has been applied for neutral backgrounds and

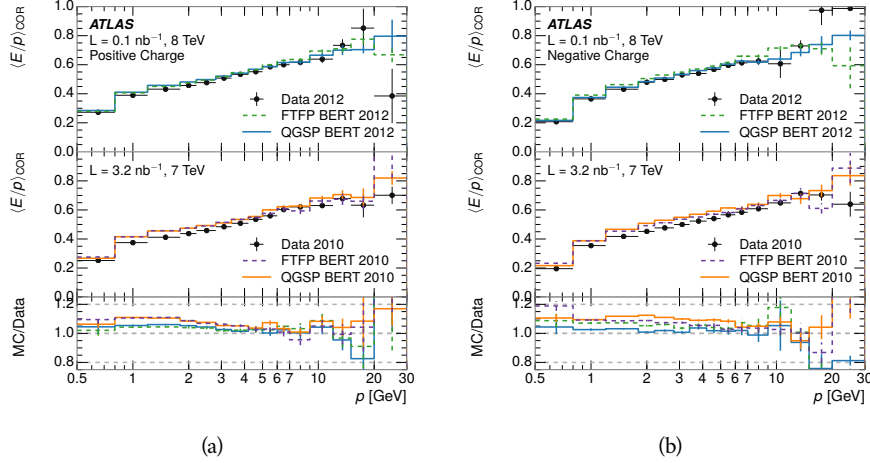


Figure 53: Comparison of the  $\langle E/p \rangle_{\text{COR}}$  for (a) positive and (b) negative tracks as a function of track momentum for tracks with  $|\eta| < 0.6$ .

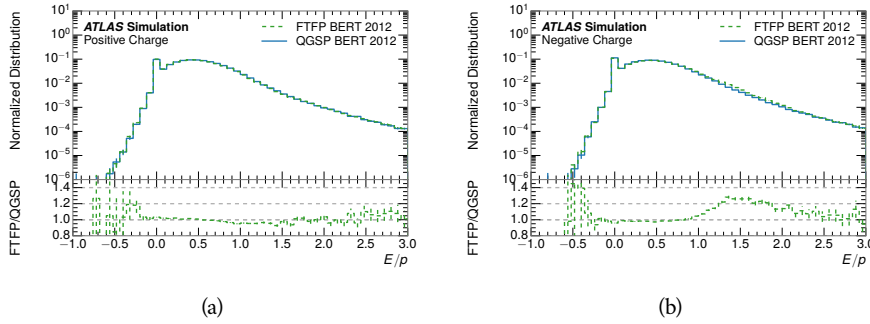


Figure 54: Comparison of the  $E/p$  distributions for (a) positive and (b) negative tracks with  $0.8 < p/\text{GeV} < 1.2$  and  $|\eta| < 0.6$ , in simulation with the FTFP\_BERT and QGSP\_BERT physics lists.

Had indicates that only clusters for the hadronic calorimeter are included<sup>2</sup>. The distributions are shown both for the original EM scale calibration and after LCW calibration. The data and simulation agree very well in this comparison, except in the lowest momentum bin where there is a 5% discrepancy that has already been seen in the measurements in Section 7.2.4.

A similar comparison can be made in the electromagnetic calorimeter by selecting particles which have no associated energy in the hadronic calorimeter. These results are measured in terms of  $\langle E/p \rangle_{\text{COR}}^{\text{EM}}$ , where EM designates that only clusters in the electromagnetic calorimeter are included and COR designates that the neutral background is subtracted as the neutral background is present in this case. Figure 56 shows the analogous comparisons to Figure 55 in the electromagnetic calorimeter. The  $\langle E/p \rangle_{\text{COR}}$  values are lower on average in the EM calorimeter than in the hadronic calorimeter, which is an expected conse-

<sup>2</sup> The RAW and COR versions of  $\langle E/p \rangle$  in this case are the same, as the neutral background is negligible in that calorimeter layer.

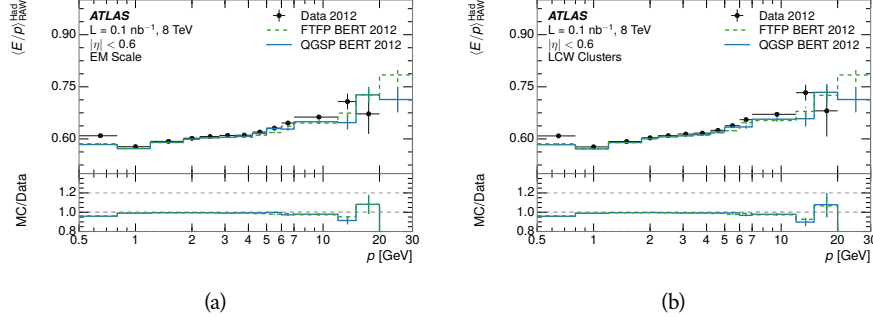


Figure 55: Comparison of the response of the hadronic calorimeter as a function of track momentum (a) at the EM-scale and (b) after the LCW calibration.

quence of their different material types (discussed in Section 5.4). In this case the disagreement between data and simulation is more pronounced, with discrepancies as high as 5% over a larger range of momenta. This level of discrepancy indicates that the description of the electromagnetic calorimeter is actually the dominant source of discrepancy in the combined distributions in Section 7.2.4.

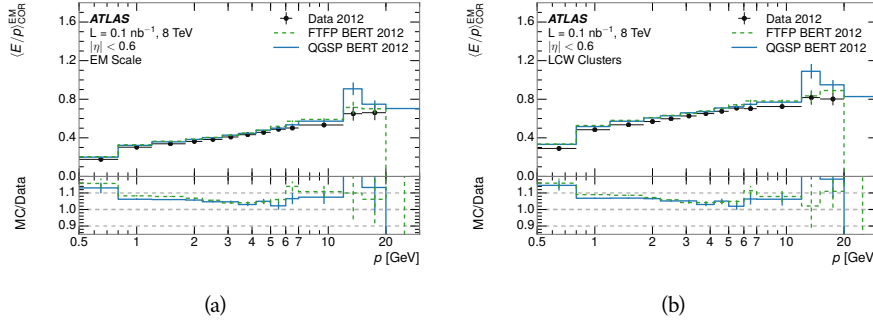


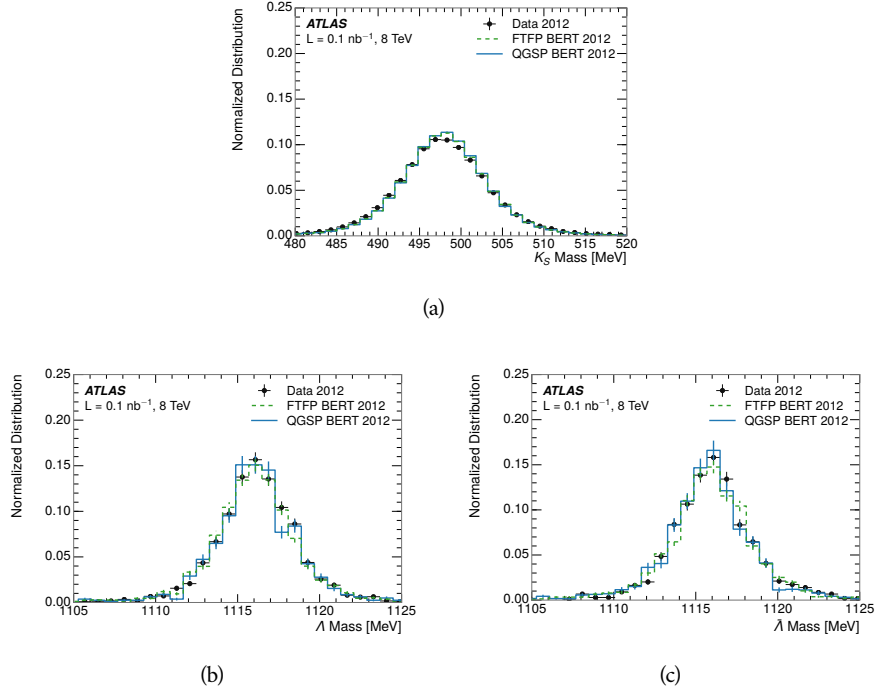
Figure 56: Comparison of the response of the EM calorimeter as a function of track momentum (a) at the EM-scale and (b) with the LCW calibration.

## 7.3 IDENTIFIED PARTICLE RESPONSE

The inclusive response measurement for hadrons can be augmented by measuring the response for specific particle species. The simulation models each particle type separately, and understanding the properties of each is important in constraining the uncertainty on jets. In order to select and measure specific hadrons, this section relies on the displaced decays of long-lived particles. Such decays can be identified by reconstructing secondary vertices with a requirement on mass. In particular,  $\Lambda$ ,  $\bar{\Lambda}$ , and  $K_S^0$  can be used to select a pure sample of protons, antiprotons, and pions, respectively.

## 2619 7.3.1 DECAY RECONSTRUCTION

2620 The measurement of the response for identified particles uses the same selection  
 2621 as for inclusive particles (Section 7.1.3) with a few additions. Each event used is  
 2622 required to have at least one secondary vertex, as described in Section 6.1.3, and  
 2623 the tracks are required to match to that vertex rather than the primary vertex.  
 2624 Pions are selected from decays of  $K_S^0 \rightarrow \pi^+ \pi^-$ , which is the dominant decay for  
 2625  $K_S^0$  to charged particles. Protons are selected from decays of  $\Lambda \rightarrow \pi^- p$  and an-  
 2626 tiprotons from  $\bar{\Lambda} \rightarrow \pi^+ \bar{p}$ , which are similarly the dominant decays of  $\Lambda$  and  $\bar{\Lambda}$   
 2627 to charged particles. The species of parent hadron in these decays is determined  
 2628 by reconstructing the mass of the tracks associated to the secondary vertex. The  
 2629 sign of the higher momentum decay particle can distinguish between  $\Lambda$  and  $\bar{\Lambda}$ ,  
 2630 which of course have the same mass, as the proton or antiproton is kinemati-  
 2631 cally favored to have higher momentum. The proton or antiproton will carry  
 2632 the higher momentum above 95% of the time. Examples of the reconstructed  
 2633 masses used to select these decays are shown in Figure 57. The mass peaks in  
 2634 data and both simulation models are very similar.



2635 Figure 57: The reconstructed mass peaks of (a)  $K_S^0$ , (b)  $\Lambda$ , and (c)  $\bar{\Lambda}$  candidates.  
 2636

2637 The dominant backgrounds for the identified particle decays are nuclear in-  
 2638 teractions and combinatoric sources. These are suppressed by the kinematic re-  
 2639 quirements on the tracks as well as an additional veto which removes candidates  
 2640 that are consistent with both a  $\Lambda$  or  $\bar{\Lambda}$  and a  $K_S^0$  hypothesis, which is possible  
 2641 because of the different assumptions on particle mass in each case [33]. After  
 2642 these requirements, the backgrounds are found to be negligible compared to the  
 2643 statistical errors on these measurements.

## 2642 7.3.2 IDENTIFIED RESPONSE

2643 With these techniques the  $E/p$  distributions are extracted in data and simulation  
 2644 for each particle species and shown in Figure 58. These distributions are shown  
 2645 for a particular bin of  $E_a$  ( $2.2 < E_a/\text{GeV} < 2.8$ ), rather than  $p$ .  $E_a$  is the energy  
 2646 available to be deposited in the calorimeter: for pions  $E_a = \sqrt{p^2 + m_\pi^2}$ , for pro-  
 2647 tons  $E_a = \sqrt{p^2 + m_p^2} - m_p$ , and for antiprotons  $E_a = \sqrt{p^2 + m_p^2} + m_p$ . In the  
 2648 pion case, the entire energy of the pion is deposited in the calorimeter, so  $E_a$  is  
 2649 just the usual energy. For protons, the proton remains after depositing its energy  
 2650 in the calorimeter, so its mass is not available and must be subtracted from  $E_a$ .  
 2651 And for antiprotons, the antiproton constituents annihilate with the quarks in  
 2652 the protons and neutrons of the calorimeter material, so it deposits its entire en-  
 2653 ergy as well as an the additional energy from the annihilation; this extra energy  
 2654 is equal to the mass of the antiproton and is added to the available energy. The  
 2655 features of the  $E/p$  distributions are similar to the inclusive case, with a peak  
 2656 around 0.5 at low momentum. The zero fraction is not as pronounced as in the  
 2657 inclusive case. There is a small negative tail from noise and a large fraction of  
 2658 tracks with zero energy from particles which do not reach the calorimeter. The  
 2659 long positive tail is noticeably more pronounced for antiprotons because of the  
 2660 additional energy generated by the annihilation of the antiproton with the mate-  
 2661 rial of the detector, and the peak of the distribution is also increased for the same  
 2662 reason. The simulation correctly captures these features, and the agreement be-  
 2663 tween data and simulation is good to within the available statistical limitations.

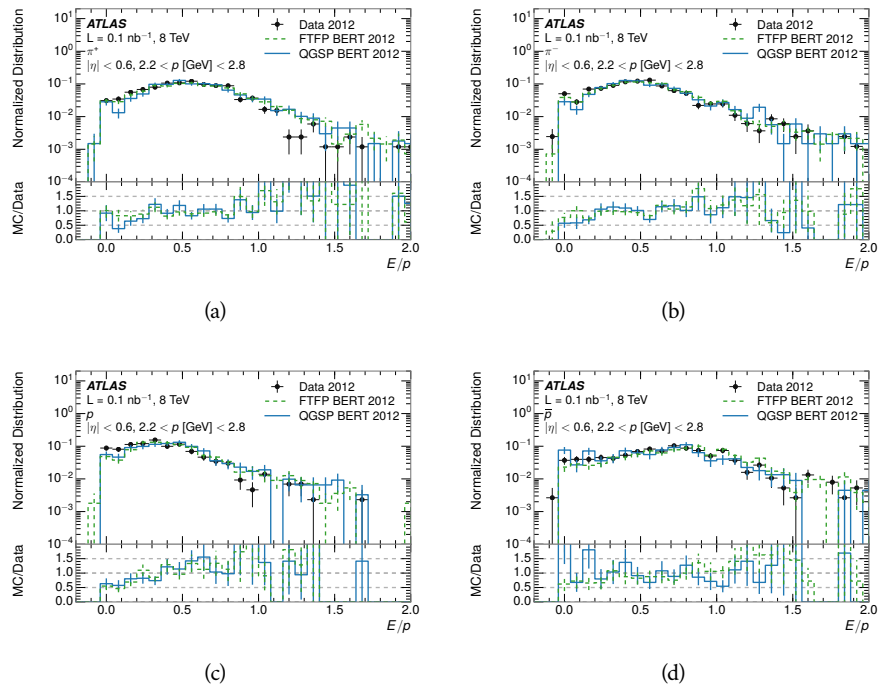


Figure 58: The  $E/p$  distribution for isolated (a)  $\pi^+$ , (b)  $\pi^-$ , (c) proton, and (d) anti-proton tracks.

The zero fraction is further explored in Figure 59 for pions and protons in data and simulation. The simulation consistently underestimates the zero fraction independent of particle species, which implies that this discrepancy is not caused by the model of a particular species but rather a feature common to all. The zero fraction is larger for  $\pi^-$  than  $\pi^+$ , which is evident in both data and simulation. However there is some suggestion that this increase in zero fraction leads to an even larger discrepancy in the modeling of  $\pi^-$  in simulation.

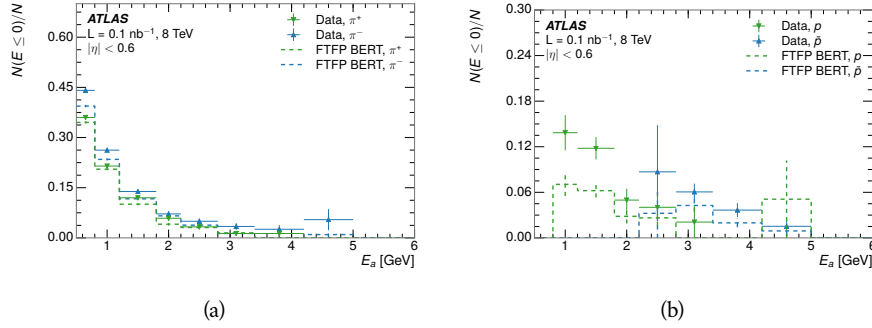


Figure 59: The fraction of tracks with  $E \leq 0$  for identified (a)  $\pi^+$  and  $\pi^-$ , and (b) proton and anti-proton tracks

It is also interesting to compare the response between the different particle species. One approach to do this is to measure the difference in  $\langle E/p \rangle$  between two types, which has the advantage of removing the neutral background. These differences are shown in various combinations in Figure 60. The response for  $\pi^+$  is greater on average than the response to  $\pi^-$  because of a charge-exchange effect which causes the production of additional neutral pions in the showers of  $\pi^+$  [55]. This effect becomes less significant as the  $\langle E/p \rangle$  increases, and the difference approaches zero. Both version of the simulation correctly model this trend. The response for  $\pi^+$  is also greater on average than the response to  $p$ , because a large fraction of the energy of  $\pi^+$  hadrons is converted to an electromagnetic shower [56, 57]. This effect is again reproduced by both simulations. The  $\bar{p}$  response, however, is significantly higher than the response to  $\pi^-$  because of the annihilation of the antiproton, but the difference decreases at higher energies where the additional energy has less relative importance. FTFP\_BERT models this effect more accurately than QGSP\_BERT because of their different descriptions of  $\bar{p}$  interactions with material.

It is also possible to remove the neutral background from these response distributions using the same technique as in Section 7.2.3. The technique is largely independent of the particle species and so can be directly applied to  $\langle E/p \rangle$  for pions. The  $\langle E/p \rangle_{\text{COR}}$  distributions for pions are shown in Figure 61, which are very similar to the inclusive results. The inclusive hadrons are comprised mostly of pions, so this similarity is not surprising. It is also possible to see the small differences between  $\pi^+$  and  $\pi^-$  response here, where  $\langle E/p \rangle_{\text{COR}}$  is higher on average for  $\pi^+$ . The agreement between data and simulation is significantly worse for the  $\pi^-$  distributions than for the  $\pi^+$ , with a discrepancy greater than 10% below 2-3 GeV.

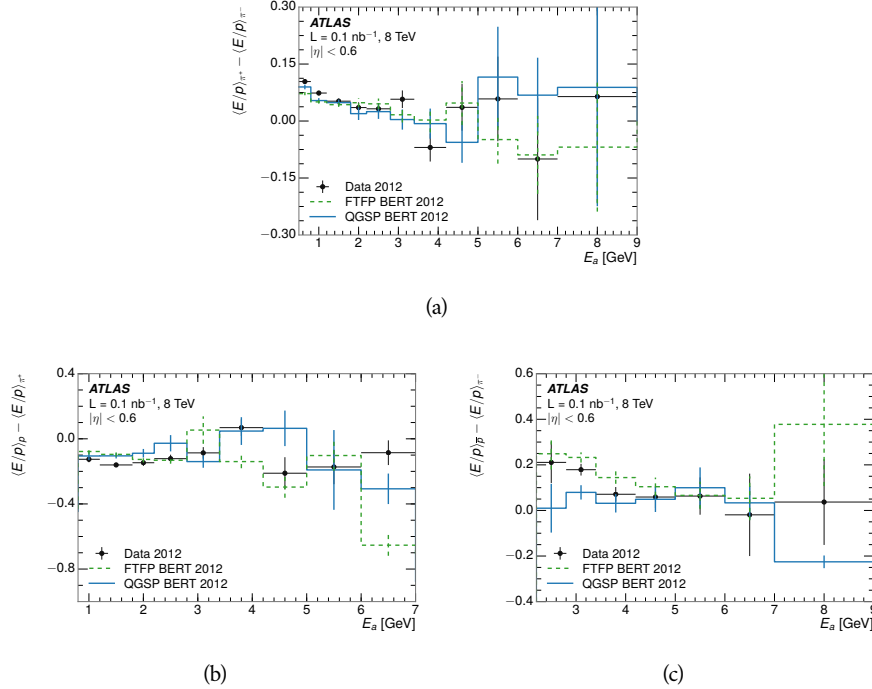


Figure 60: The difference in  $\langle E/p \rangle$  between (a)  $\pi^+$  and  $\pi^-$  (b)  $p$  and  $\pi^+$ , and (c)  $\bar{p}$  and  $\pi^-$ .

2697 7.3.3 ADDITIONAL SPECIES IN SIMULATION

2698 The techniques above provide a method to measure the response separately for  
 2699 only pions and protons. However the hadrons which forms jets include a number  
 2700 of additional species such as kaons and neutrons. The charged kaons are an im-  
 2701 portant component of the inclusive charged hadron distribution, which is com-  
 2702 prised of roughly 60-70% pions, 15-20% kaons, and 5-15% protons [32]. These  
 2703 fractions vary depending on the production mechanism, and the ranges are in-  
 2704 dicative of the variations between different events. These are difficult to measure  
 2705 in data at the ATLAS detector, as the particles which decay to kaons such as  $\phi$  and  
 2706  $D$  mesons have shorter lifetimes and are comparatively rare. These properties  
 2707 make it impractical to identify a sufficient number of decays to make statistically  
 2708 meaningful measurements. The simulation of these particles includes noticeable  
 2709 differences in response between species at low energies, which are shown in Fig-  
 2710 ure 62 for FTFP\_BERT. The significant differences in response between protons  
 2711 and antiprotons below 1 GeV are accounted for above in the definitions of  $E_a$ .

2712 7.4 SUMMARY

2713 These various measurements of calorimeter response shown above for data and  
 2714 simulation illuminate the accuracy of the simulation of hadronic interactions at  
 2715 the ATLAS detector. The results were obtained using 2010 and 2012 data at 7  
 2716 and 8 TeV, but reflect the most current understanding of the detector alignment

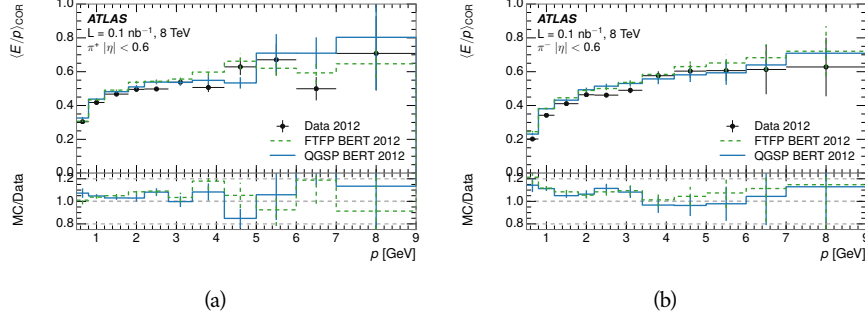


Figure 61:  $\langle E/p \rangle_{\text{COR}}$  as a function of track momentum for (a)  $\pi^+$  tracks and (b)  $\pi^-$  tracks.

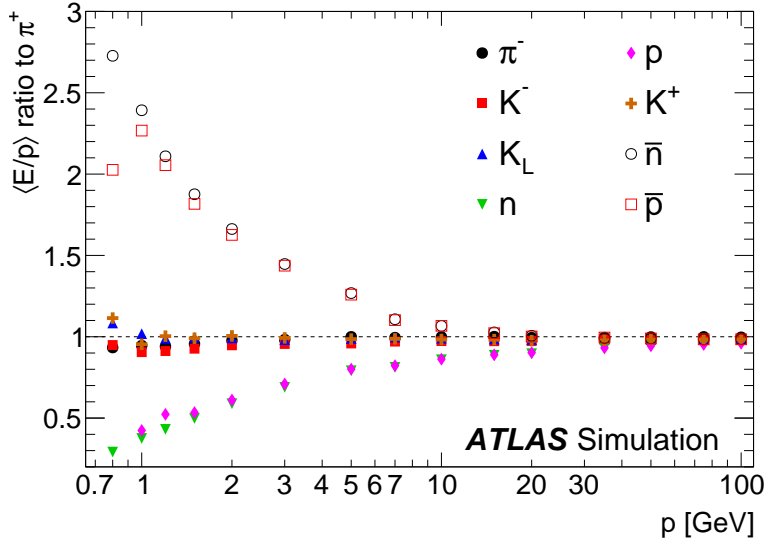


Figure 62: The ratio of the calorimeter response to single particles of various species to the calorimeter response to  $\pi^+$  with the physics list FTFP\_BERT.

and geometry. A number of measurements focusing on a comparison between protons and antiprotons suggest that FTFP\_BERT models those interaction more accurately than QGSP\_BERT. These measurements, among others, were the motivation to switch the default Geant4 simulation from QGSP\_BERT to FTFP\_BERT for all ATLAS samples.

Even with these updates, there are a number of approximately 5% discrepancies in response between the data and simulation. The differences result mostly from a difference in the modeling of the zero fraction, which is most significant at low energies. The difference in response without the zero fraction are primarily in the electromagnetic calorimeter, while the modeling of the hadronic calorimeter is accurate. At higher momenta the simulation of hadronic interactions is very consistent with data. Chapter 8 discusses how to use these observed differences to constrain the jet energy scale and its associated uncertainties.

2730

2731 JET ENERGY RESPONSE AND UNCERTAINTY

---

## 2732 8.1 MOTIVATION

2733 As jets form a major component of many physics analyses at ATLAS, it is crucial  
2734 to carefully calibrate the measurement of jet energies and to derive an uncer-  
2735 tainty on that measurement. These uncertainties are often the dominant sys-  
2736 tematic uncertainty in high-energy analyses at the LHC. Jet balance techniques,  
2737 as discussed in Section 6.4.3, provide a method to constrain the JES and its uncer-  
2738 tainty in data, and provide the default values used for ATLAS jet measurements at  
2739 most energies [58]. These techniques are limited by their reliance on measuring  
2740 jets in data, so they are statistically limited in estimating the jet energy scale at the  
2741 highest jet energies. This chapter presents another method for estimating the jet  
2742 energy scale and its uncertainty which builds up a jet from its constituents and  
2743 thus can be naturally extended to high jet momentum. Throughout this chapter  
2744 the jets studied are simulated using Pythia8 with the CT10 parton distribution  
2745 set [59] and the AU2 tune [36], and corrections are taken from the studies includ-  
2746 ing data and simulation in Chapter 7.

2747 As described in Section 6.4, jets are formed from topological clusters of energy  
2748 in the calorimeters using the anti- $k_t$  algorithm. These clusters originate from a  
2749 diverse spectrum of particles, in terms of both species and momentum, leading to  
2750 significantly varied jet properties and response between jets of similar produced  
2751 momentum. Figure 63 shows the momentum and particle distributions of sim-  
2752 ultated particles within jets at a few examples energies. Each bin for each distri-  
2753 bution shows the fraction of jet constituents of that particle type and that truth  
2754 energy for a jet of the specified energy. These show that majority of particles in  
2755 jets are charged pions and photons, and the charged pions constituent carry the  
2756 highest energies on average. The figure also demonstrates that the majority of  
2757 the particles in a jet have much lower momentum than the jet itself; for example  
2758 in 90-100 GeV jets less than 1% of particles have energies above 20 GeV. The  
2759  $E/p$  measurements provide a thorough understanding of the dominant particle  
2760 content of jets, the charged hadrons.

## 2761 8.2 UNCERTAINTY ESTIMATE

2762 A correct modeling of jets in the data by simulation requires that both the parti-  
2763 cle production inside jets as well as the response of the calorimeter to particles  
2764 are correctly modeled. Chapter 7 showed that the simulation does not perfectly  
2765 model the calorimeter response, and provided measurements that can be used  
2766 to correct for discrepancies. To determine the corrections appropriate for jets,  
2767 that is to evaluate a jet energy response, the simulated jet energies are compared

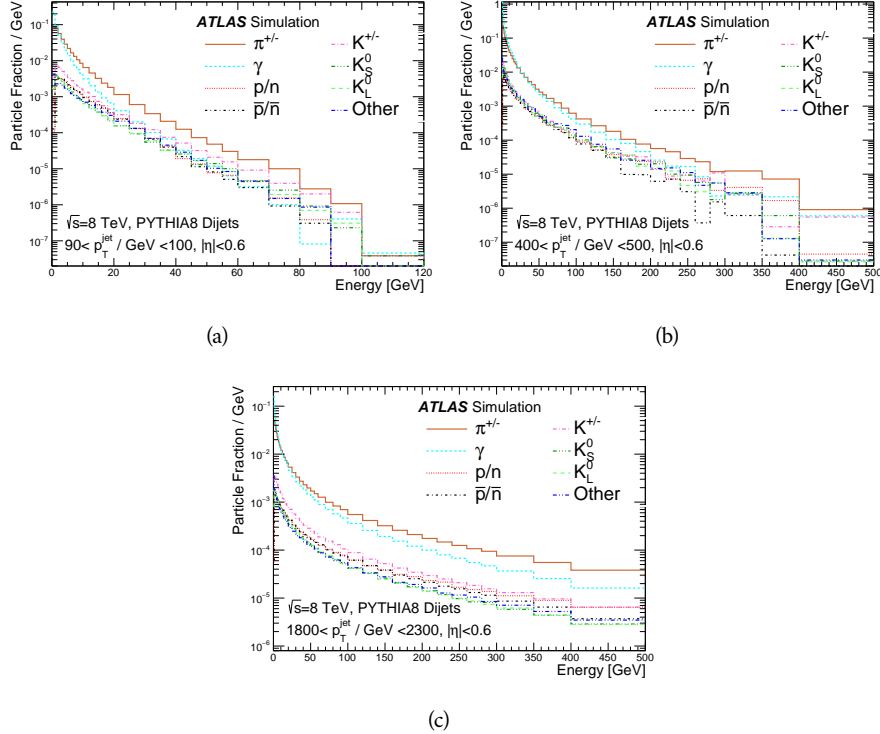


Figure 63: The spectra of true particles inside anti- $k_t$ ,  $R = 0.4$  jets with (a)  $90 < p_T/\text{GeV} < 100$ , (b)  $400 < p_T/\text{GeV} < 500$ , and (c)  $1800 < p_T/\text{GeV} < 2300$ .

2768 to a corrected jet built up at the particle level. Each cluster in a jet is associated  
2769 to the truth particle which deposited it, and the energy in that cluster is then  
2770 corrected for a number of effects based on measurements in data. The primary  
2771 corrections come from the single hadron response measurements in addition to  
2772 response measured using the combined test beam which covers higher momen-  
2773 tum particles [60]. These corrections include both a shift ( $\Delta$ ), in order to make  
2774 the simulation match the average response in data, and an uncertainty ( $\sigma$ ) asso-  
2775 ciated with the ability to constrain the difference between data and simulation.  
2776 Some of the dominant sources of uncertainty are itemized in Table 8 with typi-  
2777 cal values, and the full list considered is described in detail in the associated pa-  
2778 per [32]. These uncertainties cover differences between the data and simulation  
2779 in the modeling of calorimeter response to a given particle. The typical values  
2780 are listed as ranges to show the variation over momentum and pseudorapidity.  
2781 For the in situ  $E/p$  term, for example,  $\Delta$  corresponds to the difference between  
2782 data and simulation for  $\langle E/p \rangle_{\text{COR}}$  at the LCW scale (shown in Figure 51 (b)) and  
2783  $\sigma$  is the uncertainty on that difference including the statistical uncertainties of  
2784 both the data and simulated events. No uncertainties are added for the differ-  
2785 ence between particle composition of jets in data and simulation, as this method  
2786 focuses on providing a response correction for discrepancies of particle interac-  
2787 tions rather than differences in particle composition.

From these terms, the jet energy scale and uncertainty is built up from individual energy deposits in simulation. Each uncertainty term is treated inde-

Abbrev.	Description	$\Delta$ (%)	$\sigma$ (%)
In situ $E/p$	The comparison of $\langle E/p \rangle_{\text{COR}}$ , at the <a href="#">LCW</a> scale, as described in Chapter 7 with statistical uncertainties from 500 MeV to 20 GeV.	0-3	1-5
CTB	The main $\langle E/p \rangle$ comparison uncertainties, binned in $p$ and $ \eta $ , as derived from the combined test beam results, from 20 to 350 GeV [60].	0-3	1-5
$E/p$ Zero Fraction	The difference in the zero-fraction between data and MC simulation from 500 MeV to 20 GeV.	5-25	1-5
$E/p$ Threshold	The uncertainty in the EM calorimeter response from the potential mismodeling of threshold effects in topological clustering.	0	0-10
Neutral	The uncertainty in the calorimeter response to neutral hadrons based on studies of physics model variations.	0	5-10
$K_L$	An additional uncertainty in the response to neutral $K_L$ in the calorimeter based on studies of physics model variations.	0	20
$E/p$ Misalignment	The uncertainty in the $p$ measurement from misalignment of the ID.	0	1
Hadrons, $p > 350$ GeV	An energy independent uncertainty for all particles above the energy range or outside the longitudinal range probed with the combined test beam.	0	10

Table 8: The dominant sources of corrections and systematic uncertainties in the [JES](#) estimation technique, including typical values for the correcting shift ( $\Delta$ ) and the associated uncertainty ( $\sigma$ ).

pendently, and is taken to be gaussian distributed. The resulting scale and uncertainty is shown in Figure 64, where the mean response is measured relative to the calibrated energy reported by simulation. The mean response is slightly below one, indicating that the simulation slightly overestimates the calorimeter response on average, and this response is relatively constant as a function of the jet  $p_T$ . The dominant uncertainties come from the statistical uncertainties on the  $E/p$  measurements at lower energies and the additional uncertainty for out of range measurements at higher energies. Combined the resulting uncertainty ranges from between 1.5% at low momentum and pseudorapidity to as much as 4% at higher momentum and pseudorapidity. The total uncertainty from this method at intermediate jet energies is comparable to other simulation-based methods [61] and is about twice as large as in-situ methods using data [58]. This method is the only one which provides an estimation above 1.8 TeV, however, and so is still a crucial technique in analyses that search for very energetic jets.

These techniques can also be used to measure the correlation between bins of average reconstructed jet momentum across a range of  $p_T$  and  $|\eta|$ , where correlations are expected because of a similarity in particle composition at similar energies. Figure 65 shows these correlations, where the uncertainties on jets in neighboring bins are typically between 30% and 60% correlated. The uncertainty on all jets becomes significantly correlated at high energies and larger pseudorapidities, when the uncertainty becomes dominated by the single term reflecting out of range particles.

### 8.3 SUMMARY

The technique described above provides a jet energy scale and uncertainty by building up jet corrections from the energy deposits of constituent particles. The  $E/p$  measurements are crucial in providing corrections for the majority of particles in the jets. The uncertainty derived this way is between 2 and 5% and is about twice as large at corresponding momentum than jet balance methods. However this is the only uncertainty available for very energetic jets using 2012 data and simulation, and repeating this method with Run 2 data and simulation will be important in providing an uncertainty for the most energetic jets in 13 TeV collisions.

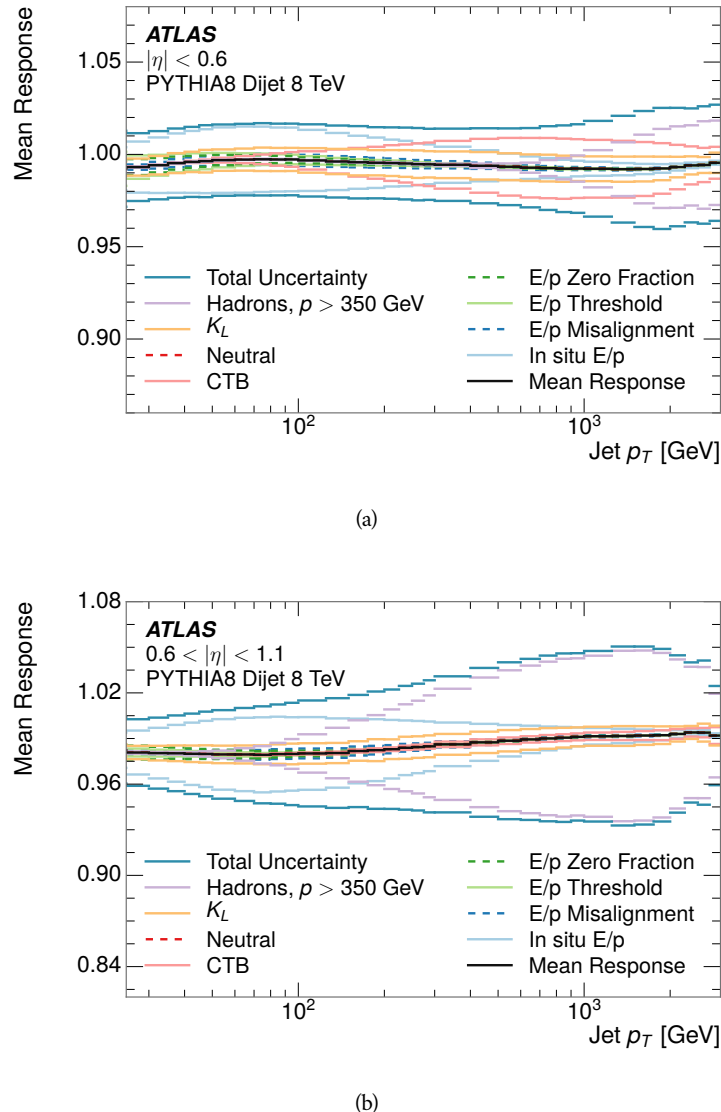


Figure 64: The JES response uncertainty contributions, as well as the total JES uncertainty, as a function of jet  $p_T$  for (a)  $|\eta| < 0.6$  and (b)  $0.6 < |\eta| < 1.1$ .

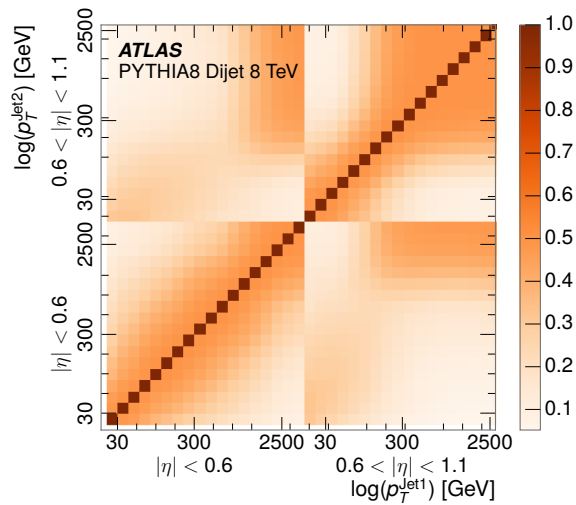


Figure 65: The correlations between bins of average reconstructed jet momentum as a function of jet  $p_T$  and  $|\eta|$  for jets in the central region of the detector.

2823

## PART V

2824

### SEARCH FOR LONG-LIVED PARTICLES

2825

You can put some informational part preamble text here.

2826

2827 LONG-LIVED PARTICLES IN ATLAS

---

2828 As discussed in Section 2.6, various limitations in the SM suggest a need for new  
 2829 particles at the TeV scale. A wide range of extensions to the Standard Model  
 2830 predict that these new particles can have lifetimes greater than approximately  
 2831 one-hundredth of a nanosecond. These include theories with universal extra-  
 2832 dimensions [62, 63], with new fermions [64], and with leptoquarks [65]. As dis-  
 2833 cussed in Section 3.3, many SUSY theories also produce these LLPs, in both R-  
 2834 Parity violating [66–68] and R-Parity conserving [69–72] formulations. Split su-  
 2835 persymmetry [5, 6], for example, predicts long-lived gluinos with O(TeV) masses.  
 2836 This search focuses specifically on the SUSY case, but many of the results are  
 2837 generic to any model with LLPs.

2838 Long-lived gluinos or squarks carry color-charge and will thus hadronize into  
 2839 color neutral bound states called R-Hadrons. These are composit particles like  
 2840 the usual hadrons but with one supersymmetric constituent, for example  $\tilde{g}q\bar{q}$   
 2841 and  $\tilde{q}\bar{q}$ . Through this hadronization process, the neutral gluino can acquire a  
 2842 charge. Gluino pair production,  $pp \rightarrow \tilde{g}\tilde{g}$  has the largest cross sectional increase  
 2843 with the increase in energy to 13 TeV, and so this search focuses on gluino R-  
 2844 Hadrons. Planned future updates will extend the case to explicitly include squark  
 2845 and chargino models, but the method covers any long-lived, charged, massive  
 2846 particle.

## 2847 9.1 EVENT TOPOLOGY

2848 The majority of SUSY models predict that gluinos will be produced in pairs at  
 2849 the LHC, through processes like  $pp \rightarrow q\bar{q} \rightarrow \tilde{g}\tilde{g}$  and  $pp \rightarrow gg \rightarrow \tilde{g}\tilde{g}$ , where the  
 2850 gluon mode dominates for the collision energy and gluino masses considered  
 2851 for this search. During their production, the long-lived gluinos hadronize into  
 2852 color singlet bound states including  $\tilde{g}q\bar{q}$ ,  $\tilde{g}qqq$ , and even  $\tilde{g}g$  [73]. The probability  
 2853 to form the gluon-only bound states is a free parameter usually taken to be 0.1,  
 2854 while the meson states are favored among the R-Hadrons [74]. The charged and  
 2855 neutral states are approximately equally likely for mesons, so the R-Hadrons will  
 2856 be charged roughly 50% of the time.

2857 These channels produce R-Hadrons with large  $p_T$ , comparable to their mass,  
 2858 so that they typically propagate with  $0.2 < \beta < 0.9$  [74]. The fragmentation that  
 2859 produces that hadrons is very hard, so the jet structure around the R-Hadron  
 2860 is minimal, with less than 5 GeV of summed particle momentum expected in a  
 2861 cone of  $\Delta R < 0.25$  around the R-Hadron [74]. After hadronization, depending  
 2862 on the gluino lifetime, the R-Hadrons then decay into hadrons and a LSP [73].

2863 In summary, the expected event for pair-produced long-lived gluinos is very  
 2864 simple: two isolated, high-momentum R-Hadrons that propagate through the  
 2865 detector before decaying to jets. The observable features of such events depend

2866 strongly on the interaction of the R-Hadron with the material of the detector  
 2867 and also its lifetime. Section 9.1.1 describes the interactions of R-Hadrons which  
 2868 reach the various detector elements in ATLAS and Section 9.1.2 provides a sum-  
 2869 mary of the observable event descriptions for R-Hadrons of various lifetimes.

2870 9.1.1 DETECTOR INTERACTIONS

2871 After approximately 0.2 ns, the R-Hadron reaches the pixel detector. If charged,  
 2872 it deposits energy into the material through repeated single collisions that result  
 2873 in ionization of the silicon substrate [3]. Because of its comparatively low  $\beta$ , the  
 2874 ionization energy can be significantly greater than expected for SM particles be-  
 2875 cause the most-probable energy loss grows significantly as  $\beta$  decreases [3]. This  
 2876 large ionization can be measured through the ToT read out from the pixel detec-  
 2877 tor as described in Section 6.1.2. Large ionization in the inner detector is one of  
 2878 the major characteristic features of LLPs.

2879 Throughout the next few nanoseconds, the R-Hadron propagates through the  
 2880 remainder of the inner detector. A charged R-Hadron will provide hits in each  
 2881 of these systems as would any other charged particle, and can be reconstructed  
 2882 as a track. The track reconstruction provides a measurement of its trajectory  
 2883 and thus its momentum as described in Section 6.1. The large momentum is  
 2884 another characteristic feature of massive particles produced at the LHC. **Note: At**  
 2885 **this point I am failing to mention that the TRT provides a possible dE/dx**  
 2886 **measurement, because no one uses it as far as I know.**

2887 As of roughly 20 ns, the R-Hadron enters the calorimeter where it interacts  
 2888 hadronically with the material. Because of its large mass and momentum, the  
 2889 R-Hadron does not typically stop in the calorimeter, but rather deposits a small  
 2890 fraction of its energy through repeated interactions with nucleons. The proba-  
 2891 bility of interaction between the gluino itself and a nucleon is low because the  
 2892 cross section drops off with the inverse square of its mass, so the interactions are  
 2893 primarily governed by the light constituents [75]. Each of these interactions can  
 2894 potentially change that quark content and thus change the sign of the R-Hadron,  
 2895 so that the charge at exit is typically uncorrelated with the charge at entry [74].  
 2896 The total energy deposited in the calorimeters during the propagation is small  
 2897 compared to the kinetic energy of the R-Hadron, around 20-40 GeV, so that  
 2898  $E/p$  is typically less than 0.1 [74].

2899 Then, 30 ns after the collision, it reaches the muon system, where it again  
 2900 ionizes in the material if charged and can be reconstructed as a muon track. Be-  
 2901 cause of the charge-flipping interactions in the calorimeter, this track may have  
 2902 the opposite sign of the track reconstructed in the inner detector, or there may  
 2903 be a track present when there was none in the inner detector and vice-versa. The  
 2904 propagation time at the typically lower  $\beta$  results in a significant delay compared  
 2905 to muons, and that delay can be assessed in terms of a time-of-flight measure-  
 2906 ment. Because of the probability of charge-flip and late arrival, there is a signif-  
 2907 icant chance that an R-Hadron which was produced with a charge will not be  
 2908 identified as a muon. The long time-of-flight is another characteristic feature of  
 2909 R-Hadrons which are reconstructed as muons.

## 2910 91.2 LIFETIME DEPENDENCE

2911 The above description assumed a lifetime long enough for the R-Hadron to exit  
 2912 the detector, which through this search is referred to as “stable”, even though  
 2913 the particle may decay after exiting the detector. There are several unique sig-  
 2914 natures at shorter lifetimes where the R-Hadron decays in various parts of the  
 2915 inner detector; these lifetimes are referred to as “metastable”.

2916 The shortest case where the R-Hadron is considered metastable is for life-  
 2917 times around 0.01 ns, where the particle decays before reaching any of the de-  
 2918 tector elements. Although the R-Hadrons are produced opposite each other in  
 2919 the transverse plane, each R-Hadron decays to a jet and an LSP. The LSPs are not  
 2920 measured, so the produced jets can be significantly imbalanced in the transverse  
 2921 plane which results in large missing energy. That missing energy can be used  
 2922 to trigger candidate events, and provides the most efficient trigger option for  
 2923 shorter lifetimes. Additionally, the precision of the tracking system allows the  
 2924 displaced vertex of the R-Hadron decay to be reconstructed from the charged  
 2925 particles in the jet. The distance of that vertex from the interaction point can  
 2926 be used to distinguish R-Hadron decays from other processes. Figure 66 shows  
 2927 a schematic diagram of an example R-Hadron event with such a lifetime. The  
 2928 diagram is not to scale, but instead illustrates the detector interactions in the  
 2929 pixel detector, calorimeters, and muon system. It includes a representation of  
 2930 the charged R-Hadron and the neutral R-Hadron, as well as the LSPs and jets  
 2931 (shown as charged hadrons) produced in the decay. Neutral hadrons may also  
 2932 be produced in the decay but are not depicted. Previous searches on ATLAS have  
 2933 used the displaced vertex to target LLP decays [76].

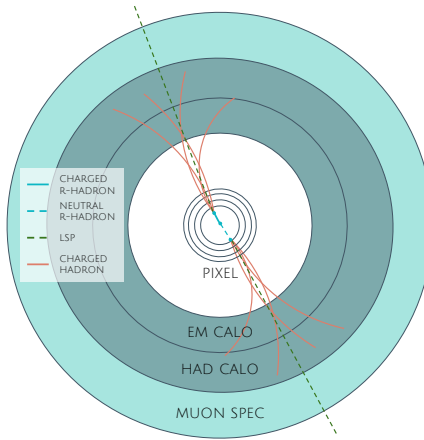


Figure 66: A schematic diagram of an R-Hadron event with a lifetime around 0.01 ns.

The diagram includes one charged R-Hadron (solid blue), one neutral R-Hadron (dashed blue), LSPs (dashed green) and charged hadrons (solid orange). The pixel detector, calorimeters, and muon system are illustrated but not to scale.

2934 The next distinguishable case occurs at lifetimes greater than 0.1 ns, where  
 2935 the R-Hadron forms a partial track in the inner detector. If the decay products  
 2936 are sufficiently soft, they may not be reconstructed, and this forms a unique sig-

2937 nature of a disappearing track. An example of such an event is illustrated in  
 2938 Figure 67, which shows the short track in the inner detector and the undetected  
 2939 soft charged hadron and LSP that are produced. A dedicated search on ATLAS used  
 2940 the disappearing track signature to search for LLP in Run 1 [77]. ***zNote: might***  
 2941 ***not be worth mentioning the disappearing track here since it is actually a***  
 2942 ***chargino search, the soft pion is pretty unique to charginos.***

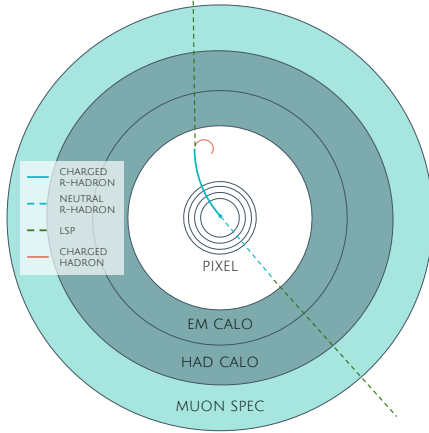


Figure 67: A schematic diagram of an R-Hadron event with a lifetime around 4 ns. The diagram includes one charged R-Hadron (solid blue), one neutral R-Hadron (dashed blue), LSPs (dashed green) and a charged hadron (solid orange). The pixel detector, calorimeters, and muon system are illustrated but not to scale.

2943 If the decay products are not soft, the R-Hadron daughters form jets, resulting  
 2944 in an event-level signature of up to two high-momentum tracks, jets, and signif-  
 2945 icant missing energy. The missing energy has the same origin as in the case of  
 2946 0.01 ns lifetimes, from the decay to unmeasured particles, and again can be large.  
 2947 The high-momentum tracks will also have the characteristically high-ionization  
 2948 of massive, long-lived particles in the inner detector. Figure 68 illustrates an ex-  
 2949 ample event with one charged R-Hadron which decays after approximately 10 ns,  
 2950 and shows how the jets from the decay can still be reconstructed in the calorime-  
 2951 ter. Several previous searches on ATLAS from Run 1 have used this signature to  
 2952 search for R-Hadrons [78, 79], including a dedicated search for metastable parti-  
 2953 cles [80].

2954 If the lifetime is longer than several nanoseconds, in the range of 15-30 ns,  
 2955 the R-Hadron decay can occur in or after the calorimeters, but prior to reaching  
 2956 the muon system. This case is similar to the above, although the jets may not be  
 2957 reconstructed, and is covered by many of the same search strategies. The events  
 2958 still often have large missing energy, although it is generated through different  
 2959 mechanisms. The R-Hadrons do not deposit much energy in the calorimeters, so  
 2960 a neutral R-Hadron will not enter into the missing energy calculation. A charged  
 2961 R-Hadron opposite a neutral R-Hadron will thus generate significant missing en-  
 2962 ergy, and close to 50% of pair-produced R-Hadron events fall into this category.  
 2963 If both R-Hadrons are neutral then the missing energy will be low because nei-  
 2964 ther is detected. Two charged R-Hadrons will also result in low missing energy  
 2965 because both are reconstructed as tracks and will balance each other in the trans-

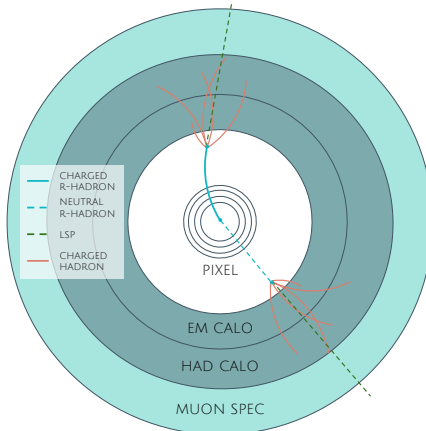


Figure 68: A schematic diagram of an R-Hadron event with a lifetime around 5 ns. The diagram includes one charged R-Hadron (solid blue), one neutral R-Hadron (dashed blue), LSPs (dashed green) and charged hadrons (solid orange). The pixel detector, calorimeters, and muon system are illustrated but not to scale.

2966      verse plane. A small fraction of the time, one of the charged R-Hadron tracks may  
 2967      fail quality requirements and thus be excluded from the missing energy calcula-  
 2968      tion and again result in significant missing energy. Figure 69 illustrates another  
 2969      example event with one charged R-Hadron which decays after approximately 20  
 2970      ns, and shows how the jets from the decay might not be reconstructed.

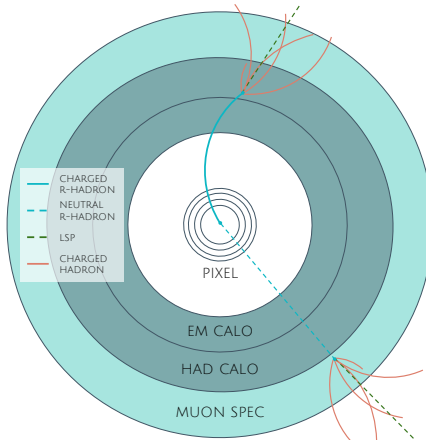


Figure 69: A schematic diagram of an R-Hadron event with a lifetime around 20 ns. The diagram includes one charged R-Hadron (solid blue), one neutral R-Hadron (dashed blue), LSPs (dashed green) and charged hadrons (solid orange). The pixel detector, calorimeters, and muon system are illustrated but not to scale.

2971      The longest lifetimes, the stable case, has all of the features of the 30-50 ns case  
 2972      but with the addition of muon tracks for any R-Hadrons that exit the calorimeter  
 2973      with a charge. That muon track can provide additional information from time-  
 2974      of-flight measurements to help identify LLPs. An example of the event topology  
 2975      for one charged and one neutral stable R-Hadron is shown in Figure 70. Some  
 2976      searches on ATLAS have included this information to improve the search reach  
 2977      for stable particles [79, 81].

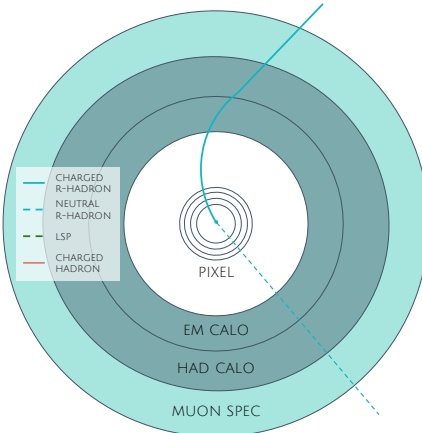


Figure 70: A schematic diagram of an R-Hadron event with a lifetime around 20 ns. The diagram includes one charged R-Hadron (solid blue) and one neutral R-Hadron (dashed blue). The pixel detector, calorimeters, and muon system are illustrated but not to scale.

## 2978 9.2 SIMULATION

2979 All of the event topologies discussed above are explored by simulations of R-  
 2980 Hadron events in the [ATLAS](#) detector. A large number of such samples are gen-  
 2981 erated to determine signal efficiencies, to measure expected yields, and to esti-  
 2982 mate uncertainties. The primary interaction, pair production of gluinos with  
 2983 masses between 400 and 3000 GeV, is simulated using [Pythia 6.4.27](#) [82]  
 2984 with the AUET2B [83] set of tuned parameters for the underlying event and the  
 2985 CTEQ6L1 [59] PDF set. The simulated interactions include a modeling of pileup  
 2986 by adding secondary, minimum bias interactions from both the same (in-time  
 2987 pileup) and nearby (out-of-time pileup) bunch crossings. This event generation  
 2988 is then augmented with a dedicated hadronization routine to hadronize the long-  
 2989 lived gluinos into final states with R-Hadrons [84], with the probability to form  
 2990 a gluon-gluino bound set at 10% [85].

2991 The cross sections used for these processes are calculated at next-to-leading  
 2992 order (NLO) in the strong coupling constant with a resummation of soft-gluon  
 2993 emmission at next-to-leading logarithmic (NLL) [86–90]. The nominal predic-  
 2994 tions and the uncertainties for each mass point are taken from an envelope of  
 2995 cross-section predictions using different PDF sets and factorization and renor-  
 2996 malization scales [91].

2997 The R-Hadrons then undergo a full detector simulation [], where the interac-  
 2998 tions of the R-Hadrons with the material of the detector are described by dedi-  
 2999 cated [Geant4](#) [29] routines. These routines model the interactions described in  
 3000 Section 9.1.1, including the ionizing interactions in the silicon modules of the  
 3001 inner detector and the R-Hadron-nucleon interactions in the calorimeters [92,  
 3002 93]. The specific routine chosen to describe the interactions of the R-Hadrons  
 3003 with nucleons, the “generic model”, uses a pragmatic approach where the scatter-  
 3004 ing cross section is taken to be a constant 12 mb per light quark. In this model

3005 the gluino itself does not interact at all except through its role as a reservoir of  
 3006 kinetic energy.

3007 The lifetimes of these R-Hadrons are then simulated at several working points,  
 3008  $\tau = 0.1, 1.0, 3.0, 10, 30, 50$  and detector stable, where the particle is required to  
 3009 decay after propagating for a time compatible with its lifetime. Only one decay  
 3010 mode is simulated for these samples,  $\tilde{g} \rightarrow q\bar{q}\tilde{\chi}_1^0$  with the neutralino mass set to  
 3011 100 GeV, which is chosen because it has the highest sensitivity among all of the  
 3012 modes studied in previous searches [80]. Heavier neutralinos have similar results  
 3013 but generate less missing energy which reduces the efficiency of triggering.

3014 All of the simulated events are then reconstructed using the same software  
 3015 used for collision data. The fully reconstructed events are then reweighted to  
 3016 match the distribution of initial state radiation in an alternative sample of events,  
 3017 generated with MG5\_aMC@NLO [94], which has a more accurate description of ra-  
 3018 diate effects than Pythia6. This reweighting provides a more accurate descrip-  
 3019 tion of the momentum of the gluino-gluino system and is important in modeling  
 3020 the efficiency of triggering and offline event selection.

3021

3022 EVENT SELECTION

---

3023 The **LLPs** targeted by this search differ in their interactions with the detector from  
 3024 **SM** particles primarily because of their large mass. When produced at the ener-  
 3025 gies available at the **LHC**, that large mass results in a low  $\beta$  (typically  $0.2 < \beta <$   
 3026  $0.9$ ). Such slow-moving particles heavily ionize in detector material. Each layer  
 3027 of the pixel detector provides a measurement of that ionization, through **ToT**, as  
 3028 discussed in Section 6.1.2. The ionization in the pixel detector, quantified in  
 3029 terms of  $dE/dx$ , provides the major focus for this search technique, along with  
 3030 the momentum measured in the entire inner detector. It is effective both for its  
 3031 discriminating power and its use in reconstructing a particle’s mass, and it can be  
 3032 used for a wide range of masses and lifetimes as discussed in Section 9.1.2. How-  
 3033 ever  $dE/dx$  needs to be augmented with a few additional selection requirements  
 3034 to provide a mechanism for triggering and to further reduce backgrounds.

3035 Ionization itself is not currently accessible for triggering, so this search in-  
 3036 stead relies on  $E_T^{\text{miss}}$  to trigger signal events. Although triggering on  $E_T^{\text{miss}}$  can  
 3037 be inefficient,  $E_T^{\text{miss}}$  is often large for many production mechanisms of **LLPs**, as  
 3038 discussed in Section 9.1.

3039 The use of ionization to reject **SM** backgrounds relies on well-measured, high-  
 3040 momentum tracks, so some basic requirements on quality and kinematics are  
 3041 placed on the tracks considered in this search. These quality requirements have  
 3042 been significantly enhanced in Run 2 by a newly introduced tracking variable  
 3043 that is very effective in removing highly-ionizing backgrounds caused by over-  
 3044 lapsing tracks. A few additional requirements are placed on the tracks consid-  
 3045 ered for **LLP** candidates that increase background rejection by targeting specific  
 3046 types of **SM** particles. These techniques provide a significant analysis improve-  
 3047 ment over previous iterations of ionization-based searches on ATLAS by provid-  
 3048 ing additional background rejection with minimal loss in signal efficiency.

3049 The ionization measurement with the Pixel detector can be calibrated to pro-  
 3050 vide an estimator of  $\beta\gamma$ . That estimate, together with the momentum measure-  
 3051 ment provided by tracking, can be used to reconstruct a mass for each track  
 3052 which traverses the pixel detector. That mass variable will be peaked at the **LLP**  
 3053 mass for any signal, and provides an additional tool to search for an excess. In  
 3054 addition to an explicit requirement on ionization, this search constructs a mass-  
 3055 window for each targeted signal mass in order to evaluate any excess of events  
 3056 and to set limits.

3057 The strategy discussed here is optimized for lifetimes of  $O(1) - O(10)$  ns.  
 3058 Pixel ionization is especially useful in this regime as particles only need to prop-  
 3059 agate through the first seven layers of the inner detector, about 37 cm from the  
 3060 beam axis. The search is still competitive with other searches for **LLPs** at longer  
 3061 lifetimes, because the primary discriminating variables are still applicable even  
 3062 for particles that do not decay within the detector [81]. Although the majority of

3063 the requirements will be the same for all lifetimes, two signal regions are defined  
 3064 to optimize separately for intermediate and long lifetime particles.

## 3065 10.1 TRIGGER

3066 Triggering remains a significant difficulty in defining an event selection with  
 3067 high signal efficiency in a search for LLPs. There are no triggers available in  
 3068 the current ATLAS system that can fire directly from a high momentum track  
 3069 with large ionization (Section 5.6). Although in some configurations a charged  
 3070 LLP can fire muon triggers, this requirement introduces significant model depen-  
 3071 dence on both the allowed lifetimes and the interactions in the calorimeter [74],  
 3072 as discussed in Section 9.1.1.

3073 For a search targeting particles which may decay prior to reaching the muon  
 3074 system, the most efficient available trigger is based on missing energy [74]. As  
 3075 discussed in Section 9.1, signal events can produce significant  $E_T^{\text{miss}}$  by a few  
 3076 mechanisms. At the trigger level however, the missing energy is only calculated  
 3077 using the calorimeters (Section 5.6) where the R-Hadrons deposit little energy.  
 3078 So, at short lifetimes,  $E_T^{\text{miss}}$  measured in the calorimeter is generated by an im-  
 3079 balance between the jets and undetected LSPs produced in R-Hadron decays. At  
 3080 longer lifetimes, without the decay products, missing energy is only produced in  
 3081 the calorimeters when the R-Hadrons recoil against an initial state radiation (ISR)  
 3082 jet.

3083 These features are highlighted in Figure 71, which shows the  $E_T^{\text{miss}}$  distribu-  
 3084 tions for simulated short lifetime (3 ns) and stable R-Hadron events. The figure  
 3085 includes both the offline  $E_T^{\text{miss}}$ , the missing energy calculated with all available  
 3086 information, and Calorimeter  $E_T^{\text{miss}}$ , the missing energy calculated using only  
 3087 information available at the calorimeter which approximates the missing energy  
 3088 available at the trigger. The short lifetime sample has significantly greater  $E_T^{\text{miss}}$   
 3089 and Calorimeter  $E_T^{\text{miss}}$  than the stable sample as expected. For the stable sam-  
 3090 ple, a small fraction of events with very large  $E_T^{\text{miss}}$  (about 5%) migrate into the  
 3091 bin with very small Calorimeter  $E_T^{\text{miss}}$  because the  $E_T^{\text{miss}}$  produced by a charged  
 3092 R-Hadron track opposite a neutral R-Hadron track does not contribute any miss-  
 3093 ing energy in the calorimeters.

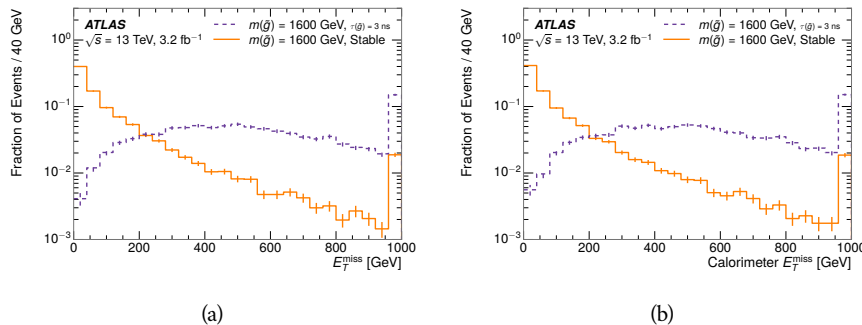


Figure 71: The distribution of (a)  $E_T^{\text{miss}}$  and (b) Calorimeter  $E_T^{\text{miss}}$  for simulated signal  
 events before the trigger requirement.

3094 So, either case to some extent relies on kinematic degrees of freedom to pro-  
 3095 duce missing energy, as the pair-produced LLPs tend to balance each other in  
 3096 the transverse plain. That balance results in a relatively low efficiency for long-  
 3097 lifetime particles, roughly 40%, and efficiencies between 65% and 95% for shorter  
 3098 lifetimes depending on both the mass and the lifetime. For long lifetimes in par-  
 3099 ticular, the presence of ISR is important in providing an imbalance in the trans-  
 3100 verse plane, and is an important aspect of modeling the selection efficiency for  
 3101 R-Hadron events.

3102 The missing energy trigger with the lowest threshold available is chosen for  
 3103 this selection in order to maximize the trigger efficiency. During 2015 data col-  
 3104 lection this was the HLT\_xe70 trigger, which used a 50 GeV threshold on miss-  
 3105 ing energy at LVL1 and a 70 GeV threshold on missing energy at the HLT. These  
 3106 formation of the trigger decision for missing energy was discussed in more detail  
 3107 in Section 5.6.

## 3108 10.2 KINEMATICS AND ISOLATION

3109 After the trigger requirement, each event is required to have a primary vertex  
 3110 reconstructed from at least two well-measured tracks in the inner detector, each  
 3111 with  $p_T > 400$  MeV. If more than one such vertex exists, the primary vertex  
 3112 is taken to be the one with the largest summed track momentum for all tracks  
 3113 associated to that vertex. The offline reconstructed  $E_T^{\text{miss}}$  is required to be above  
 3114 130 GeV to additionally reject SM backgrounds. The transverse missing energy  
 3115 is calculated using fully reconstructed and calibrated offline objects, as described  
 3116 in Section 6.5. In particular the  $E_T^{\text{miss}}$  definition in this selection uses jets recon-  
 3117 structed with the anti- $k_t$  algorithm with radius  $R = 0.4$  from clusters of energy  
 3118 in the calorimeter (Section 6.4) and with  $p_T > 20$  GeV, as well as reconstructed  
 3119 muons, electrons, and tracks not identified as another object type.

3120 The  $E_T^{\text{miss}}$  distributions are shown for data and a few simulated signals in Fig-  
 3121 ure 72, after the trigger requirement. The cut placed at 130 GeV is 95% effi-  
 3122 cient for metastable and 90% efficient for stable particles, after the trigger re-  
 3123 quirement, because of the missing energy generating mechanisms discussed pre-  
 3124 viously. The distribution of data in this figure and subsequent figures in this sec-  
 3125 tion can be interpreted as the distribution of backgrounds, as any signal contam-  
 3126 ination would be negligible if present at these early stages of the selection (prior  
 3127 to the final requirement on ionization). The background falls rapidly with miss-  
 3128 ing energy, motivating the direct requirement on  $E_T^{\text{miss}}$  for the signal region. Al-  
 3129 though a tighter requirement than the specified value of 130 GeV would seem to  
 3130 increase the search potential from these early distributions, other requirements  
 3131 are more optimal when taken as a whole. The specific values for each require-  
 3132 ment in signal region were optimized considering the increase in discovery reach  
 3133 for tightening the requirement on each discriminating variable. **NOTE: If space**  
 3134 **and time permit, I will add a whole section about signal region optimiza-**  
 3135 **tion..**

3136 It is typically the practice for searches for new physics on ATLAS to place an  
 3137 offline requirement on the triggering variable that is sufficiently tight to guar-

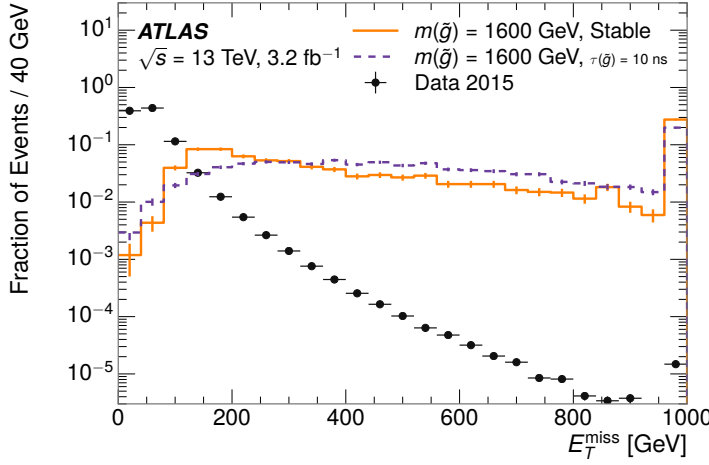


Figure 72: The distribution of  $E_T^{\text{miss}}$  for data and simulated signal events, after the trigger requirement.

3138 antee that the event would pass the trigger. Such a tight requirement makes the  
 3139 uncertainty on the trigger efficiency of the simulation negligible, as modeling the  
 3140 regime where the trigger is only partially efficient can be difficult. In this analy-  
 3141 sis, however, because of the atypical interactions of R-Hadrons with the tracker  
 3142 and the calorimeter, the offline requirement on  $E_T^{\text{miss}}$  is not sufficient to guar-  
 3143 antee a 100% trigger efficiency even at large values, as can be seen in Figure 73.  
 3144 This figure shows the efficiency for passing the HLT\_xe70 trigger as a function  
 3145 of the requirement on  $E_T^{\text{miss}}$ , which plateaus to roughly 85% even at large values.  
 3146 This plateau does not reach 100% because events which have large offline miss-  
 3147 ing energy from a neutral R-Hadron produced opposite of a charged R-Hadron  
 3148 can have low missing energy in the calorimeters. The Calorimeter  $E_T^{\text{miss}}$ , on the  
 3149 other hand, does not have this effect and reaches 100% efficiency at large values  
 3150 because it is the quantity that directly corresponds to the trigger threshold. In  
 3151 both cases the efficiency of triggering is greater for the short lifetime sample be-  
 3152 cause the late decays to hadrons and LSPs produce an imbalance in the calorime-  
 3153 ters even though they may not be reconstructed offline as tracks or jets. For this  
 3154 reason, the requirement on  $E_T^{\text{miss}}$  is determined by optimizing the background  
 3155 rejection even though it corresponds to a value of trigger efficiency significantly  
 3156 below 1.0.

3157 Potential signal events are then required to have at least one candidate LLP  
 3158 track. Although the LLPs are produced in pairs, many models do not consistently  
 3159 yield two charged particles. For example, in the R-Hadron model highlighted  
 3160 here, only 20% of events have two charged R-Hadrons while 47% of events have  
 3161 just one. A signal region requiring two charged candidates could be a powerful  
 3162 improvement in background rejection for a larger dataset, but it is not consid-  
 3163 ered in this version of the analysis as it was found to be unnecessary to reject the  
 3164 majority of backgrounds.

3165 For a track to be selected as a candidate, it must have  $p_T > 50 \text{ GeV}$  and pass  
 3166 basic quality requirements. The track must be associated to the primary vertex.

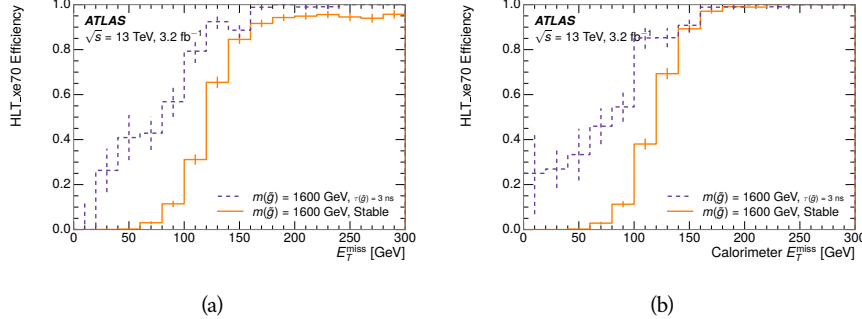


Figure 73: The trigger efficiency for the HLT\_xe70 trigger requirement as a function of (a)  $E_T^{\text{miss}}$  and (b) Calorimeter  $E_T^{\text{miss}}$  for simulated signal events.

It must also have at least seven clusters in the silicon layers in the inner detector to ensure an accurate measurement of momentum. Those clusters must include one in the innermost layer if the extrapolated track is expected to pass through that layer. And to ensure a reliable measurement of ionization, the track is required to have at least two clusters in the pixel detector that provide a measurement of  $dE/dx$ .

At this point in the selection, there is a significant high-ionization background from multiple tracks that significantly overlap in the inner detector. Previous version of this analysis have rejected these overlaps by an explicit overlap rejection between pairs of fully reconstructed tracks, typically by requiring no additional tracks within a cone around the candidate. This technique, however, fails to remove the background from tracks that overlap so precisely that the tracks cannot be separately resolved, which can be produced in very collimated photon conversions or decays of pions.

A new method, added in Run 2, identifies cluster shapes that are likely formed by multiple particles based on a neural network classification algorithm. The number of clusters that are classified this way in the pixel detector for a given track is called  $N_{\text{split}}$ . As the shape of clusters requires significantly less spatial separation to identify overlaps than it does to reconstruct two fully resolved tracks, this variable is more effective at rejecting backgrounds from overlaps. Figure 74 shows the dependence of ionization on  $N_{\text{split}}$ ; as  $N_{\text{split}}$  increases the most probable value of  $dE/dx$  grows significantly up to twice the expected value when  $N_{\text{split}} = 4$ .

This requirement is very successful in reducing the long positive tail of the  $dE/dx$  distributions, as can be seen in Figure 75. Comparing the distribution for “baseline tracks”, tracks with only the above requirements on clusters applied and before the requirement on  $N_{\text{split}}$ , to the distribution with  $N_{\text{split}} = 0$ , it is clear that the fraction of tracks with large  $dE/dx$  is reduced be several orders of magnitude. The tracks without split hits are very close to the  $dE/dx$  distribution of identified muons, which are extremely well isolated on average. Figure 75 also includes the distribution of  $dE/dx$  in an example signal simulation to demonstrate how effective  $dE/dx$  is as a discriminating variable with this isolation applied. The background falls rapidly for  $dE/dx > 1.8 \text{ MeVg}^{-1}\text{cm}^2$

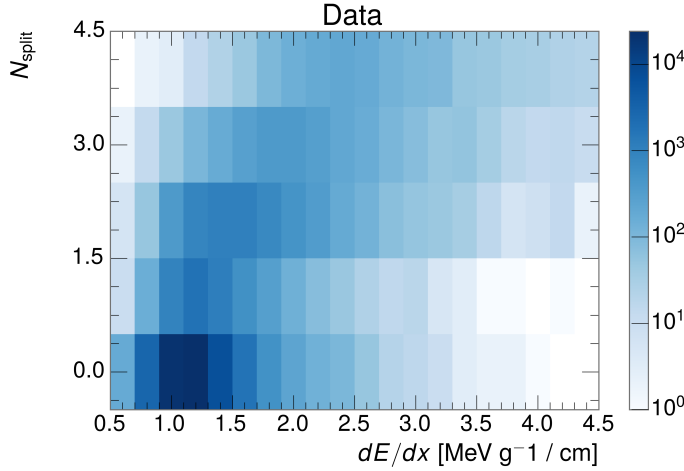


Figure 74: The dependence of  $dE/dx$  on  $N_{\text{split}}$  in data after basic track hit requirements have been applied.

3200 while the majority of the signal, approximately 90% depending on the mass, falls  
 3201 above that threshold. Over 90% of LLP tracks in simulated signal events pass the  
 3202  $N_{\text{split}}$ -based isolation requirement.

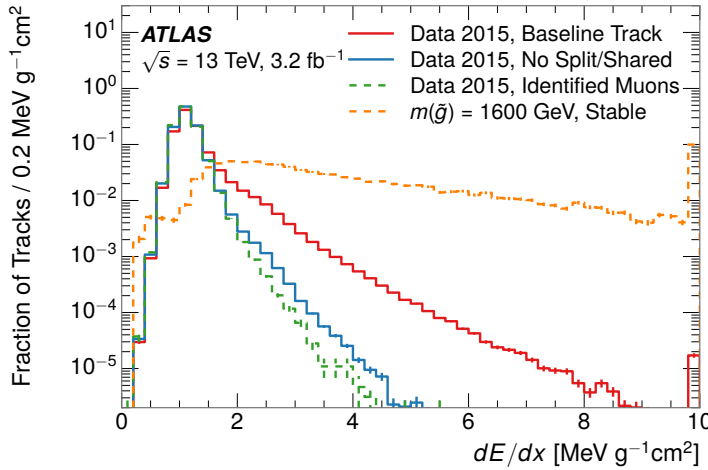


Figure 75: The distribution of  $dE/dx$  with various selections applied in data and simulated signal events.

3203 A few additional kinematic requirements are imposed to help reduce SM back-  
 3204 grounds. The momentum of the candidate track must be at least 150 GeV, and  
 3205 the uncertainty on that measurement must be less than 50%. The distribution of  
 3206 momentum is shown in Figure 76 for tracks in data and simulated signal events  
 3207 after the previously discussed requirements on clusters, transverse momentum,  
 3208 and isolation have been imposed. The signal particles are much harder on aver-

3209 age than their backgrounds because of the high energy interactions required to  
 3210 produce them. The transverse mass,  $M_T$ , defined as

$$M_T = \sqrt{2p_T E_T^{\text{miss}}(1 - \cos(\Delta\phi(E_T^{\text{miss}}, \text{track})))} \quad (20)$$

3211 estimates the mass of a decay of to a single charged particle and an undetected  
 3212 particle and is required to be greater than 130 GeV to reject contributions from  
 3213 the decay of W bosons. Figure 77 shows the distribution of  $M_T$  for data and  
 3214 simulated signal events. The signal is distributed over a wide range of  $M_T$ , with  
 3215 about 90% above the threshold value of 130 GeV. The data shows a dual-peaked  
 3216 structure, where the first peak comes from W boson decays and the second peak  
 3217 is a kinematic shaping from the requirements on  $E_T^{\text{miss}}$  and the track  $p_T$  in dijet  
 3218 events.

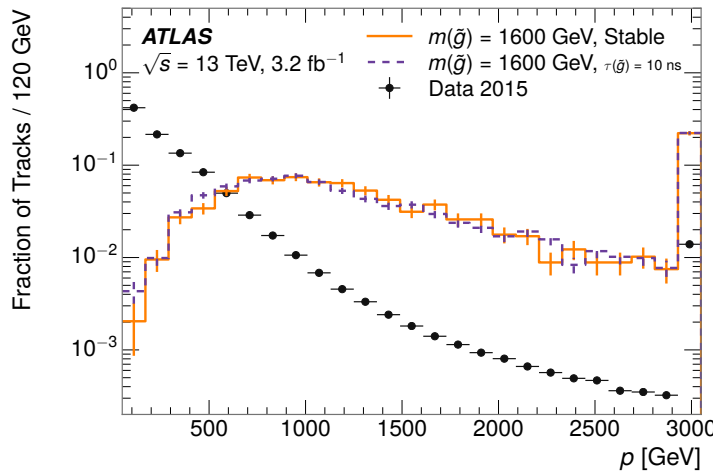


Figure 76: The distribution of track momentum for data and simulated signal events,  
 after previous selection requirements have been applied.

### 3219 10.3 PARTICLE SPECIES REJECTION

3220 The amount of ionization deposited by particles with low mass and high mo-  
 3221 mentum has a large positive tail [3], so backgrounds can be formed by a wide  
 3222 variety of SM processes when various charged particles have a few randomly  
 3223 large deposits of energy in the pixel detector. Those backgrounds can be ad-  
 3224 ditionally reduced by targeting other interactions with the detector where they  
 3225 are expected to have different behavior than R-Hadrons. The interactions with  
 3226 the detector depend on the types of particles produced rather than the processes  
 3227 which produce them, so this search forms a series of rejections to remove back-  
 3228 grounds from individual particle species. These rejections focus on using addi-  
 3229 tional features of the event, other than the kinematics of the candidate track, as  
 3230 they can provide a powerful source of background rejection with very high sig-  
 3231 nal efficiency. However, the lifetime of an R-Hadron can significantly change

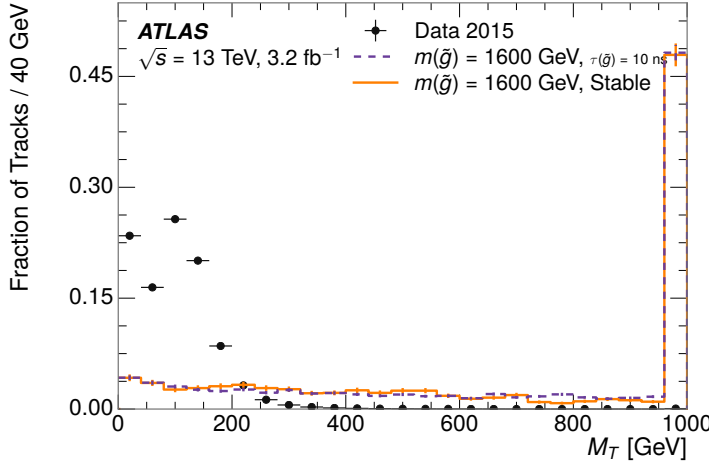


Figure 77: The distribution of  $M_T$  for data and simulated signal events, after previous selection requirements have been applied.

its detector characteristics, as discussed in Section 9.1.2. To accommodate these differences, the SM rejections defined in this section are split to form two signal regions, one for long-lifetimes particles, the stable region ( $50 \leq \tau[\text{ns}] < \infty \text{ ns}$ ), and one for intermediate lifetime particles, the metastable region ( $0.4 < \tau[\text{ns}] < 50$ ).

Jets can be very effectively rejected by considering the larger-scale isolation of the candidate track. In this case the isolation focuses on the production of nearby particles as a jet-veto, rather than the isolation from overlapping tracks based on  $N_{\text{split}}$  that was used to reduce high-ionization backgrounds. As explained in Section 9.1, the fragmentation process which produces an R-Hadron is very hard and thus is not expected to produce additional particles with a summed momentum of more than 5 GeV. The jet-veto uses the summed momentum of tracks with a cone of  $\Delta R < 0.25$ , referred to as  $p_T^{\text{Cone}}$ , which is shown in Figure 78 for data and simulated signal events. In the data this value has a peak at zero from isolated tracks such as leptons, and a long tail from jets which contains as much as 80% of the background above 20 GeV at this stage of the selection. In signal events  $p_T^{\text{Cone}}$  is strongly peaked at zero and significantly less than 1% of signal events have  $p_T^{\text{Cone}}$  above 20 GeV. This makes a requirement of  $p_T^{\text{Cone}} < 20 \text{ GeV}$  a very effective method to reject background without losing signal efficiency. For the stable signal region, this cut is further tightened to  $p_T^{\text{Cone}} < 5 \text{ GeV}$  as it is the most effective variable remaining to extend the search reach for long lifetimes.

Even for fully isolated particles, there are additional methods to reject each type of particle using information in the muon system and calorimeters. Muons can be identified very reliably using the tracks in the muon system, as described in Section 6.3. For intermediate lifetimes the LLPs do not survive long enough to reach the muon system, and so muons are vetoed by rejecting tracks that associate to a muon with medium muon identification requirements (Section 6.3). For longer lifetimes, this rejection is not applied because LLPs which reach the

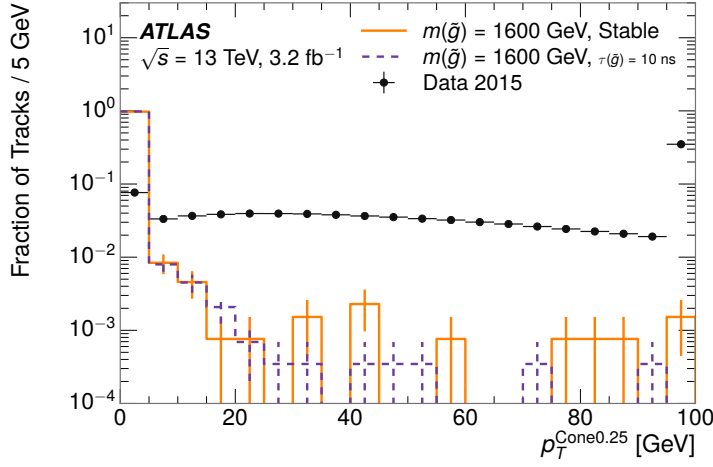


Figure 78: The distribution of summed tracked momentum within a cone of  $\Delta R < 0.25$  around the candidate track for data and simulated signal events, after previous selection requirements have been applied.

muon system can be identified as muons as often as 30% of the time in simulated samples.

Calorimeter-based particle rejection relies on the expected small deposits of energy from LLPs. When the lifetime is long enough to reach the calorimeter, a LLP deposits little of its energy as it traverses the material, as discussed in Section 9.1. Even when the particle does decay before the calorimeter, the majority of its energy is carried away by the LSP and not deposited in the calorimeter. In both cases the energy is expected to be distributed across the layers of the calorimeters and not peaked in just one layer. This can be quantified in terms of  $E/p$ , the ratio of calorimeter energy of a nearby jet to the track momentum, and  $f_{\text{EM}}$ , the fraction of energy in that jet within the electromagnetic calorimeter. When no jets fall within a cone of 0.05 of the particle,  $E/p$  and  $f_{\text{EM}}$  are both defined as zero.  $E/p$  is expected to be above 1.0 for typical SM particles because of calibration and the contributions from other nearby particles, as discussed in Chapter 7. At these momenta there is no significant zero fraction due to interactions with the detector or insufficient energy deposits (see Section 7.2.2).  $f_{\text{EM}}$  is peaked close to 1.0 for electrons, and distributed between 10% and 90% for hadrons.

These trends can be seen in the two dimensional distribution for signal in Figure 79 for stable and metastable (10 ns) events. The majority of R-Hadrons in both samples fall into the bin for  $E/p = 0$  and  $f_{\text{EM}} = 0$  because the majority of the time there is no associated jet. In the stable sample, when there often is an associated jet,  $E/p$  is typically still below 0.1, and the  $f_{\text{EM}}$  is predominantly under 0.8. In the metastable sample, on the other hand,  $E/p$  is larger but still typically below 0.1 because of actual jets produced during the decay. The  $f_{\text{EM}}$  is much lower on average in this case, below 0.1, because the 10 ns lifetime particles rarely decay before passing through the electromagnetic calorimeter. Figure 79 also includes simulated Z decays to electrons or tau leptons. From the decays

3289 to electrons it is clear that the majority of electrons have  $f_{\text{EM}}$  above 0.9. The  
 3290 tau decays include a variety of products. Muons can be seen in the bin where  
 3291  $E/p = 0$  and  $f_{\text{EM}} = 0$  because they do not have an associated jet. Electrons fall  
 3292 into the range where  $E/p > 1$  and  $f_{\text{EM}} > 0.9$ . Hadronic tau decays are the most  
 3293 common, and fall in the range of  $0.1 < f_{\text{EM}} < 0.9$  and  $E/p > 1.0$ .

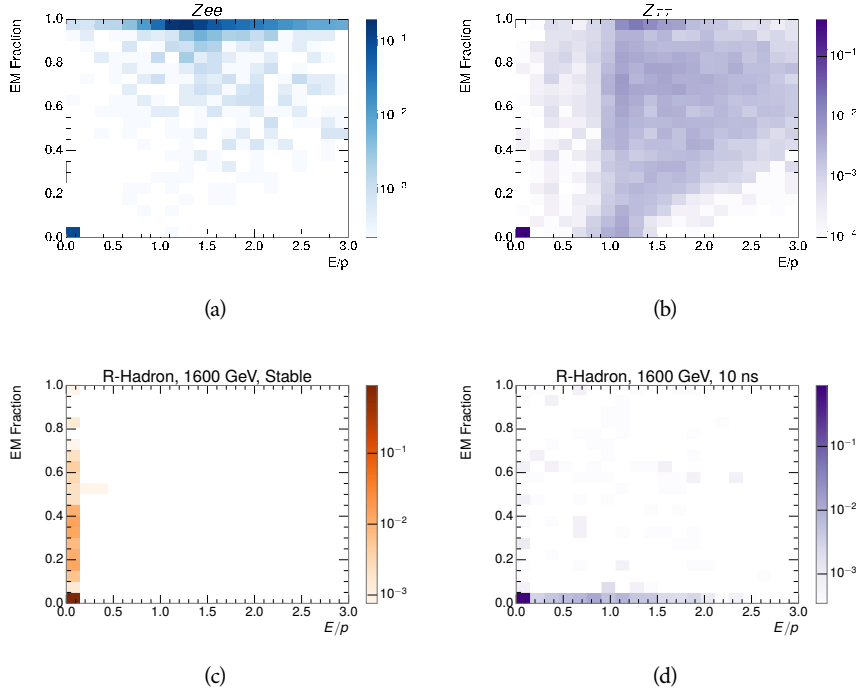


Figure 79: The normalized, two-dimensional distribution of  $E/p$  and  $f_{\text{EM}}$  for simulated  
 (a)  $Z \rightarrow ee$ , (b)  $Z \rightarrow \tau\tau$ , (c) 1200 GeV Stable R-Hadron events, and (d) 1200  
 GeV, 10 ns R-Hadron events.

3294 These differences motivate an electron rejection by requiring an  $f_{\text{EM}}$  below  
 3295 0.9. Similarly, isolated hadrons are rejected by requiring  $E/p < 1.0$ . These re-  
 3296 quirements combine to remove the majority of isolated electrons and hadrons  
 3297 but retain over 95% of the simulated signal across a range of masses and lifetimes.

## 3298 10.4 IONIZATION

3299 The final requirement on the candidate track is the primary discriminating vari-  
 3300 able, the ionization in the pixel detector. That ionization is measured in terms  
 3301 of  $dE/dx$ , which was shown for data and simulated signal events in Figure 75.  
 3302  $dE/dx$  is dramatically greater for the high mass signal particles than the back-  
 3303 grounds, which start to fall immediately after the minimally ionizing peak at 1.1  
 3304 MeV g $^{-1}$  cm $^2$ . The  $dE/dx$  for candidate tracks must be greater than a pseudorapidity-  
 3305 dependent threshold, specifically  $1.80 - 0.11|\eta| + 0.17\eta^2 - 0.05|\eta|^3$  MeV g $^{-1}$  cm $^{-2}$ ,  
 3306 in order to correct for an approximately 5% dependence of the MIP peak on  $\eta$ .  
 3307 The requirement was chosen as part of the signal region optimization, and man-

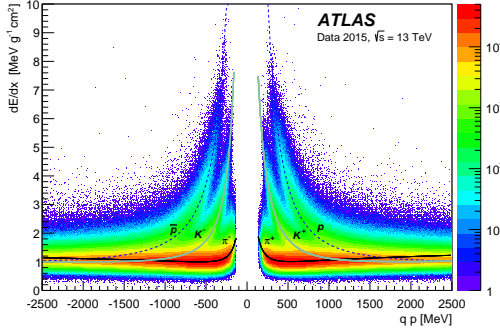


Figure 80: Two-dimensional distribution of  $dE/dx$  versus charge signed momentum ( $qp$ ) for minimum-bias tracks. The fitted distributions of the most probable values for pions, kaons and protons are superimposed.

3308 ages to reduce the backgrounds by a factor of 100 while remaining 70-90% effi-  
 3309 cient for simulated signal events depending on the mass.

#### 3310 10.4.1 MASS ESTIMATION

3311 The mean value of ionization in silicon is governed by the Bethe equation and  
 3312 the most probable value follows a Landau-Vavilov distribution [3]. Those forms  
 3313 inspire a parametric description of  $dE/dx$  in terms of  $\beta\gamma$ ,

$$(dE/dx)_{MPV}(\beta\gamma) = \frac{p_1}{\beta^{p_3}} \ln(1 + [p_2 \beta\gamma]^{p_5}) - p_4 \quad (21)$$

3314 which performs well in the range  $0.3 < \beta\gamma < 1.5$ . This range includes the ex-  
 3315 pected range of  $\beta\gamma$  for the particles targeted for this search, with  $\beta\gamma \approx 2.0$  for  
 3316 lower mass particles (O(100 GeV)) and up to  $\beta\gamma \approx 0.5$  for higher mass par-  
 3317 ticles (O(1000 GeV)). The parameters,  $p_i$ , are fit using a 2015 data sample of  
 3318 low-momentum pions, kaons, and protons as described in Ref. [95]. Figure 80  
 3319 shows the two-dimensional distribution of  $dE/dx$  and momentum along with  
 3320 the above fitted values for  $(dE/dx)_{MPV}$ .

3321 The above equation (21) is then numerically inverted to estimate  $\beta\gamma$  and the  
 3322 mass for each candidate track. In simulated signal events, the mean of this mass  
 3323 value reproduces the generated mass up to around 1800 GeV to within 3%, and  
 3324 3% shift is applied to correct for this difference. The mass distributions prior to  
 3325 this correction are shown for a few stable mass points in Figure 81. The large  
 3326 widths of these distributions come from the high variability in energy deposits  
 3327 in the pixel detector as well as the uncertainty on momentum measurements at  
 3328 high momentum, but the means converge to the expected values.

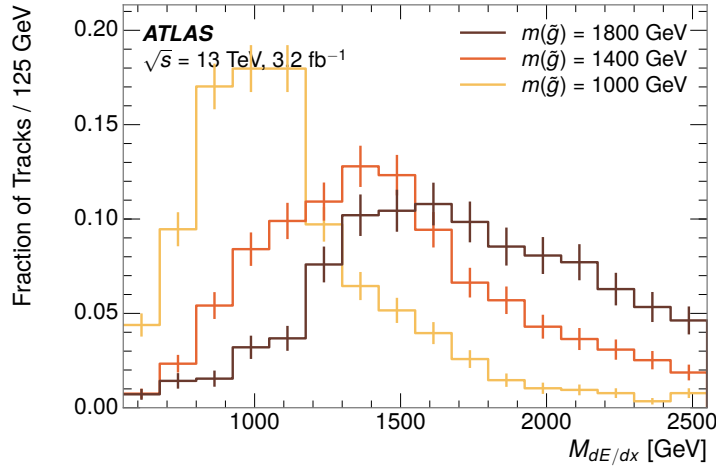


Figure 81: The distribution of mass estimated using  $dE/dx$  for simulated stable R-Hadrons with masses between 1000 and 1600 GeV.

3329     This analysis evaluates expected yields and the resulting cross sectional limits  
 3330     using windows in this mass variable. The windows are formed by fitting mass  
 3331     distributions in simulated signal events like those in Figure 81 to Gaussian distri-  
 3332     butions and taking all events that fall within  $\pm 1.4\sigma$  of the mean. As can be seen  
 3333     in Figure 81, typical values for this width are  $\sigma \approx 300 - 500 \text{ GeV}$  depending on  
 3334     the generated mass.

## 3335     10.5 EFFICIENCY

3336     The numbers of events passing each requirement through ionization are shown  
 3337     in Table 9 for the full 2015 dataset and a simulated 1600 GeV, 10 ns lifetime R-  
 3338     Hadron sample. The table highlights the overall acceptance  $\times$  efficiency for sig-  
 3339     nal events, which for this example is 19%. Between SM rejection and ionization,  
 3340     this signal region reduces the background of tracks which pass the kinematic  
 3341     requirements down by an additional factor of almost 2000.

3342     There is a strong dependence of this efficiency on lifetime and mass, with effi-  
 3343     ciencies dropping to under 1% at low lifetimes. Figure 82 shows the dependence  
 3344     on both mass and lifetime for all signal samples considered in this search. The  
 3345     dependence on mass is relatively slight and comes predominantly from the in-  
 3346     creasing fraction of R-Hadrons which pass the ionization cut with increasing  
 3347     mass. The trigger and  $E_T^{\text{miss}}$  requirements are most efficient for particles that  
 3348     decay before reaching the calorimeters. However, the chance of a particle to be  
 3349     reconstructed as a high-quality track decreases significantly at low lifetimes as  
 3350     the particle does not propagate sufficiently through the inner detector. These  
 3351     effects lead to a maximum in the selection efficiency for lifetimes around 10-30  
 3352     ns.

3353     The inefficiency of this signal region at short lifetimes comes almost exclu-  
 3354     sively from an acceptance effect, in that the particles do not reach the necessary

Selection	Exp. Signal Events	Observed Events in $3.2 \text{ fb}^{-1}$
Generated	$26.0 \pm 0.3$	
$E_T^{\text{miss}}$ Trigger	$24.8 \pm 0.3$ (95%)	
$E_T^{\text{miss}} > 130 \text{ GeV}$	$23.9 \pm 0.3$ (92%)	
Track Quality and $p_T > 50$	$10.7 \pm 0.2$ (41%)	368324
Isolation Requirement	$9.0 \pm 0.2$ (35%)	108079
Track $p > 150 \text{ GeV}$	$6.6 \pm 0.2$ (25%)	47463
$M_T > 130 \text{ GeV}$	$5.8 \pm 0.2$ (22%)	18746
Electron and Hadron Veto	$5.5 \pm 0.2$ (21%)	3612
Muon Veto	$5.5 \pm 0.2$ (21%)	1668
Ionization Requirement	$5.0 \pm 0.1$ (19%)	11

Table 9: The expected number of events at each level of the selection for metastable  $1600 \text{ GeV}$ , 10 ns R-Hadrons, along with the number of events observed in data, for  $3.2 \text{ fb}^{-1}$ . The simulated yields are shown with statistical uncertainties only. The total efficiency  $\times$  acceptance is also shown for the signal.

3355 layers of the SCT. This can be seen more clearly by defining a fiducial region  
 3356 which includes events with at least one R-Hadron that is produced with non-  
 3357 zero charge,  $p_T > 50 \text{ GeV}$ ,  $p > 150 \text{ GeV}$ ,  $|\eta| < 2.5$ , and a decay distance greater  
 3358 than 37 cm in the transverse plane. At short (1 ns) lifetimes, the acceptance into  
 3359 this region is as low as 4%. Once this acceptance is accounted for, the selection  
 3360 efficiency ranges from 25% at lifetimes of 1 ns up to 45% at lifetimes of 10 ns.

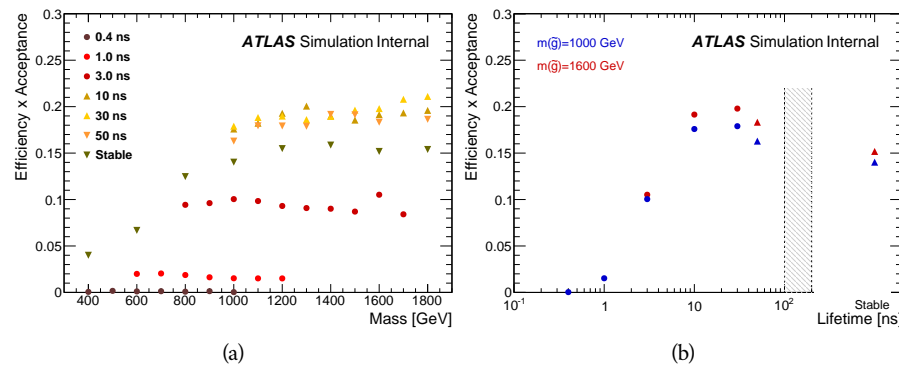


Figure 82: The acceptance  $\times$  efficiency as a function of R-Hadron (a) mass and (b) lifetime. (a) shows all of the combinations of mass and lifetime considered in this search, and (b) highlights the lifetime dependence for 1000 GeV and 1600 GeV R-Hadrons.

3361

3362 BACKGROUND ESTIMATION

---

3363 The event selection discussed in the previous section focuses on detector sig-  
 3364 natures, emphasizing a single high-momentum, highly-ionizing track. That track  
 3365 is then required to be in some way inconsistent with the expected properties  
 3366 of SM particles, with various requirements designed to reject jets, hadrons, elec-  
 3367 trons, and muons (Section 10.3). Therefore the background for this search comes  
 3368 entirely from reducible backgrounds that are outliers of various distributions in-  
 3369 cluding  $dE/dx$ ,  $f_{EM}$ , and  $p_T^{\text{Cone}}$ . The simulation can be tuned in various ways to  
 3370 do an excellent job of modeling the average properties of each particle type [96],  
 3371 but it is not necessarily expected to accurately reproduce outliers. For this rea-  
 3372 sons, the background estimation used for this search is estimated entirely using  
 3373 data.

## 3374 11.1 BACKGROUND SOURCES

3375 SM charged particles with lifetimes long enough to form tracks in the inner de-  
 3376 tector can be grouped into three major categories based on their detector inter-  
 3377 actions: hadrons, electrons, and muons. Every particle that enters into the back-  
 3378 ground for this search belongs to one of these types. Relatively pure samples of  
 3379 tracks from each of these types can be formed in data by inverting the various  
 3380 rejection techniques in Section 10.3. Specifically, muons are selected requiring  
 3381 medium muon identification, electrons requiring  $E/p > 1.0$  and  $f_{EM} > 0.95$ ,  
 3382 and hadrons requiring  $E/p > 1.0$  and  $f_{EM} < 0.95$ .

3383 Figure 83 shows the distributions of momentum and  $dE/dx$  for these cate-  
 3384 gories in data, after requiring the event level selection as well as the track re-  
 3385 quirements on  $p_T$ , hits, and  $N_{\text{split}}$ , as discussed in Section 10.2. Simulated signal  
 3386 events are included for reference. These distribution are only illustrative of the  
 3387 differences between types, as the rejection requirements could alter their shape.  
 3388 This is especially significant for momentum which enters directly into  $E/p$  and  
 3389 can indirectly affect muon identification. However the various types show clear  
 3390 differences in both distributions. The distributions of momentum are not nec-  
 3391 essarily expected to match between the various types because the production  
 3392 mechanisms for each type result in different kinematic distributions.  $dE/dx$  is  
 3393 also different between types because of incomplete isolation; although the re-  
 3394 quirement on  $N_{\text{split}}$  helps to reduce the contribution of nearby particles it does  
 3395 not completely remove the effect of overlaps. Muons are better isolated because  
 3396 they do not have the additional particle from hadronization present for hadrons  
 3397 and they are significantly less likely to interact with the detector and produce  
 3398 secondary particles compared to hadrons and electrons. Thus muons have the  
 3399 smallest fraction of  $dE/dx$  above the threshold of  $1.8 \text{ MeVg}^{-1}\text{cm}^2$ ; hadrons and  
 3400 electrons have a larger fraction above this threshold.

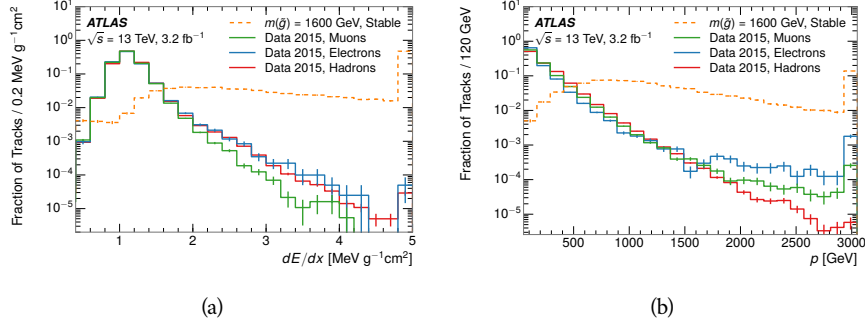


Figure 83: The distribution of (a)  $dE/dx$  and (b) momentum for tracks in data and simulated signal after requiring the event level selection and the track selection on  $p_T$ , hits, and  $N_{\text{split}}$ . Each sub-figure shows the normalized distributions for tracks classified as hadrons, electrons, and muons in data and R-Hadrons in the simulated signal.

3401 It is difficult to determine what fraction of each particle type enters into the fi-  
 3402 nal signal region. The background method will not have significant dependence  
 3403 on the relative contributions of each species, but it is useful to understand the  
 3404 differences between each when considering the various tests of the method.

## 3405 11.2 PREDICTION METHOD

3406 The data-driven background estimation relies on the independence between ion-  
 3407 ization and other kinematic variables in the event. For standard model particles  
 3408 with momenta above 50 GeV,  $dE/dx$  is not correlated with momentum; though  
 3409 there is a slight relativistic rise as momentum increases, the effect is small com-  
 3410 pared to the width of the distribution of ionization energy deposits.. So, the  
 3411 proposed method to estimate the mass distribution of the signal region is to use  
 3412 momentum from a track with low  $dE/dx$  (below the threshold value) and to com-  
 3413 bine it with a random  $dE/dx$  value from a  $dE/dx$  template. The resulting track is  
 3414 just as likely as the original, so a number of such random generations provide the  
 3415 expected distributions of momentum and ionization. These are then combined  
 3416 using the parametrization described in Section 10.4.1 to form a distribution of  
 3417 mass for the signal region.

3418 Algorithmically this method is implemented by forming two distinct Control  
 3419 Regions (**CRs**). The first **CR**, CR1, is formed by applying the entire event selec-  
 3420 tion from Chapter 10 up to the  $dE/dx$  and mass requirements. The  $dE/dx$  re-  
 3421 quirement is instead inverted for this region. Because of the independence of  
 3422  $dE/dx$ , the tracks in this control region have the same kinematic distribution  
 3423 as the tracks in the signal region, and are used to measure a two-dimensional  
 3424 template of  $p$  and  $\eta$ . The second **CR**, CR2, is formed from the event selection  
 3425 through the  $dE/dx$  requirement, but with an inverted  $E_T^{\text{miss}}$  requirement. The  
 3426 tracks in this control region are expected to have similar  $dE/dx$  distributions to  
 3427 the signal region before the ionization requirement, and so this region is used to  
 3428 measure a two-dimensional template of  $dE/dx$  and  $\eta$ .

3429     The contribution of any signal to the control regions is minimized by the in-  
 3430     verted selection requirements. Only less than 10% of simulated signal events  
 3431     have either  $dE/dx$  or  $E_T^{\text{miss}}$  below the threshold values in the original signal re-  
 3432     gion, while the backgrounds are significantly enhanced by inverting those re-  
 3433     quirements. The signal contamination is less than 1% in both control regions  
 3434     for all of the simulated masses and lifetimes considered in this analysis.

3435     With those measured templates, the shape of the mass estimation is generated  
 3436     by first selecting a random ( $p$ ,  $\eta$ ) combination from CR1. This momentum  
 3437     value is combined with a  $dE/dx$  value taken from the appropriate distribution  
 3438     of  $dE/dx$  for the selected  $\eta$  from CR2. The use of  $\eta$  in both random samplings  
 3439     controls for any correlation between  $p$ ,  $dE/dx$ , and  $\eta$ . Those values are then  
 3440     used to calculate a mass in the same way that is done for regular tracks in data,  
 3441     see Section 10.4.1. As this procedure includes all  $dE/dx$  values, the cut at 1.8  
 3442     MeVg $^{-1}$ cm $^2$  is then enforced to fully model the signal region. The generated  
 3443     mass distribution is then normalized by scaling the background estimate to the  
 3444     data in the region  $M < 160$  GeV, where signals of this type have already been  
 3445     excluded [80]. This normalization uses the distributions of mass generated with-  
 3446     out the ionization requirement.

3447     The statistical uncertainties on these background distributions are calculated  
 3448     by independently fluctuating each bin of the input templates according to their  
 3449     Poisson uncertainties. These fluctuations are repeated a large number of times,  
 3450     and the uncertainty on the resulting distribution is taken as the root mean square  
 3451     (RMS) deviation of the fluctuations from the average. As the procedure uses one  
 3452     million random combinations to generate the distributions, The statistical un-  
 3453     certainty from the actual random generations is negligible compared to the un-  
 3454     certainty from measuring the templates.

## 3455     11.3 VALIDATION

3456     The validity of the background estimation technique can be evaluated in both  
 3457     data and simulation. The underlying assumption that random combinations of  
 3458      $dE/dx$  and momentum can predict a mass distribution in an orthogonal region  
 3459     can be tested using simulated samples where concerns like multiple particle types  
 3460     can be controlled. Using the same technique in another set of signal-depleted  
 3461     regions in data then extends this confidence to the more complicated case where  
 3462     several particle species are inherently included.

### 3463     11.3.1 CLOSURE IN SIMULATION

3464     The first test of the procedure is done using a simulated sample of  $W \rightarrow \mu\nu$   
 3465     decays. These types of events provide the ingredients required to test the back-  
 3466     ground estimate,  $E_T^{\text{miss}}$  and isolated tracks, with high statistics. In this example  
 3467     there is no signal, so simulated events in the orthogonal CRs are used to estimate  
 3468     the shape of the mass distribution of the simulated events in the signal region. To  
 3469     reflect the different topology for W boson decays, the CRs use slightly modified  
 3470     definitions. In all CRs, the requirement of  $p > 150$  GeV and the SM rejection

3471 requirements are removed. Additionally, for the signal region the requirement  
 3472 on  $E_T^{\text{miss}}$  is relaxed to 30 GeV and the corresponding inverted requirement on  
 3473 CR2 is also set at 30 GeV.

3474 With these modified selections, the simulated and randomly generated distri-  
 3475 butions of  $M_{dE/dx}$  are shown in Figure 84. This figure includes the mass distri-  
 3476 butions before and after the requirement on  $dE/dx$ , which significantly shapes  
 3477 the distributions. In both cases the background estimation technique reproduces  
 3478 the shape of  $M_{dE/dx}$  in the signal region. There is a small difference in the pos-  
 3479 itive tail of the mass distribution prior to the ionization cut, where the random  
 3480 events underestimate the fraction of tracks with mass above 150 GeV by about  
 3481 20%. After the ionization requirement, however, this discrepancy is not present  
 3482 and the two distributions agree to within statistical uncertainties.

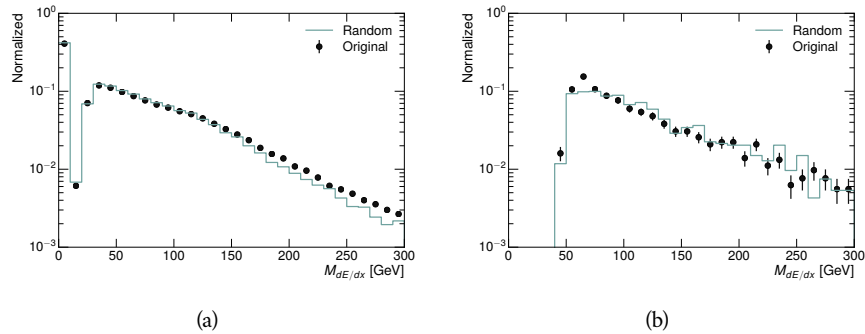


Figure 84: The distribution of  $M_{dE/dx}$  (a) before and (b) after the ionization requirement for tracks in simulated W boson decays and for the randomly generated background estimate.

3483 This ability to reproduce the shape of the mass distribution in simulated events  
 3484 shows that the technique works as expected. No significant biases are acquired  
 3485 in using low  $dE/dx$  events to select kinematic templates or in using low  $E_T^{\text{miss}}$   
 3486 events to select ionization templates, as either would result in a mismodeling of  
 3487 the shape of the mass distribution. The simulated events contain only one par-  
 3488 ticle type, however, so this test only establishes that the technique works well  
 3489 when the the CRs are populated by exactly the same species.

### 3490 11.3.2 VALIDATION REGION IN DATA

3491 The second test of the background estimate is performed using data in an or-  
 3492 thogonal validation region. The validation region, and the corresponding CRs,  
 3493 are formed using the same selection requirements as in the nominal method but  
 3494 with a modified requirement on momentum,  $50 < p[\text{GeV}] < 150$ . This allows  
 3495 the technique to be checked in a region with very similar properties but where  
 3496 the signal is depleted, as the majority of the signal has momentum above 150  
 3497 GeV while the backgrounds are enhanced below that threshold. Any biases on  
 3498 the particle composition of the CRs for the signal region will be reflected in the  
 3499 CRs used to estimate the mass distribution in the validation region.

Figure 85 shows the measured and randomly generated mass distributions for data before and after the ionization requirement. The background estimate does an excellent job of modeling the actual background before the ionization requirement, with good agreement to within the statistical uncertainties out to the limit of the mass distribution. There are very few events in the validation region after the ionization requirement, but the few observed events are consistent with the background prediction. The good agreement in this validation region provides a confirmation that the technique works even in the full-complexity case with multiple particle types entering the distributions. Any bias from changes in particle composition between regions is small compared to statistical uncertainties.

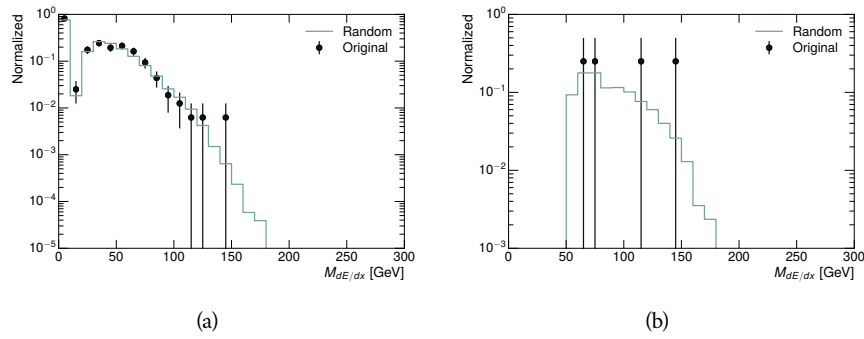


Figure 85: The distribution of  $M_{dE/dx}$  (a) before and (b) after the ionization requirement for tracks in the validation region and for the randomly generated background estimate.

3510

3511 SYSTEMATIC UNCERTAINTIES AND RESULTS

---

## 3512 12.1 SYSTEMATIC UNCERTAINTIES

3513 A number of systematic uncertainties affect the interpretation of the results of  
 3514 the search. These uncertainties can broken down into two major categories,  
 3515 those which affect the estimate of the background using data and those which  
 3516 affect the measurement of the signal yield estimated with simulated events. The  
 3517 total measured systematic uncertainties are 7% for the background estimation  
 3518 and approximately 32% for the signal yield depending on lifetime. These system-  
 3519atic uncertainties are expected to be small compared to the statistical fluctuations  
 3520 of the measured yields so that measured cross-sectional limits will be dominated  
 3521 by statistical uncertainties. The following sections describe each source of sys-  
 3522 tematic uncertainty for each of the two types.

## 3523 12.1.1 BACKGROUND ESTIMATE

3524 The systematic uncertainties on the background estimate come primarily from  
 3525 considering alternative methods for generating the background distributions.  
 3526 These uncertainties are small compared to the statistical uncertainties on the  
 3527 background estimate which come from the limited statistics in measuring the  
 3528 template distributions, as described in Section 11.2. They are summarized in  
 3529 Table 10.

Source of Uncertainty:	Value [%]
Analytic Description of $dE/dx$	4.0
Muon Fraction (Stable Region only)	3.0
IBL Ionization Correction	3.8
Normalization	3.0
Total (Metastable Region):	6.3
Total (Stable Region):	7.0

Table 10: A summary of the sources of systematic uncertainty for the data-driven back-  
 ground in the signal region. If the uncertainty depends on the mass, the maxi-  
 mum values are reported.

3530 12.1.1.1 ANALYTIC DESCRIPTION OF  $DE/DX$ 

3531 The background estimate uses a binned template distribution to estimate the  
 3532  $dE/dx$  of tracks in the signal region, as described in Section 11.2. It is also possi-

ble to fit that measured distribution to a functional form to help smooth the distribution in the tails of  $dE/dx$  where the template is driven by a small number of tracks. Both Landau convolved with a Gaussian and Crystal Ball functions are considered as the functional form and used to re-estimate the background distribution. The deviations compared to the nominal method are found to be 4%, and this is taken as a systematic uncertainty to cover the inability carefully predict the contribution from the long tail of  $dE/dx$  where there are few measurements available in data.

#### 3541 12.1.1.2 MUON FRACTION

3542 The stable region of the analysis explicitly includes tracks identified as muons,  
 3543 which have a known difference in their  $dE/dx$  distributions compared to non-  
 3544 muon tracks (Section 11.1). To account for a difference in muon fraction be-  
 3545 tween the background region and the signal region for this selection, the  $dE/dx$   
 3546 templates for muons and non-muons are measured separately and then the rel-  
 3547 ative fraction of each is varied in the random generation. The muon fraction  
 3548 is varied by its statistical uncertainty and the resulting difference of 3% in back-  
 3549 ground yield is taken as the systematic uncertainty.

#### 3550 12.1.1.3 IBL CORRECTIONS

3551 The **IBL**, described in Section 5.3.1, received a significant dose of radiation during  
 3552 the data collection in 2015. The irradiation can cause a drift in the frontend  
 3553 electronics and thus alter the  $dE/dx$  measurement which includes the **ToT** output  
 3554 by the **IBL**. These effects are corrected for in the nominal analysis by scaling the  
 3555  $dE/dx$  measurements by a constant factor derived for each run to match the  
 3556 average  $dE/dx$  value to a reference run where the **IBL** was known to be stable  
 3557 to this effect. However, this corrective factor does not account for inter-run  
 3558 variations. To account for this potential drift of  $dE/dx$ , the correction procedure  
 3559 is repeated by varying the corrections up and down by the maximal run-to-run  
 3560 variation from the full data-taking period, which results in an uncertainty of  
 3561 3.8%.

#### 3562 12.1.1.4 NORMALIZATION

3563 As described in Section 11.2, the generated distribution of masses is normalized  
 3564 in a shoulder region ( $M < 160$  GeV) where signals have been excluded by pre-  
 3565 vious analyses. That normalization factor is varied by its statistical uncertainty  
 3566 and the resulting fluctuation in the mass distribution of 3% is taken as a system-  
 3567 atic uncertainty on the background estimate.

#### 3568 12.1.2 SIGNAL YIELD

3569 The systematic uncertainties on the signal yield can be divided into three cate-  
 3570 gories; those on the simulation process, those on the modeling of the detector  
 3571 efficiency or calibration, and those affecting the overall signal yield. They are  
 3572 summarized in Table 10. The largest uncertainty comes from the uncertainty

3573 on the production cross section for gluinos, which is the dominant systematic  
 3574 uncertainty in this analysis.

Source of Uncertainty	-[%]	+[%]
ISR Modeling (Metastable Region)	1.5	1.5
ISR Modeling (Stable Region)	14	14
Pile-up Reweighting	1.1	1.1
Trigger Efficiency Reweighting	0.9	0.9
$E_T^{\text{miss}}$ Scale	1.1	2.2
Ionization Parametrization	7.1	0
Momentum Parametrization	0.3	0.0
Electron Rejection	0.0	0.0
Hadron Rejection	0.0	0.0
$\mu$ Identification	4.3	4.3
Luminosity	5	5
Signal size uncertainty	28	28
Total (Metastable Region)	30	29
Total (Stable Region)	33	32

Table 11: A summary of the sources of systematic uncertainty for the simulated signal yield. The uncertainty depends on the mass and lifetime, and the maximum negative and positive values are reported in the table.

### 3575 12.1.2.1 ISR MODELING

3576 As discussed in Section 9.2, MadGraph is expected to reproduce the distribution  
 3577 of ISR in signal events more accurately than the nominal Pythia samples. The  
 3578 analysis reweights the distribution of ISR in the simulated signal events to match  
 3579 the distribution found in generated MadGraph samples. This has an effect on the  
 3580 selection efficiency in the signal samples, where ISR contributes to the generation  
 3581 of  $E_T^{\text{miss}}$ . To account for the potential inaccuracy on the simulation of ISR at high  
 3582 energies, half of the difference between the signal efficiency with the reweighted  
 3583 distribution and the original distribution is taken as a systematic uncertainty.

### 3584 12.1.2.2 PILEUP REWEIGHTING

3585 The simulated events were generated prior to data collection with an estimate of  
 3586 the average number of interactions per bunch crossing. This estimate does not  
 3587 match the value of pileup during actual data collection, but a large fraction of the  
 3588 simulated events would be discarded in order to match the distribution in data.  
 3589 Therefore the simulated signal events are not reweighted for pileup by default  
 3590 in the analysis. The effect of the pileup on signal efficiency is not expected to  
 3591 depend on the mass or lifetime of the generated signal events, which allows all

of the generated signal events to be used together to assess the pileup dependence. To account for the potential effect of the difference in the number of interactions per bunch crossing between data and simulation, the difference in yield between the nominal signal events and the reweighted events averaged over all masses and lifetimes is taken as a systematic uncertainty on the yield for each mass and lifetime (1.1%).

### 12.1.2.3 TRIGGER EFFICIENCY REWEIGHTING

As described in Section 10.2, the selection for this analysis does not require a sufficiently large value of  $E_T^{\text{miss}}$  to be above the plateau of trigger efficiency. Therefore, some signal events which would otherwise pass the event selection can be excluded because of the trigger requirement. These effects can be difficult to estimate in simulation, and thus are constrained by comparing data and simulated events in an alternative W boson region which uses decays to muons to find a relatively pure sample of events with missing energy. The trigger efficiency for data and simulated W events are shown in Figure 86. The comparison between data and MC in this region constrains the simulation of the trigger efficiency. The simulated signal events are reweighted by the ratio of data to simulation in the W boson decays, while the difference between the data and simulation in those decays is taken as a systematic uncertainty. This results in an uncertainty of only 0.9% as the majority of events are well above the plateau and the disagreement between data and simulation is small even below that plateau.

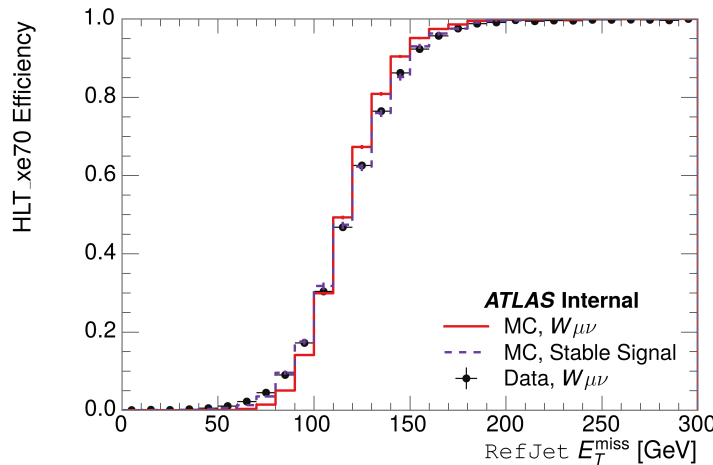


Figure 86: The trigger efficiency for the HLT\_xe70 trigger requirement as a function of Calorimeter  $E_T^{\text{miss}}$  for simulated data events with a W boson selection. Simulated signal events and simulated W boson events are also included.

### 12.1.2.4 MISSING TRANSVERSE MOMENTUM SCALE

The ATLAS Combined Performance (CP) group provides a default recommendation for systematic variations of jets and missing energy (**note: I'm not quite sure what to cite for this - I don't see any papers from the jet/met group**

Systematic Variation	-[%]	+[%]
JET_GroupedNP_1	-0.7	1.3
JET_GroupedNP_2	-0.7	1.2
JET_GroupedNP_3	-0.5	1.3

Table 12: Example of the contributing systematic variations to the total systematic for the  $E_T^{\text{miss}}$  Scale, as measured in a 1200 GeV, Stable R-Hadron signal sample.

3617 **after this was implemented).** These variations enter into this analysis only in  
 3618 the requirement on  $E_T^{\text{miss}}$ . The effect of the measured scale of  $E_T^{\text{miss}}$  is evaluated  
 3619 by varying the  $E_T^{\text{miss}}$  scale according to the one sigma variations provided by all  
 3620 **CP** recommendations on objects affecting event kinematics in simulated signal  
 3621 events. Missing energy is reconstructed from fully reconstructed objects so any  
 3622 systematic uncertainties affecting jets, muons, electrons, or the  $E_T^{\text{miss}}$  soft terms  
 3623 are included. The only non-negligible contributions found using this method are  
 3624 itemized in Table 12 for an example signal sample (1200 GeV, Stable R-Hadron),  
 3625 where the systematic is measured as the relative difference in the final signal ef-  
 3626 ficiency after applying the associated variation through the CP tools. The only  
 3627 variations that are significant are the grouped jet systematic variations, which  
 3628 combine recommended jet systematic uncertainties into linearly independent  
 3629 variations.

3630 As the peak of the reconstructed  $E_T^{\text{miss}}$  distribution in the signal is significantly  
 3631 above the current threshold for events which pass the trigger requirement, the  
 3632 effect of scale variation is expected to be small, which is consistent with the mea-  
 3633 sured systematic of approximately 2%. Events which do not pass the trigger re-  
 3634 quirement usually fail because there are no ISR jets in the event to balance the  
 3635  $R$ -hadrons' transverse momentum, so the reconstructed  $E_T^{\text{miss}}$  is low and there-  
 3636 fore also expected to be not very sensitive to scale changes.

### 3637 12.1.2.5 MOMENTUM PARAMETRIZATION

3638 The uncertainty on the signal efficiency from track momentum is calculated us-  
 3639 ing the **CP** group recommendations for tracks. In particular, only one recom-  
 3640 mended systematic variation affects track momentum, the sagitta bias for  $q/P$ .  
 3641 This uncertainty is propagated to the final selection efficiency by varying the  
 3642 track momentum by the recommended one sigma variation, and the associated  
 3643 uncertainty is found to be negligible (0.3%).

### 3644 12.1.2.6 IONIZATION REQUIREMENT

3645 The  $dE/dx$  distributions in data and simulated events have different most prob-  
 3646 able values, which is due in part to radiation effects in the detector that are not  
 3647 fully accounted for in the simulation. The difference does not affect the mass  
 3648 measurement used in this analysis, as independent calibrations are done in sim-  
 3649 ulation and in data. However, it does affect the efficiency of the high  $dE/dx$   
 3650 selection requirement. To calculate the size of the effect on the signal efficiency,

3651 the  $dE/dx$  distribution in signal simulation is scaled by a scale factor obtained  
 3652 from comparing the  $dE/dx$  distribution of inclusive tracks in data and in sim-  
 3653 ulation. The difference in efficiency for this sample with a scaled  $dE/dx$  dis-  
 3654 tribution, relative to the nominal case, is taken as a systematic uncertainty on  
 3655 signal efficiency. The uncertainty is as large as 7% for low masses and falls to a  
 3656 negligible effect for large masses.

### 3657 12.1.2.7 ELECTRON AND JET REJECTION

3658 The systematic uncertainty on the electron rejection is measured by varying the  
 3659 EM fraction requirement significantly, from 0.95 to 0.9. This is found to have  
 3660 a less than 0.04% effect on signal acceptance, on average, and so is completely  
 3661 negligible. Similarly, the uncertainty on jet rejection is measured by tightening  
 3662 the  $E/p$  requirement from 0.5 to 0.4. This is found to have no effect on signal  
 3663 acceptance, so again the systematic is again negligible.

### 3664 12.1.2.8 MUON VETO

3665 The metastable signal region requires that the candidate tracks are not identi-  
 3666 fied as medium muons because the majority of R-Hadrons in the lifetime range  
 3667 included in that region do not reach the muon spectrometers before they de-  
 3668 cay. However, the exponential tail of the R-Hadron lifetime distribution results  
 3669 in some R-Hadrons traversing the muon spectrometer. These can still fail the  
 3670 muon medium identification because they can fail on the requirement on the  
 3671 number of precision hits required to pass the loose selection because they ar-  
 3672 rive late to the muon spectrometer. This can be seen in Figure 87, which shows  
 3673 the efficiency of the muon veto as a function of  $1/\beta$ , for two simulated stable  
 3674 R-Hadron samples.

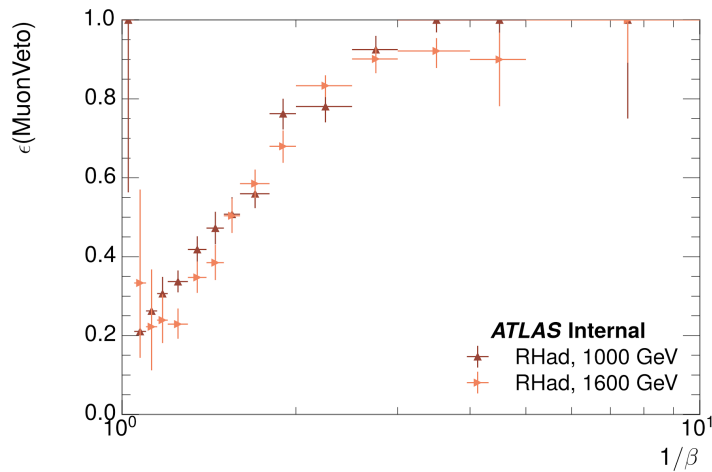


Figure 87: The efficiency of the muon veto for  $R$ -hadrons of two different masses, as a function of  $\frac{1}{\beta}$  for simulated R-Hadron tracks.

3675 Thus, the efficiency of the muon veto depends on the timing resolution of  
 3676 the spectrometer, so an uncertainty is applied to the signal efficiency to cover

3677 differences in timing resolution between data and simulation. First, a sample of  
 3678  $Z \rightarrow \mu\mu$  events is selected in data in which one of the muons has a late arrival  
 3679 time measured in the MDT. Then the reconstructed  $\beta$  distribution is compared  
 3680 to the distribution in simulated  $Z \rightarrow \mu\mu$  events; the difference between these  
 3681 two distributions reflects the difference in timing resolution between data and  
 3682 simulation. To emulate this difference in simulated signal events, the magnitude  
 3683 of the difference is used to scale and shift the true  $\beta$  distribution of R-Hadrons in  
 3684 simulation. Signal events are then reweighted based on this varied  $\beta$  distribution,  
 3685 and the difference in the efficiency of the muon veto selection is compared with  
 3686 the nominal and reweighted true  $\beta$  distributions. The difference in muon veto  
 3687 efficiency is taken as a systematic uncertainty of the muon veto.

3688 The comparison of reconstructed  $\beta$  between data and simulation is performed  
 3689 separately in the barrel, transition, and endcap regions of the spectrometer, and  
 3690 the reweighting of the true  $\beta$  distribution in signal is done per region. The com-  
 3691 parison of average reconstructed MDT  $\beta$  between data and simulation for the  
 3692 barrel region is shown in Figure 88 for  $Z \rightarrow \mu\mu$  events. As expected, The uncer-  
 3693 tainty is found to be negligible for R-hadrons with short lifetimes, and is only  
 3694 significant for lifetimes above 30 ns.

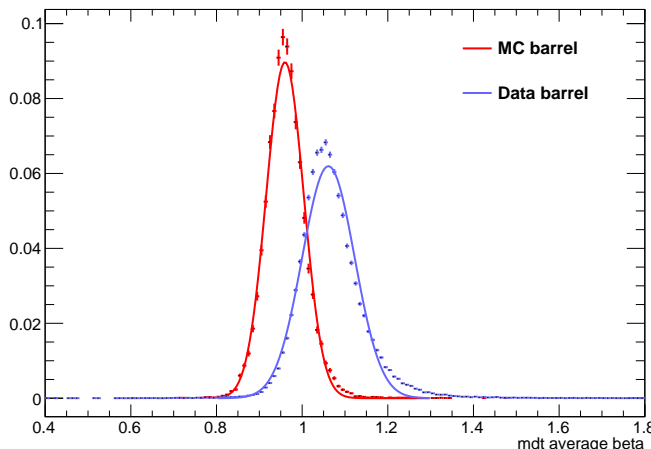


Figure 88: The average reconstructed MDT  $\beta$  distribution for  $Z \rightarrow \mu\mu$  events in which  
 one of the muons is reconstructed as a slow muon, for both data and simula-  
 tion. A gaussian fit is superimposed.

### 3695 12.1.2.9 LUMINOSITY

3696 The luminosity uncertainty is provided by a luminosity measurement on ATLAS  
 3697 and was measured to be 5% at the time of the publication of this analysis.

### 3698 12.1.2.10 SIGNAL SIZE

3699 As discussed in Section 9.2, the signal cross sections are calculated at NLO in the  
 3700 strong coupling constant with a resummation of soft-gluon emission at NLL. The  
 3701 uncertainties on those cross sections are between 14% to 28% for the R-Hadrons

Selection Region	Expected Background	Data
Stable	$17.2 \pm 2.6 \pm 1.2$	16
Metastable	$11.1 \pm 1.7 \pm 0.7$	11

Table 13: The estimated number of background events and the number of observed events in data for the specified selection regions prior to the requirement on mass. The background estimates show statistical and systematic uncertainties.

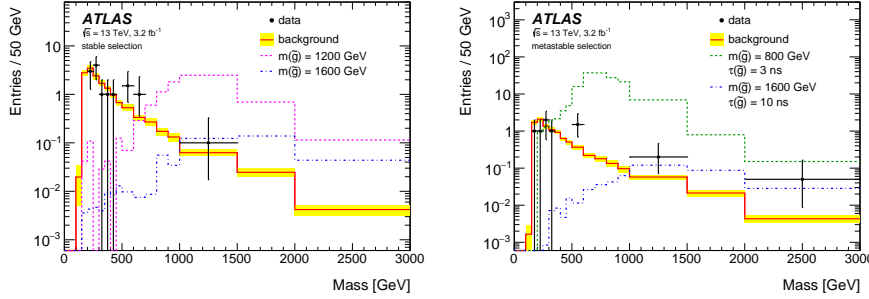


Figure 89: The observed mass distribution of events in data and the generated background distribution in (a) the stable and (b) the metastable signal region. A few example simulated signal distributions are superimposed.

3702 in the range of 400 to 1800 GeV [92, 93], where the uncertainty increases with  
3703 the mass.

## 3704 12.2 FINAL YIELDS

3705 This full analysis was performed using the  $3.2 \text{ fb}^{-1}$  from the 2015 data-taking.  
3706 Using the selections discussed in Chapter 10, sixteen events were observed in  
3707 the stable signal region and eleven events were observed in the metastable signal  
3708 region, prior to requirements on the candidate track mass. The background esti-  
3709 mate discussed in Chapter 11 predicts  $17 \pm 2.6(\text{stat}) \pm 1.2(\text{syst})$  events for the  
3710 stable region and  $11.1 \pm 1.7(\text{stat}) \pm 0.7(\text{syst})$  events for the metastable region.  
3711 These counts are summarized in Table 13.

3712 The mass estimated using  $dE/dx$  (Section 10.4.1) provides the final discrimi-  
3713 nating variable, where the signal would be expected as an excess in the falling ex-  
3714 ponential tail of the expected background. The observed distribution of masses  
3715 is shown in Figure 89, along with the predicted distribution from the background  
3716 estimate for each signal region. Both include a few example simulated signal dis-  
3717 tributions, which show the scale of an excess were the R-Hadron signals present.  
3718 There is no statistically significant evidence of an excess in the data over the back-  
3719 ground estimation. From this distribution it is clearly possible to rule out signals  
3720 with lower masses, around 1200 GeV, which have larger cross sections.

### 3721 12.3 CROSS SECTIONAL LIMITS

3722 Because there is no observed significant excess of events in the signal region, this  
 3723 analysis sets upper limits on the allowed cross section for R-Hadron production.  
 3724 These limits are set for each mass point by counting the observed events in data,  
 3725 along with the expected background and simulated signal events, in windows of  
 3726 mass. The mass windows are formed by fitting the distribution of signal events to  
 3727 a Gaussian distribution, and the window is then  $\pm 1.4\sigma$  around the center of that  
 3728 Gaussian. Two examples of the windows formed by this procedure are shown  
 3729 in Tables 14-15, for the stable and 10 ns working points. The corresponding  
 3730 counts of observed data, expected background, and simulated signal for those  
 3731 same working points are shown in Tables 16-17. Appendix B includes the mass  
 3732 windows and counts for all of the considered signal points.

$m(\tilde{g})$ [GeV]	Left Extremum [GeV]	Right Extremum [GeV]
1000	655	1349
1100	734	1455
1200	712	1631
1300	792	1737
1400	717	1926
1500	815	2117
1600	824	2122
1700	900	2274
1800	919	2344

Table 14: The left and right extremum of the mass window for each generated mass point with a 10 ns lifetime.

$m(\tilde{g})$ [GeV]	Left Extremum [GeV]	Right Extremum [GeV]
800	627	1053
1000	726	1277
1200	857	1584
1400	924	1937
1600	993	2308
1800	1004	2554

Table 15: The left and right extremum of the mass window used for each generated stable mass point.

3733 The 95% confidence level upper limits on the cross sections for a large grid of  
 3734 masses (between 800 and 1800 GeV) and lifetimes (between 0.4 and stable) are  
 3735 extracted from these counts with the  $CL_S$  method using the profile likelihood

$m(\tilde{g})$ [GeV]	Expected Signal	Expected Background	Observed Data
800	$462.83 \pm 14.86$	$1.764 \pm 0.080$	2.0
1000	$108.73 \pm 3.38$	$1.458 \pm 0.070$	1.0
1200	$31.74 \pm 0.95$	$1.137 \pm 0.060$	1.0
1400	$10.22 \pm 0.29$	$1.058 \pm 0.058$	1.0
1600	$3.07 \pm 0.09$	$0.947 \pm 0.054$	1.0
1800	$1.08 \pm 0.05$	$0.940 \pm 0.054$	1.0

Table 16: The expected number of signal events, the expected number of background events, and the observed number of events in data with their respective statistical errors within the respective mass window for each generated stable mass point

$m(\tilde{g})$ [GeV]	Expected Signal	Expected Background	Observed Data
1000	$144.48 \pm 5.14$	$1.499 \pm 0.069$	2.0
1100	$73.19 \pm 2.61$	$1.260 \pm 0.060$	2.0
1200	$41.54 \pm 1.41$	$1.456 \pm 0.067$	2.0
1300	$22.58 \pm 0.77$	$1.201 \pm 0.058$	2.0
1400	$12.70 \pm 0.42$	$1.558 \pm 0.071$	2.0
1500	$6.73 \pm 0.24$	$1.237 \pm 0.060$	2.0
1600	$3.90 \pm 0.13$	$1.201 \pm 0.058$	2.0
1700	$2.27 \pm 0.07$	$1.027 \pm 0.052$	2.0
1800	$1.34 \pm 0.04$	$1.019 \pm 0.052$	2.0

Table 17: The expected number of signal events, the expected number of background events, and the observed number of events in data with their respective statistical errors within the respective mass window for each generated mass point with a lifetime of 10 ns.

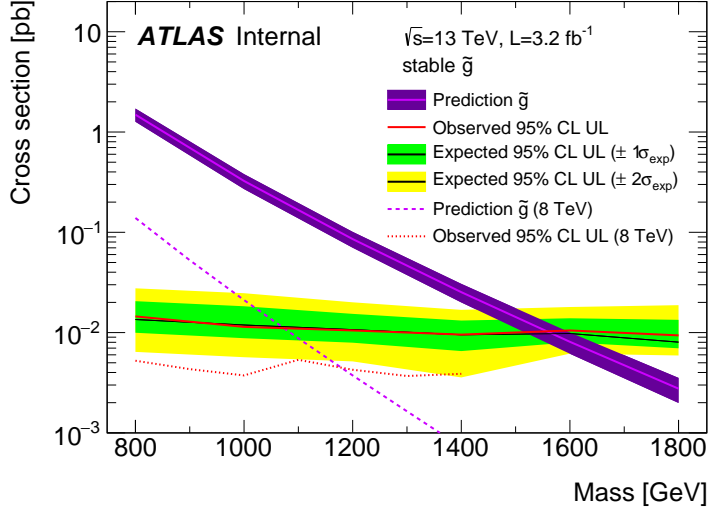


Figure 90: The observed and expected cross section limits as a function of mass for the stable simulated signal. The predicted cross section values for the corresponding signals are included.

ratio as a test statistic [97]. For this procedure, the systematic uncertainties estimated for the signal and background yields are treated as Gaussian-distributed nuisance parameters. The uncertainty on the normalization of the expected background distribution is included in the expected background events. At this point the expected cross section limit is calculated for both the metastable and stable signal region for each lifetime point, and the region with the best expected limit is selected for each lifetime. Using that procedure, the metastable region is used for lifetimes up to and including 30 ns, and the stable region for lifetimes above it.

The resulting cross-sectional upper limits are shown as a function of mass in Figure 90 and Figure 91 for each lifetime considered. The limits are interpolated linearly between each mass point, and the dependence of the limit on the mass is small as the efficiency is relatively constant for large R-Hadron masses. There is however a strong dependence on lifetime, as discussed in Section 10.5, where the probability to form a fully reconstructed track and the kinematic freedom to produce  $E_T^{\text{miss}}$  result in a local maximum in the limit at 10–30 ns. The figures also include the expected cross section for pair-produced gluino R-Hadrons for reference. For the 10 ns and stable cross section limits, both the observed limit and expected cross section for the Run 1, 8 TeV version of this analysis are included. There the cross sectional limits are lower because of the increased available luminosity, while the signal cross sections were also much lower because of the lower collision energy.

## 3758 12.4 MASS LIMITS

3759 The cross-sectional limits can then be used to derive a lower mass limit for gluino  
3760 R-Hadrons by comparing them to the theoretically predicted production cross

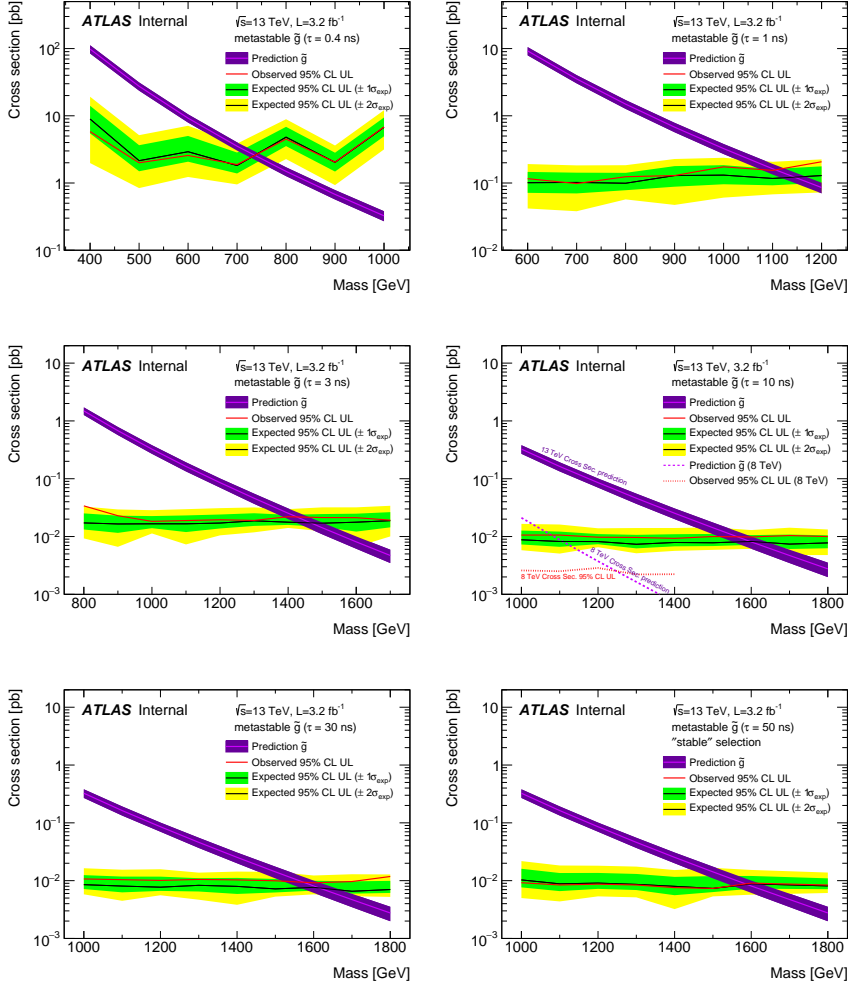


Figure 91: The observed and expected cross section limits as a function of mass for each generated lifetime. The predicted cross section values for the corresponding signals are included.

sections. These mass limits range from only 740 GeV at the lowest lifetimes considered, where the selection efficiency is very low, to up to 1580 GeV at 30 ns where the selection efficiency is maximized. The observed and expected mass limits for each lifetime point are detailed in Table 18, which also lists which selection region was used for each lifetime. These excluded range of masses as a function of lifetime is also shown in Figure 92. The Run 1 limits are included for comparison; the limits have increased by about 200 GeV on average. The search has also improved since the previous incarnation from Run 1 in optimizing the region between 30 GeV and detector-stable lifetimes by introducing the second signal region. The definition of the stable region prevents the significant drop in mass limit that occurred above 30 GeV in the Run 1 analysis.

Selection	$\tau$ [ns]	$M_{\text{obs}} > [\text{GeV}]$	$M_{\text{exp}} > [\text{GeV}]$
Metastable	0.4	740	730
"	1.0	1110	1150
"	3.0	1430	1470
"	10	1570	1600
"	30	1580	1620
Stable	50	1590	1590
"	stable	1570	1580

Table 18: The observed and expected 95% CL lower limit on mass for gluino R-Hadrons for each considered lifetime.

## 12.5 CONTEXT FOR LONG-LIVED SEARCHES

This search plays an important role in the current, combined [ATLAS](#) search for long lived particles. The mass limits provided by various [ATLAS](#) searches for long-lived gluino R-Hadrons can be seen in Figure 93. This search provides the most competitive limit for lifetimes between 3 ns up through very long lifetimes, where it is still competitive with dedicated searches for stable particles. The limits placed on gluino production are very similar to the limits on promptly decaying models.

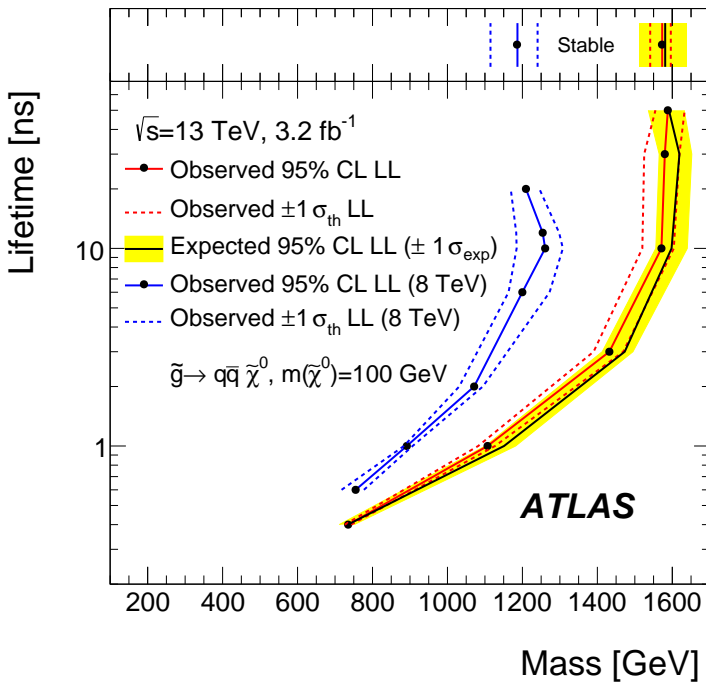


Figure 92: The excluded range of masses as a function of gluino lifetime. The expected lower limit (LL), with its experimental  $\pm 1\sigma$  band, is given with respect to the nominal theoretical cross-section. The observed 95% LL obtained at  $\sqrt{s} = 8 \text{ TeV}$  [80] is also shown for comparison.

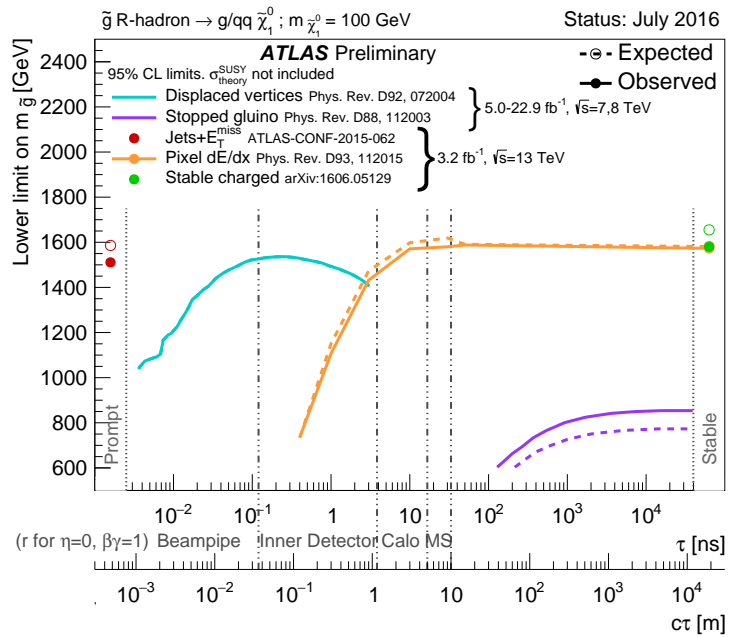


Figure 93: The constraints on the gluino mass as a function of lifetime for a split-supersymmetry model with the gluino R-Hadrons decaying into a gluon or light quarks and a neutralino with mass of 100 GeV. The solid lines indicate the observed limits, while the dashed lines indicate the expected limits. The area below the curves is excluded. The dots represent results for which the particle is assumed to be prompt or stable.

3780

## PART VI

3781

### CONCLUSIONS

3782

You can put some informational part preamble text here.

# 13

3783

## 3784 SUMMARY AND OUTLOOK

---

3785 13.1 SUMMARY

3786 13.2 OUTLOOK

3787

PART VII

3788

APPENDIX

3789

A

3790

3791 INELASTIC CROSS SECTION

---

$m(\tilde{g})$ [GeV]	Left Extremum [GeV]	Right Extremum [GeV]
1000	682	1387
1100	763	1478
1200	801	1606
1300	809	1841
1400	861	2011
1500	920	2032
1600	952	2173
1800	1017	2422

Table 19: The left and right extremum of the mass window for each generated mass point with a 50 ns lifetime.

$m(\tilde{g})$ [GeV]	Left Extremum [GeV]	Right Extremum [GeV]
1000	689	1321
1100	746	1513
1200	788	1670
1300	860	1734
1400	833	1925
1500	852	2048
1600	833	2283
1700	946	2379
1800	869	2505

Table 20: The left and right extremum of the mass window for each generated mass point with a 30 ns lifetime.

$m(\tilde{g})$ [GeV]	Left Extremum [GeV]	Right Extremum [GeV]
1000	655	1349
1100	734	1455
1200	712	1631
1300	792	1737
1400	717	1926
1500	815	2117
1600	824	2122
1700	900	2274
1800	919	2344

Table 21: The left and right extremum of the mass window for each generated mass point with a 10 ns lifetime.

$m(\tilde{g})$ [GeV]	Left Extremum [GeV]	Right Extremum [GeV]
800	531	1065
900	576	1165
1000	610	1345
1100	635	1432
1200	663	1563
1300	620	1667
1400	742	1727
1500	761	1937
1600	573	2000
1700	621	2182

Table 22: The left and right extremum of the mass window used for each generated mass point with a lifetime of 3 ns.

$m(\tilde{g})$ [GeV]	Left Extremum [GeV]	Right Extremum [GeV]
600	411	758
700	385	876
800	486	970
900	406	987
1000	408	1136
1100	555	1196
1200	516	1378

Table 23: The left and right extremum of the mass window used for each mass point with a lifetime of 1 ns.

$m(\tilde{g})$ [GeV]	Left Extremum [GeV]	Right Extremum [GeV]
400	204	510
500	295	639
600	288	702
700	323	701
800	190	771
900	277	677
1000	249	688

Table 24: The left and right extremum of the mass window for each generated mass point with a lifetime of 0.4 ns.

$m(\tilde{g})$ [GeV]	Left Extremum [GeV]	Right Extremum [GeV]
800	627	1053
1000	726	1277
1200	857	1584
1400	924	1937
1600	993	2308
1800	1004	2554

Table 25: The left and right extremum of the mass window used for each generated stable mass point.

$m(\tilde{g})$ [GeV]	Expected Signal	Expected Background	Observed Data
1000	$131.18 \pm 6.35$	$1.803 \pm 0.081$	$1.0 \pm 1.0$
1100	$71.11 \pm 3.35$	$1.409 \pm 0.069$	$1.0 \pm 1.0$
1200	$37.18 \pm 1.75$	$1.310 \pm 0.066$	$1.0 \pm 1.0$
1300	$20.76 \pm 0.95$	$1.431 \pm 0.069$	$1.0 \pm 1.0$
1400	$12.63 \pm 0.57$	$1.273 \pm 0.065$	$1.0 \pm 1.0$
1500	$6.57 \pm 0.29$	$1.115 \pm 0.059$	$1.0 \pm 1.0$
1600	$3.56 \pm 0.16$	$1.041 \pm 0.057$	$1.0 \pm 1.0$
1800	$1.27 \pm 0.05$	$0.918 \pm 0.053$	$1.0 \pm 1.0$

Table 26: The expected number of signal events, the expected number of background events, and the observed number of events in data with their respective statistical errors within the respective mass window for each generated mass point with a lifetime of 50 ns.

$m(\tilde{g})$ [GeV]	Expected Signal	Expected Background	Observed Data
1000	$144.65 \pm 6.34$	$1.328 \pm 0.063$	$2.0 \pm 1.4$
1100	$75.28 \pm 3.27$	$1.255 \pm 0.060$	$2.0 \pm 1.4$
1200	$40.51 \pm 1.75$	$1.193 \pm 0.058$	$2.0 \pm 1.4$
1300	$20.91 \pm 0.93$	$0.997 \pm 0.051$	$2.0 \pm 1.4$
1400	$11.97 \pm 0.51$	$1.131 \pm 0.056$	$2.0 \pm 1.4$
1500	$6.81 \pm 0.28$	$1.111 \pm 0.055$	$2.0 \pm 1.4$
1600	$4.19 \pm 0.16$	$1.193 \pm 0.058$	$2.0 \pm 1.4$
1700	$2.42 \pm 0.09$	$0.963 \pm 0.050$	$2.0 \pm 1.4$
1800	$1.46 \pm 0.05$	$1.138 \pm 0.056$	$3.0 \pm 1.7$

Table 27: The expected number of signal events, the expected number of background events, and the observed number of events in data with their respective statistical errors within the respective mass window for each generated mass point with a lifetime of 30 ns.

$m(\tilde{g})$ [GeV]	Expected Signal	Expected Background	Observed Data
1000	$144.48 \pm 5.14$	$1.499 \pm 0.069$	$2.0 \pm 1.4$
1100	$73.19 \pm 2.61$	$1.260 \pm 0.060$	$2.0 \pm 1.4$
1200	$41.54 \pm 1.41$	$1.456 \pm 0.067$	$2.0 \pm 1.4$
1300	$22.58 \pm 0.77$	$1.201 \pm 0.058$	$2.0 \pm 1.4$
1400	$12.70 \pm 0.42$	$1.558 \pm 0.071$	$2.0 \pm 1.4$
1500	$6.73 \pm 0.24$	$1.237 \pm 0.060$	$2.0 \pm 1.4$
1600	$3.90 \pm 0.13$	$1.201 \pm 0.058$	$2.0 \pm 1.4$
1700	$2.27 \pm 0.07$	$1.027 \pm 0.052$	$2.0 \pm 1.4$
1800	$1.34 \pm 0.04$	$1.019 \pm 0.052$	$2.0 \pm 1.4$

Table 28: The expected number of signal events, the expected number of background events, and the observed number of events in data with their respective statistical errors within the respective mass window for each generated mass point with a lifetime of 10 ns.

$m(\tilde{g})$ [GeV]	Expected Signal	Expected Background	Observed Data
800	$362.97 \pm 14.68$	$1.841 \pm 0.080$	$5.0 \pm 2.2$
900	$169.20 \pm 6.69$	$1.710 \pm 0.076$	$3.0 \pm 1.7$
1000	$84.78 \pm 3.23$	$1.727 \pm 0.076$	$2.0 \pm 1.4$
1100	$40.06 \pm 1.60$	$1.679 \pm 0.075$	$2.0 \pm 1.4$
1200	$20.06 \pm 0.81$	$1.598 \pm 0.072$	$2.0 \pm 1.4$
1300	$10.76 \pm 0.43$	$1.851 \pm 0.080$	$2.0 \pm 1.4$
1400	$5.52 \pm 0.22$	$1.374 \pm 0.064$	$2.0 \pm 1.4$
1500	$3.16 \pm 0.13$	$1.355 \pm 0.064$	$2.0 \pm 1.4$
1600	$2.13 \pm 0.11$	$2.235 \pm 0.093$	$3.0 \pm 1.7$
1700	$1.10 \pm 0.06$	$1.995 \pm 0.085$	$2.0 \pm 1.4$

Table 29: The expected number of signal events, the expected number of background events, and the observed number of events in data with their respective statistical errors within the respective mass window for each generated mass point with a lifetime of 3 ns.

$m(\tilde{g})$ [GeV]	Expected Signal	Expected Background	Observed Data
600	$431.80 \pm 36.60$	$2.418 \pm 0.099$	$3.0 \pm 1.7$
700	$192.77 \pm 15.28$	$3.267 \pm 0.126$	$3.0 \pm 1.7$
800	$69.63 \pm 5.90$	$2.125 \pm 0.089$	$3.0 \pm 1.7$
900	$28.91 \pm 2.59$	$3.114 \pm 0.121$	$3.0 \pm 1.7$
1000	$13.64 \pm 1.22$	$3.359 \pm 0.129$	$5.0 \pm 2.2$
1100	$6.13 \pm 0.57$	$1.879 \pm 0.081$	$3.0 \pm 1.7$
1200	$3.24 \pm 0.30$	$2.387 \pm 0.098$	$5.0 \pm 2.2$

Table 30: The expected number of signal events, the expected number of background events, and the observed number of events in data with their respective statistical errors within the respective mass window for each generated mass point with a lifetime of 1 ns.

$m(\tilde{g})$ [GeV]	Expected Signal	Expected Background	Observed Data
400	$181.71 \pm 75.59$	$6.780 \pm 0.238$	$4.0 \pm 2.0$
500	$103.88 \pm 30.05$	$4.310 \pm 0.160$	$4.0 \pm 2.0$
600	$28.34 \pm 9.34$	$4.868 \pm 0.177$	$4.0 \pm 2.0$
700	$13.62 \pm 4.00$	$3.908 \pm 0.147$	$4.0 \pm 2.0$
800	$2.75 \pm 1.15$	$9.001 \pm 0.308$	$8.0 \pm 2.8$
900	$2.25 \pm 0.71$	$5.045 \pm 0.183$	$5.0 \pm 2.2$
1000	$0.34 \pm 0.19$	$6.026 \pm 0.214$	$6.0 \pm 2.4$

Table 31: The expected number of signal events, the expected number of background events, and the observed number of events in data with their respective statistical errors within the respective mass window for each generated mass point with a lifetime of p4 ns.

$m(\tilde{g})$ [GeV]	Expected Signal	Expected Background	Observed Data
800	$462.83 \pm 14.86$	$1.764 \pm 0.080$	$2.0 \pm 1.4$
1000	$108.73 \pm 3.38$	$1.458 \pm 0.070$	$1.0 \pm 1.0$
1200	$31.74 \pm 0.95$	$1.137 \pm 0.060$	$1.0 \pm 1.0$
1400	$10.22 \pm 0.29$	$1.058 \pm 0.058$	$1.0 \pm 1.0$
1600	$3.07 \pm 0.09$	$0.947 \pm 0.054$	$1.0 \pm 1.0$
1800	$1.08 \pm 0.05$	$0.940 \pm 0.054$	$1.0 \pm 1.0$

Table 32: The expected number of signal events, the expected number of background events, and the observed number of events in data with their respective statistical errors within the respective mass window for each generated stable mass point

- 3795 [1] A. D. Martin, W. J. Stirling, R. S. Thorne, and G. Watt. “Parton distributions  
3796 for the LHC”. In: *Eur. Phys. J.* C63 (2009), pp. 189–285. doi: [10.1140/epjc/s10052-009-1072-5](https://doi.org/10.1140/epjc/s10052-009-1072-5). arXiv: [0901.0002](https://arxiv.org/abs/0901.0002) [hep-ph].  
3797
- 3798 [2] Prajwal Raj Kafle, Sanjib Sharma, Geraint F. Lewis, and Joss Bland-Hawthorn.  
3799 “On the Shoulders of Giants: Properties of the Stellar Halo and the Milky  
3800 Way Mass Distribution”. In: *Astrophys. J.* 794.1 (2014), p. 59. doi: [10.1088/0004-637X/794/1/59](https://doi.org/10.1088/0004-637X/794/1/59). arXiv: [1408.1787](https://arxiv.org/abs/1408.1787) [astro-ph.GA].  
3801
- 3802 [3] K. A. Olive et al. “Review of Particle Physics”. In: *Chin. Phys. C38* (2014),  
3803 p. 090001. doi: [10.1088/1674-1137/38/9/090001](https://doi.org/10.1088/1674-1137/38/9/090001).
- 3804 [4] Lawrence J. Hall, Yasunori Nomura, and Satoshi Shirai. “Spread Super-  
3805 symmetry with Wino LSP: Gluino and Dark Matter Signals”. In: *JHEP* 01  
3806 (2013), p. 036. doi: [10.1007/JHEP01\(2013\)036](https://doi.org/10.1007/JHEP01(2013)036). arXiv: [1210.2395](https://arxiv.org/abs/1210.2395)  
3807 [hep-ph].
- 3808 [5] G. F. Giudice and A. Romanino. “Split supersymmetry”. In: *Nucl. Phys. B*  
3809 699 (2004), p. 65. doi: [10.1016/j.nuclphysb.2004.11.048](https://doi.org/10.1016/j.nuclphysb.2004.11.048). arXiv:  
3810 [hep-ph/0406088](https://arxiv.org/abs/hep-ph/0406088).
- 3811 [6] N. Arkani-Hamed, S. Dimopoulos, G. F. Giudice, and A. Romanino. “As-  
3812 pects of split supersymmetry”. In: *Nucl. Phys. B* 709 (2005), p. 3. doi: [10.1016/j.nuclphysb.2004.12.026](https://doi.org/10.1016/j.nuclphysb.2004.12.026). arXiv: [hep-ph/0409232](https://arxiv.org/abs/hep-ph/0409232).  
3813
- 3814 [7] Lyndon Evans and Philip Bryant. “LHC Machine”. In: *JINST* 3 (2008), S08001.  
3815 doi: [10.1088/1748-0221/3/08/S08001](https://doi.org/10.1088/1748-0221/3/08/S08001).
- 3816 [8] C Lefevre. “LHC: the guide (English version). Guide du LHC (version anglaise)”.  
3817 2009. URL: <https://cds.cern.ch/record/1165534>.
- 3818 [9] “LEP Design Report Vol.1”. In: (1983).
- 3819 [10] ATLAS Collaboration. “The ATLAS Experiment at the CERN Large Hadron  
3820 Collider”. In: *JINST* 3 (2008), S08003. doi: [10.1088/1748-0221/3/08/S08003](https://doi.org/10.1088/1748-0221/3/08/S08003).
- 3821
- 3822 [11] S. Chatrchyan et al. “The CMS experiment at the CERN LHC”. In: *JINST*  
3823 3 (2008), S08004. doi: [10.1088/1748-0221/3/08/S08004](https://doi.org/10.1088/1748-0221/3/08/S08004).
- 3824 [12] A. Augusto Alves Jr. et al. “The LHCb Detector at the LHC”. In: *JINST* 3  
3825 (2008), S08005. doi: [10.1088/1748-0221/3/08/S08005](https://doi.org/10.1088/1748-0221/3/08/S08005).
- 3826 [13] K. Aamodt et al. “The ALICE experiment at the CERN LHC”. In: *JINST* 3  
3827 (2008), S08002. doi: [10.1088/1748-0221/3/08/S08002](https://doi.org/10.1088/1748-0221/3/08/S08002).
- 3828 [14] Daniel Froidevaux and Paris Sphicas. “General-Purpose Detectors for the  
3829 Large Hadron Collider”. In: *Annual Review of Nuclear and Particle Science*  
3830 56.1 (2006), pp. 375–440. doi: [10.1146/annurev.nucl.54.070103.181209](https://doi.org/10.1146/annurev.nucl.54.070103.181209). URL: <http://dx.doi.org/10.1146/annurev.nucl.54.070103.181209>.
- 3831

- 3833 [15] M Capeans, G Darbo, K Einsweiller, M Elsing, T Flick, M Garcia-Sciveres,  
 3834 C Gemme, H Pernegger, O Rohne, and R Vuillermet. *ATLAS Insertable B-*  
 3835 *Layer Technical Design Report*. Tech. rep. CERN-LHCC-2010-013. ATLAS-  
 3836 TDR-19. 2010. URL: <https://cds.cern.ch/record/1291633>.
- 3837 [16] T. Cornelissen, M. Elsing, S. Fleischmann, W. Liebig, and E. Moyse. “Con-  
 3838 cepts, Design and Implementation of the ATLAS New Tracking (NEWT)”. In: (2007). Ed. by A. Salzburger.
- 3840 [17] “Performance of the ATLAS Inner Detector Track and Vertex Reconstruc-  
 3841 tion in the High Pile-Up LHC Environment”. In: (2012).
- 3842 [18] A. Salzburger. “The ATLAS Track Extrapolation Package”. In: (2007).
- 3843 [19] ATLAS Collaboration. “A neural network clustering algorithm for the AT-  
 3844 LAS silicon pixel detector”. In: *JINST* 9 (2014), P09009. doi: [10.1088/1748-0221/9/09/P09009](https://doi.org/10.1088/1748-0221/9/09/P09009). arXiv: [1406.7690 \[hep-ex\]](https://arxiv.org/abs/1406.7690).
- 3846 [20] ATLAS Collaboration. *Performance of primary vertex reconstruction in proton-*  
 3847 *proton collisions at  $\sqrt{s} = 7 \text{ TeV}$  in the ATLAS experiment*. ATLAS-CONF-  
 3848 2010-069. 2010. URL: <https://cds.cern.ch/record/1281344>.
- 3849 [21] ATLAS Collaboration. “Electron reconstruction and identification efficiency  
 3850 measurements with the ATLAS detector using the 2011 LHC proton–proton  
 3851 collision data”. In: *Eur. Phys. J. C* 74 (2014), p. 2941. doi: [10.1140/epjc/s10052-014-2941-0](https://doi.org/10.1140/epjc/s10052-014-2941-0). arXiv: [1404.2240 \[hep-ex\]](https://arxiv.org/abs/1404.2240). PERF-2013-03.
- 3853 [22] ATLAS Collaboration. *Electron efficiency measurements with the ATLAS de-*  
 3854 *tector using the 2012 LHC proton–proton collision data*. ATLAS-CONF-2014-  
 3855 032. 2014. URL: <https://cds.cern.ch/record/1706245>.
- 3856 [23] ATLAS Collaboration. *Measurements of the photon identification efficiency*  
 3857 *with the ATLAS detector using  $4.9 \text{ fb}^{-1}$  of  $pp$  collision data collected in 2011*.  
 3858 ATLAS-CONF-2012-123. 2012. URL: <https://cds.cern.ch/record/1473426>.
- 3860 [24] ATLAS Collaboration. “Muon reconstruction performance of the ATLAS  
 3861 detector in proton–proton collision data at  $\sqrt{s} = 13 \text{ TeV}$ ”. In: (2016).  
 3862 arXiv: [1603.05598 \[hep-ex\]](https://arxiv.org/abs/1603.05598). PERF-2015-10.
- 3863 [25] ATLAS Collaboration. “Topological cell clustering in the ATLAS calorime-  
 3864 ters and its performance in LHC Run 1”. In: (2016). arXiv: [1603.02934](https://arxiv.org/abs/1603.02934)  
 3865 [hep-ex]. PERF-2014-07.
- 3866 [26] ATLAS Collaboration. *Properties of jets and inputs to jet reconstruction and*  
 3867 *calibration with the ATLAS detector using proton–proton collisions at  $\sqrt{s} =$*   
 3868 *13 TeV*. ATL-PHYS-PUB-2015-036. 2015. URL: <https://cds.cern.ch/record/2044564>.
- 3870 [27] Matteo Cacciari, Gavin P. Salam, and Gregory Soyez. “The anti- $k_t$  jet clus-  
 3871 tering algorithm”. In: *JHEP* 04 (2008), p. 063. doi: [10.1088/1126-6708/2008/04/063](https://doi.org/10.1088/1126-6708/2008/04/063). arXiv: [0802.1189 \[hep-ph\]](https://arxiv.org/abs/0802.1189).
- 3873 [28] ATLAS Collaboration. *Jet global sequential corrections with the ATLAS detec-*  
 3874 *tor in proton–proton collisions at  $\sqrt{s} = 8 \text{ TeV}$* . ATLAS-CONF-2015-002.  
 3875 2015. URL: <https://cds.cern.ch/record/2001682>.

- 3876 [29] S. Agostinelli et al. “GEANT4: A simulation toolkit”. In: *Nucl. Instrum. Meth. A* 506 (2003), pp. 250–303. doi: [10.1016/S0168-9002\(03\)01368-8](https://doi.org/10.1016/S0168-9002(03)01368-8).
- 3877
- 3878 [30] ATLAS Collaboration. “A study of the material in the ATLAS inner detector using secondary hadronic interactions”. In: *JINST* 7 (2012), P01013. doi: [10.1088/1748-0221/7/01/P01013](https://doi.org/10.1088/1748-0221/7/01/P01013). arXiv: [1110.6191 \[hep-ex\]](https://arxiv.org/abs/1110.6191).  
PERF-2011-08.
- 3880
- 3882 [31] ATLAS Collaboration. “Electron and photon energy calibration with the ATLAS detector using LHC Run 1 data”. In: *Eur. Phys. J. C* 74 (2014), p. 3071. doi: [10.1140/epjc/s10052-014-3071-4](https://doi.org/10.1140/epjc/s10052-014-3071-4). arXiv: [1407.5063 \[hep-ex\]](https://arxiv.org/abs/1407.5063).  
PERF-2013-05.
- 3884
- 3886 [32] ATLAS Collaboration. “A measurement of the calorimeter response to single hadrons and determination of the jet energy scale uncertainty using LHC Run-1  $pp$ -collision data with the ATLAS detector”. In: (2016). arXiv: [1607.08842 \[hep-ex\]](https://arxiv.org/abs/1607.08842).  
PERF-2015-05.
- 3888
- 3890 [33] ATLAS Collaboration. “Single hadron response measurement and calorimeter jet energy scale uncertainty with the ATLAS detector at the LHC”. In: *Eur. Phys. J. C* 73 (2013), p. 2305. doi: [10.1140/epjc/s10052-013-2305-1](https://doi.org/10.1140/epjc/s10052-013-2305-1). arXiv: [1203.1302 \[hep-ex\]](https://arxiv.org/abs/1203.1302).  
PERF-2011-05.
- 3892
- 3894 [34] ATLAS Collaboration. “The ATLAS Simulation Infrastructure”. In: *Eur. Phys. J. C* 70 (2010), p. 823. doi: [10.1140/epjc/s10052-010-1429-9](https://doi.org/10.1140/epjc/s10052-010-1429-9).  
arXiv: [1005.4568 \[hep-ex\]](https://arxiv.org/abs/1005.4568). SOFT-2010-01.
- 3896
- 3897 [35] T. Sjöstrand, S. Mrenna, and P. Skands. “A Brief Introduction to PYTHIA 8.1”. In: *Comput. Phys. Commun.* 178 (2008), pp. 852–867. doi: [10.1016/j.cpc.2008.01.036](https://doi.org/10.1016/j.cpc.2008.01.036). arXiv: [0710.3820](https://arxiv.org/abs/0710.3820).
- 3900
- 3901 [36] ATLAS Collaboration. *Summary of ATLAS Pythia 8 tunes*. ATL-PHYS-PUB-2012-003. 2012. URL: <http://cds.cern.ch/record/1474107>.
- 3903
- 3904 [37] A.D. Martin, W.J. Stirling, R.S. Thorne, and G. Watt. “Parton distributions for the LHC”. In: *Eur. Phys. J. C* 63 (2009). Figures from the [MSTW Website](#), pp. 189–285. doi: [10.1140/epjc/s10052-009-1072-5](https://doi.org/10.1140/epjc/s10052-009-1072-5). arXiv: [0901.0002](https://arxiv.org/abs/0901.0002).
- 3906
- 3907 [38] A. Sherstnev and R.S. Thorne. “Parton Distributions for LO Generators”. In: *Eur. Phys. J. C* 55 (2008), pp. 553–575. doi: [10.1140/epjc/s10052-008-0610-x](https://doi.org/10.1140/epjc/s10052-008-0610-x). arXiv: [0711.2473](https://arxiv.org/abs/0711.2473).
- 3908
- 3909 [39] A. Ribon et al. *Status of Geant4 hadronic physics for the simulation of LHC experiments at the start of LHC physics program*. CERN-LCGAPP-2010-02. 2010. URL: <http://lcgapp.cern.ch/project/docs/noteStatusHadronic2010.pdf>.
- 3910
- 3911
- 3912
- 3913 [40] M. P. Guthrie, R. G. Alsmiller, and H. W. Bertini. “Calculation of the capture of negative pions in light elements and comparison with experiments pertaining to cancer radiotherapy”. In: *Nucl. Instrum. Meth.* 66 (1968), pp. 29–36. doi: [10.1016/0029-554X\(68\)90054-2](https://doi.org/10.1016/0029-554X(68)90054-2).
- 3914
- 3915
- 3916

- 3917 [41] H. W. Bertini and P. Guthrie. "News item results from medium-energy  
 3918 intranuclear-cascade calculation". In: *Nucl. Instr. and Meth. A* 169 (1971),  
 3919 p. 670. doi: [10.1016/0375-9474\(71\)90710-X](https://doi.org/10.1016/0375-9474(71)90710-X).
- 3920 [42] V.A. Karmanov. "Light Front Wave Function of Relativistic Composite  
 3921 System in Explicitly Solvable Model". In: *Nucl. Phys. B* 166 (1980), p. 378.  
 3922 doi: [10.1016/0550-3213\(80\)90204-7](https://doi.org/10.1016/0550-3213(80)90204-7).
- 3923 [43] H. S. Fesefeldt. *GHEISHA program*. Pitha-85-02, Aachen. 1985.
- 3924 [44] G. Folger and J.P. Wellisch. "String parton models in Geant4". In: (2003).  
 3925 arXiv: [nucl-th/0306007](https://arxiv.org/abs/nucl-th/0306007).
- 3926 [45] N. S. Amelin et al. "Transverse flow and collectivity in ultrarelativistic  
 3927 heavy-ion collisions". In: *Phys. Rev. Lett.* 67 (1991), p. 1523. doi: [10.1103/PhysRevLett.67.1523](https://doi.org/10.1103/PhysRevLett.67.1523).
- 3929 [46] N. S. Amelin et al. "Collectivity in ultrarelativistic heavy ion collisions". In:  
 3930 *Nucl. Phys. A* 544 (1992), p. 463. doi: [10.1016/0375-9474\(92\)90598-E](https://doi.org/10.1016/0375-9474(92)90598-E).
- 3932 [47] L. V. Bravina et al. "Fluid dynamics and Quark Gluon string model - What  
 3933 we can expect for Au+Au collisions at 11.6 AGeV/c". In: *Nucl. Phys. A* 566  
 3934 (1994), p. 461. doi: [10.1016/0375-9474\(94\)90669-6](https://doi.org/10.1016/0375-9474(94)90669-6).
- 3935 [48] L. V. Bravin et al. "Scaling violation of transverse flow in heavy ion colli-  
 3936 sions at AGS energies". In: *Phys. Lett. B* 344 (1995), p. 49. doi: [10.1016/0370-2693\(94\)01560-Y](https://doi.org/10.1016/0370-2693(94)01560-Y).
- 3938 [49] B. Andersson et al. "A model for low-pT hadronic reactions with general-  
 3939 izations to hadron-nucleus and nucleus-nucleus collisions". In: *Nucl. Phys. B* 281 (1987), p. 289. doi: [10.1016/0550-3213\(87\)90257-4](https://doi.org/10.1016/0550-3213(87)90257-4).
- 3941 [50] B. Andersson, A. Tai, and B.-H. Sa. "Final state interactions in the (nuclear)  
 3942 FRITIOF string interaction scenario". In: *Z. Phys. C* 70 (1996), pp. 499–  
 3943 506. doi: [10.1007/s002880050127](https://doi.org/10.1007/s002880050127).
- 3944 [51] B. Nilsson-Almqvist and E. Stenlund. "Interactions Between Hadrons and  
 3945 Nuclei: The Lund Monte Carlo, Fritiof Version 1.6". In: *Comput. Phys. Com-  
 3946 mun.* 43 (1987), p. 387. doi: [10.1016/0010-4655\(87\)90056-7](https://doi.org/10.1016/0010-4655(87)90056-7).
- 3947 [52] B. Ganhuyag and V. Uzhinsky. "Modified FRITIOF code: Negative charged  
 3948 particle production in high energy nucleus nucleus interactions". In: *Czech.  
 3949 J. Phys.* 47 (1997), pp. 913–918. doi: [10.1023/A:1021296114786](https://doi.org/10.1023/A:1021296114786).
- 3950 [53] ATLAS Collaboration. "Topological cell clustering in the ATLAS calorime-  
 3951 ters and its performance in LHC Run 1". In: (2016). arXiv: [1603.02934](https://arxiv.org/abs/1603.02934)  
 3952 [[hep-ex](#)].
- 3953 [54] Peter Speckmayer. "Energy Measurement of Hadrons with the CERN AT-  
 3954 LAS Calorimeter". Presented on 18 Jun 2008. PhD thesis. Vienna: Vienna,  
 3955 Tech. U., 2008. URL: <http://cds.cern.ch/record/1112036>.
- 3956 [55] CMS Collaboration. "The CMS barrel calorimeter response to particle  
 3957 beams from 2 to 350 GeV/c". In: *Eur. Phys. J. C* 60.3 (2009). doi: [10.1140/epjc/s10052-009-0959-5](https://doi.org/10.1140/epjc/s10052-009-0959-5).

- 3959 [56] J. Beringer et al. (Particle Data Group). “Review of Particle Physics”. In:  
 3960 *Chin. Phys. C* 38 (2014), p. 090001. URL: <http://pdg.lbl.gov>.
- 3961 [57] P. Adragna et al. “Measurement of Pion and Proton Response and Lon-  
 3962 gitudinal Shower Profiles up to 20 Nuclear Interaction Lengths with the  
 3963 ATLAS Tile Calorimeter”. In: *Nucl. Instrum. Meth. A* 615 (2010), pp. 158–  
 3964 181. doi: [10.1016/j.nima.2010.01.037](https://doi.org/10.1016/j.nima.2010.01.037).
- 3965 [58] ATLAS Collaboration. “Jet energy measurement and its systematic uncer-  
 3966 tainty in proton–proton collisions at  $\sqrt{s} = 7$  TeV with the ATLAS detec-  
 3967 tor”. In: *Eur. Phys. J. C* 75 (2015), p. 17. doi: [10.1140/epjc/s10052-014-3190-y](https://doi.org/10.1140/epjc/s10052-014-3190-y). arXiv: [1406.0076 \[hep-ex\]](https://arxiv.org/abs/1406.0076). PERF-2012-01.
- 3969 [59] Hung-Liang Lai, Marco Guzzi, Joey Huston, Zhao Li, Pavel M. Nadolsky,  
 3970 et al. “New parton distributions for collider physics”. In: *Phys. Rev. D* 82  
 3971 (2010), p. 074024. doi: [10.1103/PhysRevD.82.074024](https://doi.org/10.1103/PhysRevD.82.074024). arXiv: [1007.2241 \[hep-ph\]](https://arxiv.org/abs/1007.2241).
- 3973 [60] E. Abat et al. “Study of energy response and resolution of the ATLAS barrel  
 3974 calorimeter to hadrons of energies from 20 to 350 GeV”. In: *Nucl. Instrum.*  
 3975 *Meth. A* 621.1–3 (2010), pp. 134 –150. doi: <http://dx.doi.org/10.1016/j.nima.2010.04.054>.
- 3977 [61] ATLAS Collaboration. “Jet energy measurement with the ATLAS detector  
 3978 in proton–proton collisions at  $\sqrt{s} = 7$  TeV”. In: *Eur. Phys. J. C* 73 (2013),  
 3979 p. 2304. doi: [10.1140/epjc/s10052-013-2304-2](https://doi.org/10.1140/epjc/s10052-013-2304-2). arXiv: [1112.6426 \[hep-ex\]](https://arxiv.org/abs/1112.6426). PERF-2011-03.
- 3981 [62] Nausheen R. Shah and Carlos E. M. Wagner. “Gravitons and dark matter in  
 3982 universal extra dimensions”. In: *Phys. Rev. D* 74 (2006), p. 104008. doi: [10.1103/PhysRevD.74.104008](https://doi.org/10.1103/PhysRevD.74.104008). arXiv: [hep-ph/0608140 \[hep-ph\]](https://arxiv.org/abs/hep-ph/0608140).
- 3984 [63] Jonathan L. Feng, Arvind Rajaraman, and Fumihiro Takayama. “Graviton  
 3985 cosmology in universal extra dimensions”. In: *Phys. Rev. D* 68 (2003), p. 085018.  
 3986 doi: [10.1103/PhysRevD.68.085018](https://doi.org/10.1103/PhysRevD.68.085018). arXiv: [hep-ph/0307375 \[hep-ph\]](https://arxiv.org/abs/hep-ph/0307375).
- 3988 [64] Paul H. Frampton and Pham Quang Hung. “Long-lived quarks?” In: *Phys.*  
 3989 *Rev. D* 58 (5 1998), p. 057704. doi: [10.1103/PhysRevD.58.057704](https://doi.org/10.1103/PhysRevD.58.057704).  
 3990 URL: <http://link.aps.org/doi/10.1103/PhysRevD.58.057704>.
- 3992 [65] C. Friberg, E. Norrbin, and T. Sjostrand. “QCD aspects of leptoquark pro-  
 3993 duction at HERA”. In: *Phys. Lett. B* 403 (1997), pp. 329–334. doi: [10.1016/S0370-2693\(97\)00543-1](https://doi.org/10.1016/S0370-2693(97)00543-1). arXiv: [hep-ph/9704214 \[hep-ph\]](https://arxiv.org/abs/hep-ph/9704214).
- 3995 [66] Herbert K. Dreiner. “An introduction to explicit R-parity violation”. In:  
 3996 (1997). arXiv: [hep-ph/9707435](https://arxiv.org/abs/hep-ph/9707435).
- 3997 [67] Edmond L. Berger and Zack Sullivan. “Lower limits on R-parity-violating  
 3998 couplings in supersymmetry”. In: *Phys. Rev. Lett.* 92 (2004), p. 201801. doi:  
 3999 [10.1103/PhysRevLett.92.201801](https://doi.org/10.1103/PhysRevLett.92.201801). arXiv: [hep-ph/0310001](https://arxiv.org/abs/hep-ph/0310001).

- 4000 [68] R. Barbieri, C. Berat, M. Besancon, M. Chemtob, A. Deandrea, et al. “R-  
4001 parity violating supersymmetry”. In: *Phys. Rept.* 420 (2005), p. 1. doi: [10.1016/j.physrep.2005.08.006](https://doi.org/10.1016/j.physrep.2005.08.006). arXiv: [hep-ph/0406039](https://arxiv.org/abs/hep-ph/0406039).
- 4003 [69] M. Fairbairn et al. “Stable massive particles at colliders”. In: *Phys. Rept.* 438  
4004 (2007), p. 1. doi: [10.1016/j.physrep.2006.10.002](https://doi.org/10.1016/j.physrep.2006.10.002). arXiv: [hep-ph/0611040](https://arxiv.org/abs/hep-ph/0611040).
- 4006 [70] Christopher F. Kolda. “Gauge-mediated supersymmetry breaking: Intro-  
4007 duction, review and update”. In: *Nucl. Phys. Proc. Suppl.* 62 (1998), p. 266.  
4008 doi: [10.1016/S0920-5632\(97\)00667-1](https://doi.org/10.1016/S0920-5632(97)00667-1). arXiv: [hep-ph/9707450](https://arxiv.org/abs/hep-ph/9707450).
- 4009 [71] Howard Baer, Kingman Cheung, and John F. Gunion. “A Heavy gluino as  
4010 the lightest supersymmetric particle”. In: *Phys. Rev. D* 59 (1999), p. 075002.  
4011 doi: [10.1103/PhysRevD.59.075002](https://doi.org/10.1103/PhysRevD.59.075002). arXiv: [hep-ph/9806361](https://arxiv.org/abs/hep-ph/9806361).
- 4012 [72] S. James Gates Jr. and Oleg Lebedev. “Searching for supersymmetry in  
4013 hadrons”. In: *Phys. Lett. B* 477 (2000), p. 216. doi: [10.1016/S0370-2693\(00\)00172-6](https://doi.org/10.1016/S0370-2693(00)00172-6). arXiv: [hep-ph/9912362](https://arxiv.org/abs/hep-ph/9912362).
- 4015 [73] Glennys R. Farrar and Pierre Fayet. “Phenomenology of the Production,  
4016 Decay, and Detection of New Hadronic States Associated with Supersym-  
4017 metry”. In: *Phys. Lett. B* 76 (1978), pp. 575–579. doi: [10.1016/0370-2693\(78\)90858-4](https://doi.org/10.1016/0370-2693(78)90858-4).
- 4019 [74] A. C. Kraan, J. B. Hansen, and P. Nevski. “Discovery potential of R-hadrons  
4020 with the ATLAS detector”. In: *Eur. Phys. J. C* 49 (2007), pp. 623–640. doi:  
4021 [10.1140/epjc/s10052-006-0162-x](https://doi.org/10.1140/epjc/s10052-006-0162-x). arXiv: [hep-ex/0511014](https://arxiv.org/abs/hep-ex/0511014)  
4022 [[hep-ex](#)].
- 4023 [75] Rasmus Mackeprang and David Milstead. “An Updated Description of  
4024 Heavy-Hadron Interactions in GEANT-4”. In: *Eur. Phys. J. C* 66 (2010), pp. 493–  
4025 501. doi: [10.1140/epjc/s10052-010-1262-1](https://doi.org/10.1140/epjc/s10052-010-1262-1). arXiv: [0908.1868](https://arxiv.org/abs/0908.1868)  
4026 [[hep-ph](#)].
- 4027 [76] ATLAS Collaboration. “Search for massive, long-lived particles using mul-  
4028 titrak displaced vertices or displaced lepton pairs in  $pp$  collisions at  $\sqrt{s} =$   
4029 8 TeV with the ATLAS detector”. In: *Phys. Rev. D* 92 (2015), p. 072004.  
4030 doi: [10.1103/PhysRevD.92.072004](https://doi.org/10.1103/PhysRevD.92.072004). arXiv: [1504.05162](https://arxiv.org/abs/1504.05162) [[hep-ex](#)].  
4031 SUSY-2014-02.
- 4032 [77] ATLAS Collaboration. “Search for charginos nearly mass degenerate with  
4033 the lightest neutralino based on a disappearing-track signature in  $pp$  col-  
4034 lisions at  $\sqrt{s} = 8$  TeV with the ATLAS detector”. In: *Phys. Rev. D* 88 (2013),  
4035 p. 112006. doi: [10.1103/PhysRevD.88.112006](https://doi.org/10.1103/PhysRevD.88.112006). arXiv: [1310.3675](https://arxiv.org/abs/1310.3675)  
4036 [[hep-ex](#)]. SUSY-2013-01.
- 4037 [78] ATLAS Collaboration. “Searches for heavy long-lived sleptons and R-Hadrons  
4038 with the ATLAS detector in  $pp$  collisions at  $\sqrt{s} = 7$  TeV”. In: *Phys. Lett. B*  
4039 720 (2013), p. 277. doi: [10.1016/j.physletb.2013.02.015](https://doi.org/10.1016/j.physletb.2013.02.015). arXiv:  
4040 [1211.1597](https://arxiv.org/abs/1211.1597) [[hep-ex](#)]. SUSY-2012-01.

- 4041 [79] ATLAS Collaboration. “Searches for heavy long-lived charged particles  
 4042 with the ATLAS detector in proton–proton collisions at  $\sqrt{s} = 8$  TeV”.  
 4043 In: *JHEP* 01 (2015), p. 068. doi: [10.1007/JHEP01\(2015\)068](https://doi.org/10.1007/JHEP01(2015)068). arXiv:  
 4044 [1411.6795 \[hep-ex\]](https://arxiv.org/abs/1411.6795). SUSY-2013-22.
- 4045 [80] ATLAS Collaboration. “Search for metastable heavy charged particles with  
 4046 large ionisation energy loss in  $pp$  collisions at  $\sqrt{s} = 8$  TeV using the AT-  
 4047 LAS experiment”. In: *Eur. Phys. J. C* 75 (2015), p. 407. doi: [10.1140/epjc/s10052-015-3609-0](https://doi.org/10.1140/epjc/s10052-015-3609-0). arXiv: [1506.05332 \[hep-ex\]](https://arxiv.org/abs/1506.05332). SUSY-  
 4049 2014-09.
- 4050 [81] ATLAS Collaboration. “Search for heavy long-lived charged  $R$ -hadrons  
 4051 with the ATLAS detector in  $3.2 \text{ fb}^{-1}$  of proton–proton collision data at  
 4052  $\sqrt{s} = 13$  TeV”. In: *Phys. Lett. B* 760 (2016), pp. 647–665. doi: [10.1016/j.physletb.2016.07.042](https://doi.org/10.1016/j.physletb.2016.07.042). arXiv: [1606.05129 \[hep-ex\]](https://arxiv.org/abs/1606.05129).
- 4054 [82] Torbjorn Sjöstrand, Stephen Mrenna, and Peter Skands. “PYTHIA 6.4 Physics  
 4055 and Manual”. In: *JHEP* 0605 (2006), p. 026. doi: [10.1088/1126-6708/2006/05/026](https://doi.org/10.1088/1126-6708/2006/05/026). arXiv: [hep-ph/0603175](https://arxiv.org/abs/hep-ph/0603175).
- 4057 [83] ATLAS Collaboration. *Further ATLAS tunes of PYTHIA 6 and Pythia 8*. ATL-  
 4058 PHYS-PUB-2011-014. 2011. URL: <https://cds.cern.ch/record/1400677>.
- 4060 [84] Aafke Christine Kraan. “Interactions of heavy stable hadronizing parti-  
 4061 cles”. In: *Eur. Phys. J. C* 37 (2004), pp. 91–104. doi: [10.1140/epjc/s2004-01946-6](https://doi.org/10.1140/epjc/s2004-01946-6). arXiv: [hep-ex/0404001 \[hep-ex\]](https://arxiv.org/abs/hep-ex/0404001).
- 4063 [85] M. Fairbairn et al. “Stable massive particles at colliders”. In: *Phys. Rept.* 438  
 4064 (2007), p. 1. doi: [10.1016/j.physrep.2006.10.002](https://doi.org/10.1016/j.physrep.2006.10.002). arXiv: [hep-ph/0611040](https://arxiv.org/abs/hep-ph/0611040).
- 4066 [86] W. Beenakker, R. Hopker, M. Spira, and P. M. Zerwas. “Squark and gluino  
 4067 production at hadron colliders”. In: *Nucl. Phys. B* 492 (1997), p. 51. doi:  
 4068 [10.1016/S0550-3213\(97\)00084-9](https://doi.org/10.1016/S0550-3213(97)00084-9). arXiv: [hep-ph/9610490](https://arxiv.org/abs/hep-ph/9610490).
- 4069 [87] A. Kulesza and L. Motyka. “Threshold resummation for squark-antisquark  
 4070 and gluino-pair production at the LHC”. In: *Phys. Rev. Lett.* 102 (2009),  
 4071 p. 111802. doi: [10.1103/PhysRevLett.102.111802](https://doi.org/10.1103/PhysRevLett.102.111802). arXiv: [0807.2405 \[hep-ph\]](https://arxiv.org/abs/0807.2405).
- 4073 [88] A. Kulesza and L. Motyka. “Soft gluon resummation for the production  
 4074 of gluino-gluino and squark-antisquark pairs at the LHC”. In: *Phys. Rev. D* 80 (2009), p. 095004. doi: [10.1103/PhysRevD.80.095004](https://doi.org/10.1103/PhysRevD.80.095004). arXiv:  
 4076 [0905.4749 \[hep-ph\]](https://arxiv.org/abs/0905.4749).
- 4077 [89] Wim Beenakker, Silja Brening, Michael Kramer, Anna Kulesza, Eric Lae-  
 4078 nen, et al. “Soft-gluon resummation for squark and gluino hadroproduction”. In: *JHEP* 0912 (2009), p. 041. doi: [10.1088/1126-6708/2009/12/041](https://doi.org/10.1088/1126-6708/2009/12/041). arXiv: [0909.4418 \[hep-ph\]](https://arxiv.org/abs/0909.4418).
- 4081 [90] W. Beenakker, S. Brening, M.n Kramer, A. Kulesza, E. Laenen, et al. “Squark  
 4082 and Gluino Hadroproduction”. In: *Int. J. Mod. Phys. A* 26 (2011), p. 2637.  
 4083 doi: [10.1142/S0217751X11053560](https://doi.org/10.1142/S0217751X11053560). arXiv: [1105.1110 \[hep-ph\]](https://arxiv.org/abs/1105.1110).

- 4084 [91] Michael Krämer et al. *Supersymmetry production cross sections in pp collisions*  
 4085 *at  $\sqrt{s} = 7 \text{ TeV}$* . 2012. arXiv: [1206.2892 \[hep-ph\]](#).
- 4086 [92] Rasmus Mackeprang and Andrea Rizzi. “Interactions of Coloured Heavy  
 4087 Stable Particles in Matter”. In: *Eur. Phys. J.* C50 (2007), pp. 353–362. doi:  
 4088 [10.1140/epjc/s10052-007-0252-4](#). arXiv: [hep-ph/0612161 \[hep-ph\]](#).
- 4089 [93] Rasmus Mackeprang and David Milstead. “An Updated Description of  
 4090 Heavy-Hadron Interactions in GEANT-4”. In: *Eur. Phys. J.* C66 (2010), pp. 493–  
 4091 501. doi: [10.1140/epjc/s10052-010-1262-1](#). arXiv: [0908.1868 \[hep-ph\]](#).
- 4092 [94] J. Alwall, R. Frederix, S. Frixione, V. Hirschi, F. Maltoni, O. Mattelaer, H. S.  
 4093 Shao, T. Stelzer, P. Torrielli, and M. Zaro. “The automated computation of  
 4094 tree-level and next-to-leading order differential cross sections, and their  
 4095 matching to parton shower simulations”. In: *JHEP* 07 (2014), p. 079. doi:  
 4096 [10.1007/JHEP07\(2014\)079](#). arXiv: [1405.0301 \[hep-ph\]](#).
- 4097 [95] “dE/dx measurement in the ATLAS Pixel Detector and its use for particle  
 4098 identification”. In: (2011).
- 4099 [96] ATLAS Collaboration. “The ATLAS Simulation Infrastructure”. In: *Eur.*  
 4100 *Phys. J.* C70 (2010), pp. 823–874. doi: [10.1140/epjc/s10052-010-1429-9](#). arXiv: [1005.4568 \[physics.ins-det\]](#).
- 4101 [97] Alexander L. Read. “Presentation of search results: The CL(s) technique”.  
 4102 In: *J. Phys.* G28 (2002). [,11(2002)], pp. 2693–2704. doi: [10.1088/0954-3899/28/10/313](#).
- 4103
- 4104
- 4105
- 4106

4107 DECLARATION

---

4108 Put your declaration here.

4109 *Berkeley, CA, September 2016*

4110

---

Bradley Axen

4111

4112 COLOPHON

4113 Not sure that this is necessary.